A Study of Vitreous-Bonded Abrasive Materials

Mark James Jackson, M. Eng., A.M.I.Mech.E., A.M.I.M.

A thesis submitted in partial fulfilment of the requirements of Liverpool John Moores University for the degree of Doctor of Philosophy

December 1995

ACKNOWLEDGEMENTS

My wife, Joanne, for her support and encouragement during the past four years.

Professors Ben Mills and Neil Barlow, my supervisors, for their guidance and encouragement.

Professor W.B.Rowe for use of the laboratory facilities.

Dr. Diane Holland and Professor M.H.Lewis, Centre for Advanced Materials-University of Warwick, for differential thermal analysis of clays and fluxes.

Professor Gordon Lorimer, Materials Science Centre-University of Manchester, for quantitative metallography of workpiece materials.

Dr. Richard Hall and Mr. Paul Dando, Unicorn Abrasives' Central R. and D. Laboratory, for continued support since September 1992.

Mrs. Jacqueline Nash for typing this thesis.

Mrs. Pat Williams, Inter-library Loans Unit, and Mrs. Paula Gorman and Miss Gillian Williams, Engineering Library, for all their help over the past four years.

Mr. A. Cunningham and Mr. Stephen McCarthy for assistance during the grinding trials.

Mr. P. Wright and Mr. S. Ebbrell for technical support and manufacture of moulds.

This work was supported by the Engineering and Physical Sciences Research Council under grant number 9156287X.

VITA

Mark James Jackson began his engineering career in 1983 studying for his O.N.C. part I examinations and completing his first-year apprenticeship training course in 1984 at Halton College. The author then studied for his Ordinary National Diploma in Engineering gaining distinctions in his final-year subjects, and was awarded the I.C.I. prize for achievement in 1986.

While studying for a thick-sandwich engineering degree, the author was employed as a plant engineer at I.C.I. Pharmaceuticals in Macclesfield and Anglo Blackwells in Widnes. The author graduated in 1991 with a Master of Engineering degree with Distinction in Mechanical and Manufacturing Engineering from the then Liverpool Polytechnic after successfully defending a dissertation on 'Mechanical Stirring of Aluminium-Boron Alloys'.

The author then began research work on vitreous-bonded grinding wheels under the supervision of Professors Mills and Barlow at Liverpool John Moores University. After a period of study at Gonville and Caius College, University of Cambridge, and at the University of Liverpool studying electron microscopy, the author published a number of conference and research papers on aspects of his doctoral studies and lectured on the science of materials and manufacturing technology.

Since completing his research work, the author gained employment with Unicorn Abrasives' Central R & D Laboratory conducting research into diamond and C.B.N. abrasive products. The author is actively publishing his research work, is currently writing a book on the tribology of abrasives, and is also compiling a databook on C.B.N. and diamond grinding.

The author is an Associate Member of the Institution of Mechanical Engineers, Associate Member of the Institute of Materials, and has served on the Institute of Materials' North-West Regional Co-ordinating Committee. The author was elected Honorary Secretary of the Liverpool and North Wales Materials Society for the 1995/96 season.

PAPERS PUBLISHED DURING THIS RESEARCH WORK

1. CONFERENCE PAPERS

1.1. M.J.JACKSON and B.MILLS, 'A Review of C.B.N. Grinding Wheel Performance', Presented at the 6th International Manufacturing Conference with China, Hong Kong, 10th-12th March 1993.

1.2. M.J.JACKSON, N.BARLOW and B.MILLS, 'The Effect of Bond Composition on the Strength of Vitreous-bonded Grinding Wheels' , Presented at the Society of Glass Technology's Research Forum on Glass, University of Warwick, 14th December 1993.

1.3. M.J.JACKSON, N.BARLOW and B.MILLS, 'Dependence of Glass Content on the Safety of Vitreous-bonded Grinding Wheels', Presented at the Second Research Forum on Glass (Society of Glass Technology), University of Warwick, 4th April 1995.

2. RESEARCH PAPERS

2.1. M.J.JACKSON and B.MILLS, 'A Review of C.B.N. Grinding Wheel Performance', Proceedings of the 6th International Manufacturing Conference with China, Volume 2, International Academic Publishers, March 1993, p.p. 93-95.

2.2. M.J.JACKSON, N. BARLOW and B.MILLS, 'Effect of Bond Composition on the Strength of Partially-bonded Ceramic Abrasives', Journal of Materials Science Letters, (1994), 13, p.p. 1287-1289.

2.3. N. BARLOW, M.J.JACKSON, B.MILLS and W.B.ROWE, 'Optimum Clamping of Conventional and C.B.N. Vitreous-bonded Grinding Wheels', International Journal of Machine Tools and Manufacture (1995), 35, p.p. 119-132.

2.4. M.J.JACKSON, N.BARLOW, B.MILLS and W.B.ROWE, 'Mechanical Design Safety of Vitreous-bonded Cylindrical Grinding Wheels', British Ceramic Transactions (1995), 94, p.p. 221-229.

ABSTRACT

This thesis has focused primarily on the effect of bond and workpiece composition on the performance of vitreous-bonded alumina grinding wheels. The effect of bond composition considered in this work can equally be applied to grinding wheels which use silicon carbide (carborundum) as the abrasive medium.

The bonds considered in this study are described as sintering bonds (high clay content), used in silicon carbide grinding wheels, and fusible bonds (high glass content), used in vitreous bonding systems suitable for use in aluminium oxide grinding wheels.

The initial part of the research work deals with a review of the mechanisms of grinding and the evaluation of wheel performance. The effect of grinding conditions, abrasive compositions, and workpiece material composition on the mechanisms of grinding wheel wear in conventional wheels was studied. The analysis of grinding wheel wear was examined and compared with experimental data.

Reactions in grinding wheel bond materials were examined by comparing theoretical equilibrium compositions with actual reaction products using experimental techniques such as x-ray powder methods and differential thermal analysis.

Experimental studies were carried out to investigate the vitrification behaviour of sintering and fusible bonds. This was achieved by examining the relationship between theoretical equilibrium liquid and silica contents and experimental vitrification conditions. A semi-empirical model was developed for determining optimum firing conditions for sintering and fusible bonds.

The effect of bond composition on the strength of sintering and fusible bonds, under fixed firing conditions, was investigated. This resulted in some bonds failing by cracks around quartz particles, whilst bonds with high glass contents failed by a combination of pore-flaws. A model was also developed which predicted the amount of quartz remaining after heat treatment. The model was shown to be accurate when compared with experimental data.

Based on the results of the experimental work on bond characterisation, the effect of bond and workpiece composition was compared with grinding wheel performance data. This was achieved by grinding a variety of hardened tool steels with abrasive segments manufactured with optimised grades. An empirical model was developed which showed that wheel wear was a function of bond strength and the nature of complex carbides present in the microstructure of the tool steels.

CONTENTS

NOMENCLATURE

A	-	subscript denoting mixture.
A	-	constant related to bond/workpiece material composition.
A	-	constant referring to elements Ni,Co,Mn,Cr,Fe,V and Ti.
A_n	-	abrasive number (kg/mm^2).
A_{actual}	-	actual area of contact between wear flats and the workpiece material (mm^2).
A	-	density of abrasive (kg/m^3).
A_v	-	volume of abrasive (m^3).
A_w	-	weight of abrasive (kg).
A.P.	-	apparent porosity (%).
a	-	depth of cut (mm), constant, and a constant related to particle size distribution.
a	-	constant related to oxide contribution to thermal expansion of glass.
B	-	subscript denoting clay solid.
B	-	constant related to bond/workpiece material composition.
B	-	constant referring to elements Mo,Ta,Hf,W, and Nb.
B	-	density of bond (kg/m^3).
B_v	-	volume of bond (m^3).
B_w	-	weight of bond (kg).
B_x	-	bond size.
b	-	constant and grinding width (mm).
b_1, b_2, b_3	-	constant.
C	-	refers to the element carbon.
C	-	wt. % clay.
C	-	constant.
C	-	crack length (mm).
C*	-	volume fraction carbides in workpiece material.

D, D_o, D_T - diffusion constants.

d_e - effective diameter (mm).

d_s - diameter of grinding wheel (mm).

E - Young's modulus (N/mm^2).

F - wt. % flux.

F_t - tangential grinding force (N).

F_n - normal grinding force (N).

f_{grit} - grinding force acting on the grit (N).

G - grinding ratio (mm^3/mm^3).

G - % glass content (wt.%).

H_{matrix} - hardness of matrix (kg/mm^2).

$H_{carbide}$ - hardness of carbide (kg/mm^2).

h_m - maximum depth of cut (µm).

h' - depth of cut at the onset of cutting (µm).

i - ignition loss or % lost in bond weight when fired.

K - constant, reaction rate.

K_A - wt.% K_2O in the mixture.

K_B - wt.% K_2O in the clay solid.

K_L - wt.% K_2O in the liquid.

L - subscript denoting liquid, spacing between porosity (µm).

L_o - original length between particle centres (µm).

$\triangle L$ - change in length between particle centres (µm).

$\triangle L/L_o$ - linear shrinkage (%).

l	-	arc length of segment (mm).
Δl	-	increase in length of test specimen (mm).
l_1	-	original length of test specimen (mm).
l_2	-	final length of test specimen (mm).
l_c	-	contact length (mm).
M	-	wt.% mullite content, original mass of quartz (kg).
m	-	Weibull modulus, mass of quartz after time t(s).
m_b	-	mass of bond (kg).
$m_{dextrin}$	-	mass of dextrin (kg).
m_{grit}	-	mass of grit (kg).
N_s	-	structure number.
n	-	constant.
P	-	power (kW).
p	-	porosity (vol.%), weighting factor for a particular oxide.
p_o	-	structural wheel characteristic.
p	-	average constant pressure (N/mm^2).
Q	-	wt.% quartz content, activation energy (k cal/mol).
Q_w	-	volumetric metal removal rate (mm^3/s).
$Q_{w,n}$	-	structural wheel characteristics.
Q_s	-	volumetric wheel wear rate (mm^3/s).
q_s	-	attritious wear parameter.
R	-	universal gas constant (J/kg K).
r	-	rate of heating (°C/hr), radius of contacting particle (µm).
r'	-	quartz particle radius after time, t, (µm).
Δr	-	penetration depth (µm).

S	-	strength (N/mm^2).
S_o	-	strength at zero porosity (N/mm^2).
S_A	-	wt.% silica in mixture.
S_B	-	wt.% silica in clay solid.
S_L	-	wt.% silica in liquid.
T	-	temperature (°K.).
$\triangle T$	-	temperature range for measuring coefficient of linear expansion (°K).
T.P.	-	% true porosity.
t	-	time (s).
t	-	heating time above the eutectic temperature.
u	-	constant, specific grinding energy (J/mm^3).
V	-	degree of vitrification, absolute volume (m^3).
V_o	-	original volume (mm^3).
$\triangle V$	-	change in volume (m^3).
$\triangle V/V_o$	-	volume shrinkage (%).
V_B	-	wt.% bond.
$1/V_B$	-	bond weakness factor.
v	-	volume after time t (m^3).
V_b	-	volume of bond (m^3).
V_{clay}	-	volume of clay (m^3).
V_{bar}	-	volume of bar (m^3).
$V_{carbide}$	-	volume of carbide (m^3).
V_{flux}	-	volume of flux (m^3).
V_g	-	volume of grit (m^3).
V_{matrix}	-	volume of matrix (m^3).
V_p	-	volume of porosity (m^3).
V_{quartz}	-	volume of quartz (m^3).
v_s	-	wheel speed (m/s)
v_w	-	workpiece speed (mm/s).
v_{ft}	-	feedrate in the tangential direction (mm/min).

W_{bond} - weight of bond (kg).

W_{grit} - weight of grit (kg).

W_{total} - total weight of bond mixture (kg).

W.A. - % water absorption.

X - constant.

x - distance from centre to neck of two contacting particles (μm), molar fraction of Na_2O (mol.%).

Z - volume of quartz dissolved (m^3).

α - rake angle, constant related to bond/workpiece composition, coefficient of linear expansion (/°C).

α_{exp} - experimental coefficient of linear expansion (/°C).

$\alpha_{segment}$ - angle subtended by abrasive segment.

β - constant related to bond and workpiece composition and G-ratio, attack angle, constant.

γ - constant.

γ_i - fracture initiation energy (J/m^2).

γ_t - surface tension (J/m^2).

ε - mean size of crystalline particles (μm).

λ - constant, Saint Venant volume (m^3).

η - viscosity (Pa s), type of carbide.

τ - constant.

μ - coefficient of friction.

ρ - density (kg/m³).

ρ_{real} - real density (kg/m³).
$\rho_{apparent}$ - apparent density (kg/m³).
ρ_{wheel} - wheel density (kg/m³).
$\rho_{mixture}$ - mixture density (kg/m³).
ρ_{bond} - bond density (kg/m³).

σ_t - tensile strength (N/mm²).
σ_b - bending strength (flexure) (N/mm²).
$\sigma_{failure}$ - average failure stress (N/mm²).
σ_o - strength of ceramic body at zero porosity (N/mm²).

LIST OF FIGURES

LIST OF TABLES

INTRODUCTION

A grinding wheel is composed of an abrasive phase which cuts the workpiece material being ground, a bond phase which holds the abrasive phase in a complex three-dimensional matrix, and a distribution of pores which provides clearance for workpiece swarf and supplies coolant to the working face. Grinding and polishing techniques have been developed by man since the Neolithic ages [1].

The development of vitreous-bonded grinding wheels was started in England by Henry Barclay in 1842 who patented a process for 'an emery wheel using equal parts of Stourbridge clay and emery, pressing the wet mixture into moulds, and subjecting it to a bright red heat' [2].

This was further developed in Germany when, in 1861, a porcelain factory at Engersburg produced grinding wheels using quartz sand mixed with various clays and fired to glass hardness.

Developments in the U.S.A. advanced these grinding wheels when Swen Pulson announced that he had improved Gilbert Hart's silicate-bonded wheel. Pulson, a potter in Franklin Norton's factory in Worcester, Massachusetts, mixed emery, clay and slip clay to form wheels, which at first, melted and ran or blistered when fired. Some years later Pulson used feldspar in place of slip clay with huge success [1].

Modern abrasives are mostly synthesized conventional and superabrasive types which use a variety of bonding systems to give a desired grinding performance.

Conventional abrasives such as alumina and silicon carbide use vitreous bonds with different compositions owing to the chemical reactions between grit and bond.

Vitrified alumina wheels are bonded with fusible bonds (high glass content), whereas vitrified silicon carbide wheels are bonded with sintering bonds (high clay content).

Vitrified superabrasive grinding wheels utilizing diamond or cubic boron nitride as the abrasive, require bonds which can be fired at lower temperatures in order to minimise the reaction between bond and abrasive. Diamond and cubic boron nitride (C.B.N.) grits are sometimes coated with metals such as titanium which allows higher firing temperatures to be used.

The performance of vitreous-bonded grinding wheels is controlled by material properties such as the type of grit used, grit size, shape, and the type of bond used. Grade, hardness and structure also play an important part.

The performance of a grinding wheel is therefore dependent on the workpiece composition, the nature of the grinding operation, the grade of wheel and the abrasive grit, and bond used. Traditionally, 'black art' has been used to match a particular wheel specification to a particular workpiece.

The aim of the research was to investigate the effect of bond and workpiece composition on the performance of vitreous-bonded grinding wheels. The major objectives were to study the effects of heat treatment on vitreous bond and grinding wheel properties, and to study the effect of vitreous bond and workpiece material composition on grinding wheel performance.

The research programme was structured into four sections. The first section focused on a thorough review of the literature concerning the theory of grinding and the evaluation of grinding wheel performance.

Grinding wheel wear mechanisms and the analysis of wear were reviewed; these showed the relationship between wheel wear and grinding wheel performance in terms of grit, and grinding conditions. The effect of heat on the reactions in vitreous bonds was also reviewed.

The second section focused on experimental studies concerned with the vitrification behaviour of 'sintering' and 'fusible' vitreous bonds. Theoretical equilibrium compositions were compared with experimental reaction products using equilibrium diagrams, x-ray powder methods, and differential thermal analysis. As a result of this work, an empirical model was developed for determining optimum firing conditions for different bond compositions. The model was based on the degree of vitrification attained during the heating, soaking, and cooling periods of heat treatment. However, optimum firing conditions were not applied when the effect of bond composition on strength was examined.

The third section focused on the characterisation of grinding wheel bonds. All bond compositions were subjected to the same heat treatment so that some bonds were under-fired, fully vitrified, and over fired. These compositions were subjected to strength testing. This resulted in some bonds failing by cracks around quartz particles and some failing by pore-crack flaws. A theoretical model was developed that predicted the amount of quartz remaining after heat treatment. The model compared well with experimental data from the present study. The model also proved to be accurate when compared with experimental data from previous studies.

The fourth section focused on relating the studies on bond characterisation to grinding wheel performance. A selection of tool steels were ground with grinding wheel structures having optimised grades for the workpiece materials being ground.

The grades were specified in Unicorn Abrasives' Grinding Data Book [3]. An empirical model was developed from the results which showed that grinding wheel wear was an exponential decay function of bond strength and workpiece material composition.

The final section of this thesis provides a general discussion on grinding wheel performance in relation to the work presented in this thesis and the work done by other investigators.

SECTION 1

LITERATURE SURVEY

1. GRINDING MECHANISMS AND WHEEL PERFORMANCE

1.1 INTRODUCTION

Material removal during grinding occurs as abrasive grits interact with the workpiece. The penetration depth is dependent on the topography of the wheel surface and the geometric and kinematic motion of the wheel and the workpiece.

In order to identify the grinding mechanisms involved in abrasive-workpiece interactions a number of approaches can be considered. Firstly, the shape of grinding swarf can be analysed using a scanning electron microscope (S.E.M.) in order to theorise possible mechanisms of chip formation. Secondly, grinding forces and power may be monitored over a range of grinding conditions in order to derive the specific grinding energy which is defined as the energy expended per unit volume of material removed. The significance of this parameter allows one to satisfy an energy balance which can account for the magnitude of the specific energy used in the process depending on the proposed abrasive-workpiece interaction mechanisms. A more direct observation of the interaction of abrasive and workpiece can be obtained from cutting experiments with single abrasive grits, or with tools shaped like grits.

Grinding wheel performance can be determined quantitatively by measuring the ratio of volume of workpiece to wheel - removed (G-ratio) and specific grinding energy for each grade of grinding wheel tested.

1.2. MICROSCOPIC OBSERVATIONS

The similarities between grinding detritus and larger-scale metal cutting chips are shown in Figures 1.1 and 1.2.

The micrographs show swarf recovered after grinding a plain-carbon steel.

Curled chips are usually found that are irregular in size and shape and are due to the variations in penetration depth and cutting-point shape. The chip shown in Figure 1.1 has a lamellar structure (spacing $\approx$ 0.5μm) which is caused by an instability mainly due to intense plastic deformation. This results in massive localised heating and a decrease in the shear resistance of the material being formed into a chip [4].

Two types of debris are also formed - short blocky chips and spheres. Blocky-chip formation is caused by an extrusion-like bulging process with extreme negative rake angles [5]. Spherical grinding particles have fine dendritic microstructures appearing on their surface which indicates that these small grinding chips were initially molten then solidified rapidly.

These chips react exothermally with oxygen surrounding the workpiece and wheel.

1.3. GRINDING FORCES AND SPECIFIC ENERGY

Forces developed in grinding metals for surface grinding operations are shown in Figure 1.3. The total force vector exerted by the workpiece against the wheel can be separated into a tangential force component, F_t and a normal force component, F_n. When grinding with a traverse feed, there is an additional force component parallel to the wheel axis.

The grinding power associated with the wheel shown in Figure 1.3 can be written as,

$$P = F_t\ (v_s - v_w) \qquad \ldots(1.1)$$

This indicates that down-grinding is used, i.e. when both velocities are in the same direction. Since v_w is much lower than v_s the total power approximates to,

$$P = F_t \cdot v_s \qquad \ldots(1.2)$$

A fundamental parameter derived from this equation and the machining conditions is the specific cutting energy, which is defined as the energy per unit volume of material removed. The specific grinding energy ,u, is given by,

$$u = \frac{P}{Q_w} \qquad \ldots(1.3)$$

where P is power and Q_w is the volumetric metal removal rate, which, in terms of grinding parameters is,

$$Q_w = V_{ft}.a.b \qquad \ldots(1.4)$$

where b is the grinding width and a is depth of cut, and V_{ft} is the feedrate in the tangential direction.

1.4. GRINDING MECHANISMS FOR CONVENTIONAL ABRASIVES

1.4.1. Energy considerations and the size effect

Measurements of forces and specific energies in grinding began in the 1950's which showed that specific energies were much larger than in single-point metal cutting operations [6,7].

Larger specific energies are also obtained by reducing the undeformed chip thickness which is caused by changing the process parameters.

According to Merchant [8] chip formation produces an extremely thin shearing zone followed by friction as the chip slides over the tool-rake face. Shearing accounts for about 75% of the total chip-formation energy, and chip-tool friction the remaining 25%. An attempt was made to interpret grinding forces in terms of Merchant's model [7].

Assuming the tool geometry to be ideal, estimates of the shear stress for plastic deformation during chip formation were obtained, however, these shear stresses exceeded the known flow stress of the material being ground. In addition large shear stresses were generally obtained with smaller undeformed chip thicknesses.

A 'size effect' theory was subsequently proposed which attributes the increase in flow stress with smaller undeformed chip thicknesses producing small volumes of sheared material free of strength-impairing flaws, i.e. dislocations. However, dislocation theory predicts high dislocation densities in the shear zone which has been experimentally verified using transmission electron microscopy [9]. It has also been proved that specific grinding energies are higher than the energy required for melting the workpiece which seems, at first, to be inconceivable.

1.4.2. Sliding forces and energy

Much of the energy used in grinding is expended by mechanisms other than by chip formation. One mechanism involves the generation of wear flats on abrasive grit tips without removing any workpiece material [10]. The growth of wear flats is offset, somewhat, by 'self-sharpening' due to wear of the wheel whereby some wear flats are removed by grit fracture or grit dislodgement from the bond.

Wear flat areas indicate that some of the energy expended during grinding is due to their sliding against the workpiece. Assuming grinding conditions do not change, the normal and tangential forces increase with wear flat area. Tests conducted on various workpiece materials have shown that workpiece burn occurred with various steels due to phase transformations in the material being ground.

Malkin and Cook [10] considered that specific energy consisted of cutting and sliding components. When the wear flat area is zero cutting forces are due to cutting and additional values are due to sliding, such that

$$F_t = F_{t,cutting} + F_{t,sliding} \qquad ...(1.5)$$

and

$$F_n = F_{n,cutting} + F_{n,sliding} \qquad ...(1.6)$$

where $F_{t,cutting}$ and $F_{n,cutting}$ are tangential and normal components of cutting forces, and $F_{t,sliding}$ and $F_{n,sliding}$ are tangential and normal components of sliding forces. This situation is illustrated in Figure 1.4. The proportional relationships developed before the onset of workpiece burn implies that a constant average contact stress $\bar{p}$ and coefficient of friction μ exists between the wear flats and the workpiece. Therefore, equations 1.5 and 1.6 can be expressed as

$$F_t = F_{t,cutting} + \bar{p}.\mu.A_{actual} \qquad ...(1.7)$$

and

$$F_n = F_{n,cutting} + \bar{p}.A_{actual} \qquad ...(1.8)$$

where A_{actual} is the actual area of contact between the wear flats and the workpiece. The area A_{actual} is calculated by multiplying the grinding zone area, which is the contact length multiplied by the grinding width, by the fraction of wheel surface containing wear flats, hence,

$$A_{actual} = b.l_c.A \qquad ...(1.9)$$

the contact length, l_c, can be expressed by,

$$l_c = \sqrt{d_e.a} \qquad ...(1.10)$$

Therefore equation 1.8 becomes,

$$A_{actual} = \sqrt{d_e.a.A} \qquad ...(1.11)$$

where d_e is the equivalent diameter of the wheel and a is the depth of cut. Combining equations 1.7, 1.8 and 1.11 yields,

$$F_t = F_{t,cutting} + \mu.\bar{p}.b.\sqrt{d_e.a.A} \qquad ...(1.12)$$

and $$F_n = F_{n,cutting} + \bar{p}.b.\sqrt{d_e.a.A} \qquad ...(1.13)$$

The magnitudes of μ and $\bar{p}$ can be evaluated by combining equations 1.7 and 1.8

$$F_n = \frac{1}{\mu} F_t + \mu\frac{F_{n,cutting} - F_{t,cutting}}{\mu} \qquad ...(1.14)$$

For constant grinding conditions $F_{t,cutting}$ and $F_{n,cutting}$ are constant, therefore, a graph of F_n versus F_t should give a straight line with a gradient equal to $1/\mu$. This behaviour is shown in Figure 1.5 for grinding plain carbon steel [11].

The initial slope shown in Figure 1.5 up to the discontinuity point gives a coefficient of friction of 0.4. Beyond this point the workpiece burns and the slope becomes steeper.

The average contact pressure $\bar{p}$ can be obtained by differentiating equation 1.13 with respect to A which gives,

$$\bar{p} = \frac{dF_n}{dA} \qquad \ldots(1.15)$$

$b\sqrt{d_e}.a$

It appears that the contact pressure increases with the magnitude of the curvature difference, which is defined as the difference between the wheel radius and the cutting path radius, as shown in Figure 1.6 [12]. Malkin and Cook [10] have found experimental evidence that materials which have higher hot hardness values develop higher contact pressures.

The sliding energy concept allows the influence of wheel grade and dressing conditions to be related, quantitatively, to grinding forces. With harder grade wheels and finer dressing conditions, the wear-flat area is larger and so sliding forces are larger.

1.4.3. Ploughing and chip-forming energies

The specific energy for cutting is calculated from the relationship,

$$u_{cutting} = \frac{F_{t,cutting}.V_s}{b.a.V_{wt}} \qquad \ldots(1.16)$$

The numerator is the power associated with cutting and the denominator is the metal removal rate.

The tangential cutting force $F_{t,cutting}$ is equivalent to that of a perfectly sharp wheel, i.e. wear-flat area is zero. Experiments performed on a range of steels, with varying levels of hardness, exhibited nearly the same specific cutting energy ($u_{cutting} \approx 40 J/mm^3$) at constant metal removal rate [10].

The result was surprising considering the vast differences in recorded workpiece hardness.

After subtracting sliding energy from the equation, it is apparent that a 'size effect' still exists. At slower metal removal rates, which correspond to a finer undeformed chip thickness, the specific cutting energy becomes very large and its magnitude cannot be explained using classical chip-forming models. This suggests that only a small fraction of the specific cutting energy is associated with chip formation. Another mechanism involved in grinding is ploughing. Ploughing energy is expended by deforming the workpiece without metal removal. Ploughing is associated with side flow of workpiece material from the cutting path into ridges, on plastic deformation under the tool face.

Ploughing deformation occurs as the abrasive initially cuts the workpiece as shown in figure 1.7 [5,12-16].

As the cutting point on the abrasive grit passes through the grinding zone, its depth of cut increases from zero to a maximum value h_m at the end of each cut. Initially the grit makes elastic contact followed by plastic deformation (ploughing) of the workpiece. Chip formation occurs after the grit has penetrated some critical depth which is affected by wheel sharpness, cutting-point rake angle and friction angle.

After chip formation begins, ploughing will exist with some material appearing at the side of the chip removal path. This type of action has been investigated by cutting experiments using triangular-based tools to simulate cutting points. The tool is set orthogonally, with one face perpendicular to the cutting edge, or set obliquely with the edge of the tool between two adjacent faces at the front. The orientation of the tilted orthogonal tool is defined by an attack angle ß (Figure 1.8a) corresponding to a rake angle α ;

$$\alpha = ß - 90° \qquad ...(1.17)$$

For ß < 90° as shown in Figure 1.8b, α is negative. For orthogonal cutting tools with triangular-based geometries, a critical rake angle has been found. Below this threshold, sideflow ploughing occurs, above it chip formation occurs [17,18].

The transition point was found to occur within a narrow range of rake angles where ploughing and chip formation occurs. The material removed in this region is in the form of chips, short and blocky, and oblique particle orientations which increase sideflow ploughing.

The use of the down-grinding mode in place of up-grinding should reduce or even eliminate initial ploughing. This is because each grit particle initially engages the workpiece at its maximum depth of cut.

The total specific grinding energy during grinding consists of chip formation, ploughing and sliding components, thus,

$$u = u_{chip} + u_{ploughing} + u_{sliding} \qquad ...(1.18)$$

The specific chip formation energy is the only part of the equation expended during chip formation. Furthermore, it is relatively insensitive to alloying or heat treatment of the workpiece. Experiments have shown that the same minimum grinding energy is required for both low carbon steels and hardened high-speed tool steels [12,20].

It has also been established [19-21] that the specific energy of shearing for iron is roughly 10.4J/mm^3 which is identical to the melting energy required for iron per unit volume. This situation is attributed to large deformations and adiabatic conditions during chip formation in grinding. Cutting points on wheels have extremely large negative rake angles which are more negative than -60° [22]. Larger shear strains are predicted for large negative angles which have been verified experimentally [23].

For adiabatic deformations to large strains, the plastic deformation energy should not exceed the melting energy of the workpiece material. This is shown in Figure 1.9 where a hypothetical stress-strain curve is presented for adiabatic shear [19,20]. The plastic work/volume is converted into heat.

Initial strain hardening is followed by strain softening at an increasing rate, with plastic shear resistance dropping toward zero as the melting point is reached. This does not imply that melting occurs in the material, it tells us that the shear energy approaches the melting energy of the material.

This correlation can be applied to other metallic materials as shown in Figure 1.10. These experiments were carried out using a sharp grinding wheel [19-21].

It has been reported by these authors that heat treatment and alloying of the workpiece has little effect on the minimum specific energy owing to the fact that the melting energy is insensitive to these factors.

1.5 GRINDING WHEEL PERFORMANCE

1.5.1. Introduction

Grinding wheel performance is not only affected by the structure and properties of the finished wheel, but is also affected to a great extent by the metallurgical composition of the workpiece. This research thesis focuses on the effect of alloying constituents and bond composition on grinding wheel performance.

Tarasov [24] ranked tool steels according to a grindability index. The index is limited in scope regarding the performance of wheels because it was based solely on wheel wear.

However, other parameters that affect grinding wheel performance such as grinding forces and power, workpiece surface roughness and bulk hardness of the workpiece are as important as wheel wear.

1.5.2. Evaluating the performance of grinding wheels

An important problem is how to evaluate the performance of abrasive wheels. Traditionally, wheel performance has been judged by the wheel-wear parameter G-ratio. High G-ratios are desirable, but a more wear resistant wheel will lead to higher grinding forces and energies, which will result in thermal damage to the workpiece.

Grinding wheel performance can be measured in a better way by measuring G-ratio and grinding power under fixed conditions [25,26].

The form of the test is to grind a workpiece material with a series of wheels with different grades rather than a single wheel; it is possible to distinguish between wheel quality and wheel hardness effects. Reichenbach [26] studied the effects of using different types of alumina grits and grit sizes on two different die steels. The results indicated that finer grit sizes reduced wheel wear and that the strength and friability of the abrasive also affected wheel performance. The results are shown in Figure 1.11.

Recalling equation 1.18 at a fixed metal removal rate, the ploughing and chip formation components of equation 1.18 remain constant. However, specific sliding energy can be expressed in terms of a volumetric wheel-wear rate Q_s and the attritious wear parameter q_s of the abrasive as [27],

$$u_{sliding} = \frac{P_o \cdot q_s}{Q_{w,n} \cdot Q_s} \qquad ...(1.19)$$

where P_o and $Q_{w,n}$ are structural wheel characteristics which are assumed to be independent of grade [27]. For a volumetric metal removal rate Q_w, the G-ratio is,

$$G = \frac{Q_w}{Q_s} \qquad ...(1.20)$$

Combining equations 1.18, 1.19 and 1.20 yields an expression for specific grinding energy,

$$u = (u_{chip} + u_{ploughing}) + \left\{ \frac{P_o}{Q_{w,n} \cdot Q_w} \right\} q_s.G \qquad \ldots(1.21)$$

Plotting the specific grinding energy versus G-ratio for a series of grinding wheels of different grades should produce a straight line whose gradient is proportional to q_s.

Malkin [27] illustrated the test method used for evaluating grinding wheel performance using a series of wheels with different grades.

Two series of wheels shown in Figure 1.12 have identical grit contents but with different vitrified bonds referred to as VX and VY bond. In general harder wheels tend to have higher specific energies, but their corresponding G-ratios tend only to follow the reverse of the predicted theoretical result. Soft-grade wheels tend to follow the expected linear behaviour. At around the K-grade of each wheel, there is a reversal in the curve which is caused by workpiece burn and/or accelerating wear of the wheel.

Higher G-ratios are recorded for VY-bond for the same energy level and metal removal rate. According to equation 1.21, the straight-line extensions of both curves would lead to the specific energy for a perfectly sharp wheel, i.e. $u_{chip} + u_{ploughing}$. Tests carried out by Reichenbach [26] are presented in the form of grinding power versus G-ratio (Figure 1.11). However, these results have no effect on the final result for testing at a fixed metal removal rate. The conclusion drawn from these tests apply only to the particular grinding method and workpiece material used.

The technique is also used by wheel manufacturers for quality control purposes in order to check wheel-to-wheel consistency and uniformity.

1.6 CONCLUSION

A review of the literature has provided a mathematical foundation that quantifies wheel performance in terms of grinding parameters and wheel wear up to the burn boundary of a particular workpiece tested.

The transformation of these fundamental factors presented in the form of performance diagrams show optimum bond compositions and wheel grades for a particular workpiece-wheel combination under pre-determined operating conditions.

2. GRINDING WHEEL WEAR

2.1. INTRODUCTION

The grinding process is accompanied by wear of the abrasive wheel, and the rate of this wear plays an important role in determining the efficiency of the grinding process and the quality of the workpiece.

Krabacher [28] pointed out that wear mechanisms in grinding wheels appear to be similar to that of single-point metal cutting tools, the only difference being in the size of swarf.

The general form of the wheel-wear curve with the volume of workpiece material removed (or time) is shown in Figure 2.1. [16,28,29-30]. The wear behaviour observed is similar to that observed in other wear processes - high initial wear is followed by steady-state wear. A third accelerating wear regime usually indicates 'catastrophic' wear where the wheel requires to be re-dressed. Accelerating wear is usually accompanied by workpiece burn.

The performance index usually used to characterise wheel-wear resistance is the 'grinding ratio', or G-ratio, and is the ratio of the volume of workpiece removed to the volume of grinding wheel removed, thus,

$$G = \frac{V_w}{V_s} \qquad \ldots(2.1)$$

An alternative definition for the grinding ratio has been given by equation 1.20; however, this form is less often used than equation 2.1.

G-ratios cover a wide range of values ranging from less than 1 for vanadium-rich high-speed steels [24] to over 60,000 when internally grinding bearing races using C.B.N. wheels [31].

Attempts have been made on vitrified wheels to address the problems related to the wear of abrasive grits in terms of the theory of brittle fracture [10,32]. The conclusions of various researchers lead us to believe that the variety of different and interacting wear mechanisms involved, namely plastic flow of abrasive, crumbling, chemical wear etc., makes grinding wheel wear too complex to be explained using a single theoretical model.

This chapter explores the various types of wheel wear reported by many academic researchers and investigates their relative importance.

2.2. GRINDING WHEEL WEAR MECHANISMS

The four distinct wheel wear mechanisms to which overall wheel wear can be attributed have been shown to be:-

(i) Attritious wear (grit dulling);
(ii) Fracture of bond bridges;
(iii) Mechanical failure of grits and grit flaking; and
(iv) Fracture at the interface between grit and bond.

Figure 2.2. illustrates the main wheel wear mechanisms [33, 34, 35, 10, 28, 36-39].

2.2.1. Attritious Wear

Grit dulling is the gradual deterioration of abrasive cutting edges leading to loss of sharpness. The sources of minute scale wear are:-

(i) Attritious wear due to mechanical friction [10, 40-41];

(ii) Plastic flow experienced by the abrasive at high temperatures and pressures [32, 36-37, 16];

(iii) Crumbling due to thermal or mechanical shock [32, 36-37, 16];

(iv) Chemical reaction between abrasive and workpiece material at elevated temperatures and in the presence of grinding fluids [28, 32, 39].

The last mechanism can induce lowering the resistance of the grit to other wear mechanisms. Grit dulling leads to the growth of wear flats on active grits which increases the area of contact and the amount of rubbing between grit and workpiece. Figure 2.3 shows a smooth plateau on an active grit caused by attritious wear.

At the point of grit dulling very high temperatures existing in the area of contact greatly enhances adhesion and chemical reaction between the two surfaces. If grit or bond post fracture does not occur the plateau area on the grit widens, and hence the wear rate increases. If fracture is further delayed, as with hard grade wheels, the wheel becomes glazed and the workpiece tends to burn.

It has been shown experimentally [39] that chemical affinity between the abrasive and workpiece material can be used as a guide for the selection of grinding wheels. Their observations of solid diffusion of silicon carbide into ferrous materials explains the catastrophic wear rates exhibited by these 'workpiece-wheel' combinations.

The most common method for measuring wear flat area is by measuring wear flats at the grinding wheel surface using optical or electron microscopic techniques [10, 40].

Hahn [16] observed and analysed theoretically the effect of the wear flat area through attritious wear during plunge grinding of various workpiece materials. Hahn concluded that grinding forces will gradually increase during wear-flat formation up to a point where the wheel will restore its sharpness due to grit fracture.

2.2.2. Fracture Wear

Grit and bond fracture are usually considered simultaneously for the following reasons.

(i) They are of the same nature, i.e. fracture of brittle materials and hence the theory of brittle fracture is applicable to both bond and grit [10, 32, 42]. The applied thermal and mechanical loads usually under cyclic conditions cause initiation and further development of cracks which leads to fracture and the formation of new irregular surfaces;

(ii) They are related to the dressing methods used and occur simultaneously. The initial and final stages of wheel life between dressing exhibit exclusively fracture wear which is a combination of grit and bond fracture;

(iii) The relative amounts of bond and grit fracture cannot always be found. An investigation into precision grinding [10], where light grinding conditions were involved, employed a soft wheel which gave a high percentage of bond fracture whereas a hard wheel gave mainly partial grit fracture - attritious wear occurring in both cases.

However, the combination of grinding parameters such as equivalent chip thickness and workpiece material determines the effective wheel hardness, and so no single feature of the grinding process can be used to predict the fracture pattern of the wheel in advance.

The main difficulty in relating wheel wear due to fracture to the particular grinding condition arises from the lack of knowledge about the loads applied to both the grit and bond and their response to these applied loads.

Tarasov [33] suggests that grit fracture occurs as a result of mechanical forces due to chip formation or thermal shock induced by instantaneous high temperatures. Hahn [16] proposed a thermal stress hypothesis to explain the fracture of abrasive grits. Plunge grinding tests were conducted under fixed normal force conditions. Hahn asserted that as wear progresses, measurements of torque indicated that the tangential force actually decreases, therefore grit fracture due to mechanical loading will not occur. Mechanical stresses were also considered as an explanation for wear rates of wheels tested.

Bhattacharyya et al. [43] observed grit loss due to fracture using an electron microscope. They concluded that they could not differentiate between Peklenik's 'crystal splintering', i.e. grit flaking due to thermal stress, and grit fragmentation. However, they did explain their results in terms of Hahn's thermal shock hypothesis. Hahn's experimental conditions suggested that attritious wear was expected to have a major contribution to the thermal shock hypothesis as Mohun [44] observed with abrasive discs. The wear measurements of Hahn [16] were based on the reduction in wheel diameter which Malkin and Cook [10] attributed to attritious wear.

Wear rates recorded, however, were of the order of 50μ inch/sec. on wheel diameter. For purely attritious wear, wheel wear rates of the order of 5μ inch/sec. are normally observed.

This indicated that the wear mechanism was not solely due to attritious wear. The amount of fracture wear present may consist of fragments of uniform average size particles due to partial mechanical grit fracture, or thermal flaking.

Malkin and Cook [10] collected wheel wear particles for each grade of wheel tested when grinding with a fixed set of operating conditions then analysed their size distribution statistically. They found that with a soft grade wheel (G-grade), approximately 85% of the total wheel wear was due to bond fracture whilst with a harder K-grade wheel, this value reduces to around 55%. Attritious wear particles accounted for only 4% of the total wear in both cases.

The strongest evidence in support of the idea of fracture due to mechanical loading is that fracture occurs at some distance away from the cutting tips [34, 32]. Yoshikawa [32] concluded that the heat generated by cutting has no effect on grit fracture since the peak temperature of the grit occurs at the surface of the grit in contact with the workpiece where fracture would be initiated upon cooling according to the thermal stress hypothesis. The hypothesis does not take into account any difference in coefficient of thermal expansion between grit and bond materials, and also of the effect of thermal shocks due to the quenching action of grinding fluids on the grit leaving the cutting zone. Saito and Kagiwada [45] analysed the latter case and reported that the thermal stress in a grit due to a pulsating heat source showed that the magnitude of the maximum tensile stress is not large enough to cause fracture of the grit.

Eiss [42] and Malkin and Cook [10] both adopted the mechanical loading approach. Eiss applied a theoretical model of an idealised grit and compared it with grinding data.

Malkin and Cook [10] derived an expression, from first principles, for the probability of bond fracture against the bond stress factor, $(F_t - 20F_n)/V_B$.

Yoshikawa and Sata [34] and Yoshikawa [32] developed expressions for the probability of grit and bond post fracture as functions of grit stress, σ_{grit}, and the product $(1/V_B \cdot f_{grit})$, where f_{grit} is the grit grinding force, V_B is the percentage of bond in the wheel by weight, and $1/V_B$ is the bond weakness factor.

Although bond and grit fracture are similar mechanisms they have a different effect on the economics of the grinding process. The first mechanism results in a rapid loss of wheel, and the second mechanism, on a comparable scale with the uncut-chip thickness, generates sharp cutting edges and is known as the self-dressing action. Both mechanical and thermal stresses seem to be responsible for fracture wear. The effect of heat at the grit interface is responsible for locally changing the mechanical properties of the abrasive material, however, fragments of larger sizes are likely to occur through mechanical loading which governs both grit pull-out wear and the self-sharpening action.

2.2.3. Importance of Wheel Wear Mechanisms

In view of the large numbers of independent variables involved in grinding it is self-evident that the more dominant wheel wear mechanisms depend greatly on the conditions applied to each grinding application.

As shown here, grinding wheel wear consists of a large variety of physical and chemical mechanisms of very different nature.

The wear processes involved in grinding are classified as follows:

- attritious wear, i.e. progressive wear leading to loss of grit form leading to a deterioration of cutting ability, and to excessive heat generation, and;

- fracture wear (of grit and bond) which restores the cutting ability of the wheel and removes worn grits and allows grinding to progress efficiently.

A typical sequence of events for a grinding wheel according to Tarasov [33], involves dulling of the active grits by attritious wear and then to regain sharpness by fracture wear until bond post failure releases the grit.

After the wheel has been dressed, stage I of the wheel wear diagram illustrates the removal of weakened grits by the fracture wear mechanism.

Tsuwa and Yasui [46] reported the existence of a layer on the wheel surface after dressing which is progressively removed after grinding has started. High wear rates are also exhibited during the final stage of grinding where catastrophic breakdown of the wheel occurs due to mechanical overloading of the grinding grits.

The area exposed on the surface of active grits directly affects the magnitude of the grinding energy required for metal removal and, hence, the amount of power required before the onset of workpiece burn.

The steady-state wear regime (stage II) occurs due to the combined effects of attritious wear and fracture wear.

However, the ability of the grinding grits and bond posts to fracture, when the load exceeds some limit, determines the duration of this stage and prevents forces from becoming too excessive. Fracture also limits the amount of heat generated at the cutting zone and gives better workpiece quality. Grisbrook [30] found that the greatest amount of wheel wear results from diamond dressing rather than from wheel wear, which emphasises the need for longer steady-state periods and fewer dressings.

Stetiu and Lal [47] found that the mechanism of wheel wear can be changed from attritious wear to one of fracture wear by selecting the appropriate wheel hardness without changing the grinding conditions. The particle-size distributions gave evidence of a self-dressing action. In terms of volumetric wear Malkin and Cook [10] found that in plunge-feed grinding experiments only 4% of the total wear volume was due to attritious wear, the rest being due to grit and bond fracture according to wheel grade when the grinding parameters are fixed.

Tsuwa [35-37] recorded the changes occurring in wheel cutting edges during grinding. He stated that the section of grit that forms a cutting edge is always the worn surface of the grit, and that edges which fracture by a considerable amount cease to become active. It was concluded that self-dressing takes place only if the attritious wear is very great, or the operation is continued up to a very high degree of dulling of the active grits so that fracture edges become active.

It is certain that the rate of wear is dependent upon this fracturing tendency and that forces upon the grit will undoubtedly increase.

There is a fundamental difference between the two forms of grinding wheel wear. Attritious wear is undesirable and in that case all practical measures aim to reduce it.

This form of wear is very similar to the corresponding mechanism which causes deterioration of the cutting ability of turning tools were large scale failure is unlikely to occur [48].

Fracture wear in grinding is advantageous in that it can be a controlled form of wear. Although it is a form of volumetric wheel loss it opposes attritious wear in terms of grinding efficiency.

Fracture wear gives the wheel its functional significance and considering very little is known about fracture behaviour in abrasive particles, it is clearly important to understand how grit and bond composition affects fracture behaviour of grinding wheels and their performance.

2.3. WHEEL WEAR AND GRINDING FORCES

Grinding forces and their effect on wheel wear of grinding tools have been subjected to detailed investigations. The earliest dynamometer used for the measurement of grinding forces was probably one used by Marshall and Shaw [49]. For simplicity, two force components operate, namely : the normal force, F_n; and the tangential force, F_t. A notable feature of grinding force measurements is the high F_n/F_t ratio ranging from 1½ to 3. This value seems high compared with conventional machining operations where a typical value lies between ½ and 1.

The difference is attributed to the different effective cutting geometries and the pattern of metal removal by the grits.

Grisbrook et al. [30] and Grisbrook [50] recorded the magnitude of grinding force components during the whole period of wheel life between dressings, and for fixed downfeed conditions.

The typical change in force pattern can be divided into four phases.

(i) An unstable phase where forces rise abruptly up to a peak, then fall to a steady-state value as the initial high wear rate (stage I), due to the effects of dressing, slows down. Davis and Rubenstein [51] showed that the rate of change in grinding force increases slightly after a transition point is reached then settles down to steady-state conditions.

Pattison and Chisholm [29] showed that grinding forces are affected by the dressing conditions which has recently been confirmed by Rowe et al. [52-53];

(ii) A phase where forces are constant and heat flow into the grit and workpiece is in equilibrium. The region coincides with the self-dressing action of the wheel. Bond bridge fracture does not normally occur in this region although bond strength does play an important part here as it determines the magnitude of the applied load the grit can sustain without fracture;

(iii) A third phase where there is a progressive build-up of power and grinding forces. The mechanism that proceeds from the second phase assumes that grits adopt stable geometries and shapes which are harder to fracture, and from then on the number of fractures decreases and grits become dull. At this point, grits are prone to overheating and grinding becomes inefficient.

As rubbing and ploughing increases, and since the metal removal rate is constant, the normal force component increases at a much higher rate than the tangential force component. However, higher forces at this stage are not accompanied by higher wear rates which indicates that the rate of wheel wear is a function of the absolute values of the forces and their relative magnitude, i.e. F_t/F_n, which is referred to as the grinding coefficient. Marshall and Shaw [49] suggested that a higher grinding coefficient produced a more efficient grinding process.

This is explained by considering that the normal force component induces compressive stresses into the abrasive grit whilst the tangential force component causes tensile stresses to be exerted at the rake face of the grit. Therefore, a higher F_t/F_n ratio means a higher probability of grit fracture since the grit material has a lower tensile than compressive strength which means that cutting edges retain their sharp facets for a greater period of time.

(iv) In this period, the rate of change of grinding forces becomes less and the effects of vibration become evident. This phase corresponds to stage III of the wheel-wear curve (Figure 2.1) where wear rates are detrimental to economic grinding.

The progress of wear of grinding wheels operated under fixed normal force conditions has been studied by Hahn [16]. High force values lead to increases in depths of cut and rapid catastrophic wear due to fracture. For very low force intensities Hahn found that metal removal ceases quickly, and the wheel subsequently glazes and the wear rate becomes negligible.

Lindsay [54] and Lindsay and Hahn [55] found that radial wheel wear is linearly proportional to the normal force existing between wheel and workpiece, irrespective of whether the force is applied under fixed force conditions, or under fixed infeed conditions. Volumetric wear is reported in Lindsay and Hahn's further work in precision grinding [56]. They related volumetric wear to be an approximate quadratic function of normal force intensity. Their conclusions showed that wheel wear could be related to any wheel-work geometry, or conformity, in terms of interface force intensity and contact pressure.

2.3.1. Assessment of Grinding Forces and Wear

The dominant wear mechanisms in grinding wheels are attritious and fracture wear. In the author's opinion, fracture wear (bond and grit) should be considered the most important wear mechanisms for these reasons:

(i) Fracture wear constitutes approximately 95% of the total volumetric wheel wear;

(ii) Wear during the initial and final stages of the wheel-wear curve (I and III) is due to gross fracture;

(iii) The dressing mechanism which affects wheel life and grinding forces is essentially fracture-sharpening of cutting edges.

(iv) Fracture wear reduces grinding forces and heat generation which results in lower power consumption, and smaller workpiece distortion.

(v) Fracture wear, in the form of self-dressing, affects the duration of useful wheel life (region II of the wheel-wear curve).

It should be noted that the mechanism of grinding wheel fracture is an extremely complex process caused by the action of thermal and mechanical stresses induced into the grit. Thermal stresses are thought to be responsible for grit flaking whilst larger fragments are associated with mechanical stresses which are directly related to forces acting upon the grinding grit.

Fracture wear due to mechanical loading seems to be dependent on absolute force components and their relative magnitude.

For fixed normal force operations the force is sufficiently large to allow fracture to occur at a controlled rate. Too high a force will cause catastrophic wear rates to dominate, whilst very small forces will impair metal cutting.

For fixed-feed operations the grinding force components increase steadily during stage II of the wheel-wear curve.

If the cutting conditions produce a friable wheel then metal cutting will take place efficiently. The rate of change of force depends upon the initial value of the force component ratio.

2.4. EFFECT OF WORKPIECE MATERIAL ON WHEEL WEAR

The suitability of abrasive materials to grind workpiece materials efficiently depends on their attritious wear resistance. The abrasive should be harder than the workpiece material being ground, however, hardness is not the most dominant factor.

In fact one would not use the two hardest known of natural abrasives, diamond and silicon carbide, to grind ferrous alloys.

Attritious wear of grits is both mechanical and chemical [39, 57-61]. Chemical effects are significant when the abrasive is appreciably harder than the workpiece material and its associated metallurgical phases. At higher temperatures during cutting, chemical reactions may occur between workpiece, grinding fluid, the surrounding atmosphere and the abrasive and bond.

Diamond is not suitable for grinding ferrous metals despite its hardness. This is attributed to attritious wear caused by reversion from diamond to graphite [62]. Degradation of diamond appears to be aggravated in the presence of iron low in carbon. Loladze and Bockuchava [63] listed five types of diamond wheel wear based on adhesion, abrasion and diffusion wear. Figures 2.6 illustrates the five types of diamond wheel wear. Cubic boron nitride is more stable than diamond in the presence of ferrous metals. However, the success of C.B.N. on various steels is dependent on the complex carbide phases within the steel workpiece.

Figure 2.7 illustrates the effect of complex carbide on the wheel-wear parameter, G-ratio, for steels of varying hardness. The hardness of the carbides are quoted as 'abrasive numbers' which are essentially weighted averages of their Vickers' hardness values [64].

When grinding ferrous metals with aluminium oxide abrasives, the most important chemical reaction usually involves the oxidation of iron and the reaction of the oxide with the abrasive to form the spinel $F_eAl_2O_4$ [57], thus

$$2\ F_e + O_2 + 2Al_2O_3 \longrightarrow 2\ F_eAl_2O_4 \qquad \ldots[2.2]$$

The spinel is an intermediate compound between the oxidised workpiece material and aluminium oxide.

A high attritious wear rate on steel in humid air rather than dry air was found to be due to the catalytic effect of water on the oxidation of iron [57].

However, despite the role of oxygen and water to promote adhesion and attrition during grinding, their elimination by grinding in a vacuum has a dramatic effect on the process [65-67]. Chemical reaction between workpiece and abrasive was reported to be reduced, however, loading of the wheel surface increased.

Surface oxidation and corrosion in normal grinding environments tends to reduce adhesion between metal particles and the workpiece. This same effect might explain the difficulties encountered when grinding high-temperature oxidation-resistant metals, including stainless steels, nickel-base alloys, and titanium [68].

Silicon carbide abrasives are harder than aluminium oxide abrasives but are inferior when grinding ferrous materials. The main chemical reaction tends to involve the dissociation of silicon carbide [59, 69] which promotes attritious wear when grinding titanium and other non-ferrous metals.

In addition to chemical affinity, mechanical factors contribute significantly to attritious wear. When grinding carbon and alloy tool steels, the G-ratio is greatly reduced when grinding the material in its fully hardened state [70], which suggests that a mechanical effect is taking place. However, hardness is not indicative of grindability especially when the material's hardest phases are softer than the abrasive.

High-speed tool steels contain complex carbides that tend to reduce grindability of alumina abrasive wheels.

The hardest carbides in high-speed steels are carbides of tungsten, molybdenum and vanadium The volume fraction, C*, of these carbides in tool steels relative to that of tungsten carbide by itself can be approximated in terms of the weight percentages of tungsten (W), molybdenum (Mo), and vanadium (V) as [70];

$$C^* = W + 1.9Mo + 6.3V \qquad ...(2.3)$$

The effect of this parameter on the G-ratio is shown in Figure 2.8. The relative grinding ratio G* is the G-ratio for different tool steels expressed as a percentage relative to that of an M2 tool steel. The results tend to indicate that a higher carbide content reduces grindability of alumina grinding wheels. This can be compared favourably with a similar correlation between G-ratio and the vanadium content for grinding high-speed tool steels with aluminium oxide wheels [24]. Higher G-ratios have been obtained for materials produced by powder metallurgical methods which result in a fine dispersion of small hard carbides which tends to be less abrasive than large hard carbides [71].

2.5. EFFECT OF ABRASIVE AND BOND COMPOSITION ON WHEEL WEAR AND PERFORMANCE

Attempts were made to describe the process of wheel wear in terms of mechanical stresses applied to abrasive grits during stage II of the wheel-wear curve. Graham and Voutsadopoulos [72] presented data which supported the argument that fracture-type wear is the most important wear mechanism related to the loss of abrasive material from the grinding operation as a consequence of high stresses induced in the abrasive grit by grinding forces.

Grit fracture was assumed to be caused by induced tensile stresses of relatively small magitude. These workers used existing experimental data to correlate G-ratio to a number of process variables using a finite-element model of an idealised wedge (Figure 2.9). The wedge was assumed to be rigidly held in an infinitely-strong bond. The deflection pattern, due to tangential and normal reactions, is shown in Figure 2.10. Graham and Voutsadopoulos [72] applied a tangential force of 5.4lbs force and a normal force of 10.4lbs force to produce a stress pattern showing lines of constant maximum shear stress (isochromatics) as shown in Figure 2.11.

They applied Griffith's brittle fracture criterion to the post-processed finite element results in order to locate areas of compressive, tensile and neutral stresses within the model grit (Figure 2.12). The area of brittle failure was also located on this diagram in order to illustrate points at which the abrasive material is likely to fail, i.e. tensile fracture of the grit. A good correlation was found between the maximum tensile stress in the grit and the G-ratio using experimental data contained in the literature.

However, Graham and Voutsadopoulos assumed that grit fracture was the pre-dominant wear mechanism assuming the grit to be rigidly held.

Wear during this period of grinding (stage II) is mixed, i.e. bond and grit fracture which explains why the correlation is close but not exact. The vitrified bond is not infinitely stronger than the grit, and its magnitude governs the duration of stage II wear. These workers postulated that wear during stages I, II and III was probably due to tensile stresses induced in the bond and the grit material,i.e. grit fracture and pull-out.

The main criticism of the work is due mainly to the assumption of a rigidly held wedge finite element model, and the correlation of results of this model to wear data relating to stages I, II and III of the wheel-wear curve.

2.5.1. Strength of Clay-Based Materials

2.5.1.1. Background

The tensile strength of a ceramic material is determined by the most serious flaw in it. Such flaws are known as Griffith flaws and can appear as cracks, pores or irregular-shaped grains that have a sharp notch acting as a stress raiser around the notch to a high level.

Any inclusion which has a different elastic modulus from the matrix will produce a small stress concentration in its vicinity, e.g. a perfectly spherical pore will increase the average tensile stress by a factor of three at the pore surface on a plane perpendicular to the tensile stress direction. The low strengths observed in many ceramics must be caused by the presence of sharp notches. In ceramics of moderate strength (> 70MN/m^2), flaws are typically 100μ and will be frequently found to be pores.

In ceramics showing high strength (350-700MN/m^2), flaws are considerably smaller and are of grain size dimensions such as grain boundary cracks or fractured grains - grain sizes typically a few microns. The most serious flaw on a body is one situated at the surface orientated so that its maximum dimension is perpendicular to the applied tensile stress. Surface flaws are the most serious because the effective flaw length is the complete flaw length, whereas inside the volume of the stressed body, the effective flaw size is less than the flaw length.

In addition, if the body is subject to bending, for example a bond post connected to two abrasive grains, it will experience the highest stress at its surface.

Factors other than flaws that affect the strength of the body are related to the nature of the body, i.e. composition, grain size and general porosity.

These factors are important since they control the energy required to extend the flaw. The energy required for fracture initiation is higher than the energy required to form a new surface, i.e. the surface energy.

This is partly because it includes the energy absorbing process of plastic deformation that occurs in the highly stressed region of the crack tip. Generally for ceramics the fracture initiation energy γ_i is usually a few times $10J/m^2$. This value varies with fracture surface roughness so that smooth surfaces, such as glassy materials, have low values of γ_i.

In the ideal case of a dense, homogeneous material containing a single flaw, the stress multiplication factor of a flaw can be evaluated for some simple flaw geometries.

The expression relating the stress at failure, σ, to the size of the flaw causing failure, and the failure energy for fracture initiation for an elliptical crack is,

$$\sigma_{failure} = \sqrt{\frac{2.E.\gamma_i}{\pi.C}} \qquad ...(2.4)$$

where E is Young's modulus, C is the crack length if it is a surface flaw or half a crack length of it is an internal flaw, and $\sigma_{failure}$ is taken as the average stress calculated from the specimen's geometry and dimensions and the applied load. This is Griffith's equation but for any flaw geometry it is expected that,

$$\sigma_{failure} \propto \sqrt{\frac{E.\gamma_i}{\pi C}} \qquad \ldots(2.5)$$

This equation should be valid for bodies containing several well-separated serious flaws. The stress, $\sigma_{failure}$, includes any residual stresses in the body which are usually of unknown magnitude.

Many experimental studies on ceramics have shown that strength depends on the total porosity, i.e. small and large pores have an effect. An empirical relationship between the failure stress and the porosity, p, of a body has been found to be:

$$\sigma_{failure} = \sigma_o \, e^{-bp} \qquad \ldots(2.6)$$

where σ_o is the strength found by extrapolating the data to zero porosity, and b is a constant determined from the experimental data plotted as ln $\sigma_{failure}$ versus porosity, p.

The value of b has been found to vary considerably for the same ceramic material depending on the shape, size and distribution of the porosity [73]. The relationship is known as the Ryshkewitch-Duckworth [74,75] equation and was shown by Knudsen [76] to be based on the increased average stress caused by the reduction in load-bearing area resulting from the porosity.

However, Knudsen did not consider factors that control strength at zero porosity. Carniglia [73] considered that the flaw should be enclosed within a volume λ, i.e. the Saint Venant volume, such that at the periphery of this volume the stress re-distributing effect of the flaw was negligible. This volume was then considered in relation to the spacing, L, between general porosity. Carniglia showed that the Ryshkewitch-Duckworth equation was applicable only when $\lambda >> L$. This is, when the Griffith flaw that initiates fracture is larger than the pores which form the general porosity, and when the spacing between pores is small compared to the size of the Griffith flaw.

Under these conditions, the average flaw stress acting on the Griffith flaw has increased by the reduction in load-bearing area and can be considered as uniform. When $\lambda << L$, a local stress model, such as the Griffith model for an elliptical crack, can be used. That is the stress magnification produced by a single flaw, with no interference from other flaws, that causes failure. The case when $\lambda < L$ cannot be treated theoretically in a general manner, because each Griffith flaw is close to another stress re-distributing flaw and therefore the average stress around each flaw is highly variable.

In practice, $\lambda >> L$ would occur quite frequently for ceramics. Most ceramics contain a number of smaller pores and frequently more serious Griffith flaws. If the samples tested have constant Griffith fracture initiating flaws and the general porosity is variable, then the strength data should fit the Ryshkewitch-Duckworth equation. Carniglia [73] developed a more complex equation which showed the Ryshkewitch-Duckworth equation to be an approximation. If the general porosity remains constant but the size of the Griffith flaws is variable, then the fracture strength values, $\sigma_{failure}$, should yield a straight line when plotted against $\sqrt{(\gamma_i/C)}$.

This approach should work because either γ_i and E are determined for the material containing the same general porosity.

Flaws can be classified as gross macroscopic, microscopic and sub-microscopic [77]. This means this classification encompasses size only. A flaw is considered to be gross if it is readily visible to the unaided eye, so that the origin of failure can be viewed, i.e. large surface cracks, inclusions at the surface, etc.

A microscopic flaw is not easily identifiable and is usually a small crack, void or a small inclusion. A sub-microscopic flaw is identified using a scanning electron microscope.

Flaws in ceramics result from several causes, i.e. pores might be caused by differential firing shrinkage on a small scale of size, burn-out of organic matter (dextrin and fillers), gaseous evolution caused by a reaction on firing, diffusion of gases or some other mechanism etc.

Differential shrinkage on a small scale of size, is caused by the non-uniformity of the characteristic properties on a related scale of size. The characteristic properties are porosity, particle size, composition or particle alignment.

Large-scale non-uniformities of any of these characteristics can cause the constituent materials to re-distribute during firing and may possibly lead to splitting of the body. The tensile stress may be relieved by the formation of one large fissure or possibly by the formation of numerous small fissures.

A number of factors involved in pressing these bodies which could be responsible for the non-uniformity of porosity on a large scale include, segregation of fines, friction at the die wall, non-uniform powder packing on deposition and variations in compaction ratio.

In addition to these, lamination problems might occur, depending on the state of the powder and the pressing technique used. It is caused by the elastic recovery of the compact, that occurs when the compaction pressure is removed, as a result of the entrapment of air, particularly in fine powders [222].

Spontaneous micro-cracking on cooling from the firing temperature is a common source of cracks around large inclusions of a different phase. This micro-cracking occurs either because of stresses arising from either a mismatch in thermal expansion of the inclusion and the matrix, or is caused by a phase transformation of the inclusions.

In general, pores in ceramic bodies may be described by pores, cracks, fissures, inclusions, large grains, and surface defects. These flaws might be combined and produce complicated fracture-initiating combinations.

2.5.1.2. Effect of Particle Size of Constituent Materials

Parmalee and Morgan [78] found that decreasing the particle size of quartz altered the vitrification behaviour and strength of a ceramic body.

The bodies examined were classed as coarse, commercial, and fine, with average diameters of quartz of 68, 45 and 11μm, respectively. The finer the quartz, the greater the reduction in porosity and the higher the strength.

Koenig [79] studied the effects of feldspar, quartz, and kaolin particle size in a vitreous china body. It was found that firing shrinkage and flexural strength were greater for the finer-ground feldspar body, and that there was less water absorption. The bodies containing finely-ground quartz, as well as feldspar, had considerably greater strength than the regular china clay body, and they showed greater strength in which fine quartz and regular feldspar, or regular quartz, and fine feldspar were used. Koenig concluded that more finely-divided quartz affects vitrification quite markedly and that finely-ground feldspar increases vitrification behaviour.

Sane and Cook [80] discovered that ball milling for 100 hours reduced the final porosity of a clay-feldspar-quartz composition from 17.1% to 0.3% using the same firing conditions. The change is caused by intimate mixing of the constituents and the reduced distances fluxing ions are required to diffuse during firing to enhance chemical reactions.

Increased densification of the fired body, due to smaller particle sizes, tended to produce a stronger body.

During vitrification of the body, a large mass of viscous liquid is formed. The liquid wets solid particles which are pulled together under the action of surface tension when the liquid flows into the pores. When the firing temperature is increased, more melt is formed which is less viscous.

However, the dissolution of quartz opposes this reduction in viscosity which helps grinding wheel manufacturers, as well as manufacturers of clay-based materials, to fire products over a wide range of soaking temperatures. Fine grinding of quartz produces more surface area of quartz per unit volume, which promotes its dissolution in the liquid phase, and consequently aids vitrification which increases strength.

Finer quartz particles have also been reported to inhibit inversion cracking at 573°C [81].

2.5.1.3. Effect of Mullite and Glass Contents

It is generally accepted that the development of interlocking fine mullite needles in the body increases the strength of the clay-based material. However, this hypothesis is not free from controversy. According to Zoellner [82] and Budnikov [83], mullite provides porcelain its strength. Zoellner dissolved pieces of porcelain in a cold 25-33% solution of hydrofluoric acid for several days.

The vitreous matrix and quartz were dissolved and the crystalline phase remained.

Zoellner assumed that these crystals were sillimanite, since mullite at that time was unknown. He suggested that increasing the firing time and temperature to increase the formation of these crystals would increase the strength of porcelain.

Budnikov [83] published data concerning the strength of electrical porcelain and mullite, from which the strength of mullite is greater than porcelain. Geller [84] showed that the effect of firing increased the size of mullite crystals to such an extent that the strength of porcelain decreased. This was reported also by Krause and Keetman [84] and Eitel [86].

Grofcsik [87] reported that the total Al_2O_3 content of kaolinite transforms by exothermic reaction into mullite at about 960°C. Therefore,repeated or prolonged firing will not change the amount of mullite but may change its size.

According to Krause and Keetman [85], the size of mullite crystals will increase with the logarithm of firing time at a suitable soaking temperature.

They found that by maintaining the samples at 1400°C for 6,60,600 and 6000 minutes, the average length of acicular crystals of mullite increased in size to 5, 7.2, 11 and 14.2 μm, respectively.

Sane and Cook [80] milled a clay-based body (20% feldspar, 30% quartz, 42.5% kaolin and 7.5% ball clay) for different periods of time which were fired at three different temperatures.

They discovered that increasing milling time would increase the wt.% glass in the body and reduced the amount of quartz. However, it was discovered that increasing the mullite content of the body, increased the strength of the body.

The glassy phase was considered the major component of porcelain which was considered the weakest part. This aspect of the body has attracted much attention to the strength of clay-based materials.

Mattyasovsky-Zsolnay [88] assumed that the tensile strength of porcelain is influenced by stresses set-up in the glassy phase rather than by the amount and size of mullite crystals. He suggested that if mullite controls the strength of porcelain then an increase in the Al_2O_3 content (by increasing kaolinite fraction) to form more mullite would increase the strength of porcelain. Mattyasovsky-Zsolnay demonstrated that mechanical strength increased when quartz content was increased and reduced when kaolinite content was increased.

This statement is in contradiction to the experimental data published by Weidman [89]. Weidman increased the kaolin content and the result was an increase in strength.

Experimental samples containing 50, 60, 65 and 70% weight kaolin (corresponding to 30, 16, 10, 1% weight quartz and 20, 24, 25 and 29% weight feldspar) showed bending strengths of 71, 91, 94 and 130 MPa, respectively.

Kalnin et al. [90] published results on the strength and elasticity of quartz-free clay-based bodies using compositions of kaolin and nepheline syenite, focusing on mullite content and porosity. They concluded that elastic moduli and flexural strength of the bodies increased with the proportion of mullite present over the range 11 - 36% weight.

In kaolin-rich preparations, i.e. 2:1 and 1:1 kaolin: nepheline syenite ratios, the amount of mullite obtained by powder x-ray methods agrees with that calculated assuming complete decomposition of kaolin into mullite and silica. However, in the nepheline syenite system (1:2 ratio), the amount of mullite present is much less than expected, and it appears that in this case silica and alumina dissolved in vitrified nepheline syenite.

Koch [91] noted that porcelain bodies should be fired such that the microstructure contains plate-like primary mullite, and a high proportion of fine acicular secondary mullite concentrated in the glassy phase and also at grain boundaries to give a felted structure. Lach [92] explained that the presence of a viscous, glassy phase aids the diffusion of cations so that mullite forms more regular-shaped crystals. Therefore, in sintering wheel bonds, high temperatures are needed to obtain well-developed mullite crystals.

It has been shown that using mineralisers such as TiO_2 [93] and MgO [94], the mullite content can be increased.

Primary mullite is formed by the decomposition of clays and secondary mullite is formed by re-crystallization. It is possible that both forms of mullite affect mechanical strength in many ways [95].

2.5.1.4. Effect of Quartz Content

The study of the effect of quartz on the strength of clay-based materials has concentrated on finding an optimum size of quartz particle that inhibits 'de-bonding' from the matrix.

The 'pre-stress theory' espoused by many researchers, was proposed to account for observed increases in strength that occurred with an increase in fine quartz content. It was assumed that fine quartz generates a compressive stress in the matrix and that any applied tensile force would be effectively reduced by the 'pre-stress'. Therefore, higher tensile stresses would be required to cause failure [88, 96 - 98].

However, cracks were found around small particles after loading that were not present before loading. This indicated that small quartz particles should have a weakening effect on the matrix rather than a strengthening effect [99]. The weakening effect of quartz was demonstrated by comparing the strength of the matrix material, composed of equal weight fractions of kaolin and nepheline syenite, fired to 1265°C and subsequently ground; with and without quartz. The ground matrix was isostatically pressed with an equal amount of quartz of different sizes, then fired to a pre-determined bulk density.

The maximum strength was found to occur at a quartz particle size of 25μm having a sharp fall above and a slight decrease below this size.

But the matrix material without the quartz was much stronger, which contradicts the 'pre-stress theory'. Weyland [100] showed that the strength of clay-feldspar-alumina porcelain bodies greatly decreased when a small percentage of quartz was added.

Another problem is that when Al_2O_3 replaced SiO_2, in the composition of clay-based materials, the alumina-containing body showed higher strength [101-103].

German [104] suggested that the development of high strength with alumina was probably due to a reduction in the number of Griffith cracks which can be caused by silica inversion.

Smothers [105] opposed the 'pre-stress theory'. He performed hot-strength tests on both quartz and alumina-containing bodies. Above the transition temperature of quartz the strength of the quartz body was as high as that for the alumina body. Weyl [107] and Dunsmore et al. [108] have also shown that the strength of a quartz-containing body is higher above the displacive polymorphic change of quartz.

On cooling a clay-based material from the soaking temperature, the quartz transforms at 573°C. This transformation which involves a contraction of the quartz particles, produces stresses both in the quartz particles and in the matrix, and can cause circumferential cracks surrounding the quartz grains in a quasi-pore within the matrix. However, it has been reported in studies in both porcelain bodies [106] and on model systems [109] that it is only above a critical size that circumferential cracking tends to occur during cooling.

Investigations have led to relationships being proposed which relate the effect of quartz particle size on strength and the existence of an optimum grain size. However, the reported optimum value of the quartz size varies significantly between researchers. Krause [110-112] carried out experiments with finely milled and graded quartz and established that the maximum bend strength is obtained with quartz of particle sizes in the range 15-20μm.

The data showed that up to 45μm particle size, the body with the highest % weight quartz gave the strongest matrix.

Ludas [113] reported that the highest mechanical strength of porcelain occurred when quartz was sieved to the size of 30-35μm.

Beech and Norris [114] investigated a porcelain made using 40% weight quartz of particle size 10-30μm which produced the highest strength.

Beech and Norris also varied the firing conditions. Their results indicated that the maximum strength occurred at a temperature below that required for maximum bulk density.

Grofcsik [87] used the disc compression test on circular discs to investigate the effect of quartz particle size on mechanical properties. Experimenting with a series of bodies of different composition, particle size and firing schedule, Grofcsik concluded that for fine quartz, increasing the quartz content increases strength. He also pointed out that having optimum grains of 20-60μm may be causing the grains to dissolve in the glassy phase during firing, whilst coarser grains allow harmful stresses to accumulate.

Many researchers have published data on optimum particle sizes for quartz.

However, it must be borne in mind that the strength of clay-based materials depends not only on quartz particle size, but also on other characteristics of the fired body. Therefore, it is difficult to relate the strength of clay-based materials on quartz particle size alone.

Dinsdale and Wilkinson [115] related the properties of whiteware bodies to the size of constituent particles. By assuming $\mathcal{E}$ to represent the mean size of the crystalline particles present in the fired system, they suggested the modulus of rupture, S, to be,

$$S = K.\mathcal{E}^{-a} \qquad ...(2.7)$$

where K is a constant and the index 'a' would be expected from Griffith's crack theory to be about 0.5.

Work on single phase crystalline materials has shown that there is an exponential relationship between the strength, S, and the true porosity, P, of the form.

$$S = S_o e^{-bp} \qquad ...(2.8)$$

where S_o is the strength at zero porosity. Knudsen [76] presented the above equations as,

$$S = K.\mathcal{E}^{-a}.e^{-bp} \qquad ...(2.9)$$

where K, a and b are empirical constants. Dinsdale and Wilkinson [115] agreed that the grain size distribution of the starting materials will strongly influence both the porosity and the grain size in the fired body. If the size of the filler material such as quartz is increased, packing may be increased, and unfired porosity reduced.

However, fired strength is adversely affected. Improvements in fired strength can be attained by reducing filler size which is obtained at the expense of firing contraction.

In a paper by Evans and Linzner [116], an acoustic emission study was carried out on a clay-based material as it was loaded to failure.

This showed that the acoustic emission rate increased rapidly as the stress in the sample approached the failure value. The sound pulses were expected to arise from cracks which debond quartz particles, cracking of quartz particles, themselves and cracks linking up or starting to run after being arrested.

The results of this study indicate that quartz particles that remain attached to the matrix after cooling, and are therefore residually stressed, can be detached when the applied stress reaches a sufficiently high value.

As the highest stresses in the material, resulting from the applied stress, occur adjacent to the tips of many cracks in the sample, the formation of a process zone around a crack which starts to grow can be expected if bonded quartz particles are in its vicinity.

In another acoustic emission study of porcelain [117], it was found that a maximum acoustic emission rate occurred at a temperature below the ß - to ∝ - quartz transition point. This suggests that the residual stress, resulting from the transition, increased as a result of the thermal expansion mismatch between the quartz particles and the matrix on cooling below 573°C. It was also found that the temperature at which the maximum emission rate occurred was reduced as the quartz particles were made smaller.

This is consistent with the assumption that smaller inclusions require higher stresses to become debonded. A further interesting finding was that a second maximum emission rate occurred at 200°C, the phase transition from ß - to - ∝ - cristobalite. The presence of cristobalite arises from the conversion of quartz during densification heat treatment.

Results published by Oral et al. [118] showed that for a variety of clay-based material compositions, the strength of ring specimens showed considerable scatter in test pieces that had optimum heat treatments.

Failure was reported to occur by cracks around quartz particles or by quasi-spherical pores.

2.5.2. CERAMIC BONDING MATERIALS AND BOND STRENGTH

During grinding, the action of tangential and normal grinding forces create stresses within the abrasive grit and adjacent bond posts which inevitably causes bond-post failure.

When the bond strength is optimised, this process takes place gradually, i.e. when abrasive grits have lost their ability to cut the workpiece.

The most frequently used bonding materials for vitreous-bonded grinding wheels containing clay minerals, quartz and feldspar which contain crystalline phases that reduce their melting points. As previously mentioned, bonding materials used for alumina wheels resemble high-strength tough enamels (vitreous), and those for silicon carbide wheels are referred to as stoneware or soft porcelain bonds.

In alumina grinding wheels, the bond not only dissolves other crystalline phases in the bond, but also dissolves the surface of the alumina grain. The bond must not produce any 'rounding' of the grains, therefore, the bond must produce the same 'hardness' at the interface of the bond/grit couple. This explains why it is possible to fire grinding wheels at temperatures 200 or 300°C higher than the melting point of the bonds without discharging the bonding material or deforming the wheel itself [119].

Guilleaume [120] characterised vitreous bonds using the Seger formulae. He tested 60 types of clay bond which were described by the formula:

$$RO.(1.25\text{-}3.0Al_2O_3).(4.5\text{-}10SiO_2) \qquad ...(2.10)$$

Where RO is the sum of alkali oxides contained in the bond, i.e. CaO, MgO, MnO etc. These bond compositions were composed of a 'clay substance', feldspar, and quartz with powdered marble and magnesite as mineralisers. Guilleaume [121] first examined fired bonds without the admixture of alumina grains, then determined the strength of bar specimens containing the alumina grains. Specimens were fired at different temperatures and specimens with variations in bond composition fired at constant temperature.

The effects on strength and hardness were examined. Guilleaume's results gave only a limited understanding since no information was provided on mineral composition and fired bond composition. Furthermore, firing conditions characterised by Seger cones (Sg) do not represent well-defined conditions. Firing conditions characterised by the same Sg temperature can produce grinding wheels with very different properties. Franz [122] reported that a deeper analysis on the properties of bonding materials on the performance of grinding wheels is required.

He examined the bonding materials used by Guilleaume and reported that on firing grinding wheels containing bonds of the same composition in a small temperature range (between Sg8 and Sg12 - a temperature difference of 100°C), deviations in bond hardness were as high as 7 degrees [121]. Rieke and Haeberle [123] noted that the strength of specimens prepared with bond materials that have low melting points are higher than those wheels prepared with classic bonding materials.

Filonenko and Lavrov [119] pointed out that during the cooling period of firing, when grinding wheels are quickly cooled from peak temperature to 800°C, de-vitrification is inhibited. Thereafter, slow cooling is required in order to relieve internal stresses. The mechanical strength of the bond is dependent on the amount of its vitreous phase.

According to Filonenko and Lavrov [119] of all the crystalline compounds, only spinel ($MgO \cdot Al_2O_3$) is capable of raising the strength of vitreous bonds. This compound surrounds alumina grains, as a quasi-embedding material, with octahedral spinel crystals smaller than 8μm diameter formed in the alumina-rich melt zone developed at the interface between bond and grit.

The high strength bonds used were located in the proximity of the SiO_2 peak in the Na_2O-SiO_2-Al_2O_3 ternary diagram. As a consequence of the alumina-rich melting zone, the following compounds may be formed: anorthite, cordierite, mullite, spinel, plagioclases, anastase, rutile, heamatite and magnetite [119].

The composition of ceramic bonds is important from the view point of strength.

In order to achieve complete penetration of the abrasive grain surface, the viscosity of the melt plays an extremely important part in complete adhesion between grit and bond. The flow characteristics of ceramic bonds has recently been investigated by a number of researchers. Moser [124] used a heating microscope to observe, qualitatively, the changes in contact angle of various bonding materials up to 1460°C. Bond materials and bond containing alumina grains were examined using three crude bond compositions, viz, (i) illite bond, (ii) modified illite bond, and (iii) fritted borosilicate bond.

It was found that the fritted borosilicate bond melted at a lower temperature and produced better wetting characteristics. Moser reasoned that increased wetting of bond to grit would increase wheel strength.

Hartline [125] conducted work on the strength and fracture of alumina abrasive wheels and concluded that the fracture process involved in grinding wheels proceeds through the bond, and fractography conducted on bond posts showed signs of de-vitrification and porosity. Hartline stated that increases in strength were achieved by developing uniform bond post strengths and/or higher strength wheel structures.

Experimental grinding wheel bonds were examined by Barry, Lay and Morrell [126] using novel glass-ceramics and conventional feldspar bonds.

It was concluded that the strongest bonds were those based on traditional clay-feldspar-quartz composition, and that strength was dependent on wetting and flow properties of the bond on the surface of the grit.

Ogawa and Okamoto [127] found that increasing the feldspar content of bonds increased the adhesion of bond to grit in alumina wheels by producing a less viscous mixture at the soaking temperature.

The development of superabrasive grinding wheels has resulted in a number of papers published on ceramic bonding of diamond and C.B.N. [128-130].

Yang et al. [129] have published results concerning the strength of vitreous-bonded C.B.N. wheels. They concluded that the strength of their specimens was dependent on glass composition and, to a much lesser extent, on porosity.

The bonds examined were full of pores with an optimum composition of 51% SiO_2, 15% Al_2O_3, 26% B_2O_3, 3% Na_2O and 5% CaO.

Recently, Jackson, Barlow and Mills [131] concluded that the strength of vitreous-bonded alumina wheels depended on the K_2O-CaO ratio. They reasoned that the increased mass of glass-network modifiers would release liberated gases within the bonds by reducing the bond's viscosity. It appears that a reduction in bond viscosity not only releases gases liberated during the breakdown of clays and fluxes, but also improves interface strength by improving wetting and flow characteristics of the glassy bond.

2.6. EFFECT OF INTERFACIAL COHESION ON BOND STRENGTH AND WHEEL WEAR

Interfacial cohesion in vitreous-bonded grinding wheels is as important, if not more important, as the effect of bond composition on their strength and performance.

In grinding wheels, interfacial strength dictates whether a grinding grain cuts efficiently or not at all. According to Hondros [132], a knowledge of interfacial properties holds the key to the design of bulk properties.

Moseley, Briggs and Lewis [133] compared the cohesion of various borosilicate bonding materials in contact with white-fused alumina (containing 99% wt Al_2O_3) and impurity phases 3% wt TiO_2, 1% wt SiO_2 and MgO, CaO, Fe_2O_3 and ZrO_2 in smaller quantities. They compared the properties of each grit/bond composition by measuring their fracture toughness and related these values qualitatively to observations of fracture surfaces and interfaces. Fired test specimens were inspected which showed preferential etching along crystallographically controlled directions in white alumina grit.

This was observed to be dissolution of planar blocks of sodium aluminate or ß-alumina ($Na_2O.11Al_2O_3$) present in α-alumina (essentially pure Al_2O_3), established by x-ray diffraction of samples.

ß-alumina is thought to be detrimental to grit strength which, when in small well-dispersed amounts, can control the self-sharpening effect during grinding. However, in large amounts leads to loss of strength of the grit.

Bragg, Gottfried and West were the first to determine the crystal structure of ß-alumina in 1931. Beevers and Ross [134] came to the same conclusion as Bragg et al. when they discovered that the crystal structure and chemical composition do not readily agree with each other.

Deviations in the chemical composition, noted by various workers, report: $Na_2O.9Al_2O_3$; $Na_{1.5}Al_{10.83}O_{17}$; & $Na_2O6Al_2O_3$

According to Harata [135] the non-stoichiometric composition alters the measured lattice parameters. Based on his own measurements, ß-alumina is represented by the formula,

$$(1.16+ x)\ Na_2O.11Al_2O_3 \qquad ...(2.11)$$

where x denotes the molar fraction of Na_2O, which varies from 0.19 to 0.59. Below this limit, α-Al_2O_3 separates from ß-alumina, above it $NaAlO_2$ dissociates. Moser [136] performed electron microscopic studies on white-fused alumina grits. He observed that ß-alumina was present as spots and bands on the surface of the grits, and noted that heating uncoated grits up to a temperature of 1000°C led to a lower amount of ß-alumina due to the evaporation of Na_2O above 900°C, thus leaving α-alumina. He further observed that grits coated with borosilicate bonding material contained a higher level of Na_2O at the interface.

The most likely cause of increasing the strength of white alumina grinding wheels is the dissolution of ß-alumina which would locally enrich the melted bond with Na_2O which promotes fluidity in alumino-borosilicate and alumino-alkalisilicate glasses. The glassy phase would then fill dissolution bands created in the surface of the grit thus promoting a better mechanical bond between grit and glass phase, i.e. enhanced shear resistance when subjected to grinding forces. In their samples, Moseley et al. [133] also identified small (50µm dia x 10µm thick) Ca-rich platelets, of which two types were identified; alite (Ca_3SiO_5) and an unnamed oxide, $NaCaAlO_3$, known to have several polymorphic forms.

S.E.M. analysis performed by Moseley et al. on brown-fused alumina grit, showed that the grit contained 96-98 wt. %,Al_2O_3, 1-2% wt. TiO_2 and up to 0.5 wt. SiO_2. The amount of TiO_2 in solution is inconsistent with earlier work which had determined that the maximum solubility of TiO_2 in Al_2O_3 is less than 0.3 mol.%. at 1300°C [137].

However, it was stated that MgO may increase solubility of TiO_2 in alumina. Examination of this section of brown-fused grit showed the appearance of blade-like inclusions at the grit-bond interface. This morphology is consistent with rutile needles observed in some synthetic sapphires [138]. These inclusions accounted for the variability in TiO_2 content and hence its solubility in alumina.

Further examination of the fired specimens in both white and brown-grit samples, showed evidence of crystal formation in the glassy bond. These crystals were lath-shaped with square sections distributed evenly throughout the glass. X-ray diffraction indicated an alumino-borate with a high alumina content.

The best match was with $Al_{18}B_4O_{33}$. Titanium was considered deleterious to fracture toughness due to the presence of rutile needles on the surface of the grit and titania in the bond itself.

Moseley et al. suggested using oxides to allow the formation of titanates instead of rutile needles. Unfortunately, Mn-doped glasses did not improve strength appreciably. A second attempt was made to form a protective coat around the grit. Oxides such as MgO, ZnO and CoO were used to form spinel layers between grit and bond. Unfortunately, the test specimens were lower in strength.

They concluded that white-fused alumina grits were stronger due to planar dissolution of ß-alumina, whilst brown-fused alumina grits were considered weaker due to rutile needle formation at the interface between bond and grit.

Similar interfacial studies were conducted on alumina abrasives [139] and silicon carbide vitreous-bonded wheels [140].

Comparison of wheel performance using wheels with brown-fused and white-fused alumina grits was examined by Reichenbach [26].

Interface studies of metals in contact with superabrasive grits have recently been conducted by Scott et al [141]. These workers provided substantial quantitative information on the wetting behaviour of copper-base alloys on diamond (Figure 2.13). This work was further extended by Evens et al. [142] who correlated G-ratio of abrasive buttons with interfacial bond strength (Figure 2.14).

Evens et al. concluded that increases in titanium and tin concentrations enhance wetting to the (III) plane of diamond, and that titanium segregated to the interface where alloy compositions promoted wetting on the diamond surface and to the free surface where alloy compositions did not promote wetting. The interfacial layer was characterized by electron probe analysis to be composed of bronze ($\alpha + \delta$) eutectoid and $CuSnTi_2$. Good interfacial bonding was found not to be associated with good wetting. The interfacial bonding layer with promoted wetting was identified as a 100 nm reaction product (TiC) which was associated with low temperatures, i.e. 900-950°C. The best composition was found to be a mixture of 20wt.% copper -10wt.% tin-titanium alloy which wets and bonds well to diamond at 900-950°C. Evens et al. [142] stated that better bonding and wetting was achieved with nickel-coated diamond grinding buttons.

Shilo et al. [143] conducted a comprehensive study on the wettability of glass on substrates of C.B.N. They found that wettability was dependent on the reaction product at the grit/bond interface, which was identified as B_2O_3. In the case of sodium-borosilicate glasses, with Na_2O/B_2O_3 ratios less than or equal to 0.5, boron atoms tend to co-ordinate from ternary to tetrahedral form owing to the introduction of oxygen atoms by alkali oxides.

The best wetting conditions were achieved at 900°C using glasses of the system Na_2O-B_2O_3-PbO-SiO_2. The addition of 4% wt.-7 % wt. Li_2O was responsible for the best wetting condition which was due to the network modifying effect of Li_2O.

2.7. CONCLUSION

A review of the literature has provided an insight into the causes and effects of wheel wear in terms of applied grinding loads and abrasive strength.

Relationships have also been formulated and tested that relate the wheel wear parameter, G-ratio, and the maximum tensile stress acting within the abrasive material. However, the effect of bond composition on wheel wear and performance has not been examined.

A review of the strength of clay-based materials thus provides a basis for studying the effect of bond composition on bond strength and wheel performance. Studies of the influence of workpiece material composition on grinding wheel wear also ensures that any study on grinding wheel performance should include factors that affect workpiece hardness and vitreous-bond strength.

3. REACTIONS IN CERAMIC BONDS

Reactions in bond compositions used in this study are similar to those that occur in clay-based materials used in whiteware bodies. The reactions outlined in this chapter form the basis for studies on the effect of bond composition on wheel performance.

3.1. BOND MATERIALS

Clays provide the wheel bond with plasticity for forming and strength in the green state. The two principal clays used for wheel bonds are china clay and ball clay. Both clays are primary clays formed from decomposed feldspar.

The main mineral constituents in both china and ball clay is kaolinite ($Al_2O_3.2SiO_2.2H_2O$). However, clays differ in purity and plasticity. Kaolinite has a layered structure and the particles reflect this by having a platey morphology. Figures 3.1 and 3.2 show x-ray diffraction spectra of ball clay and china clay complete with crystallographic planes of mineral phases and their interplanar distances.

Fluxes are used in bonds in order to lower the firing temperature by reacting primarily with the clay to form a viscous liquid phase which promotes densification. The flux is usually a feldspathic mineral such as feldspar, nepheline syenite, Cornish stone, talc and sometimes lithia. The complete range of fluxes has been reviewed by Royle [144].

The fluxing effect of feldspar in clay-based materials was studied by Schramm and Hall [145]. Orthoclase ($K_2O.Al_2O_3.6SiO_2$) and albite ($Na_2O.Al_2O_3.6SiO_2$) and a combination of these fluxes are the most used fluxes in the formulation of clay-based materials.

In high strength bonds, used for conventional and superabrasives vitreous products, the fluxing effect is provided by powdered glass frits and borax in addition to feldspar. These additions provide the bond with fluxes that melt over a wider temperature range than those using traditional bond materials. This reduces the firing temperature which tends to promote increased adhesion between grit and bond.

3.2. DENSIFICATION AND PHASE ANALYSIS

When a grinding wheel has been formed, it is fired at an appropriate soaking temperature to be densified in order to mature to the optimum state. During firing the bond materials, abrasive, and fillers initially behave independently of one another. Water occurring in the pores and in the clay is driven off below 250°C, whilst at 500°C, the organic matter has been burnt off.

3.2.1. Theoretical phase analysis - use of equilibrium diagrams

The overall final composition of clay-based grinding wheel bonds is composed of unreacted quartz, mullite, glass and sometimes cristobalite depending on the reaction conditions. The formation and growth of mullite crystals is thought to occur in the following manner:

(i) formation in the kaolinite platelets;

(ii) formation in the feldspar platelets;

(iii) formation in the mica platelets;

(iv) growth by recrystallisation; and

(v) formation during cooling.

Reaction rates and mechanisms of mullite formation may be different when the mullite is formed in the mica, kaolinite and feldspar platelets. The formation rate in one region is influenced by formations in other regions unless concentration gradients of atoms are distributed in such a way as to promote equal reaction rates throughout the total reaction volume.

It is clear that the formation of mullite in clay-based bonds is very complicated. The formation of mullite can be explained qualitatively using equilibrium diagrams, and quantitatively by comparing equilibrium phases with experimental results.

The application of equilibrium diagrams to ceramic manufacturing processes has been discussed by many authors. However, when applied to clay-based materials, Bowen [146], Hall and Insley [147] and Foster [148] express reservations in using them due to the coarseness of the clay particles, the high viscosity of molten feldspar [149,150], and the slow diffusion of alkali ions which tend to prevent equilibrium and homogeneity of the mass. Shelton [151] used equilibrium diagrams with success to correlate the properties of fired whiteware bodies to the amount of eutectic melt formed. Dietzel and Padurow [152] used phase diagrams in their discussion of quartz dissolution in porcelain.

Although equilibrium is not obtained for clay-based bonds, equilibrium diagrams are useful for describing reaction rates towards equilibrium. The equilibrium diagram used in this work is the K_2O-Al_2O_3-SiO_2 ternary system derived by Schairer and Bowen [153].

When heating a body consisting of quartz, kaolinite and potash feldspar, there are no appreciable reactions that take place between quartz, feldspar and kaolinite relicts until the temperature approaches the eutectic temperature of the total system, 985°C. In each isolated sub-system below 985°C, quartz has transformed to its high temperature form ß-quartz and the feldspar grains have transformed to sanidine. Kaolinite has lost its chemically bonded water and the decomposition products have been transformed to γ-Al_2O_3 and an amorphous phase with a high SiO_2 content. This is the primary composition of the reaction system.

Considering complete equilibrium conditions within the total system, according to Figure 3.3, immediately under the eutectic temperature there are three solid phases, feldspar, tridymite and mullite. When the system is heated to the eutectic temperature a fourth phase is formed, a melt phase with a composition of the eutectic.

With continued heating at constant temperature the amount of the melt phase is increased until one of the phases is consumed. If feldspar is consumed the composition point of the melt moves with rising temperature along the boundary line between the primary phase regions of tridymite and mullite until one of these two phases is consumed. The composition point then enters the remaining solid phase in the direction of the composition of the total system.

If tridymite is first consumed at the phase reaction in the eutectic, the composition point of the melt moves along the boundary line between the feldspar and mullite regions.

If neither of these two phases is consumed before 1140°C, the ternary invariant point is reached where feldspar is consumed and leucite occurs as a new phase.

After this phase reaction is completed the composition follows the boundary line until one of the solid phases has been consumed. The consumption of phases is dependent on the rate of reaction of the body until equilibrium conditions have been reached.

These conditions are applicable under conditions of equilibrium. For clay-based bonds equilibrium is rarely achieved and as a consequence, the grain size of the raw material is the most important reaction rate variable. Quartz shows very low reactivity up to the eutectic temperature. At that temperature, the quartz phase present is not affected by the other phases.

3.2.2. Formation of mullite in kaolinite clays

The effect of heat on ceramic raw materials has been studied by many workers as far back as 1887 when le Chatelier [183] charted discontinuities in the thermal analysis of kaolinite. Ford [184] and Todor [185] presented differential thermal analysis curves for china clay and ball clay and these can be compared with those obtained by the present author (Figures 3.4 and 3.5). The typical D.T.A. trace for potash feldspar is shown in Figure 3.6. The major phase transformations, as measured using a DuPont 1600 D.T.A. cell, of kaolinite ⟶ metakaolinite ⟶ spinel-type phase ⟶ mullite occurs as heating continues.

There appears to be a controversy regarding the products formed in heat treatment.

One theory suggests that, on dehydroxylation, kaolinite forms a mixture of alumina and amorphous silica. The other theory considers the dehydrated product as an aluminosilicate.

To explain the exothermic reaction it is believed that γ-Al_2O_3 is formed, and in the other case, an Al-Si spinel is formed.

Comeforo et al. [154] show the appearance of hexagonal particles far above the temperature for dehydroxylation, illustrating a residual structure still present in the non-crystalline compound of metakaolin.

Many researchers have investigated reactions that occur in clay-based materials containing these compounds. Weiss et al. [155] announced that the cubic phase which appeared at 900°C from kaolinite was an Al-Si spinel. These workers isolated the spinel phase by leaching amorphous SiO_2 from the fired kaolinite and found that its chemical formula agreed with the theoretical formula. The Al-Si spinel analysed by Weiss et al. is different from the γ- Al_2O_3 spinel because its lattice constant is 0.002nm lower owing to the replacement of Al-ions by smaller Si-ions present in the cubic γ -Al_2O_3 spinel structure [156]. However, other researchers have supported the crystallisation of γ -Al_2O_3 as the cause of the exothermic peak near 100°C [157-161].

There are two other exothermic peaks due to the crystallisation of primary mullite and formation of cristobalite from amorphous silica which occur at 1150°C and 1250°C respectively.

The transformation of pure kaolinite to mullite has been reviewed by Chaudhuri [162]. The sequence of transformation events is shown in Figure 3.7.

3.2.3. Effect of heat on feldspar and quartz

∝ - quartz is known to invert to ß-quartz at 573.3°C [163]. The transition is accompanied by a 0.8% volume expansion and is reversible and rapid. Any cristobalite present in the matrix is transformed (∝ ⟶ ß structure) between 200-270°C [81].

The breakdown and melting of potash feldspar has been studied by Morey and Bowen [164] who reported incongruent melting at 1170°C. However, the thermal behaviour of feldspar has had little attention paid to it.

The solubility of quartz in feldspar [165] and the solubility of quartz in clay and feldspar [166] has been investigated extensively. These workers report that mullite ($3Al_2O_3.\ 2SiO_2$) crystallises in molten feldspar.

3.2.4. Effect of heat on clay-based materials

Clay-based materials principally contain the oxides SiO_2, Al_2O_3, K_2O and Na_2O. Equilibrium diagrams were used by Lundin [167] to study the formation of mullite in detail. For mullite content, the experimental values were 3.4% lower than those calculated from the phase diagram. For glass content, the difference was 5% lower. Lundin concluded that the quartz had only partly reacted.

The difficulty in attaining equilibrium in clay-based materials is thought to be due to the high viscosity of molten feldspar, retarded dissolution of quartz, and the slow diffusion of partially mixed and partially melted constituents

When the temperature increases mullite dissolves partially in the melt if equilibrium is achieved.

At around 1000°C the surface tension of the liquid draws unreacted/partially reacted particles together which reduces porosity and increases bulk density. A loss in surface area causes shrinkage in the body. The porosity is initially interconnected and is referred to as open porosity. However, the reduction in the volume of the body produces closed porosity. When the open porosity is removed, the body is vitrified.

The densification of the body is slow because of the high viscosity of the liquid phase. The decrease in the viscosity is expected from the increase in temperature which is partially offset by the enrichment of the liquid with silica by partial dissolution of quartz. In practice, the slow dissolution of quartz results in bonds having wide ranges of firing.

The initial densification of clay-based bonds can be modelled simply using two contacting spherical particles. The rate of initial neck growth is,

$$\frac{x}{r} = \sqrt{\frac{3 . \gamma_{s} t}{2 . \eta . \rho}} \qquad \ldots(3.1)$$

The increase in contact diameter is proportional to t, and the increase in area between particles should be directly proportional to time. The factors affecting the rate of densification are surface tension, γ_s, viscosity, η , and particle size, r. The volume shrinkage, or linear shrinkage which takes place is determined by the approach between particle centres is given by the model as,

$$\frac{\Delta V}{V_o} = 3 \frac{\Delta L}{L_o} = \frac{9 . \gamma_{s} t}{4 . \eta . r} \qquad \ldots(3.2)$$

This equation shows that the initial rate of shrinkage is directly proportional to the viscosity and particle size.

As firing develops, more liquid is formed and mullite crystals appear. Primary mullite is formed from clay relicts whilst secondary mullite is formed from the melt. At 1200°C, a considerable amount of mullite is formed in quartz-rich bonds.

Shelton and Meyer [168] reported that increased rates of heating cause less liquid and mullite formation, less quartz corrosion, and more pores. An optimum heating rate of 50°C-90°C per hour was preferred. The crystallisation of glasses in the K_2O-SiO_2-Al_2O_3 system was studied extensively by Hermansson and Carlsson [169]. They concluded that crystallisation from this high viscosity ternary system is possible.

Tuttle and Cook [170] claimed to have found quartz, mullite, cristobalite and wollastonite as the crystalline constituents of kaolin-flint-feldspar blends. However, in many cases only quartz and mullite, and occasionally cristobalite are the phases present in clay-based kaolin-quartz-feldspar composites.

3.2.5. Effects of cooling

When densification occurs, the cooling rate is reduced in order to prevent thermal stress cracking of the body. It is better to reduce the cooling rate when crystalline inversions occur that involve volume changes. The inversion ranges for quartz and cristobalite are 550-580°C and 200-300°C, respectively.

When quartz-containing bonds begin to cool from the soaking temperature, it is considered that the liquid phase relieves stresses resulting from thermal expansion mismatch between itself and the phases ß-quartz, ß-cristobalite and mullite to at least 800°C.

At 800°C, stresses will develop in quartz particles and the matrix which causes micro-cracking. The shrinkage behaviour of quartz and the glass phase has been described by Storch et al.[171].

Between the temperature range 573<T<800°C, the glass phase shrinks more than the quartz phase which causes tangential tensile stresses to form cracks in the matrix. At 573°C, ß-quartz transforms to ∝-quartz which causes tensile residual stresses to produce circumferential cracking around quartz particles. Some of these cracks have been observed to propagate into the glass phase [172]. Similar observations occur in the cristobalite phase.

Spontaneous cracking of quartz has been found to occur over a temperature range that depends on the size of the quartz particles [173]. Particles larger than 600µm diameter cracked spontaneously at 640°C whereas smaller particles (<40µm diameter) cracked at 573°C. This observation agrees with temperature-dependent microcracking reported elsewhere [117].

3.3. CONCLUSION

The fired microstructure of all clay-based materials will depend on the structure of the raw materials used, the processing sequence and the heat treatment schedule.

The fired microstructure can contain:

(i) feldspar;
(ii) quartz and possibly cristobalite;
(iii) a glass phase of variable composition;
(iv) cracks around quartz and cristobalite particles;
(v) mullite-primary and secondary; and

(vi) pores-open and/or closed, depending on the heat treatment, and fissure-like pores resulting from differential shrinkage.

The complexity of the bond can be appreciated given the shape, size, amount, distribution and orientation of constituent particles and how these variables affect the bond's mechanical properties.

SECTION 2

CHARACTERISATION OF SINTERING AND FUSIBLE BONDS

4. VITRIFICATION BEHAVIOUR IN SINTERING AND FUSIBLE BONDS

Vitrification in mixtures used for grinding wheel bonds is studied in this chapter. This chapter has three objectives. The first is to correlate the degree of vitrification of the bond mixtures to the theoretical amount of liquid formed, the second is to understand how the mixtures densified in order to select the appropriate firing treatment, and the third is to attain optimum firing conditions based on first-order reaction kinetics.

4.1. EXPERIMENTAL PROCEDURES, MATERIALS AND EQUIPMENT

The first section of this chapter deals with the vitrification of bond mixtures. The raw materials used are described in appendix B and were composed of mixtures of ball clay, china clay, potash feldspar and quartz. The clay component of the bond was made up of 50% wt. ball clay and 50% wt. china clay. The mixtures used for the analysis are illustrated in Figure 4.3 and decribed in Table 4.1. together with equilibrium constitution data at 985°C. The experimental mixtures were mixed, sieved and dried to a pre-pressing moisture of 7% wt. Samples of bond weighing 25 grammes each were pressed in a hydraulic press at a pressure of 500 p.s.i. into discs of 40mm diameter and between 8-10mm thickness. After drying in an oven (110°C for 24 hours), the discs were then fired in a Carbolite 1400 HTF2 programmable cycle furnace at a constant soaking temperature of 1150°C. The heating rate was 2.9°C per minute. The measures of vitrification were measured in accordance with the method outlined in appendix A.

The experimental results were correlated with the theoretical amount of liquid formed.

For this purpose it was necessary to approximate the composition to a ternary equilbrium system, and since the K_2O content was much higher than the Na_2O content, the K_2O-Al_2O_3-SiO_2 system was chosen (Figure 4.1). Previous work on the softening behaviour of CaO-Al_2O_3-SiO_2 mixtures [173] had shown that the dominant factor was the amount of eutectic liquid theoretically formed which, according to the K_2O-Al_2O_3-SiO_2 ternary system (Figure 4.1), occurs at 985°C. The experimental vitrification data was compared with the theoretical predictions.

The second section of this chapter relates firing behaviour to a chemical reaction model provided by Norton and Hodgdon [175], whilst the third section of this chapter deals with the mesurement of the degree of vitrification relative to a range of soaking temperatures and firing durations. The firing range at the soaking temperature varied from 10 hours to 80 hours, depending on the characteristics of the clays. The measures of vitrification were measured in accordance with appendix A. The time-temperature condition and experimentally-determined apparent porosity data are given in Table 4.6. The bonds chosen for this analysis are illustrated in Figures 4.3 and shown in Table 4.1 together with equilibrium constitution data. The bonds studied were made with mixtures H, J, K, L, P, R, T, V, W and X. These mixtures were chosen due to their rapid approach to optimum vitrification in the temperature range 1100°C-1250°C.

4.2. VITRIFICATION OF BONDS

4.2.1. Heat Treatment of Ceramics

To understand the results of the heating process, two factors need to be understood: first, the equilibrium condition towards which the system is moving is given by

thermodynamics; secondly, the rate at which equilibrium is approached which is described by kinetics.

Thermodynamic factors are concerned with the condition of chemical equilibrium which are described by phase diagrams. Depending on the composition and temperature at which equilibrium is obtained, the changes that occur during the approach to equilibrium conditions are chemical and physical, i.e. a change of state from solid to liquid, or a change of surface area. The driving force for each of these conditions is the reduction in free energy of the system. The surface energy factor is of great importance and can be related to particle size by multiplying the surface energy by the area of surface present.

Kinetic factors are dependent upon atomic diffusion within the system and can be exploited in two ways; firstly, an approach to equilibrium at high temperature where some of the original constituents are preserved; secondly, a partial approach to equilibrium on cooling where the appearance of new phases is prevented. Therefore, the properties of ceramic bodies are dependent on composition, temperature, rate of heating/cooling and viscosity of molten phases. Equilibrium is not obtained on firing the bond mixtures and later results are discussed in these terms.

4.2.2. Composition and Constitution of Bond Mixtures

The folowing section explains how theoretical quantitative constitution data at 985°C, for a wide range of bond mixtures, were calculated.

The first step was to calculate the contributions made by the three raw materials as follows:-

Wt % Compound	Clay	Potash Feldspar	Quartz
Potash (K_2O)	1.65	11.01	0.00
Alumina (Al_2O_3)	37.10	18.01	0.00
Silica (SiO_2)	48.2	66.6	100
% Total	86.95	95.62	100

The clay content is composed of equal proportions of ball clay and china clay.

Letting C=% clay, F=% flux and Q=% quartz gives:

$$\% K_2O = 0.0165C + 0.1101F \quad ...(4.1)$$

$$\% Al_2O_3 = 0.371C + 0.1801F \quad ...(4.2)$$

$$\% SiO_2 = 0.482C + 0.666F + 1.00Q \quad ...(4.3)$$

Total oxide content (%) = 0.8695C + 0.9562F + (100-C-F)

$$= 100-0.1305C-0.044F \quad ...(4.4)$$

If the total oxide content is equal to D, the ternary compositions of the mixtures are,

$$\% K_2O = 100.K_A = ((0.0165C+0.1101F)x100)/D \quad ...(4.5)$$

$$\% Al_2O_3 = ((0.371C+0.1801F) \times 100)/D \quad ...(4.6)$$

$$\% SiO_2 = 100.S_A = ((0.481C + 0.666F+ [100-C-F])/D \quad ...(4.7)$$

$$= ((100-0.518C-0.334F)+100)/D \quad ...(4.8)$$

where S_A is the % SiO_2 in the bond mixture and K_A is the % K_2O in the bond mixture.

In the K_2O-Al_2O_3-SiO_2 ternary system (Fig 4.2), L, A and B are the respective compositions of the liquid, mixture and the solid; the equilibrium constitutions being silica, mullite and liquid. The construction to obtain the liquid content is the same for all mixtures with this constitution.

The weight percentage liquid content is given by.

$$100.\frac{K_A}{K_L} \qquad \ldots(4.9)$$

where K_L = % K_2O in the liquid phase. At 985°C, K_L = 9.3% and the liquid content is given by,

$$\frac{100.(0.0165C+0.1101F)}{0.093D}=\frac{17.74C + 118.38F}{D} \qquad \ldots(4.10)$$

Calculation of the constitution of the solid in equilibrium with the liquid is obtained from the silica content of the liquid, mixture and solid which, from Figure 4.2, are S_L, S_A and S_B, respectively. From Figure 4.2,

$$\frac{BA}{BL}=\frac{K_A}{K_L}=\frac{S_A-S_B}{S_L-S_B} \qquad \ldots(4.11)$$

hence,

$$(K_A.S_L)-(K_A.S_B)=(K_L.S_A)-(K_L.S_B) \qquad \ldots(4.12)$$

where,

$$S_B = \frac{K_L.S_A-K_A.S_L}{K_L-K_A} \qquad \ldots(4.13)$$

The percentage Al_2O_3 in the solid = 100 - S_B, assuming that the solid contains a negligible amount of K_2O. The percentage alumina in the solid is given by,

$$\%Al_2O_3 = \frac{K_L(100-S_A)-K_A(100-S_L)}{K_L-K_A} \quad ...(4.14)$$

Since mullite ($3Al_2O_3.2SiO_2$) contains 71.8 wt% Al_2O_3, the % mullite in the solid is,

$$\% \text{ mullite (clay)} = \frac{100-S_B}{0.718} \quad ...(4.15)$$

and,

$$\% \text{ mullite (mixture)} = \frac{(1-L).(100-S_B)}{0.718} \quad ...(4.16)$$

where (1-L) is the solid fraction which is equal to,

$$1 - \frac{K_A}{K_L} \quad ...(4.17)$$

hence, the % mullite in the mixture is,

$$\frac{K_L.(100-S_A)-K_A.(100-S_L).(K_L-K_A)}{0.718.(K_L-K_A)} \qquad \frac{K_L}{} \quad ...(4.18)$$

therefore the % mullite in the mixture is,

$$\frac{(100-S_A-2.172K_A)}{0.718} \quad ...(4.19)$$

$$K_A = \frac{(1.65C+11.01F)}{D} \text{ and } S_A = \frac{(10000-51.8C-33.4F)}{D}$$

and,

$$D=100-0.1305C-0.044F \quad ...(4.20)$$

The % mullite can now be calculated. The remainder of the solid, called 'free silica' for convenience, is given by,

$$100\text{-}\%\ \text{mullite} - \%\ \text{liquid} \qquad \ldots(4.21)$$

The calculated results for a series of mixtures of varying clay and feldspar contents are given in Table 4.1 where the calculated equilibrium constitutions are given by,

$$\%\ \text{mullite} = \frac{48.98C+7.09F}{D} \qquad \ldots(4.22)$$

and,

$$\%\ \text{liquid} = \frac{17.74C+118.38F}{D} \qquad \ldots(4.23)$$

The calculated theoretical equilibrium liquid and silica contents of the bond mixtures shown in Figure 4.3 are plotted as a function of the bond components: flux; clay; and quartz (Figures 4.4. and 4.5). The bonds were fired at 1150°C. The figures allow the constitution of any bond mixture to be found.

Apparent porosity and water absorption provide a measure of the amount, or degree of vitrification, and since vitrification is produced by the development of liquid drawing solid grains together [174], correlation of the bond mixtures shown in Figure 4.3 with equilibrium constitution was first attempted.

The results show that the degree of vitrification increased as the liquid content at equilibrium increased. Conversely the degree of vitrification decreased as the silica content increased.

A double correlation was attempted between apparent porosity and water absorption and equilibrium silica and liquid contents.

This was first attempted using the following equations and using the regression data for test pieces with the highest silica contents and lowest liquid contents (best correlation).

$$\sum WA = b_1 L + b_2 S + nb_3 \qquad ...(4.24)$$

$$\sum AP = b_1 L + b_2 S + nb_3 \qquad ...(4.25)$$

To find constants b_1 and b_2 we must solve

$$\sum' WL = b_1 \sum' L^2 + b_2 \sum' SL \qquad ...(4.26)$$

$$\sum' WS = b_1 \sum' S^2 + b_2 \sum' SL \qquad ...(4.27)$$

where

$$\sum L'^2 = \sum (L-\bar{L})^2 \qquad ...(4.28)$$

$\therefore b_1 = 0.1345$, $b_2 = 0.3725$ (for water absorption equation).

Placing these values into the above equation for water absorption and apparent density yields,

$$W.A. = 0.1345L + 0.3725S - 11.396 \qquad ...(4.29)$$

$$A.P. = 0.281L + 0.445S - 18.79 \qquad ...(4.30)$$

Considering the water absorption equation, the coefficient for the liquid content has a positive correlation coefficient. Considering water absorption data, good agreement was obtained between theoretical and experimentally-determined results. This is shown in Figure 4.10. However, apparent porosity data did not produce the same agreement (Figure 4.11).

Which is thought to be caused by inaccuracies during the measurement of apparent porosity data.

The double correlation cannot be explained easily, since equilibrium conditions were not established in the fired mixtures, but it can be used to derive 'vitrification diagrams' or 'maps'. These maps can be used to predict bond compositions with optimum vitrification properties. This was achieved by substituting equations 4.22-4.23 into the double regression equations 4.29 and 4.30.

$$W.A. = \frac{2586 - 25.84C - 31.95F}{100 - 0.1305C - 0.044F} \quad ...(4.31)$$

$$A.P. = \frac{2521 - 27.69C - 23.18F}{100-0.1305C - 0.044F} \quad ...(4.32)$$

From these equations, vitrification maps are drawn for the bond system considered (Figures 4.12 and 4.13).

4.3. EFFECT OF FIRING TIME ON VITRIFICATION BEHAVIOUR

This section is concerned with the densification behaviour of the compositions chosen as a function of firing time.

Knowledge of how the mixtures densified is required for the selection of the appropriate firing treatment, and for the subsequent study of bond strength.

4.3.1. Measures of Vitrification in Grinding Wheel Bonds

Apparent porosity results for various heat treatments are given in Table 4.6. The values of apparent porosity at 1200°C are plotted as a function of soaking time - Figures 4.14 - 4.17.

It can be seen that the vitrification of the test pieces occurs at a faster rate for those containing the most clay. These two components provide the glassy phase which is thought to control the vitrification behaviour.

To reach a specified degree of vitrification, it was decided to see if the apparent porosity data fitted the relationship obtained by Norton and Hodgdon [175]. These workers considered that the vitrification process obeyed an Arrhenius-type equation of the form,

$$\log\left\{\frac{k_2}{k_1}\right\} = A \left\{\frac{1}{T_1} - \frac{1}{T_2}\right\} \qquad \ldots(4.33)$$

where k_1 and k_2 are reaction rates at temperatures, T_1 and T_2 (Kelvin), and A is a constant dependent on composition. Norton and Hodgdon assumed that the reaction rate k_1 at a soaking time t_1 was inversely proportional to t_1. Thus the equation may be re-written as;

$$\log\left\{\frac{t_1}{t_2}\right\} = A \left\{\frac{1}{T_1} - \frac{1}{T_2}\right\} \qquad \ldots(4.34)$$

Two measures of vitrification were used by Norton and Hodgdon; these were linear shrinkage and apparent density. In the present study, apparent porosity is considered.

The assumption of the reaction rate being inversely proportional to the soaking time, t, may be written as,

$$\frac{d(A.P.)}{dt} = \frac{\lambda}{t} \qquad \ldots(4.35)$$

where λ is a constant. Separating the variables and integrating,

$$\int d(A.P.) = \lambda \int \frac{dt}{t} \qquad \ldots(4.36)$$

$$\therefore A.P. = (\lambda \log_e t + \beta) \qquad \ldots(4.37)$$

where β is a constant at a certain temperature and composition. Therefore, the assumption that the reaction rate is inversely proportional to soaking time leads to the relationship that apparent porosity is linearly related to the logarithm of soaking time.

An Arrhenius equation would have the form:

$$\frac{d(A.P.)}{dt} = \gamma \exp\left\{\frac{-Q}{R.T}\right\} \qquad \ldots(4.38)$$

where Q is the activation energy of the vitrification process for a given composition, R is the universal gas constant and γ is a constant. Equating equations 4.35 & 4.38 yields,

$$\frac{\lambda}{t} = \gamma \exp\left\{\frac{-Q}{R.T}\right\} \qquad \ldots(4.39)$$

$$\log_e \lambda - \log_e t = \log_e \gamma - \frac{Q}{R.T} \qquad \ldots(4.40)$$

The values of t and T are matched for a given state of vitrification so that for t_1 and t_2, the appropriate temperatures T_1 and T_2 are,

$$-\ln t_1 = (\ln \gamma - \ln \lambda) - \frac{Q}{R.T_1} \qquad \ldots(4.41)$$

$$-\ln t_2 = (\ln \gamma - \ln \lambda) - \frac{Q}{R.T_2} \qquad \ldots(4.42)$$

provided that is independent of temperature. Subtracting equations 4.41 and 4.42 yields,

$$\ln\left(\frac{t_1}{t_2}\right) = \frac{Q}{R}\left\{\frac{1}{T_1} - \frac{1}{T_2}\right\} \qquad \ldots(4.43)$$

This equation is equivalent to the Norton-Hodgdon relationship where,

$$A = \frac{Q}{2.303R} \qquad \ldots(4.44)$$

Therefore, the Norton-Hodgdon relationship requires that,

$$\frac{d(A.P.)}{dt} = \frac{\lambda}{t} \qquad \ldots(4.45)$$

where λ is independent of temperature but depends on the composition and other variables such as the particle size of the raw materials and the method of compaction. Therefore, if the Norton-Hodgdon relationship is obeyed, and apparent porosity is plotted as a function of the logarithm of soaking time for a series of temperatures, a series of parallel straight lines for a given composition will result for a standardised preparation of the mixture.

The apparent porosity data were therefore plotted as a function of logarithm of soaking time for all the compositions as shown in Figure 4.3 at the soaking temperatures 1150°C, 1175°C and 1200°C, respectively.

One example for each clay content is shown in Figure 4.18 - 4.26. These show that the apparent porosity is linearly related to the logarithm of soaking time at 1200°C, except at short soaking times. The apparent porosity values after one hour's soaking time are generally lower than the linear relationship predicts.

This is because a large proportion of the vitrification process that had occurred for these test pieces took place in the heating and cooling stage of the firing process. Obviously, for the firing treatment to be characterised by the soaking time, vitrification occurring in the heating and cooling stages must be insignificant compared with the soaking period.

There are cases to which the Norton-Hodgdon relationship cannot be applied. Also, the apparent porosity data itself is prone to scatter, and ideally, several test pieces should be fired simultaneously to obtain a reliable mean value.

4.4. OPTIMUM FIRING CONDITIONS FOR VITREOUS-BONDED GRINDING WHEELS

Studies on grinding wheel manufacture have been conducted by a number of workers. Shinozaki et al. [176] carried out an extensive study measuring variables such as bulk density, Young's modulus and tensile bending strength of grinding wheel samples as functions of firing time. Optimum values of these variables were achieved after 20 hours' firing and remained constant up to 120 hours' firing.

However, variations in grinding wheel performance are apparent when grinding workpieces with identical wheels manufactured to the same grade under the same firing conditions.

Variations in surface roughness and number of components per dress ultimately indicate that grinding wheel performance is affected primarily by properties of the vitreous bond during heat treatment. Studies in sections 1 and 2 of this chapter indicate that apparent porosity of the bond can decrease and subsequently increase depending on the firing duration.

The increase in apparent porosity in grinding wheel bonds is thought to be caused by the effects of bloating.

Grinding wheel performance has traditionally been measured in terms of component quality, grinding power used during the grinding cycle, grinding ratio, wheel wear, etc. Interpretations of grinding trials are related to grinding wheel grade (which varies from manufacturer to manufacturer), wheel structure (hardness, grit size etc.), and recently grit-bond strength which is derived from tensile bending strength and the number of grits in the wheel [177]. However, grinding wheel performance should be related to tensile grit strength and tensile bond strength which relate more closely to wheel wear.

4.4.1. Optimum Firing Conditions

Firing is one of the most important processes in the manufacture of grinding wheels. Properties such as wheel and bond strength, porosity, thermal expansion and hardness are determined by the abundance of various phases resulting from the influence of reaction kinetics during the firing process.

Firing also affects performance of the grinding wheel significantly. Considerations such as rate of heating, peak temperature and isothermal soaking time are therefore important to grinding wheel performance.

These considerations have always been dealt with by trial and error, therefore a scientific approach is needed to determine optimum firing conditions based on wheel performance.

A method of computation of firing conditions for triaxial whitewares was proposed by Meyer [178] and Shelton and Meyer [179], which may be applied to the thermal treatment of vitreous-bonded grinding wheels which usually have higher glass contents than triaxial whiteware bodies. An expression was derived for bodies made with feldspar to determine compatible heat treatment based on values of A_m, i.e. the area under the reaction rate-temperature curve. However, assumptions used for deriving these expressions were based on known properties of pyrometric cones; an approach which is open to criticism when applied to whiteware bodies. Recently, Boghawatta and Poole [180] derived equations for determining optimum firing conditions for bricks based on first-order reaction kinetics and involved using vitrification measures to derive a semi-empirical vitrification equation. However, the equation did not include vitrification during the cooling period of such bricks. The formation of mullite is known to continue during the cooling period of some whiteware bodies [167].

The effect of heat treatment on the degree of vitrification is characterised by properties such as apparent porosity, water absorption and bulk density. The following changes in whiteware bodies during heat treatment are well known: first, volume shrinkage ceases and swelling begins; secondly, apparent porosity and water absorption increases and bloating occurs; and thirdly, bulk density decreases and deformation begins. In ceramic abrasive bodies, Shinozaki et al. [176] observed that bulk density achieved a maximum value and remained constant, however, grinding wheel performance is variable from wheel to wheel indicating that bulk density or some other vitrification measure in bonds must reach a maximum during heat treatment.

The present investigation relates optimum firing conditions to maximum mechanical bond strength.

4.4.2. Kinetic Analysis

The kinetics of kaolinite decomposition have been studied and results interpreted in terms of a diffusion model and a model based on first-order reaction kinetics [181]. Norton and Hodgdon [175] first treated the vitrification of whiteware bodies as a chemical reaction. This investigation uses the logarithmic time method of kinetic analysis of isothermal data based on Arrhenius's equation. The temperature dependence of the rate of vitrification is expressed by the Arrhenius equation as,

$$\ln k = -\left\{\frac{Q}{R.T}\right\} + \ln A \qquad \ldots(4.46)$$

$$k = A.\exp\left\{\frac{-Q}{R.T}\right\} \qquad \ldots(4.47)$$

where k is the rate of reaction (rate of vitrification), Q is the activation energy, R is the universal gas constant, T is absolute temperature, and A is a constant.

Redfern [182] showed that the time required to attain a degree of vitrification, t, under isothermal conditions is proportional to 1/k, i.e.

$$t = \frac{c}{k} \qquad \ldots(4.48)$$

where c is a constant. Therefore,

$$\ln t = \left\{\frac{Q}{R.T}\right\} - \ln \tau \qquad \ldots(4.49)$$

where τ is equal to A/c. Therefore, a plot of ln t versus 1/T gives Q/R as the gradient. Equation 4.49 can be re-arranged as,

$$\ln\left(\frac{k_1}{k_2}\right) = \frac{Q}{R}\left(\frac{T_1-T_2}{T_2T_1}\right) \qquad \ldots (4.50)$$

where k_1 and k_2 are the rates of vitrification at temperatures T_1 and T_2 respectively.

Vitrification of the bond mixture was assumed to commence at the eutectic temperature of 985°C. Therefore, the rate of vitrification of the mixture above 985°C relative to that at 985°C was considered to be a measure of the overall rate of vitrification at that particular temperature. Therefore, if k_t is the rate of vitrification at t°C relative to that at 985°C (1258K), i.e. if $k_1 = k_t$ and $k_2 = k_{985} = 1$, then equation 4.50 reduces to,

$$\ln k_t = \frac{Q}{R}\left(\frac{1}{1258} - \frac{1}{(t+273)}\right) \qquad \ldots(4.51)$$

For each grinding wheel bond, isothermal firing trials were performed at four temperatures and variations in the soaking period ranged from 10 hours to 80 hours. Apparent porosity data and soaking period for mixtures H,J,K,L,N,P,R,T,V, W and, X, appear in Table 4.7. The optimum vitrification point when the % apparent porosity reaches its lowest value. After this point, the % apparent porosity value increases and 'bloating' occurs.

The soaking period corresponding to the optimum degree of vitrification, as shown by the changes in apparent porosity data, was used to construct ln t - reciprocal temperature plots (Figure 4.27).

The experimental factor calculated using data presented in Figure 4.27 was used in equation 4.51 to determine the relative rates of vitrification at different firing temperatures.

The kinetic analysis involves calculating the magnitude of reactions taking place during the heating-soaking-cooling duration in each bond mixture. If k_t is the relative rate of reaction, i.e. degree of vitrification, of a certain bond mixture at t°C, then the degree of vitrification, V, attained during heating above the eutectic temperature of 985°C for potash feldspar grinding wheel bonds is given by,

$$V_{heating} = \int_{t_{melt}}^{t_{optimum}} k_t.dt \qquad ...(4.52)$$

where t is time in hours and ($t_{optimum} - t_{melt}$) is the time interval during which time the temperature was raised from T_{melt} (1258K) to the maximum firing temperature T(K) at a constant rate. This represents the first curvilinear area under the rate of reaction-time diagram (Figure 4.28). The degree of vitrification during soaking is given by,

$$V_{soaking} = k_t.\ t_{soaking} \qquad ...(4.53)$$

where $t_{soaking}$ is the soaking time. This is represented by the rectangular area under the rate of reaction-time diagram. The degree of vitrification during cooling is:

$$V_{cooling} = \int_{t_{optimum}}^{t_{solid}} k_t.dt \qquad ...(4.54)$$

The overall degree of vitrification attained during heat treatment of the wheel according to the fixed firing schedule is,

$$V_{total} = \int_{t_{melt}}^{t_{optimum}} K_t.dt + K_t.t_{soaking} + \int_{t_{optimum}}^{t_{solid}} K_t.dt \quad \ldots(4.55)$$

where (t_{solid} - $t_{optimum}$) represents the time interval during which the temperature decreased to T_{solid} (1258K) from the maximum firing temperature T(K) at a constant firing rate.

4.4.3. Effect of Isothermal Firing on Vitrification Measures

The effects of isothermal firing on the apparent porosity of wheel bond specimens are shown in Figures 4.14-4.17. The apparent porosity data are shown in Table 4.7. Bulk density of bond specimens increased with firing time, except for mixture H at 1200°C and J at 1150°C, as shown in Table 4.8. It was observed that bond mixtures H and J did not reach their optimum bulk density; these bond samples were therfore assumed to be under-fired. However, bulk density data for wheel samples remained relatively constant for each bond content (Table 4.9). The latter set of results agree with the observations by Shinozaki et alia [176].

A relationship between the bulk density of the bond and the soaking period existed for all samples due to the increased amount of interstitial glass and fewer pores at higher temperatures.

The changes in bulk density reversed at the optimum vitrification point due to the effects of bloating in the bond samples and lamination/bloating in the wheel samples.

At this point, the effect of bloating has counteracted the favourable effects caused by increased mullite due to the

reduction in strength caused by an increase in the size of pores; heat treatments exceeding the optimum soaking period produced a deterioration in the properties.

The vitrification properties based on the experimental data were used to determine the optimum soaking period at different firing temperatures. The data on optimum heat treatment for different bonds are shown in Table 4.10. Figure 4.27 shows optimum heat treatment data plotted as the natural logarithm of time as a function of inverse absolute temperature. The plots tend to deviate from linearity at high temperatures due to non-isokinetic behaviour of the clays [182]. Between 1100°C and 1200°C the mechanism approaches isokinetic behaviour and the plots show a high degree of correlation. Experimental factors (Q/R) have been calculated from the linear dependence obeyed below 1200°C.

4.4.4. Time-Temperature Relationships

Data on optimum heat treatments of bonds are given in Table 4.10. In Figures 4.27a and 4.27b, the data regarding optimum heat treatments are plotted in order to find the theoretical and empirical vitrification rate equations.

Between 1100°C and 1200°C, however, the mechanism approaches linearity, i.e. isokinetic behaviour, and therefore, experimental factors (Q/R) have been calculated from their linear dependence obeyed below 1200°C. The experimental factors are derived thus, for bond-mixture H the experimental factor (Q/R) is given by figure 4.27a to be 1954.6. Letting,

$$\ln k_t = \frac{Q}{R}\left\{\frac{1}{t_{melt}+273} - \frac{1}{t+273}\right\} \qquad \ldots(4.56)$$

where the vitrification temperature is referred to as t_{melt}.

From the K_2O-Al_2O_3-SiO_2 ternary phase diagram, the ternary eutectic temperature is 985°C. For bond-mixture H,

$$\ln K_t = 1854.6 \left\{ \frac{1}{985+273} - \frac{1}{t+273} \right\}$$

$$\ln K_t = 1.474 - \left\{ \frac{1854.6}{t+273} \right\}$$

$$K_t = \frac{e^{1.474}}{e^{1854.6/t+273}} \qquad \ldots(.4.57)$$

This equation gives the temperature dependence of vitrification, K_t. The integration of this equation with respect to time gives a measure of the degree of vitrification during heating. However, the integration is cumbersome, therefore, an empirical equation which describes the kinetic behaviour of each bond-mixture was derived as follows,

$$\ln K_t = 1854.6 \left\{ \frac{1}{1258} - \frac{1}{t+273} \right\}$$

$$\ln K_t = 1854.6 \left\{ \frac{(t+273) - (1258)}{1258(t+273)} \right\}$$

$$\ln K_t = 1854.6 \left\{ \frac{t - 985}{1258(t+273)} \right\}$$

$$\text{Let } X = \frac{1854.5}{1258(t+273)} \qquad \ldots(4.58)$$

$$\ln K_t = X\,(t-985) \qquad \ldots(4.59)$$

The factor X calculated, between 1100°C and 1250°C, varied between 0.001± 0.0001 - letting X equal to 0.001 yields the empirical equation.

$$\ln K_t = 0.001\,(t-985) \qquad \ldots(4.60)$$

Transformed exponentially yields,

$$K_t = e^{0.001(t-985)}$$

$$\text{or} \quad K_t = e^{0.001\,r\,t'} \qquad \ldots(4.61)$$

where r = constant rate of heating (°c/h)
and t' = heating time above 985°C.

Therefore, the two equations for the rate of vitrification are:

$$K_{t\ empirical} = e^{0.001rt'} \text{ or } e^{0.001(t-985)} \qquad \ldots(4.62)$$

$$K_{t\ theoretical} = \frac{e^{1.474}}{e^{(1854.6/rt'+1258)}} \text{ or}$$

$$\frac{e^{1.474}}{e^{(1854.6/t+273)}} \qquad \ldots(4.63)$$

The rate equations for sintering and fusible bonds appear in Table 4.11. A comparison was made between empirical and experimental degrees of vitrification for the bond mixtures H - X at temperatures ranging from 1100°C - 1400°C. The data is shown in Table 4.12. Figures 4.29a and 4.29b show the relationship between the rate of vitrification and firing temperature for bond mixtures H and K.

4.4.5. Extent of Vitrification

The relative degree of vitrification was determined by the sum of the partial degrees of vitrification during the whole period of heat treatment. The partial degrees of vitrification were arrived at by:

1. calculation of the degree of vitrification resulting from $V_{heating}$. The integration of equation 4.61, the empirical rate equation, for the grinding wheel bond within the required time limits, and under the conditions of constant rate of heating, produced the value of $V_{heating}$;

2. calculation of the degree of vitrification resulting from soaking ($V_{soaking}$);

3. calculation of the degree of vitrification resulting from cooling ($V_{cooling}$).

The rate of vitrification (K_t) at the maximum temperature of firing obtained by the exact rate equation (equation 4.57) when multiplied by the soaking period gave $V_{soaking}$.

The sum of the three partial degrees of vitrification gave the total degree of vitrification.

Considering bond-mixture K, at the lowest soaking temperature, 1100°C, according to Table 4.7a the maximum soaking period which yields the lowest apparent porosity is 70 hours. The heating rate of each bond mixture was 175°C/hr - which was used to calculate the heating time above the ternary eutectic temperature.

The contribution of heating to the degree of vitrification is given by integrating the following equation with respect to time,

$$V_{heating} = \int_{t_{melt}}^{t_{optimum}} K_t \, dt$$

Transforming K_t into a time-dependent form yields

$$V_{heating} = \int_{t_{melt}}^{t_{optimum}} e^{0.0025rt'}\, dt' \qquad \ldots(4.64)$$

further integration produces,

$$V_{heating} = \left\{ \frac{e^{0.0025rt'}}{0.0025r} \right\}_{t_{melt}}^{t_{optimum}} \qquad \ldots(4.65)$$

For bond-mixture K,

$V_{heating} = 3.05$

The degree of vitrification due to soaking at maximum temperature is given by equation 4.53.

where k_t at the soaking temperature is,

$$K_t = \frac{e^{3.71}}{e^{(4673.2/t+273)}} \qquad \ldots(4.66)$$

and the optimum soaking time is 70hrs, therefore,

$$V_{soaking} = \frac{e^{3.17}}{e^{(4673.2/1100+273)}} \times 70 \qquad \ldots(4.67)$$

$\therefore V_{soaking} = 95.09$

The degree of vitrification from cooling is given by equation 4.54.

Application of the limits of integration would produce a negative degree of vitrification indicating a cooling process. Changing the limits of integration would produce a positive total net degree of vitrification, hence for bond mixture K,

$$V_{total} = \int_{t_{melt}}^{t_{optimum}} e^{0.0025\,rt'}\,dt' + \frac{e^{3.71}}{e^{(4673.2/t+273)}} \cdot t_{soak} + \int_{t_{solid}}^{t_{optimum}} e^{0.0025\,rt'}\,dt' \qquad \ldots(4.68)$$

$\therefore \quad V_{total} = 101.19$

The contribution of heating and cooling to the total degree of vitrification, for bond-mixture K at 1100°C, is 6.02%. The contribution to all bond-mixtures appears in Table 4.13.

Table 4.15 shows the degree of vitrification data for bond-mixture K which shows the highest degree of vitrification imparted by the 1150°C heat treatment with a soaking period of 70 hours. The resulting specimens fired at three time-temperature combinations had superior vitrification properties compared with the other specimens. Table 4.14 summarises the optimum combination of time and temperature for achieving the highest level of vitrification for the bond mixtures used in this study.

The variation in the rate of vitrification for bond-mixture K using the empirical and theoretical rate equations are shown in Table 4.15.

The % difference shown in Table 4.15 shows that for bond-mixture K, the difference in the rate of vitrification measured is negligible and that this error is within the limits of experimental tolerances. It can be seen from Figure 4.29 that the degree of vitrification predicted from the empirical equation is slightly lower than that calculated from the theoretical rate equation over the temperature range 1100°C-1200°C. However, reaction rates in engineering ceramics are usually slower at any given temperature than those predicted by the exact rate equation. Therefore, the empirical rate equation can be expected to provide a realistic measure of the extent of reactions in grinding wheel bonds.

4.5. CONCLUSION

It is implicit from experimental evidence that the most favourable heat treatment for attaining the highest degree of vitrification can be gained by measuring vitrification properties at different temperatures and soaking times then subjecting the data to further mathematical treatment.

It has been shown that optimum heat treatment schedules exist for all grinding wheel bond materials and are summarised in Table 4.14.

If the degree of vitrification is known for a particular bond which satisfies the appropriate measure of vitrification, then from a knowledge of its thermal history, any combination of two of three conditions of firing can be transposed to find the desired combination. The three conditions of firing are: (i) rate of heating; (ii) soaking time, and (iii) maximum temperature.

5. STRENGTH OF SINTERING AND FUSIBLE BONDS AS A FUNCTION OF COMPOSITION

5.1. INTRODUCTION

The tensile strength of grinding wheel bonds is of paramount importance when designing a grinding wheel which gives optimum performance for a particular workpiece material and a particular application. The tensile strengths of such bonds have been investigated as a function of composition in the present work.

An investigation which optimises a particular vitrification measure is possible. However, considering the compositions used here, the optimised vitrified state would be reached under different heat treatment conditions which would involve a large amount of time and effort. It was therefore decided to fire the compositions used in the present study at a temperature of 1200°C (soaking temperature) for 40 hours. This provided the opportunity to study the effect of under-and over-firing on the properties and performance of sintering and fusible bond materials.

5.2. VITRIFIED BOND CONSTITUTION

The relationship between bond composition and fired strength was investigated by crushing samples , used for vitrification experiments, into a finely divided powder then quantitatively measuring the crystalline phases using the powder x-ray method outlined in Appendix D. The composition of the raw materials appears in Appendix B.

Plots of mullite, quartz, and glass content were drawn as a function of clay content are shown in Figures - 5.1, 5.2 and 5.3, respectively.

Also shown are superimposed details of feldspar and quartz content. Work on the constitution of clay-based materials has been carried out by Chaudhuri [186,187]. The relationship between equilibrium and experimental constitutions could not be quantified owing to the fact that in all the mixtures used, the clay content was constant at 45% wt. Earlier work also lacks information on equilibrium data.

A paper by Brindley and Ougland [188] provided more detailed information regarding the comparison of composition measured by x-ray analysis and theoretical predictions. Table 5.1 shows the experimental data obtained by these workers. They kept the quartz content constant at 30% wt and varied the amount of feldspar up to 60% wt. It was expected that equilibrium would be reached in a shorter time due to the higher alkali content. However, a firing duration of two hours was used which was insufficient for equilibrium conditions to be reached. Brindley and Ougland incorrectly assumed that good agreement was obtained between measured and theoretically calculated equilibrium constitutions. There appears to be discrepancies in their work due to the fact that the first three calculated constituents add up to 74.6%, 75.6% and 90.3% and not to 100% (Table 5.1). These workers calculated the constitution of each mixture by treating them as equilibrium reaction products using the K_2O-Al_2O_3-SiO_2 ternary phase diagram. However, it appears that some mistakes may have been made. Brindley and Ougland's calculations cannot be checked due to the lack of information regarding the chemical composition of the feldspar used in their work.

The degree of conversion of the original quartz content increased with increasing feldspar content which was expected owing to the increased amount of alkali ions.

Comparing Brindley and Ougland's data (Table 5.1) with the present work (Tables 5.2), it can be seen that the mixture containing 58% clay, 12% feldspar and 30% quartz corresponds to mixture B in the present work. Table 5.2 shows that mixture B was found to have 31.69% silica, which is 1.69% more than the initial value of 30%. In all the test samples, even after 40 hours' firing time, the initial quartz content had not decreased even with increasing feldspar content, and cristobalite had not been detected. The % silica column in Table 5.2 does not provide a comparison between observed and calculated values due to the fact that quartz was experimentally observed, whilst the theoretical phase is 'free silica' as tridymite and/or cristobalite. These phases are assumed to have reacted into the liquid during the soaking period. This accounts for the slightly higher observed liquid contents. The difference between experimental and theoretical liquid contents increased with increased feldspar content. It is noted at 30-40% wt. feldspar content that the experimental and theoretical liquid contents agree with each other. Figure 5.4 shows an optical micrograph of mixture P (40% wt. clay, 50% wt. feldspar and 10% wt. quartz) polished using silicon carbide grinding papers and 5μ and 1 μ diamond-grit polishing paste. The sample is composed of ∝ - alumina, glass, mullite crystals plus a large number of pores. Figure 5.5. shows the electron microprobe analysis of the two mullite forms contained in mixture P. The samples were etched in 40% Hydrofluoric Acid for two minutes.

The theoretical constitutions given in Table 5.2 were calculated using expressions derived in Chapter 4 allowing for the change in composition of the liquid phase as the temperature increased from 985°C to 1200°C.

These results agreed with previous results showing that during the 40 hours' soaking period, quartz had not reacted. This was thought to be due to large quartz particle sizes.

Therefore, it was considered appropriate to compare the results by assuming that the mixtures were composed of clay and feldspar only. Expressions were derived using the technique described in Chapter 4 and these were used to calculate values shown in Table 5.3. It can be seen that the expressions derived produced negative results for % silica content for some mixtures high in liquid content. Clearly in this case, the theoretical technique proved to be unreliable.

5.3 BOND POROSITY

The apparent and true porosity data for each bond mixture is shown in Table 5.4. Figure 5.6 illustrates the effect of glass content on the % apparent porosity for all test pieces fired at 1200°C for 40 hours. The graph shows that apparent porosity decreases linearly as glass content increases until a value of 1% apparent porosity has been reached. The relationship is independent of composition variations and is not solely a function of initial clay content. Figure 5.7 illustrates the relationship between true and apparent porosities as a function of clay content. For a particular value of true porosity, open porosity is greater for specimens that contain the most clay content. Figure 5.8 shows the level of true porosity as a function of feldspar content which was measured in accordance with the method oulined in Appendix C. Apparent porosity was measured in accordance with the method outlined in Appendix A.

The percentage of true porosity decreases linearly with increasing feldspar content. Up to 25wt.% feldspar content the true porosity decreases linearly as a function of feldspar content, then deviates from linearity which is indicative of over-firing. Over-firing results in the growth of pores caused by de-gassing within the bond. The effect is amplified somewhat in specimens containing more glass.

Figure 5.9 confirms this observation. The existence of large closed pores contained in the bond for materials made with high glass contents is shown in Figure 5.10.

Apparent porosity is dependent to a great extent on the amount of glass within the bond and since gases released in the bond are due mainly to the breakdown of feldspar, it is expected that the growth of pores will be greater in bonds containing the most glass. This is due to the fact that gases cannot easily escape from highly viscous glass melts, thus resulting in a reduction in the apparent porosity.

5.4. STRENGTH OF SINTERING AND FUSIBLE BONDS

The strengths of the test pieces of bond material were tested in flexure using the experimental procedure outlined in Appendix E. The displacement speed of the ram was 5mm/s. The results of the tests together with the Weibull modulus for each set of test pieces, and the average tensile strength for each composition are given in Table 5.5. Figure 5.11 shows the flexural strength as a function of glass content for all bond compositions.

Figure 5.12 shows the average tensile strength of bonds as a function of glass content. The tensile strength was calculated by considering differences in stressed volumes in geometrically-similar test pieces. This involved using both the procedure outlined in Appendix E and the Weibull moduli of the bond compositions.

Correlation of the test results with x-ray determined bond constitution resulted in a very good correlation with % wt. glass content (r=0.93), and poor correlations with % wt. mullite content (r=0.52) and % wt. quartz content (r=0.34). The results are shown in Figures 5.12-5.14.

The general trend observed was that the strength of bonds increases with increasing glass content.

This contradicts Grofcsik's [87] opinion that clay-based materials containing higher glass contents possess lower strengths. It is considered here that increasing the glass content decreased the deleterious effects of porosity which resulted in higher observed strengths in addition to a decrease in mullite and quartz contents .

Figures 5.15 and 5.16 shows the average tensile strength as a function of mullite and quartz content which depends on the initial clay content of the bond mixtures. The results are linear and show strength increases with decreasing clay and quartz content.

Strength is controlled by defects in the microstructure which is determined by the composition of the bond and the inherent defects.

Cracks around quartz particles were observed in all the bond samples, the largest quartz grains being 500μm in diameter. In addition to this, all bond compositions contained porosity which is known to decrease the strength of ceramic materials by reducing the load bearing area. A certain number of bond compositions are known to have been overfired. These bonds contained over 55% wt. glass content and resulted in large pores similar in size to the size of the largest quartz grains.

On a smaller scale of size the largest pores range in size from 50μm to 100μm observed in some fractured bond bridges of grinding wheels made with fusible bonds studied in this work (Figure 5.10). Figure 5.17 shows the fracture pattern of a bond bridge.

The fracture origin observed is a small pore surrounded by mirror, mist and hackle regions.

Figure 5.18 shows the relationship between the natural logarithm of fracture strength and true porosity.

Owing to the scatter of the results, a line of best fit has been drawn through the data. The value of the slope of the line is approximately 4.1. The range for ceramic materials varies between 4 and 11. Owing to the wide scatter of strengths in the test pieces, a linear relationship is not established. One reason is that the quartz content will create residual stresses in the matrix which will be added to the stress derived from the applied load, which will become more pronounced as the quartz content increases. Additionally, the shape of the pores will be variable from mixture to mixture and has been shown to affect the slope of the gradient of the Ryshkewitch-Duckworth curve [75]. Another reason why data scatter should not produce a linear relationship stated by Warshaw and Seider [106], is due to the nature of the quartz particles. These workers stated that large quartz grains exist within a quasi-pore due to the quartz breaking away from the matrix during cooling. When determining porosity levels in these bonds, only a fraction of the volume will be measured. However, since the quartz particle de-bonds from the matrix the full volume of each quasi-pore should be included in the value of true porosity used in the strength-porosity relationship.

Additionally the quasi-pore will not be able to carry any load. It is also possible that the level of true porosity is underestimated due to the small size of the test pieces.

Owing to the geometry of the specimen, evolving gases would be liberated to atmosphere leading to a decrease in the size of the pores. One would expect the experimental data to fit the Ryshkewitch-Duckworth equation approximately.

If the data did fit the Ryshkewitch-Duckworth equation then the Griffith flaw in each specimen would be of comparable severity. However, the decrease in strength due to higher quartz contents implies a further factor contributing to an increased Griffith flaw size.

This may occur by cracks formed around quartz particles linking up to each other.

The decrease in strength observed with higher quartz contents occured because there is a reduction in the load bearing area. This was thought to be caused by quartz particles de-bonding from the matrix and/or cracks around quartz particles linking-up to each other thus contributing to larger Griffith flaws in the bond.

Figure 5.19 illustrates the relationship between Weibull modulus and quartz content as a function of clay content. An increase in the Weibull modulus with increased quartz content for higher quartz-containing bonds in consistent with the probability of finding the most serious flaws at the surface of the specimen in the region of the highest tensile stress.

However, the increase in the m-parameter for the lower quartz content materials indicates another type of Griffith flaw is operating and that specimens are failing because of this type of flaw. This type of flaw must be associated with the formation of larger pores caused by de-gassing.

The flaw must be a combination of a pore and a crack because large spherical pores do not produce such high stress concentrations unless they contain a sharp notch.

In certain parts of the bond it has been observed that quartz particles appear at the surface of a pore wall. This may also produce a Griffith flaw. It is apparent that these flaws must be of the same order of severity as quasi-pores owing to the fact they are not reflected in the strength-quartz content relationship (Figure 5.14).

Figure 5.20 shows the effect of glass content on the Weibull modulus of bond compositions used in this work.

The schematic diagram at the top of Figure 5.20 shows the nature of the microstructure as observed from fracture specimens, and coincides with observartions made fracture surfaces of whiteware bodies [118]. The right-hand side of this curve indicates the increased number of pores due to the increased glass content, whilst the left-hand side indicates the reduction in strength-impairing flaws due to the decreased quartz content. It appears, from the graph, that at high glass contents the scatter remains relatively constant although the number of pores is increasing. This indicates that the glass content itself affects scatter of the data.

It is assumed that specimens on the left-hand side of the curve fail by cracks around quartz particles and those on the right-hand side of the curve fail by pore-crack flaws. Those specimens not represented by the extremes of this curve must fail by a combination of pore-crack flaws and linked cracks eminating from quartz particles. Figure 5.20 shows the microstructual mechanisms responsible for failure with increasing glass content.

The results presented can clearly be explained in terms of defects in the microstructure of the bond. The composition primarily affects the strength of the specimen and the nature of the defect when fired at the same time and temperature.

The large flaws which control the fracture pattern are either cracks around large quartz particles , or pore-crack flaws where the large pores are formed by released gases from the feldspar into the glassy matrix.

In terms of the published literature, the above summary might be applied to the work carried out by Beech and Norris [114], Ludas [113], Eitel [86], and Grofcsik [87].

It was found by a number of workers that repeated firing of clay-based materials decreased the strength of the body. Eitel [86] claimed that this was due to the coarsening effect of mullite. Repeated firing would lead to coarsening of the pores thus increasing their size and contributing to failure by pore-crack flaws. Grofcsik [87] produced two sets of specimens with identical composition each containing quartz of maximum particle size, 10μm. One set of specimens was fired using a standard heat treatment schedule whilst the other set of specimens was subjected to repeated firing. The second set of specimens was found to be weaker. Grofcsik concluded that the reduction in residual quartz content had decreased the strength of the specimens owing to the increase in the number of cracks around quartz particles. However, from the present study, it is apparent that repeated firing will increase pore size and since the quartz particle size was small in Grofcsik's specimens, it seems likely that pores would not have to be very much larger than the initial quartz particle size to become the most serious flaws in the specimens tested.

In order to explain an increase in strength found by several workers using fine quartz at high quartz contents, an alternative explanation to the 'pre-stress theory' is required. It is suggested that strength in these bodies is controlled by pores of larger size rather than by cracks around quartz particles.

The increase in quartz content would reduce the tendency to overfire with a corresponding decrease in the size and number of pores resulting in an increase in the strength.

Beech and Norris observed that the maximum strength occurred below the maximum bulk density which suggested that the level of true porosity can be reduced further.

This should raise strength whilst Griffith flaws become more serious. Physically, larger closed pores are growing in size as smaller pores shrink.

A rapid decrease in strength was observed by Ludas [113] when using quartz particles below their optimum size. This was not observed by Warshaw and Seider [106] who fired their samples to maximum bulk density. This may be explained by the fact that really fine quartz enhances vitrification of these compositions such that the specimens become over-fired. Here, it is possible that pore-crack flaws dominate the strength of the body to such an extent that a range of optimum sizes of quartz particles for different bodies is plausible.

5.5. CONCLUSION

The results presented in this chapter can clearly be explained in terms of defects in the microstructures of the bonds tested. With reference to Figure 5.20 the sharp decrease in Weibull modulus appears to be due to a transition from failure due to cracks around quartz particles to failure by pore-crack flaws caused by an increase in the size and number of pores in the microstructure. The resulting scatter in the results decreases due to a decrease in the number of quartz particles, but, is still relatively low due to the increase in size and number of pores in the microstructure. These observations are similar to those made by Oral, Sallam and Messer [118].

6. QUARTZ DISSOLUTION IN SINTERING AND FUSIBLE BONDS

6.1. INTRODUCTION

In a heterogeneous reaction there is a reaction interface between the reacting phases, such as a nucleus and the matrix or crystal and melt. For the reaction to proceed, three stages are required; (i) material transport to the interface; (ii) reaction at the phase boundary; and (iii) material transport of reacted products away from the reaction interface. Reactions at the interface also absorb or liberate heat thus changing boundary temperatures and limiting the rate of the process. Any of these processes determines the overall rate of the process since the overall reaction rate is determined by the slowest of these series of steps.

The dissolution of quartz in grinding wheel bonds requires no nucleation step. One process that can determine the rate of the overall reaction is the phase-boundary reaction rate which is fixed by the movement of atoms across the interface. However, reaction at the phase boundary leads to an increased concentration at the interface. Atoms must diffuse away from the interface so that the reaction continues. The rate of material transfer and the diffusion rate is controlled by molecular diffusion in the presence of a high viscosity liquid phase.

The fraction of quartz remaining is quite important when considering the heat treatment of grinding wheels. Early investigations of the dissolution of quartz focused on porcelain bodies using feldspar as the liquid solvent [165-166].

The fraction of quartz remaining as a function of firing time was studied by Krause and Keetman [189], Hamano [190] and Mattyasovsky-Zsolnay [88].

Considerable data was produced for whiteware bodies by Lundin [167] on residual quartz content using x-ray diffraction techniques. Lundin attempted to fit the relationships derived as functions of time to his data but without success.

A model was presented here which describes quartz dissolution and was compared with Lundin's data and experimental data from the present work. A mathematical model was developed which was compared with experimental data generated using the x-ray powder method in accordance with the method outlined in Appendix D. The powder samples were crushed in a mortar and pestle to a size suitable for x-ray diffraction. Lundin explained the difficulty in developing a realistic model for quartz dissolution. The difficulty arises from the fact that the phase boundary between quartz and melt moves during the diffusion process. The problem of a fixed phase boundary can be solved without difficulty although this is not equivalent to actual conditions.

It was also found from this study that Jander's equation [191] provides a good fit for quartz dissolution.

6.2. DISSOLUTION MODEL

The model was based on the assumption that at a constant temperature, T, a particle of quartz melts in the surrounding viscous melt, and that the rate of change of the volume of quartz is proportional to the volume of the quartz present at that instant in time, i.e.

$$\frac{dv}{dt} \propto v \qquad \ldots(6.1)$$

The assumption is based on the fact that alkali ions diffuse from the viscous melt to the quartz particle boundary thus producing a dissolution rim around each particle.

A high reaction rate will initially occur which will continuously decrease as the quartz particle will be converted to a viscous melt.

Previous work on quartz dissolution has considered spherical quartz particles with the same diameter or average diameter. With an increase in time at an isothermal temperature, the radius of the particles decreases. The equation relating the original radius of the particle and its penetration depth is,

$$r' = r - \Delta r \qquad \ldots(6.2)$$

where r' is the particle radius at any time, r is the original particle radius, and Δr is the penetration depth. Figure 6.1 shows a typical quartz particle with a penetration depth, Δr.

The penetration depth is equivalent to the diffusion distance for the movement of alkali ions during time, t, from the start of the reaction. As time proceeds, Δr increases as r' reduces which results in the decrease in the fraction of quartz remaining and a reduction in the dissolution rate.

It is assumed that the reaction rate is inversely proportional to the original particle size distribution and the penetration depth. This assumes that quartz particles have a relatively complicated particle size distribution which is true for clays used for grinding wheel bonds, hence,

$$\frac{dv}{dt} \propto \frac{1}{a.\Delta r} \qquad \ldots(6.3)$$

were a is a constant relating to the original particle size distribution.

The constant of proportionality is related to the diffusivity or diffusion coefficient at a temperature T owing to the diffusion-controlling mechanisms of alkali ion mobility to and from the reaction boundary. Equating 6.1 and 6.3 and introducing the diffusion constant, D_T, and a constant u to ensure dimensional homogeneity, yields the differential equation,

$$\frac{dv}{dt} = - u . D_T . \frac{V}{a . \Delta r} \qquad ...(6.4)$$

The negative coefficient indicates a decrease in quartz volume as time, dt, increases in magnitude. The temperature dependence of diffusivity is expressed by Arrhenius's equation,

$$D_T = D_o \, e^{(-Q/RT)} \qquad ...(6.5)$$

where D_o is a constant for the given chemical state, Q is the experimental activation energy for diffusion of species, R is the universal gas constant, and T is absolute temperature.

Fick's law states that diffusion distance Δr is a function of time and absolute temperature and is described by the equation,

$$\Delta r \approx \sqrt{D_T . \, t} \qquad ...(6.6)$$

Inserting values of D_T and Δr from equation 6.5 and 6.6. into equation 6.4 yields,

$$\frac{dv}{v} = - \frac{u}{a} . D_o^* . \exp\left\{-\frac{Q}{2RT}\right\} . \frac{dt}{t^*} \qquad ...(6.7)$$

To solve equation 6.7 at an isothermal temperature, T, and assuming that the original volume fraction, V, at zero time changes to a final volume, v, within a time, t, the differential equation can be integrated.

$$\int_{V}^{v} \frac{dv}{v} = - \frac{u.D_o^{\frac{1}{2}}}{a} \exp\left\{-\frac{Q}{2RT}\right\} \int_{o}^{t} \frac{dt}{t^*} \qquad \ldots(6.8)$$

The principal equation becomes,

$$\ln\left\{\frac{v}{V}\right\} = - \frac{u.D_o^{\frac{1}{2}}}{a} t^*.\exp\left\{-\frac{Q}{2RT}\right\} \qquad \ldots(6.9)$$

grouping the constants together

$$A = \frac{u.D_o^{\frac{1}{2}}}{a} \qquad \ldots(6.10)$$

$$\text{and } B = Q/2R \qquad \ldots(6.11)$$

The constants A and B can be evaluated using two values of volume of quartz fraction at the same or different soaking times at two different temperatures T_1 and T_2.

The two equations can be solved simultaneously,

$$\ln\left\{\frac{v_1}{V}\right\} = - A.t_1^*. \exp\left\{-\frac{B}{T_1}\right\} \qquad \ldots(6.12)$$

$$\ln\left\{\frac{v_2}{V}\right\} = - A.t_2^*. \exp\left\{-\frac{B}{T_2}\right\} \qquad \ldots(6.13$$

From these equations the constant B is,

$$B=\frac{T_1T_2}{T_1-T_2}.\ \ln\left\{\frac{\ln\left[\frac{V_1}{V}\right]/t_1^*}{\ln\left[\frac{V_2}{V}\right]/t_2^*}\right\} \qquad \ldots(6.14)$$

The volume of quartz remaining after a period of heat treatment at the soaking temperature is,

$$v_{T,t} = V.\ \exp\{-A.t^*.\ \exp\ (-B/T)\} \qquad \ldots(6.15)$$

The mass fraction of quartz is the usual measure of quartz fraction using quantitative x-ray methods of determination. Expressing equation 6.15 in terms of mass fraction yields,

$$\frac{m_{T,t}}{\varrho_{\beta\text{-quartz}}} = \frac{M}{\varrho_{\alpha\text{-quartz}}}\exp\left[-A.t.^*.\exp\left\{\frac{-B}{T}\right\}\right] \qquad \ldots(6.16)$$

The density of α-quartz is quoted as 2651kg/m³ and ß-quartz as 2640kg/m³ [192]. Therefore,

$$m_{T,t} = M.\ \frac{\varrho_{\beta\text{-quartz}}}{\varrho_{\alpha\text{-quartz}}}.\exp\left[-A.t^*,\exp.\left\{\frac{-B}{T}\right\}\right] \qquad \ldots(6.17)$$

6.3. VERIFICATION OF MODEL

The dissolution model is tested using data provided by Lundin [167] who used a triaxial bond composition of 25%wt quartz (particle size= 13.2µm), 50% wt clay (kaolin), and 25% flux (potassium feldspar-less than 2.7µm particle size).

The model was also compared with experimental data generated using the same composition specified by Lundin. Potassium feldspar was supplied by Cookson Materials, kaolinite in the form of English china clay was supplied by E.C.C., and quartz powder (average particle size = 10.5µm) supplied by Hepworth Minerals.

The raw materials used in the present study are shown in Appendix B. The initial quartz content was 25.36%wt. which, when expressed as an absolute weight and divided by the density of quartz at ambient temperature, has a volume of $9.943 \times 10^{-3} m^3$. Using equations 6.12 and 6.13

$$\ln\left\{\frac{8.863\times10^{-3}}{9.943\times10^{-3}}\right\} = -A(2)^{*} \exp\left\{-\frac{B}{1473K}\right\} \qquad ...(6.18)$$

and

$$\ln\left\{\frac{7.803\times10^{-3}}{9.943\times10^{-3}}\right\} = -A(2)^{*} \exp\left\{-\frac{B}{1523K}\right\} \qquad ...(6.19)$$

where $8.863 \times 10^{-3} m^3$ relates to a quartz content of 23.4% wt., and $7.803 \times 10^{-3} m^3$ relates to a quartz content of 20.6% wt. Solving simultaneously yields,

$$A = 5.6216\times10^{8}$$

$$B = 333374$$

from which the experimental activation energy is,

$$Q = 2BR$$

$$Q = 33374.\ (2\times1.98725\times10^{-3})\ \text{ k cal/mole}$$

$$Q = 132.65 \text{ k cal/mole}$$

The residual quartz content is therefore,

$$m_{r,t} = 26.145 \exp\left[-5.6216\times10^{8}.(t)^{*}.\exp\left\{-\frac{33374}{T}\right\}\right] \qquad ...(6.20)$$

The data comparing Lundin's experimental results, the author's experimental results and the dissolution model is presented in Table 6.1.

The present model was tested using experimental results presented in Table 6.1 and Lundin's results. If the data values of ln (-In(m/M)/t*] are plotted against the reciprocal of absolute temperature, 1/T, then all data points should fit a straight-line relationship. The slope of the graph was calculated to be 33374, which is equivalent to constant B, using only two points. The example using the least squares method gave the slope to be 32962 for Lundin's experimental results and 34000 for the present work. This suggests that activation energies for both systems are approximately 131k cal/mole for Lundin's work and 135 k cal/mole for the present work. Figures 6.2 and 6.3 show the theoretical and experimental results for Lundin's work and the present investigation. Figures 6.4 and 6.5 show the effect of time on residual quartz content at different temperatures according to equation 6.20 together with comparative experimental data. Table 6.2 illustrates the accuracy of the model at various firing temperatures at a constant soaking time of 10 hours.

6.4. COMPARISON OF DISSOLUTION MODELS

A comparison is made from the literature with other quartz dissolution models. One of the earliest models was derived by Jander [191]. The equation can be expressed as,

$$(1-(1-Z)^{1/3})^2 = \left\{\frac{C_1 D}{r^2}\right\}.t \qquad \ldots(6.21)$$

where Z is the volume of quartz that has been dissolved, r is the original particle radius and D is the diffusion coefficient for the diffusing species.

This equation can be transformed into mass fractions using Archimedes' law, thus,

$$\left\{1-\left[\frac{m}{M}\right]^{1/3}\right\}^2 = C_2.t \qquad \ldots(6.22)$$

where C is a constant dependent on soaking temperature and initial particle size of quartz.

Krause and Keetman [189] expressed the dissolution of quartz as a function of isothermal firing time and is,

$$M - m = C_3 \ln.t. \qquad \ldots(6.23)$$

where M is the initial quartz content, m is the residual quartz content after time t. The unit of time here is seconds such that after one second of firing the residual quartz content should be the initial value.

Mattyasovsky- Zsolnay [88] expressed the dissolution equation in terms of the corrosion of quartz particles, i.e. the thickness of the dissolved layer, as the time-dependent variable,

$$r - r' = C_4 \ln t \qquad \ldots(6.24)$$

where r is the original particle radius and r' is the radius of the particle at time t. Transformation of equation 6.24 yields,

$$1 - \left\{\frac{m}{M}\right\}^{1/3} = C_5. \ln t \qquad \ldots(6.25)$$

The equation of the present model for isothermal firing conditions is transformed into,

$$\ln\left\{\frac{m}{M}\right\} = - C_6. \quad t \qquad \ldots(.6.26)$$

All constants are calculated using the time data point at 18 hours. The constants are specified in terms of time dimensioned in seconds.

6.5 DATA FITTING

The equations in the previous section have been used to test against experimental results generated by Lundin [167] for a bond mixture 40% wt. Kaolin, 40% wt quartz and 20% wt. flux. The quartz possessed an average particle size of 13.2 μm. The constants in the above models were obtained using mass fraction of quartz after 18 hours' firing. The mass fractions of all models were calculated using the following data,

(i) Jander's model $m = M(1-C_2.t)^{3/2}$

i.e. $m = 41.9(1-[1.55653x10^{-6}.t])^{3/2}$

(ii) Krause & Keetman's model $m = M - (C_3\ In\ t)$

i.e. $m = 41.9-(2.5814.Int)$

(iii) Mattyasovsky-Zsolnay's model $m = M\ (1-C_5.Int)^3$

i.e. $m =41.9(1-0.0287Int)^3$

(iv) Theoretical model $m = \exp(lnM-C_6\sqrt{t})$

i.e. $m = \exp\ (3.73-4.5079x10^{-3}\sqrt{t})$

It can be seen from the results in Table 6.3 that the values obtained using the equations by Krause & Keetman, Jander and Mattyasovsky-Zsolnay did not agree with Lundin's experimental data. The values obtained from the theoretical model are in much better agreement compared with Lundin's data. However, at long soaking times, the model produces smaller values of remaining mass fraction of quartz than the experimental results observed by Lundin.

6.6 CONCLUSION

A theoretical model for the prediction of quartz content in vitrified bonds during vitrification has been derived in this chapter. The theoretical model compares well with the experimental results and fits the experimental data better than other dissolution models. Over longer periods of time the model becomes less accurate. This is thought to be caused by the loss of mobility of alkali ions due to the local increase in viscosity at the reaction interface owing to the increased concentration of silica.

SECTION 3

GRINDING WHEEL PERFORMANCE TRIALS

7. EFFECT OF WORKPIECE AND BOND COMPOSITION ON GRINDING WHEEL PERFORMANCE

7.1. INTRODUCTION

The oxide content in vitreous bonds and the composition of workpiece materials not only affects the properties of the grinding wheel bond and the steel workpiece, but, also affects to a great extent the grinding performance of the wheel. Workpiece surface quality and productivity are also important in industrial grinding.

This chapter is composed of three parts: firstly, the effect of composition of a number of tool steels on carbide structure and mechanical properties is studied; secondly, an account is given of grinding wheel structure and the matching of grit to bond; and thirdly, a description of grinding test results is given using a range of bonds to grind eleven different tool steels at a constant rate of infeed in the surface grinding mode. The parameters measured were surface roughness, grinding forces and grinding power, and the volume of metal removed per width of wheel.

7.2. ALLOY CONSTITUENTS IN FERROUS WORKPIECE MATERIALS

Tool steel materials contain various alloying elements which characterise their properties. These elements have different effects when added to the steel. The most important elements are chromium, vanadium, tungsten, carbon and molybdenum.

7.2.1. Effects of Alloying Elements

Chromium - chromium with carbon forms M_7C_3 (Cr_7C_3) and $M_{23}C_6$ ($Cr_{23}C_6$) carbides. Cr_7C_3 has been observed in high-carbon tool steels which partially dissolves during hardening treatment. Chromium carbide $Cr_{23}C_6$ is completely soluble at temperatures higher than 1100°C. Chromium is responsible for increasing hardenability of tool steels, and a reduction in oxidation and scaling during heat treatment.

Vanadium - vanadium is the hardest carbide formed in tool steels and exists as an MC (VC) carbide. Its hardness accounts for the difficulty in grinding steels high in vanadium content.

Tungsten - tungsten forms a hard complex carbide in the form M_6C (Fe_4W_2C and Fe_3W_3C) when in the presence of iron and carbon. This carbide partially dissolves when the temperature exceeds 1000°C, tungsten improves hot hardness which is retained by the precipitation of secondary hardening carbides.

Carbon - in plain carbon steels, carbon forms iron carbide Fe_3C. In tool steels, carbon forms complex carbides with V, W, Mo and Cr to produce MC, M_6C and $M_{23}C_6$ carbide structures. Many carbide particles in high carbon steels remain undissolved in a martensite matrix. The amount of the surrounding matrix, i.e. a low-carbon content steel will produce a ferritic matrix of low hardness, whilst a high-carbon content steel will have a martensitic matrix as well as a fine dispersion of complex carbides.

Molybdenum - Molybdenum forms the same carbides as tungsten, i.e. M_6C (Fe_4Mo_2C and Fe_3Mo_3C) and $M_{23}C_6$ ($Fe_{21}Mo_2C_6$).

7.2.2. Heat Treatment of Tool Steels

Tool steels are subjected to two basic heat treatments:

(i) A hardening (austenitising and quenching) heat treatment which results in a hardened martensitic matrix rich in carbon and other alloying elements, some retained austenite, and some undissolved residual carbides;

(ii) A tempering heat treatment, which results in stress relief, transformation of retained austenite with multiple tempering and, most importantly, the precipitation of secondary carbides responsible for hardening of the steel.

7.2.3. Carbide Structure

The microstructure of annealed tool steels consists of a ferritic matrix and an excess of alloy carbide. The carbide (M_6C) was the first carbide to be discovered in annealed high speed steel in 1928, having a f.c.c. crystal structure of lattice parameter 1.104nm and a chemical composition in the range Fe_3W_3C to Fe_4W_2C [193].

Since tool steels contain several cabride-forming elements, these alloy carbides contain more than one of these elements rather than being pure carbides.

Annealed tool steel carbides may be classified as follows:

(i) M_6C - a tungsten - or molybdenum - rich carbide corresponding to the double η carbide. Its composition was first reported as $W_{3-2}Fe_{3-4}C$. However, other workers reported the composition of η_2 double carbide as Mo_4Fe_2C [194,195]. Generally carbide is classified as η_1, or η_2 according to its composition, i.e.

$$\eta_1 = A_4B_2C - A_3B_3C \qquad ...(7.1)$$

$$\eta_2 = A_2B_4C \qquad ...(7.2)$$

where A is an atom of the elements (Ni, Co, Mn, Cr, Fe, V and Ti), and B corresponds to the elements (Mo, Ta, Hf, W and Nb) [194].

The lattice parameter of η_2 carbide is always larger than that of the η_1 carbide for the same elements [194, 195]. However, it has been reported that the lattice parameter of the M_6C carbide varies with composition [196].

(ii) $M_{23}C_6$ - an f.c.c. carbide corresponds to the pure $Cr_{23}C_6$ carbide of lattice parameter 1.0638nm [197]. The double carbide role of $M_{23}C_6$ is also reported [198]. The following reaction occurs due to the addition of tungsten or molybdenum to iron in solution:

$$Cr_{23}C_6 \xrightarrow{(+Mo/W)} (Fe,Cr)_{21}(Mo/W)_2C_6 \xrightarrow{(+Mo/W)} M_6C. \qquad ...(7.3)$$

The transformation of $M_{23}C_6$ to M_6C is also reported to occur in chromium steels containing molybdenum and/or tungsten [199];

(iii) MC (M_4C_3) - this carbide corresponds to the pure cubic vanadium carbide VC, usually reported as V_4C_3 because it had not been detected in its stoichiometric form as VC in steels. This carbide is very stable because it forms directly out of its matrix without prior formation of any metastable phases, and does not transform to any other carbide at high temperature.

Since tool steel carbides are not pure carbides, their composition and lattice parameters of MC, M_6C and $M_{23}C_6$ carbides are shown in Table 7.1.

7.2.4. Workpiece Metallography

The carbide phases existing in tool steels can be distinguished using the etching techniques described by Blickwede et al. [206]. The volume of carbide phases can be quantitatively represented by lineal analysis and point counting [207]. The technique used in this study was image analysis using a computer to provide quantitative data. This work was carried out at The University of Manchester.

Specimens were cut from bar stock and set in resin mountings. The samples were ground using 320-grade SiC paper then using a 600 grade paper. The samples were thoroughly washed so that debris was not transferred to the smoother papers.

Samples were rotated at right angles during grinding so that striation marks were completely removed.

The samples were transferred to polishing discs using 6µm, 1µm then 0.25µm diamond paste.

The samples were then prepared for etching. Three types of carbide, MC, M_6 C, and $M_{23}C_6$ are evident in tool steels etched in 2% nital (etchant A). Various etching times were used on different tool steels in order to obtain the correct contrast between the dark matrix and the bright carbide particles for use on the image analyser. The polishing/etching techniques were performed at the University of Manchester. The chemical composition of the tool steels used appears in Table 7.2.

M_6C carbide particles were stained brown when etched with a 4% aqueous solution of sodium hydroxide saturated with potassium permanganate, $KMnO_4$ (etchant B).

MC carbides were blackened by eletrolytically etching in a 1% aqeous solution of freshly-prepared chromic acid at 3 Volts (etchant C). The specimen was connected as the anode whilst a stainless steel cathode was employed. The experimental etching bath is shown schematically in Figure 7.1. The etching time depended on the level of contrast required for the image analysis.

The quantitative analysis on each specimen was performed after applying each etchant to the specimen under scrutiny. At first M2 tool steel was etched in etchant A for 5 minutes. All carbides were revealed against a dark matrix. The number of carbide areas intercepted were counted together with particle size distribution, phase proportion, and mean carbide diameter. M2 was then etched in etchant B which stained M_6C particles brown, thus revealing $MC+M_{23}C_6$ carbides.

The specimen was again analysed and, results taken. Finally, the specimen was etched in etchant C to reveal $M_{23}C_6$ carbides. In this case, the specimen was stained black indicating that $M_{23}C_6$ carbides do not exist in M2 tool steel.

Considering C_A to be the total volume of carbide phase (after being etched by etchant A), i.e. $M_{23}C_6+M_6C+MC$, C_B to be the volume of the carbide phase $MC+M_{23}C_6$ (after being etched by etchant B), and C_C to be the volume of $M_{23}C_6$ (after being etched by etchant C). then:

C_A-C_B yields the volume of M_6C carbides;
C_B-C_C yields the volume of MC carbide; and
C_C yields the volume of $M_{23}C_6$ carbides.

The results of the quantitative analysis appears in Table 7.3.

7.3. GRINDING WHEEL STRUCTURE

The structure of a grinding wheel is defined by the volume ratio of grit, bond and porosity and is designated by a structure number, N_s, which defines the percentage volume contribution of grit to the overall volume. The wheel may be dense (close) or open (wide), depending on the bond volume. One particular grinding wheel manufacturer defines the structure number as,

$$V_g = (62-2N_s)\ [\%] \qquad ...(7.4)$$

where the constants in the equation are found by derivation from a graph of grit volume versus structure number.

The constants in this empirical equation depend on how each wheel manufacturer assigns grades to their wheels. The structure number corresponding to values of abrasive grit volume contribution from one particular grinding wheel manufacturer is given in Table 7.4.

The grade of the grinding wheel relates to the composition of the wheel. It is assumed that the ingredients are unchanged and that the manufacturing process is under control. A variation in the composition will influence these characteristics and thus the grade scale is then related to the composition of the grinding wheel and the bond. The ternary diagram shown in Figure 7.2 relates the volume contributions of bond (V_b), grit (V_g) and porosity (V_p) together on the same diagram. The sum of these volumes is equal to the total apparent volume (V);

$$V = V_g + V_b + V_p \qquad ...(7.5)$$

This equation implies that the sum of % grit, % bond, and % porosity is equal to 100%.

Most wheel manufacturers use different bond mixes and proportions of abrasive and bond to achieve a given grade (hardness) of wheel, therefore, iso-grade lines do not usually coincide with iso-porosity lines. An example of a manufacturer's grading for wheels with different compositions is shown in Figure 7.3. Wheels with the same grade plotted as straight lines against overall composition are uniformily inclined to the iso-porosity lines, rather than coinciding with them.

Each manufacturer uses his own methods to achieve a particular wheel grade and structure number. Moreover, bond formulations and methods of manufacture vary between manufacturers, although with apparently identical abrasive grit, bond and pore contents and having the same letter grade and structure number, wheels can expect to perform differently. The secret lies in the composition of the bond; for vitrified wheels, the differences in performance may be attributed to whether a sintering or a fusible bond is used.

For the compositions used in this work, Table 7.5 shows the approximate relationship between hardness grade, structure number and the volume contributions made by grit, bond and porosity. The data presented in Table 7.5 is from one particular grinding wheel manufacturer. The relationships are not strictly adhered to in this study owing to the grading system used at Universal. However, Table 7.5 illustrates the relationships between wheel composition and grade.

The bonds used in the structures selected for wheel performance testing were composed of a clay compound, to maintain green strength and shape whilst firing and provide plasticity when forming,

a flux to provide the vitreous phase to bond the grits together, and quartz which occurs naturally in both the clay and the flux. For the purpose of testing wheel performance using different bond compositions, it was decided to use sintering bonds and fusible bonds. A sintering bond is one with a high clay content, and a fusible bond is one with a high glass content (controlled by the clay/flux ratio). Thirteen bond compositions were initially used for the wheel structures. However, owing to manufacturing problems, six compositions were used - these being bond mixtures P, R, T, V, W and X. The vitrification properties of these bond compositions are given in chapter 4.

7.3.1. Cold-Pressed Wheel Structures

There are two ways of producing a vitreous-bonded grinding wheel; pressing to density and pressing to pressure. When pressing to a known density, the structure is calculated on a volume basis and pressed to a known volume and density. For example, the following table may be constructed thus,

	Density	Volume %	Mass (ϱV)	Mass %
Abrasive	A_ϱ	A_v	A_w	A_w (%)
Bond	$B_{\varrho 2}$	Bv_1	Bw_1	Bw_1 (%)
Binder 1	$B_{\varrho 2}$	Bv_2	Bw_2	Bw_2 (%)
Binder 2	$B_{\varrho 3}$	Bv_3	Bw_3	Bw_3 (%)
Porosity	-	p -	-	-
		100%	W_{total}	W_{total} (%)

where p is the total volume of porosity in the grinding wheel structure. From this, porosity is induced by the binder content and pressing the structure to a known density.

From this table, the mould charge can be calculated using the following equation,

$$\text{Mould charge (mass)} = \text{volume of mould.} \quad \frac{W_{total}}{V_{total}} \qquad \ldots(7.6)$$

To calculate the approximate real density of the structure the following equation is used,

$$\varrho\,\text{real} = \frac{A_w + B_{w1}}{A_v + B_{v1}} \qquad \ldots(7.7)$$

The approximate apparent porosity is,

$$\%\ \text{porosity} = \frac{\varrho\,\text{real} - \varrho\,\text{apparent}}{\varrho\,\text{real}} \times 100 \qquad \ldots(7.8)$$

When pressing to pressure, known masses of grit and bond are pressed in order to achieve different levels of pressed density. Mixtures of grit, bond, and binder are pressed at different pressures, and measurements of apparent density are recorded.

In order to correlate grinding wheel performance with different workpiece materials, hardness measurements were made on a series of grading bars at the Universal Grinding Wheel Company.

To calculate the relative volume contributions of grit, bond and porosity, the bond size, % loss of mass on ignition, density of grit and bond should be known. The bond size is,

$$B_x = \frac{1000.\ m_b}{m_g} \qquad \ldots(7.9)$$

The ratio of bond to grit masses. The volume % grit, bond and porosity is thus calculated using the following equations,

$$\text{vol. \% grit, } V_g = \frac{100000.\ \varrho\,\text{wheel}}{\left\{1000 + \frac{B_x(100-i)}{100}\right\}\ \varrho\,\text{grit}} \qquad \ldots(7.10)$$

$$\text{Vol. \% bond, } V_b = \frac{100.\ B_x\left\{\frac{(100-i)}{100}\right\}.\ \varrho\,\text{wheel}}{\left\{1000 + \frac{B_x(100-i)}{100}\right\}.\ \varrho\,\text{bond}} \qquad \ldots(7.11)$$

$$\text{Vol. \% porosity, } V_p = 100 - V_g - V_b \qquad \ldots(7.12)$$

Where i is the ignition loss in the clay on firing, i.e. due to loss of water or burning of carbonaceous matter. In the present study, bond compositions P, R and T are used in K-grade structures containing 60-grit white alumina which are used to manufacture grading bars and abrasive segments. These bonds were used in K-grade structures owing to the ability to match K-grade structures manufactured at Universal. To achieve the correct proportions for the mixes it was necessary to establish the bond and grit densities, and the corresponding pressed densities.

The abrasive grit used was 60 grit (approximately 220μm diameter) white alumina (>99.7% purity) with density 3960 kg/m³. The bond was formed from equal mass proportions of potash feldspar and clay (ball clay blended with china clay). The densities of the flux and clay mixture were 2600 and 2850 kg/m³, respectively. Dextrin was used as a temporary binder. Considering bond mixture P (40wt. % clay, 50wt. % flux, 10wt % quartz),

$$V_{clay} = \frac{0.4kg}{2850kg/m^3} = 1.4 \times 10^{-4}\ m^3$$

$$V_{flux} = \frac{0.5kg}{2600kg/m^3} = 1.923 \times 10^{-4}\ m^3$$

$$V_{quartz} = \frac{0.1kg}{2640kg/m^3} = 3.787 \times 10^{-5}\ m^3$$

The density of the mixed bond, ϱ_{bond}, is,

$$\varrho_{bond} = \frac{M_{clay} + M_{flux} + M_{quartz}}{V_{clay} + V_{flux} + V_{quartz}} \qquad ...(7.13)$$

$$\therefore \varrho_{bond} = \frac{0.4 + 0.5 + 0.1}{(1.4\times10^{-4})+(1.923\times10^{-4})+(3.787\times10^{-5})}$$

$$\varrho_{bond} = 2701.46\ kg/m^3$$

The ratio of bond to grit mass for a K-grade (structure 6) wheel structure, based on information provided by Universal, is,

$$\frac{m_b}{m_g} = \frac{13.6wt.\%}{86.4wt.\%} = 0.157$$

The apparent density of the mixture is,

$$\varrho_{mixture} = \frac{M_{grit} + M_{bond}}{V_{grit} + V_{bond}} \qquad ...(7.14)$$

$$\therefore \varrho_{mixture} = \frac{M_{grit} + 0.157M_{grit}}{V_{grit} + V_{bond}}$$

Therefore, the mass of grit in this structure occupies 50% volume of the total wheel volume, hence,

$m_{grit} = 0.5.V_{bar}.\ \varrho_{grit}$

where V_{bar} is the volume of a grading bar which was approximately $1.4 \times 10^{-5}m^3$

$\therefore\ m_{grit} = 0.027kg$

The volume of the grit is given by the following expression,

$$V_{grit} = \frac{m_{grit}}{\varrho_{grit}} = \frac{0.027kg}{3960kg/m^3} = 6.8\times10^{-6}\ m^3$$

also

$$V_{bond} = \frac{m_{bond}}{\varrho_{bond}} = \frac{0.157m_{grit}}{\varrho_{bond}} = 1.57\text{x}10\text{-}6m^3$$

$$\therefore\ \varrho_{mixture} = \frac{m_{grit}+0.157m_{grit}}{V_{grit}+V_{bond}} = \frac{m_{grit}(1+0.157)}{V_{grit}+V_{bond}}$$

$$\therefore\ \varrho_{mixture} = \frac{1.157\text{x}0.027kg}{(6.8\text{x}10^{-6}+1.67\text{x}10^{-6})m^3} = 2702.14kg/m^3$$

The required mass of each grading bar is,

$m_{bar} = \varrho_{mixture} \cdot V_{bar}$

Therefore, the mass of the grading bar is 37.8g. For the composition of the grading bar,

$\frac{m_{bond}}{m_{grit}} = 0.157$

also $m_{grit} + m_{bond} = m_{bar}$

hence, $m_{grit} = 32.69g$ and $m_{bond} = 5.14g.$

The required mass for a K-grade (structure 6) grading bar is 37.83g of which the mass of grit is 32.69g and the mass of bond is 5.14g. All bars were graded at Universal Grinding Wheel Company at Stafford. From the bars tested only six composition appeared to have the predicted grade. These bars contained bond compositions P, R, T, V, W, and X. These bars were subsequently made into segments and tested for grinding performance. For the bars considered, the relative proportion of masses of grit and bond is given in the following table.

Bond Composition	Measured Grade	Mass Of Bar (g)	Mass Of Grit (g)	Mass Of Bond (g)	Mass Of Dextrin (g)	Mass Of Water (g)
P	K+	37.83	32.69	5.14	2.05	1.03
R	K	37.25	32.19	5.06	2.02	1.11
T	K	37.18	32.13	5.05	2.02	0.96
V	L	37.25	37.25	5.06	2.02	0.96
W	L	37.12	32.08	5.04	2.02	0.96
X	L+	36.92	31.91	5.00	2.01	0.96

mass of bar ≡ $m_{bar} = \varrho_{bar} V_{bar}$

mass of dextrin ≡ $m_{dextrin} = 0.4\ m_{bond}$

(i.e. 40% of bond mass)

mass of water ≡ $m_{water} = 0.03\ m_{grit}$

(i.e.3% of grit mass)

The same procedure was followed for L-grade structures using V, W and X bond compositions. The mixture was pressed in a custom-built mould so that double-ended compaction of the mould charge was achieved. The charge was pressed under the compression platens of a 20 tonne capacity Denison universal testing machine. The grading bar mould appears in Figure 7.5.

7.3.2. Cold-Pressed Abrasive Segments

When testing the performance of vitrified alumina grinding wheels, segments were attached to a steel backing which is connected to a steel hub such that two segments are in contact with the workpiece. The segments are designed so that the radii of the segment and segment holder are common to the centre of the arbor. The geometry of the segment appears in Figure 7.4. The angle subtended by the segment is therefore,

$$\alpha = \frac{57.3\ell}{r} \qquad \ldots(7.15)$$

The effective surface area is the product of the length of the segment and the width of the segment, hence,

$$S.A._{effective} = \frac{r.\alpha.\ w}{57.3} \qquad \ldots(7.16)$$

For the segment shape used in this work, the angle subtended α is 40.36° which gives an effective surface area of $1.429 \times 10^{-3} m^2$.

The force required to press each segment is calculated to be 17.65kN based on data supplied by the Universal Grinding Wheel Company. The relative proportions of masses of grit and bond for the abrasive segments using the six bond compositions are given in the table below,

Bond Composition	Measured Grade	Mass Of Bar (g)	Mass Of Grit (g)	Mass Of Bond (g)	Mass Of Dextrin (g)	Mass Of Water (g)
P	K	46.34	40.05	6.29	2.52	1.20
R	K	45.61	41.12	4.49	1.79	1.23
T	K	45.52	39.34	6.18	2.47	1.18
V	L+	45.62	39.43	6.19	2.47	1.18
W	L	45.45	39.28	6.17	2.47	1.18
X	L	45.22	39.08	6.14	2.46	1.17

The abrasive segments were heat treated in the same way as the grading bars, i.e. heated using a heating rate of 2.9°C/min up to 300°C in order to burn-off chemically-bound water, held for one hour, heated to 600°C to burn-off dextrin, held for 2 hours, heated using a heating rate of 2.9°C/min up to 1200°C, thermally soaked for 40 hours at 1200°C then cooled at a rate of 1.8°C/min to room temperature.

A doubled-ended compaction mould was designed for producing the abrasive segments. This is shown in Figure 7.6.

7.3.3. Grinding Wheel Safety

The abrasive segments were bonded to the steel backings using Permabond F246 epoxy acrylic adhesive. The adhesive had a tensile strength of 28N/mm². Each pair of abrasive segments was screwed to the steel hub and speed tested (1.5x maximum operating speed) at the Universal Grinding Wheel Company. The speed tests were performed in a brake-controlled speed-test machine up to 45m/s surface speed. All segments survived this test speed and were inspected afterwards for signs of cracks/deterioration. The test certificate appears in Appendix F.

7.3.4. Wheel Manufacture

Owing to manufacturing problems during preparation and pressing of abrasive mixtures, it was noted that the soft-grade bars were hard and the hard-grade bars were soft. Grade bars in the hardness range J-L were extremely accurate when grade tested at Universal Grinding Wheel Company. The tests were conducted by measuring the torque of a penetrating chisel. Some test bars had experienced 'pin-holing' which can affect the measured grade and density, especially on small samples.

'Pin-holing' is caused by burn-out of lumps of binder during firing which produces fairly large holes. This was allevitated by thoroughly mixing and sieving the bond mixtures.

A number of harder grade bars bloated and laminated during heat treatment. This problem causes bars to have low densities and soft grades. Bloating and lamination is related to mixing quality which occurs in products with high bond content, especially if the bond is fusible or contains a high amount of volatile products.

This is usually alleviated by using fusible bonds for soft grades and sintering, or refractory, bonds for harder grades. For the grades used in this work, a limited number of fusible and sintering bond compositions could be tolerated. Another important aspect to consider when manufacturing grinding wheels is the problem of thermal stress fracture. This problem is caused by thermal expansion mismatch between abrasive grit and bond. The coefficient of thermal expansion of alumina in the temperature range 20°C-500°C is reported to be 8-9.5 x 10^{-6}/°C [192]. C.B.N. is more critical having an expansion coefficient between 2-5 x 10^{-6}/°C (20°C-500°C). The thermal expansion mismatch causes cracks to appear between grit and bond when the wheel is in the furnace during the cooling cycle.

The thermal expansion of glasses is dependent on the oxide content of the glass. The additive property of various oxides contributing to the overall coefficient of thermal expansion of the glass has led to the formulation of the general equation,

$$\alpha = a_1p_1 + a_2p_2 + a_3p_3 + ... + a_np_n \qquad ...(7.17)$$

or $$\alpha = \sum_{i=1}^{n} a_np_n \qquad ...(7.17a)$$

This equation assumes linear behaviour below the glass transition point of the glass where α is the coefficient of linear expansion, a is a constant for the oxide contributing to the expansion of the glass and p is the weighting function for each oxide. Silica has a low expansion coefficient, whereas, soda (Na_2O) and potash (K_2O) have very large expansion coefficient owing to their large atomic volumes.

A number of researchers have calculated constants for each oxide based on experimental data. Table 7.6 shows the constants for each oxide contributing to the thermal expansion of glass according to various researchers [208-211]. It should be noted that Winklemann and Schott's results [208] were based on a mathematical model, English and Turner's results [209] were measured in the temperature range 25°C to 90°C, Gilard and Dubrul's results [210] measured in the range 100°F to 130°F, and Hall's results [211] were measured from 25°C to the lower limit of the critical temperature range of the glasses tested.

As stated, matching the coefficient of thermal expansion between C.B.N. and glass bond is extremely critical. General Electric Superabrasives [212] has conducted some experimental work on the thermal expansion of alumino-borosilicate glass frits. General Electric measured the thermal expansion of various glass frits compared with C.B.N. The present work has made a comparison between General Electric's experimental work and the models published in the literature [208-211]. The results appear in Table 7.7. From the table, it is obvious that frits F2 and F4 have too high a thermal expansion coefficient for C.B.N. abrasive grits. However, the bonds used in this work are alumino-silicate bonds.

It can be seen from Table 7.7 that Winkelmann and Schott's empirical model [208] best predicts the coefficient of thermal expansion of alumino-borosilicate glass bonds. For alumino-borosilicate glass bonds used in this work a comparison was made between experimentally-determined expansion coefficients and Hall's results [211]. It was decided to use Hall's results owing to their repeatibility with Al_2O_3-Na_2O-CaO-SiO_2 glasses [213]. Table 7.8 shows the comparison using compositions used in this work. The Table shows good correlation between Hall's empirical results and the current experimental work.

The measurement of the coefficient of linear expansion appears in Appendix G.

7.4. GRINDING WHEEL PERFORMANCE

The performance of grinding wheels is measured using wheel structures with optimum grades for particular workpiece materials. The structures selected for use in the current experimental study have been formulated in the form of segments appropriately graded to machine hardened tool steels using data provided in Unicorn Abrasives' Grinding Data Book [3]. All grinding trials were carried out on commercially-available tool steels containing a wide variety of alloying elements and having standard heat treatments which produced similar hardness levels (see Table 7.2). The wheel structures used were manufactured with six bond compositions in order to compare the effects of bond composition on wheel performance. Variables measured were volume of metal removed, normal and tangential grinding forces, grinding power, surface roughness, G-ratio, wheel wear and workpiece abrasive number. A further objective of this experimental section is to show that bond strength affects G-ratio during stage II of the grinding wheel wear curve. Experiments were designed to ensure that bond fracture was the predominant wear mechanism. This allowed the present author to prove or refute Graham and Voutsadopoulos's assumption that bond strength, and composition, controls wheel wear and grinding wheel performance.

7.4.1. Experimental Procedure

The grinding trials were designed so as to replicate, as close as possible, the conditions under which bond fracture is predominant [214].

These conditions give a true understanding of the effect of bond composition, in terms of tensile bond strength, on the performance of the wheel structures tested.

When considering the design of grinding experiments, there are three ways of performing the experiments viz, sequential testing, alternate or pseudo-random testing and random testing where each test permutation is generated using a random-number scheme.

Psuedo-random testing has been deemed appropriate when comparing the wear of two or more abrasive types or wheel structures [215]. This type of testing allows variables such as diamond dresser wear, grinding fluid temperature and supply to affect the complete run of experiments and minimise their effects.

Complete randomisation of such tests would require wheels to grind workpiece materials in any order thus requiring abrasive segments, used in the current work, to be removed after each test run. Therefore, owing to lack of time to conduct these tests, the experiments were performed in a pseudo-random manner. Table 7.9 shows the pseudo-random order of experiments.

The system used for measuring grinding forces and power is shown in Figure 7.7. The experimental apparatus is shown in Figure 7.8. A Kistler three-component force dynamometer was used to measure grinding forces. The three orthogonal components of force were detected using piezoelectric force sensors. For each force component a proportional electric charge is converted into an analogue D.C. voltage in the charge amplifier. A separate charge amplifier is used for each force component.

A low-pass Butterworth filter is connected downstream from the charge amplifier input stage which suppresses high-frequency interference vibrations while the force measurement is logged.

An oscilloscope was used to monitor power signals which were taken from the analogue output port of the functionmeter. The functionmeter was used to measure electrical output from one-phase of the three-phase motor. An instrument transformer was used to measure instantaneous voltage and current at the spindle motor.

The product is shown as the active power (spindle output from one phase) on the display unit and must be multiplied by three to give the total power used. The peak power is then used to form wheel stabilisation charts for each workpiece material-bond combination. Output from the oscilloscope's time base was used to determine table speed.

A P.C.-based data-logging system was developed at Liverpool John Moores University which transformed logged data signals in to tables and diagrams. The grinding machine used for research purposes was a modified ABWOOD 5025 surface grinding machine. Maximum spindle speed was 3400 R.P.M., minimum table speed was 0.025m/s, maximum table speed was 0.37m/s and the maximum spindle power was 10kW.

The method of wheel-wear measurement chosen was the 'razor-blade' technique. The method involved grinding a workpiece which was narrower than the grinding wheel. A groove was worn into the wheel profile which was measured with reference to the non-grinding portion of the wheel using a razor blade. The blade was then lowered into position with the wheel just touching the blade.

The table was then traversed and the wheel lowered until the wear profile was replicated onto the razor blade. The profile was then measured using a Form Talysurf measuring instrument. Figure 7.9 shows a typical wheel wear trace generated by the Talysurf instrument. Figure 7.1- shows the schematic diagram for measuring wheel wear using the 'razor-blade' technique.

The dressing procedure adopted used a single-point diamond which was traversed across the full width of the wheel at 0.2mm per revolution.

Ten passes of the dresser at a working removal depth of 20µm removed 200µm of abrasive on wheel radius, or 400µm on diameter.

When the wheel was dressed, a layer of ink was applied to both abrasive segments and the workpiece conditioning blocks so that the wheel-workpiece combination was true. This process was repeated until the ink was removed from both wheel and workpiece conditioning block.

The conditioning block was used to establish steady-state grinding conditions when the experimental data was being collected. The conditioning blocks were cut from each workpiece material and used in combination with the abrasive segments made with different bond compositions. Once the steady-state conditions were achieved, the depth removed from each workpiece conditioning block was noted and applied to the amount of material to be removed from the test blocks.

In order to replicate conditions of bond fracture wear [214], the depth of cut for all grinding tests was maintained at 10µm, the table speed was set to 0.2m/s, and the wheel speed was set to 30m/s.

The abrasive segments were made with 60 grit white alumina abrasive grits with structure number 6, and hardness K and L.

For each workpiece-bond combination, a typical grinding test sequence involved truing the workpiece-wheel combination, establishing steady-state grinding conditions by grinding the prescribed depth of material, removing 10μm of workpiece material, measuring the variables-surface roughness, volume of material removed, grinding forces, power used and wheel wear, inspecting each segment after use, then finally correlating wheel data to grinding conditions. Figure 7.11 shows the assembled segmented grinding wheel whilst Figure 7.12 illustrates some uneven wear experienced by one of the segments. The coolant used throughout the grinding trials was Trim VHPE200 50:1 dilution with water.

7.4.2. Effect Of Volume Of Metal Removed On Grinding Forces

Wheel wear in aluminium oxide wheels is due purely to mechanical wear of the wheel in the form of grit flaking and bond fracture in contact with the work surface. As a consequence of the dressing process cracks induced in the grits cause the rake and flank faces to become rough.

From the results presented it appears that the variation in grinding forces with respect to the volume of metal removed produces the following sequence of events.

(i) Grits that have been cracked due to dressing are loosened and completely, or partially, removed. Owing to the sharpness of the wheel the initially small wear-flat areas and the work surface will develop enough pressure to produce plastic flow of the asperities on the work surface.

As cutting proceeds the wear-flat area increases, the wear rate of the wheel increases and the force components increase accordingly. These variables appear to retard to a much slower rate of increase which forms a stable region;

(ii) The stable range is shown as a linear increase in the normal grinding force which indicates that the grinding process is progressing efficiently due to the combined effects of grit attrition and fracture thereby increasing the wear flat area;

(iii) The wheel finally enters the terminal stage of its cutting life which is apparent only for workpiece materials M15, T4 and T15. Here, a decrease in force components is apparent accompanied by a high wheel wear rate. A reduction in the number of cutting grits causes a reduction in the wear-flat area present at the wheel-workpiece interface which consequently increases the grinding force per grit. This causes the wear rate to be extremely high to such an extent that the wheel rubs the workpiece leading to workpiece burn. Figures 7.13-7.15 illustrate the effect of the volume of material removed per unit width on the normal grinding force component. The wheel structure used for illustrating the effect of workpiece materials on the grinding parameters contains P-type bond, white alumina (60 grit), and is manufactured to a K-grade structure.

A similar trend can be seen from the power signals recorded during grinding - this can be seen in Figures 7.16-7.18. Figures 7.19-7.21 confirm the relationship between grinding force components for each workpiece material to be linear

7.4.3. Effect Of Workpiece Material On Surface Finish

The quality of ground components is characterised by their surface finish.

Figures 7.22-7.24 show the effect of the volume of metal removed on the workpiece surface finish. In all cases almost the same roughness was measured in all workpiece materials, approximately 0.25µm Ra before being ground. During the metal removal process the surface roughness deteriorated rapidly, the rate of which seemed to depend on the workpiece material.

The workpiece materials all had approximately the same hardness value (63HRC), therefore one can assume that they will cause the same material pile-up height assuming the grinding conditions are the same and that the surface temperature does not exceeed the tempering temperature of the material. The workpiece material, however, has the effect of dulling the wheel surface, or indeed, loading the wheel surface. The variations in the wheel surface may lead to a reduction in the number of active cutting edges. In the present work, the wheel loading effect was probably eliminated due to the use of hardened tool steel workpiece materials, and because the test period was restricted to removing 196mm^3/mm of material.

Initial differences in surface roughness are due to the different characteristics exhibited by each workpiece material when initially dressed. As metal removal proceeds the rate of grit dulling is very much dependent on the workpiece material.

This is shown in the force/power diagrams. Dulling of the grits increases the pile-up height far above the original surface. As grinding proceeds into the terminal period of the metal removal process, the number of active grits will decrease thus increasing the surface roughness even further.

7.4.4. Effect Of Alloying Elements And Bond Composition On Grinding Wheel Wear

Workpiece materials M1, M42, T1 and T4 were used to study the effect of cobalt content on the grinding ratio, materials M1, M2 and M15 were used to study the effect of vanadium content on G-ratio, whilst steels 01 and D3 were used to study the effect of chromium content. For comparison purposes the effect of carbon content is not included since the amount of carbon is purposely controlled in order to allow the correct amount of complex carbides to precipitate during heat treatment.

Differences in the grindability of the tool steel materials with the same hardness is attributed to the break down of grits at a rate dependent on the shape, size and quantity of the carbides in the matrix of the workpiece material.

Vanadium carbide, which is reported as having a very high hardness value, has a significant effect in reducing the grinding ratio with a slight discontinuity occurring just below 2wt.% vanadium This is shown in Figure 7.25. Chromium was found to be effective in decreasing the G-ratio when grinding D3 die steel. This is thought to be caused by the occurrence of chromium carbide which is hard and blocky. This is shown in Figure 7.26.

Cobalt, in the presence of tungsten, was found to be deleterious to G-ratio. This was also confirmed by research conducted by Tarasov [216]. Figure 7.27 confirms this observation using an abrasive wheel with bond compositions R and X. The figure shows that the reduction in G-ratio is also dependent on the strength of the bond bridges that hold the grits firmly in a three-dimensional matrix.

The quality and hardness of carbide particles can therefore be classed as the most important factor in determining the grindability of these widely used engineering materials. Graham and Nee [217] postulated that the amounts and hardnesses of these carbides can be combined linearly to give an abrasive number which is essentially a weighted average of the Vickers' hardness values of complex carbides in the workpiece materials. The abrasive number, A_n, is given as,

$$A_n = V_{matrix}.\ H_{matrix} + \sum(V_{carbide}.H_{carbide}) \qquad ...(7.18)$$

where V_{matrix} is the volume of the matrix, H_{matrix} is the hardness of the matrix, $V_{carbide}$ is the volume of the carbide, and $H_{carbide}$ is the hardness of the carbide.

Graham and Nee [217] correlated the abrasive number to the G-ratio of a series of tool steels ground with a diamond wheel. These researchers asserted that the grinding ratio was inversely proportional to the abrasive number. The hardness of the matrix was taken as the average hardness reading using a Vickers' pyramid diamond. According to the linear law of mixtures the high amount of complex carbides would probably affect the bulk hardness value. Therefore, it must be borne in mind that the calculated abrasive number is approximate.

It is also assumed that the grinding zone temperature does not exceed the tempering temperature of the workpiece material which implies that the bulk hardness is the same as that measured at room temperature. Hardness of the various carbides are given in the literature [218]. For the carbides used in this work, the hardnesses are:-

Chromium carbide, $M_{23}C_6$: 1300kg/mm^2

Tungsten and molybdenum carbide, M_6C : 1650kg/mm²

Vanadium carbide, MC : 2840kg/mm²

Using equation 7.18 together with the data above, the abrasive number for the workpiece materials used in this work is shown in Table 7.3. Figure 7.28 shows the wheel-wear parameter G-ratio plotted against abrasive number. The results excluded from the figure are omitted for clarity. The complete set of results include tests involving all six bond compositions are shown in Table 7.10. The curve shows an exponential decay of the form:

$$G = A.\exp[-BA_n] \qquad ...(7.19)$$

where A and B are constants dependent on bond and workpiece composition. To obtain the constants, the equation 7.19 was transformed into its linear form, i.e.

$$\log_e G = \log_e A - BA_n \qquad ...(7.19a)$$

For the six bond compositions used in the abrasive structures, a set of G-ratio results were produced. The results appear in Table 7.10. The data were transformed into their linear form so that the constants were evaluated for each bond composition. Tabulated results appear below. Figure 7.29 illustrates the linear relationship.

Bond	Characteristic Empirical Relationship	Correlation Coefficient, r.
P	$G = 8262\exp\{-0.0075An\}$	0.93
R	$G = 9278\exp\{-0.0077An\}$	0.93
T	$G = 9511\exp\{-0.0076An\}$	0.95
V	$G = 7862\exp\{-0.0072An\}$	0.96
W	$G = 8045\exp\{-0.0073An\}$	0.95
X	$G = 6902\exp\{-0.007An\}$	0.95

A comparison between empirically-determined G-ratio using equation 7.19 and experimentally-determined G-ratio for all workpiece materials appear in Figure 7.30. Bonds R and X have been shown for clarity. Good approximation is predicted using the empirical relationship. The transformed linear form of the above equations are presented below.

Bond	Characteristic Empirical Relationship	Correlation Coefficient, r.
P	$\log_e G = 9.01-0.0075A_n$	0.93
R	$\log_e G = 9.15-0.0077A_n$	0.93
T	$\log_e G = 9.16-0.0076A_n$	0.95
V	$\log_e G = 8.96-0.0072A_n$	0.96
W	$\log_e G = 8.98-0.0073A_n$	0.95
X	$\log_e G = 8.83-0.007A_n$	0.95

From these equations the constant A is reported to be a function of the bond composition, primarily. When plotted $\log_e$ A is,

$$\log_e A = 9.99 - 0.019\,\sigma_t \;:\; r = 0.62$$

The constant B is reported to be 0.0073 ±0.0004. The above equation has the form,

$$\log_e A = C_1 - C_2\sigma_t \qquad ...(7.20)$$

Substituting equation 7.20 into 7.19a produces,

$$\log_e G = (C_1 - C_2\,\sigma_t - BA_n)$$

Applying the exponential function to the above equation yields,

$$G = \exp[C_1] \cdot \exp[-C_2\sigma_t] \cdot \exp[-BA_n]$$

letting $\propto = \exp[C_1]$ and $ß = C_2$ makes the wheel-wear parameter (G-ratio) an exponential decay function of bond and workpiece composition, i.e.

$$G = \propto \cdot \exp[ß\sigma_t - BA_n] \qquad ...(7.21)$$

From the experimental data presented, the evaluated constants modify equation 7.21, thus,

$$G = 21807\ \exp[-0.0073A_n - 0.019\sigma_t] \qquad ...(7.21a)$$

Figure 7.31 illustrates the correlation between experimental and predicted G-ratios for the workpiece materials used in this work.

For bond composition R the correlation coefficient is 0.93, and for bond composition X the correlation coefficient is 0.96. Although the empirical equations predict the G-ratio quite accurately in the present work, the aforementioned assumptions lead the author to conclude that drawing conclusions from the empirical data should be treated with caution unless the surface temperature and the hardness of the matrix and carbides at that temperature is known when substituted in the linear law of mixtures. A further reservation in the use of the linear law of mixtures is the possibility of the effect of carbide constituents possessing a greater hardness than the abrasive which might produce an adverse effect in damaging the abrasive. Here a lower G-ratio would result.

7.4.5. Effect Of Bulk Hardness On The Grindability Of Tool Steels

The effect of the matrix retaining the carbide was examined and its effect on the grindability assessed. The workpiece materials tested were M2 and 01 tool steels. The difference in hardness was achieved by overtempering the specimens at temperatures 700°C, 760°C and 400°C, 550°C respectively, producing hardnesses of 46 and 34HRC (for M2) and 45, 43HRC for 01 tool steel.

Figure 7.32 shows the effect of bulk hardness on G-ratio for the two materials. In general the G-ratio increases with a decrease in bulk hardness. This is, however, more pronounced for 01 than for M2. The difference between the two steels is due to the presence of complex carbides in M2 tool steel. In M2 steel, the carbides remain unchanged in hardness and volume in the over-tempered steel.

The decrease in G-ratio with the reduction in bulk hardness with M2 suggests that the ability of the matrix to retain these complex carbides controls the effectiveness of the carbides, This implies that the wear resistance of the steel is determined by the amount and volume of the complex carbide and the hardness of the matrix which retains these carbides. The stronger the retention of the matrix the more likely the carbide particles will act as an abrasive against the flanks of the grits.

7.5. CONCLUSION

The results presented in this chapter clearly show the effect of workpiece material composition and grinding wheel bond composition on factors which affect the performance of alumina grinding hardened tool steels. The performance indicators measured were surface finish, G-ratio, grinding force components and power.

An empirical model has been developed which describes wheel wear as an exponential decay function of grinding wheel bond strength and workpiece material composition. The limitations of using the linear law of mixtures when applied to calculating the workpiece abrasive number have been highlighted.

SECTION 4

DISCUSSION, CONCLUSIONS AND FURTHER WORK

8. GENERAL DISCUSSION ON GRINDING PERFORMANCE

Section 1 of this thesis provided a firm foundation for measuring the performance of vitreous-bonded grinding wheels. Malkin [27] provided this basis when he developed a test procedure which incorporated not only the wheel-wear parameter (G-ratio) but, also, the specific grinding energy. The test ensured that the best grinding wheel produced the highest grinding ratio without burning the workpiece.

Section 2 of this thesis provided the basis to compare grinding wheel performance by characterising the bond used in sintering and fusible bonds. The effect of bond composition on the performance of vitrified grinding wheels requires a thorough understanding of grinding wheel wear, and the reactions in vitreous bonds, in order to design meaningful grinding experiments. The most important region of the wheel wear curve (stage II) plays an important role in assessing the performance of grinding wheels. The main wear mechanisms were abrasive wear of the grit, grit fracture, bond fracture and fracture at the bond/grit interface.

Studies on the effect of grit and bond type and workpiece material composition showed that the G-ratio could be expressed in terms of an abrasive number which is calculated using the weighted hardnesses of complex carbides in the micro-structure of hardened tool steels. The implications for choosing the grit/bond combination was highlighted by Graham and Nee [64] for CBN, and Koenig and Messer [70] for conventional abrasives.

The process of grinding wheel wear in terms of mechanical stresses applied to abrasive grits was proposed by Graham and Voutsadopoulos [72].

The model assumed that grit fracture alone was taking place during stage II of the grinding wheel wear curve. To take account of this fact, the abrasive grit was assumed to be rigidly held in a matrix of theoretically infinite strength. The corresponding finite-element generated data were correlated to the wheel-wear parameter, G-ratio. However, the measurement of G-ratio is difficult in stage II of the wheel-wear curve unless measurements are taken under steady-state operating conditions. Graham and Vountsadopoulos [72], however, measured total G-ratio which is the grinding ratio measurement of stages I, II and III. Therefore, it would have been more appropriate if Graham and Voutsadopoulos [72] had produced a finite-element model which incorporated bond bridges of finite strength holding the abrasive grit in place. A more accurate correlation between G-ratio and tensile strength in the abrasive grit and bond bridge would have resulted. Graham and Voutsadopoulos [72] did assume that bond strength controls wheel wear and, ultimately, grinding wheel performance under fixed grinding conditions. The results presented in this thesis indicated that bond strength does play a major role in the performance of grinding wheels. This is particularly appropriate when considering the increase in performance one could expect from a diamond/ C.B.N. wheel.

Reactions in the ceramic bonds were found to produce quartz, mullite and glass in the post-fired bond composition. Again, the importance of understanding the role of reactions in vitrified C.B.N. and diamond grinding wheels is of great importance.

The breakdown of clays and fluxes at the vitrification temperature was found to produce porosity within the bond bridges themselves.

This action produced an optimum level of porosity whereby the bond attained its highest strength.

This led to the conclusion that there must be an optimum degree of vitrification which is a function of maximum soaking temperature and thermal soaking time. A semi-empirical model was derived based on previous work on the heat treatment of clay bodies and bricks. The model produced data relating to soaking time and temperature required for attaining the maximum degree of vitrification. However, during the course of this work, the model has not been verified.

The appropriate measures of vitrification were correlated with the % liquid in equilibrium constitution. This produced an accurate correlation showing water absorption and apparent porosity to be an almost linear function of theoretical liquid content (Figures 4.6. and 4.8). A double correlation was then produced in terms of initial bond content. This was used to draw vitrification maps which are used to depict the compositions of bond that will produce zero porosity, or in other words, optimum bond properties at the particular heat treatment. The vitrification maps are shown in Figures 4.12 and 4.13. In terms of high-performance C.B.N. and diamond grinding wheels, the compositions which give 0% water absorption and apparent porosity are dependent on the composition of the bond itself. This provides wheel manufacturers with opportunities to increase performance and still maintain good strength characteristics. It was also shown that the Norton-Hodgdon relationship was applicable to most of the bond compositions used in this work, although some compositions vitrified over a much shorter time period.

These compositions possessed very high glass contents which indicates that understanding chemical processes in glass materials may provide a better model for predicting vitrification behaviour.

The strength of sintering and fusible bonds was studied by firing bars on bond using compositions with varying amounts of clay, quartz and flux. The samples were fired at constant soaking temperature for a fixed period of time in order to produce specimens that were under-fired and over-fired and ones with optimum bond properties, i.e. fully vitrified.

It was found that sintering bonds possessed low strength and appeared to fail by cracks around quartz particles due to the inversion of quartz on cooling. Bonds with a higher glass content (fusible bonds) were considered to fail from pore-crack flaws, i.e. cracks caused by inverted quartz particles linking up to pores in close proximity causing failure to the bond. These bonds tended to have a higher strength but a considerably lower Weibull modulus (Figure 5.20). This was thought to be caused by the increased glass content contributing to significant scatter in strength results. This observation was in accordance with results published by Oral, Sallam and Messer [118].

From the strength results, it was considered that failure in vitreous bonds was caused by quartz cracking, pore-crack flaws and stress-raising pores. These problems may be alleviated by reducing quartz particle size, changing the shape of the pore by forming more liquid in bond, and preventing quartz particles from de-bonding from the glassy matrix.

Owing to the deleterious effects of quartz particles in the bond bridge, it was considered that a way of predicting the mass of quartz remaining after thermal treatment of the grinding wheel would prove to be of use to grinding wheel manufacturers. Existing mathematical models did not provide the accuracy with which to estimate the amount of quartz remaining after a particular thermal soaking period. The proposed model considered that the rate of change of volume

of quartz is proportional to the volume of quartz remaining at any instant in time - an assumption based on the fact that alkali ions diffuse from the glass melt to the boundary of the quartz. The model takes account of the differences in density in the two forms of quartz (∝ and ß-quartz), and has been shown to produce good agreement with the experimental data (Figures 6.3. and 6.5). Additional data was supplied by Lundin [167] who provided an extensive study on quartz dissolution in white ware bodies. The model developed in this thesis also compared well with Lundin's experimental data (Table 6.1 and 6.3). The model provides grinding wheel manufacturers with the ability to control the amount and number of fracture-initiating flaws.

Section 3 of this thesis combined the knowledge of grinding wheel wear, performance testing, fracture models and reactions in bonds then related this knowledge to grinding wheel performance data. The information published in Unicorn Abrasives' Grinding Data Book [3] provided the author with optimised wheel structures with which to grind hardened tools steels.

In order to replicate Graham and Voutsadopoulos's [72] experimental conditions of predominantly fracture wear during the machining of the workpiece materials, grinding conditions under which fracture wear was predominant with the wheel structures used were specified by Bhattacharyya and Moffatt [214].

A series of grinding tests were conducted with a segmented wheel using abrasive structures with different bond compositions. A number of hardened tool steels with different volumes and types of complex carbides were ground in order to quantify the effect on wheel wear and the effect of using bonds with different levels of strength. The wheel-wear parameter (G-ratio) was found to be an exponential decay function of bond strength and workpiece material composition (Figure 7.28).

The models developed provided data relating grinding wheel performance to vitreous-bond strength, which is controlled by composition, heat treatment, and workpiece material composition.

The experimental results indeed showed that Graham and Vontsadopoulos's [72] finite-element model would have provided better correlation with their experimental results if bond bridges of known strength had been incorporated into their model. Further experimental evidence of the effect of workpiece material composition on wheel performance was provided when the abrasive number was found to have a significant effect on the results, although the use of the linear law of mixtures did prove to be prone to error. This was due to the assumptions that carbide hardness was higher than the abrasive hardness and that the surface temperature of the workpiece was lower than the tempering temperature during the grinding cycle. Grinding wheel performance was also found to be a function of the wear resistance of the matrix of the workpiece material. The results are shown in Figures 7.28 and 7.32.

In summary, the work presented in this thesis suggested that:

(i) The relationship between bond composition and heat treatment can be provided by studying the reactions in grinding wheel bonds;

(ii) Models for predicting the amount of quartz in vitreous bonds give grinding wheel manufacturers some limited control over the amount and number of fracture-initiating flaws;

(iii) A standardised wheel performance test relating grinding wheel performance with bond composition and workpiece material composition provides wheel

manufacturers with the ability to match grinding wheel structure/composition to workpiece material without recourse to trial and error procedures;

(iv) The wheel wear parameter (G-ratio) is highly dependent on bond strength and the composition that controls it.

9 CONCLUSIONS

i. The fired microstructure of grinding wheel bonds used in this work contained quartz, mullite in the form of acicular needles crystallised from the molten glass and platelets precipitated from clay relicts, and a glass phase of variable chemical composition.

ii From the experimental evidence presented in this thesis, it is clear that the most favourable heat treatment can be gained from measuring vitrification criteria of bonds with different compositions at different temperatures and thermal soaking times.

iii. An optimum heat treatment schedule exists for every bond composition. From a knowledge of the thermal history of a particular bond composition, the extent of vitrification can be quantified by knowing the rate of heating, the thermal soaking time and/or the maximum temperature.

iv. An empirical model describing the extent or degree of vitrification has been used to calculate the total degree of vitrification. Further experimental work is required to prove the validity of using the model.

v. The strength of grinding wheel bonds is determined by failure resulting from cracks around quartz particles, or from pore-crack flaws assuming that thermal soaking time and temperature is constant for a particular set of specimens with different bond compositions. The type of failure depends on the composition of the bond.

vi. Bonds containing a high glass content have a high tensile strength. However, a higher glass content tends to increase the statistical scatter in bond strength.

vii. The theoretical model derived for predicting the amount of quartz remaining in a grinding wheel bond after thermal treatment compared well with experimental results presented in this thesis. However, over longer periods of time, the model becomes less accurate which is thought to be caused by a reduction in the rate of material transfer at the reaction interface between quartz particles and the glass melt.

viii. The wear of a vitreous-bonded grinding wheel when grinding hardened and tempered tool steel workpiece materials has been shown to be an exponential decay function of grinding wheel bond strength and workpiece material composition. The limitations of using the linear law of mixtures when applied to calculating the workpiece abrasive number have been demonstrated.

10. FURTHER WORK

The following suggestions for further work are given below:

i. A model can be developed to incorporate the effects of the increased concentration of silica at the reaction interface between a quartz particle and the glass melt. The model should incorporate the concept of a variable melt viscosity and the resulting change in the diffusion of the glass melt.

ii. Experiments should be conducted on the effect of optimised bond heat treatment on grinding wheel performance. The empirical model developed for predicting the total degree of vitrification should be compared with these experimental results.

iii. Heat treatment schedules should be extended to include alumino-borosilicate bonds which are used in vitrified C.B.N. grinding wheels.

iv. An investigation into the effect of glass composition on the statistical scatter of strength in grinding wheel bonds with a high glass content should be undertaken.

v. The effect of quartz content on the strength of grinding wheel bonds should be investigated using raw materials that contain an appreciable amount of quartz (feldspar and china clay) and no quartz (nepheline syenite).

vi. A finite element model of an abrasive grit with bond bridges subjected to normal and tangential forces should be constructed and compared with experimental data presented in this thesis and by other researchers.

vii. Interfacial studies should be made on grinding wheels made with C.B.N. and diamond abrasive grits. The reaction products identified at the interface should then be correlated with grinding test results.

viii. The post-fired vitrified bond composition in C.B.N. and diamond grinding wheels should be investigated.

ix. Grinding wheel performance trials should be repeated with grinding wheels made with C.B.N. and diamond abrasive grits bonded to each other by alumino-borosilicate glass bonds.

x. Grinding wheel performance trials should also be conducted with other engineering materials such as titanium and nickel alloys, gamma titanium aluminide and other advanced ceramic materials.

11. REFERENCES

1. R.S. WOODBURY, "History of the Grinding Machine - A Historical Study in Tools and Precision Production", Technology Press, Massachusetts Institute of Technology, U.S.A. (1959).

2. A.H. BATEMAN, Journal of the Society of Arts, London, March 22nd, 1878, p.362.

3. THE GRINDING DATA BOOK, Unicorn Abrasives, Stafford, England, 1995.

4. J.T. BLACK, Trans. A.S.M.E, J. of Eng. for Industry, (1979), 101, p.403.

5. G.W. ROWE and A.G. WETTON, J. Inst. Met. (1969), 97, p193.

6. E.R. MARSHALL & M.C. SHAW, Trans. A.S.M.E. (1952), 74, p.51.

7. W.R. BACKER, E.R. MARSHALL & M.C. SHAW, Trans. A.S.M.E. (1952), 74, p.61.

8. M.E.MERCHANT, J. Appl. Phys. (1945), 16, p.207.

9. E.D. DOYLE AND R.L. AGHAN, Metall. Trans. B (1975), 6B, p.143.

10. S. MALKIN and N.H. COOK, Trans. A.S.M.E., J of Eng. for Ind., (1971), 93, p.1120.

11. S. MALKIN, and T. MURRAY, Proc. Fifth North American Metalworking Research Conference (1977), S.M.E., U.S.A., p.278.

12. S. KANNAPAN and S. MALKIN, Trans. A.S.M.E., J of Eng. for Ind. (1972), 94, p.833.

13. T. SHONAZAKI & H. SHIGEMATU, Bull. Jap. Soc. of Prec. Eng., (1966), 2, p.8.

14. N. TAKENAKA, Proc. Int. Conf. on Manf. Tech., (1967), Ann Arbor, Mich., U.S.A., p.617.

15. K. OKAMURA and K. NAKAJIMA, Proc. Int. Conf. Grinding (1972), Pittsburgh, U.S.A., p.305.

16. R.S. HAHN, Proc. 3rd. Int. Mach. Tool Des. & Res. Conf. (1962), U.K., p.129.

17. E.D. DOYLE and S.K. DEAN, Annals of the C.I.R.P., (1980), 29, p.571.

18. T.O. MULHEARN and T.O. SAMUELS, Wear (1963), 6, p.457.

19. S. MALKIN, Proc. Ninth North American Metalworking Research Conference (1981), U.S.A., p.235. Carnegie Press.

20. S. MALKIN, Proc. Third North American Metalworking Research Conference (1975), U.S.A., p.453. Carnegie Press.

21. S. MALKIN & S. JOSEPH, Wear (1975), 32, p.15.

22. G. WERNER, Doctoral Dissertation, Technische Hochschule Aachen, 1971.

23. S. MALKIN, Annals of the C.I.R.P., (1979), 29, p.209.

24. L. TARASOV, American Soc. of Metals (1951), 43, p.1144.

25. H. OPITZ, W. ERNST & H MEYER, Proc. 6th Int. M.T.D.R. Conf. (1962), Manchester, England, p.155.

26. G.S. REICHENBACH, A.S.T.M.E. Paper no. MR67-594, (1967), U.S.A., p.1.

27. S. MALKIN, "Grinding Technology", (1989), Ellis Horwood, England.

28. E.J. KRABACHER, Trans. A.S.M.E. - J of Eng. for Industry (1959), 81, p.187.

29. E. PATTINSON & A. CHISHOLM, Int. Conf. on Manufacturing Technology, A.S.T.M.E. (1967), p.601.

30. H. GRISBROOK, R.H. HOLLIER & P.G. VARLEY, Int. J. Production Res. (1961-62) 1, p.57.

31. H.K. TONSHOFF & T. GRABNER, Proc. 5th Int. Conf. on Prod. Engg., Jap. Soc. of Precision Engrs. (1984), Tokyo, p.326.

32. H. YOSHIKAWA, Int. Research in Prod. Engg., A.S.T.M.E. (1963), Paper no. 23, p.209.

33. L.P. TARASOV, Int. Research in Prod. Engg., A.S.T.M.E. (1963), paper no.21, p.196.

34. H. YOSHIKAWA & T SATA., Trans. A.S.M.E., J of Eng. for Industry (1963), 85, p.39.

35. H. TSUWA, Tech. Rep. of Osako Univ., Japan (1960), 10, p.733.

36. H. TSUWA, Tech. Rep. of Osaka Univ., Japan (1961), 11, p.287.

37. H. TSUWA, Tech. Rep. of Osaka Univ., Japan (1961), 11, p.299.

38. Y. TANAKA & N. IKAWA, Tech. Rep. of Osaka Univ., Japan (1962), 12, p.345.

39. G.J. GEOPFERT & J.L. WILLIAMS, Mech. Engg., (1959), 81, p.69.

40. H. TSUWA, Trans. A.S.M.E. - J of Eng. for Industry (1964), 86, p.371.

41. G.K. LAL & M.C. SHAW, Proc. Int. Grinding Conf., Pittsburgh, Pennsylvania, U.S.A. (1972), p.107.

42. N.S. EISS, Trans. A.S.M.E. - J of Eng. for Ind. (1967), 89, p.463.

43. S.K. BHATTACHARYYA, H. GRISBROOK & H. MORAN, Microtechnic, (1965), 22, p.114.

44. W. MOHUN, Trans. A.S.M.E., J of Eng. for Industry, (1962), 84, p.431.

45. K. SAITO & T. KAGIWADA, Bull. Jap. Soc. of Precision Engg., (1974), 8, p.125.

46. H. TSUWA and H. YASUI, Proc. of the Int. Grinding Conf. (1972), Pittsburgh, Pennsylvania, U.S.A., p.142.

47. G. STETIU and G.K. LAL, Wear (1974), 30, p.229.

48. E.M. TRENT, "Metal Cutting", 3rd Edition, Butterworth-Heinemann (1991), p.113.

49. E.R. MARSHALL & M.C. SHAW, Trans. A.S.M.E. (1952), 72, p.51.

50. H. GRISBROOK, The Production Engineer, (1960), 37, p.p.251-269 and 341-346.

51. C.E. DAVIS & R. RUBENSTEIN, Int. J. of Mach. Tool. Des. and Res. (1972), 12, p.165.

52. W.B. ROWE, X. CHEN, M.N. MORGAN, Proc. 30th Int. Mach. Tool Des. and Res. Conf. (1993), Manchester, U.K., p.195.

53. W.B. ROWE, X. CHEN, B. MILLS, Proc. 31st Int. Mach. Tool Des. & Res. Conf. (1995), Manchester, U.K., p.415.

54. R.P. LINDSAY, Trans. A.S.M.E., J of Eng. for Industry (1970), 92, p.683.

55. R.P. LINDSAY, amd R.S. HAHN, Proc. 4th All India Mach. Tool Des. Res. Conf., Indian Institute of Technology, Madras, India, p.537.

56. R.P. LINDSAY and R.S. HAHN, Society of Manufacturing Engineers' Technical Report no.MR71 (1971), U.S.A.

57. L. COES, "Abrasives", Springer-Verlag, New York (1971), chapter 14.

58. J.A. KIRK and W.S. SYNUITA, Proc. 2nd North American Metalworking Research Conference (1974), p.572.

59. E.J. DUWELL, I.S. HONG, W.J. McDONALD, Wear (1966) 9, p.417.

60. N.S. EISS & R.C. FABINIAK, J. Amer. Ceram. Soc. (1966), 49, p.221.

61. R. KOMANDURI, Ann. C.I.R.P. (1976), 25/1, p.161.

62. N. IKAWA and T. TANAKA, Ann. C.I.R.P., (1971), 19, p.153.

63. T.N. LOLADZE & G.V. BOCKUCHAVA, "The wear of diamonds and diamond wheels", (1967), Mashinostroeniye, Moscow, U.S.S.R.

64. W. GRAHAM and A.Y.C. NEE, Production Engineer, (1974), June 1974, p.186.

65. Y. TANAKA and T. UEGUCHI, Ann C.I.R.P. (1971), 19, p.449.

66. J.O. OUTWATER and M.C. SHAW, Trans. A.S.M.E., (1972), 74, p.73.

67. E.J. DUWELL, I.S. HONG & W.J. McDONALD, A.S.L.E. Trans. (1969), 12, p.86.

68. S. YOSSIFON and C. RUBENSTEIN, Trans. A.S.M.E., J of Eng. for Industry (1981), 103, p.144.

69. R. KOMANDURI and M.C. SHAW, Trans. A.S.M.E., J of Eng. for Industry (1976), 98, p.1125.

70. W. KONIG & J. MESSER, Ann. C.I.R.P. (1981), 30. p.457.

71. R. KOMANDURI and M.C. SHAW, Proc. 3rd North American Metalworking Research Conference (1975), U.S.A., p.481.

72. W. GRAHAM and C.M. VOUTSADOPOULOS, Int. J. Mach. Tool Des. & Res. (1978), 18, p.95.

73. S.C. CARNIGLIA, J Amer. Ceram. Soc. (1972), 55, p.610.

74. E. RYSHKEWITCH, J. Amer. Ceram. Soc. (1953), 55, p.610.

75. W. DUCKWORTH, J. Amer. Ceram. Soc. (1953), 36, p.68.

76. F.P. KNUDSEN, J. Amer. Ceram. Soc. (1959), 42, p 376.

77. D.C. FIERO, B.F. DEWEY and F.E. CROCKER, I.E.E.E. Trans. on Power Apparatus & Systems (1970), 89, p.680.

78. C.W. PARMALEE and W.R. MORGAN, Ceram. Ind. (1934), 22, p.146.

79. J.H. KOENIG, Bull. Amer. Ceram. Soc. (1940), 19, p.424.

80. S.C. SANE & R.L. COOK, J. Amer. Ceram. Soc. (1951), 34, p.145.

81. W.D. KINGERY, H.K. BOWEN, D.R. UHLMANN, "Introduction to Ceramics", (1976), 2nd Edition, John Wiley & Sons, New York.

82. H. ZOELLNER, Sprechsaal (1908), 41, p.71.

83. P.P. BUDNIKOV, Technologie der Keramischen Erzeugnisse (1958), V.E.B. Verlag, Berlin, p.532.

84. R.F. GELLER, Amer. Ceram. Soc. Bull (1933), 12, p.18.

85. O. KRAUSE and E. KEETMAN, Sprechsaal (1935), 68, p.177.

86. W. EITEL, Phys. Chem. der Silic. Barth (1941), 2, p.649.

87. J. GROFCSIK, Proc. 8th Conf. Silicate Ind. (1965), Budapest, Hungary, p.367.

88. L. MATTYASOVSKY-ZSOLNAY, J. Amer. Ceram. Soc. (1957), 40. p.299.

89. T. WEIDMAN, Sprechsaal (1959), 92, p.2.

90. I.C. KALNIN, P. CUCKA, S.I. WARSHAW, R. SEIDER, Bull. Amer. Ceram. Soc. (1968), 47, p.498.

91. H. KOCH, Ber. Deut. Keram. Ges. (1970), 47, p.538.

92. V. LACH, Intern. Ceram. (1974), 23, p.27.

93. A.I. AVGUSTINIK and I.P. ADAMASHVILI, Ceram. Abst. (1971), p.98h.

94. R.V. LELE, Cent. Glass Ceram. Res. Inst. Bull., (1955), Calcutta, India, 2, p.5.

95. P.S. AGGERWAL, R.V. LELE, B.L. MITRA, Trans. Indian Ceram. Soc. (1977), 36, p.12.

96. A. DIETZEL, Sprechsaal (1953), 86, p.251.

97. H. MARZAHL, Ber. Deut. Keram. Ges. (1955), 32, p.203.

98. A. WINTERLING, Ber. Deut. Keram. Ges. (1961), 38, p.9.

99. S.I. WARSHAW and R. SEIDER, J. Amer. Ceram. Soc. (1967), 50, p.337.

100. J.D. WEYLAND, M. Sc. Thesis (1964), University of Missouri, U.S.A.

101. C.R. AUSTIN, H SCHOFIELD, N.L. HALDY, J Amer. Ceram. Soc. (1946), 29, p.341.

102. R.W. BATCHELOR & A. DINSDALE, 7th International Ceram. Congress (1961), p.31.

103. C.J. ALLEN, Trans. Brit. Ceram. Soc. (1964), 63, p.13.

104. D. PASS and W.L. GERMAN, Ceramics (1969), 20, p.15.

105. W.J. SMOTHERS, Discussion at the end of a paper by Warshaw and Seider [106].

106. S.I. WARSAW and R. SEIDER, Ceramic Microstructures (1966), Ed. R.M. FULRATH and J.A. PASK, John Wiley and Sons, New York, p.559.

107. D. WEYL, Ber. Deut. Keram. Ges. (1959), 36, p.319.

108. G.K. DUNSMORE, J.E. FENSTERMACHER, F.A. HUMMEL, Bull. Amer. Ceram. Soc. (1961), 40, p. 310.

109. R.W. DAVIDGE and T.J. GREEN, J. Mater. Sci. (1968), 3, p.629.

110. O. KRAUSE, Sprechsaal (1937), 70, p.611.

111. O. KRAUSE, Sprechsaal (1939), 72, p.611.

112. O. KRAUSE, Sprechsaal (1942), 75, p.229.

113. M. LUDAS, Proc. 6th Conf. Silicate Ind. (1961), Budapest, Hungary, p. 297.

114. D. BEECH and A.W. NORRIS, Trans. J. Brit. Ceram. Soc. (1961), 60, p.556.

115. A. DINSDALE and W.T. WILKINSON, Trans. J. Brit. Ceram. Soc. (1966), 65, p.391.

116. A.G. EVANS and M. LINZNER, J. Amer. Ceram. Soc. (1973), 56, p.575.

117. G. KIRCHHOFF, W.POMPE, H.A. BAHR, J Mater. Sci. (1982), 17, p.2809.

118. M.S. ORAL, E.M.H. SALLAM, P.F. MESSER, Trans. J. Brit. Ceram. Soc.(1983), 82, p.31.

119. N.E. FILONENKO and J.V. LAVROV, "Petrography of Artificial Abrasives", (1958), Mashgiz, Moscow, U.S.S.R.

120. A. GUILLEAUME, Berichte der Deut. Keram. Ges. (1930), 11, p.284.

121. A. GUILLEAUME, Doctoral Dissertation, Technische Hochschule Berlin, Germany, 1927.

122. W. FRANZ, Doctoral Dissertation, Technische Hochschule Braunschweig, Germany, 1936.

123. R. REIKE and C. HAEBERLE, Berichte der Deut.Keram. Ges. (1934), 24, p.117.

124. M. MOSER, "Microstructure of Ceramics", Akademiai Kiado, Budapest, Hungary, 1980.

125. S.D. HARTLINE, Ph.D. Thesis, Pennsylvania State University, U.S.A. (1975).

126. T.I. BARRY, L.A. LAY, R.MORRELL, Trans. J Brit. Ceram. Soc. (1980), 79, p.139.

127. S. OGAWA and T. OKAMOTO, Bull. Jap. Soc. Prec. Engg. (1986), 20, p.264.

128. T. TANAKA, N. IKAWA, N. UENO, S. OKADA, Bull. Jap. Soc. Prec. Engg. (1985), 19, p.221.

129. J. YANG, D. KIM, H. KIM, Ceramics International (1993), 19, p.87.

130. A.N. KUZNICHENKO, I.M. BOGODIST, R.V. KOMOVA, E.K. MENNINIK, Steklo i Keramika (1983), 8, p.22.

131. M.J. JACKSON, N. BARLOW and B. MILLS, J. Mat. Sci. Letters (1994), 13, p.1287.

132. E.D. HONDROS, Brit. Ceram. Trans. J. (1991), 90, p.139.

133. D. MOSELEY, K.A.BRIGGS, M.H. LEWIS, Brit. Ceram. Trans. J. (1989), 88, p.41.

134. C.A. BEEVERS and M.A. ROSS, Zeitschrift fur Kristallographie (1937), 97, p.59.

135. M. HARATA, Materials Research Bulletin (1971), 6, p.461.

136. M. MOSER, "Ceramically-bonded grinding tools", Akademiai Kiado (1971), Budapest, Hungary.

137. E.R. WINKLER, J.F. SARVAR, I.B. CUTLER, J. Amer. Ceram. Soc. (1966), 49, p.634.

138. W.A. DEER, R.A. HOWIE, J. ZUSSMAN, "Rock-forming Minerals" - volume 5 : Non-silicates, Longman (1962).

139. M MOSER, Proc. Int. Conf. Grinding, Pittsburgh, Pennsylvania (1972), p.91.

140. M. MOSER, Period Polytech. Chem-Eng. (1977), 21, p.27.

141. P.M. SCOTT, M. NICHOLAS, B. DEWAR, J. Mat. Sci. (1975), 1, p.1833.

142. D. EVENS, M. NICHOLAS, P.M. SCOTT, Ind. Dia. Review (1977), September 1977, p.306.

143. A.E. SHILO, V.G. MALOGOLOVETS, G.I. KHIZHNYAK, Sverkhtverdye Materialy (1983), 5, p.5.

144. J.D. ROYLE, Trans. J. Brit. Ceram. Soc. (1974), 73, p.291.

145. E. SCHRAMM and F.P. HALL, J. Amer. Ceram. Soc. (1936), 19, p.159.

146. N.L. BOWEN, J. Am. Ceram. Soc. (1943), 26, p.285.

147. F.P. HALL and H. INSLEY, "Phase diagrams for Ceramists" Columbus Press (1947), U.S.A.

148. W.R. FOSTER, J. Am. Ceram. Soc. (1951), 34, p.151.

149. I. N'DALA, F. CAMBIER, M.R. ANSEAU, G. URBAIN, Brit. Ceram. Trans. J. (1984), 83, p.105.

150. M. DELETTER, F. CAMBIER, I. N'DALA, G. URBAIN, Brit. Ceram. Trans. J. (1984), 83, p.108.

151. G.R. SHELTON, J. A. Ceram. Soc. (1948), 31, p.39.

152. A. DIETZEL and N.N. PADUROW, Ber. Deut. Keram. Ges. (1954), 31, p.7.

153. J.F. SCHAIRER and N.L. BOWEN, American J. of Science (1947), 245, p.193.

154. J.E. COMEFORO, R.B. FISCHER, W.F. BRADLEY, J Amer.Ceram. Soc. (1948), 31. p.254.

155. A. WEISS, K.J.RANGE, J. RUSSON, Proc. Int. Clay Conf. (1969), Tokyo, Edited by L. Heller, Israel Universities Press, Jerusalem, volume 2, p.34.

156. G.W. BRINDLEY and M. NAKAHIRA, J. Amer. Ceram. Soc. (1959), 42, p.319.

157. J.F. HYSLOP and H.P. ROOKSBY, Trans. Ceram. Soc. (1928), 42, p.299

158. A.H. JAY, Trans. Brit. Ceram. Soc. (1939), 38, p.455.

159. E.B. COLEGRAVE and G.R. RIGBY, Trans. Brit. Ceram. Soc. (1952), 51, p.355.

160. H.M. RICHARDSON and F.G. WILDE, Trans. Brit. Ceram. Soc. (1952), 51, p.387.

161. S. MAZUMDAR and B. MUKHERJEE, J. Amer. Ceram. Soc. (1983), 66, p.610.

162. S.P. CHAUDHURI, Trans. Indian Ceram. Soc. (1977), 36, p.71.

163. T.N. McVAY, J. Amer. Ceram. Soc. (1936), 19, p.195.

164. G.W. MOREY and N.L. BOWEN, Amer. J. Sci. 5th Series, 4, p.1.

165. A.A. KLEIN, Trans. Amer. Ceram. Soc. (1916), 18, p.377.

166. C.W. PARMALEE and C.R. AMBERG, J. Amer. Ceram. Soc. (1929), 12, p.699.

167. S.T. LUNDIN, "Studies on triaxial whiteware bodies", (1959), Almqvist and Wiksell publishers, Stockholm, Sweden.

168. G.R. SHELTON and W.W. MEYER, J. Amer. Ceram. Soc. (1938), 21, p.371.

169. L. HERMANSSON and R. CARLSSON, Trans. J. Brit. Ceram. Soc. (1978), 77, p.32.

170. M.A. TUTTLE and R.L. COOK, J. Amer. Ceram. Soc. (1949), 32, p.279.

171. W. STORCH, H. RUF, H. SCHOLZE, Berichte Deut. Keram. Ges. (1984), 61, p.335.

172. E. BINNS, Science of Ceramics, (1962), 1. p315.

173. W.F. FORD and J WHITE, Trans. J. Brit. Ceram. Soc. (1951), 50, p.461.

174. J. BRECKER, J. Amer. Ceram. Soc. (1974), 57, p.486.

175. F.H. NORTON and F.B. HODGDON, J. Amer. Ceram. Soc. (1931), 14, P.177.

176. K. SHINOZAKI, et al., J Jap. Ceram. Soc. (1980), 88, p.418.

177. C.B. ZHU. Ph.D. Thesis, University of West England, 1992.

178. W.W. MEYER, J. Amer. Ceram. Soc. (1938), 21, p.75.

179. G.R. SHELTON and W.W. MEYER, J. Amer. Ceram, Soc. (1938). 21, p.371.

180. V. BOGAHAWATTA and A.B. POOLE, Trans. Brit. Ceram. Soc. (1991), 90, p.52.

181. P. MURRAY and J. WHITE, Trans. Brit. Ceram. Soc. (1949), 48, p.187.

182. S.A. REDFERN, Clay Minerals (1978), 22. p.447.

183. H. LE CHATELIER, Z. Phys. Chem. (1887), 1, p.396.

184. W.F. FORD, 'The Effect of Heat on Ceramics', (1967), Mc Claren and Sons Ltd, London.

185 D.N. TODOR, 'Thermal Analysis of Minerals' (1976), Abacus Press, England.

186. S.P. CHAUDHURI, Trans. J. Brit. Ceram. Soc. (1974), 73, p.37.

187. S.P. CHAUDHURI, J. Amer, Ceram. Soc. (1974). 53, p.169.

188. G.W. BRINDLEY and R.M. OUGLAND, Trans. J. Brit. Ceram. Soc. (1962), 61, p.599.

189. P. KRAUSE and E. KEETMAN, Sprechsaal (1936), 69, p.45.

190. K. HAMANO, J. Jap. Ceram. Soc. (1955), 63, p.432.

191. W. JANDER, Z. Anorg, U. Allgem. Chem.(1927), 163, p.1.

192. THE OXIDE HANDBOOK, Compiled by O. SAMSONOV (1973), Plenum Press, London.

193. A. WESTGREN and G. PHRAGMEN, Trans. Am. Soc. for Steel Making (1928), 13, p.539.

194. H.S. GOLDSCHMIDT, 'Interstitial Alloys', Butterworth, London, 1967.

195. K. KUO, Acta. Metall. (1953), 1, p.301.

196. A.C. FRAKER and H. STADELMAIER, Trans. of the Metall. Soc. of A.I.M.E. (1969), 245, p. 847.

197. Powder Diffraction Data File Index (1983), International Centre for Diffraction Data, U.S.A., Index No. 14-407.

198. H.J. GOLDSMITH, Metallurgia (1949), 40, p.103.

199. A. INOUE and T. MASUMOTO, Metall. Trans. (1980), 11A, p.739.

200. H.J. GOLDSMITH, J.I.S.I. (1948), 160, p.345.

201. H.J. GOLDSMITH, J.I.S.I. (1957), 186, p.68.

202. K.W. ANDREWS et.al., 'Interpretation of Electron Diffraction Patterns', 2nd Edition, Adam Hilger (London), 1971.

203. K. KIM, A.P. JOHNSON, W.F. HOSFORD in 'Processing and Properties of High-Speed Steels', edited by M.G.H. WELLES (1980), Las Vegas, U.S.A. The Metallurgical Society of A.I.M.E., p.32.

204. K. KUO. J.I.S.I. (1953), 173, p. 363.

205. Powder Diffraction File Index, Index Nos. 3-980, 5-0721, and 15-457 (1983), U.S.A., International Centre for Diffraction Data.

206. D.J. BLICKWEDE, M. COHEN and G.A. ROBERTS, Trans. A.S.M. (1950), 42, p.1161.

207. R.T. HOWARD et.al., 'Quantitative Metallography by Point Counting and Lineal Analysis', Trans. A.I.M.E. (1974), p.413.

208. A. WINKELMANN & O. SCHOTT, Ann. Physik (1984), 51, p.730.

209. S. ENGLISH & W.E.S. TURNER, J. Amer. Ceram. Soc. (1927), 10, p.551.

210. P. GILARD & L. DUBRUL, Verre & Silicate Industriels (1934) 5, p.122.

211. F.P. HALL, J. Amer. Ceram. Soc. (1930), 13, p.182.

212. General Electric Superabrasives, Unpublished Research.

213. G.W. MOREY, 'Properties of Glass', (1938), Reinhold Publishers, London, U.K.

214. S.K. BHATTACHARYYA and V.L. MOFFATT, Int. J. Mach. Tool Des. and Res., (1976), 16, p.325.

215. J.L. METZGER, Superabrasive Grinding, Butterworth-Heinemann, (1986), Oxford, England.

216. L.P. TARASOV, Proc. Int. Conf. on Manufacturing Technology, A.S.T.M.E. (1967), U.S.A. P.689.

217. W. GRAHAM and A.Y.C. NEE, Int. J. Mach. Tool Des. and Res. (1974), 14, p.175.

218. P.L. EWING, Trans. Amer. Soc. Metals (1952), 44, p.348.

219. I.E. ALEXANDER and H.P. KLUG, Anal. Chem. (1948), 20, p.886.

220. S.K. KHANDEWAL and R.L. COOK, Amer. Ceram. Soc. Bull (1970), 49, p.522.

221. E.J. GUMBEL, 'Statistics of Extremes', (1958), Columbia Press, New York.

222. H.A.M. AL-JEWAREE and H.W. CHANDLER, Brit. Ceram. Trans. J., (1990), 89, p.207

BIBLIOGRAPHY

1. J.L. METZGER, Superabrasive Grinding, Butterworth-Heinemann (1986), Oxford, England.

2. R. HOLZ and J. SAUREN, Grinding with Diamond and C.B.N., Ernst Winter and Sohn, 1st Edition (1988), Hamburg, Germany.

3. R.W. DAVIDGE, Mechanical Behaviour of Ceramics, Cambridge University Press (1979), Cambridge, England.

4. T. TAWAKOLI, High Efficiency Deep Grinding, Mechanical Engineering Publications (1993), London, England.

5. J. BORKOWSKI and A. SZYMANSKI, Uses of Abrasives and Abrasive Tools, Ellis Horward (1992), Chichester, England.

6. C. ANDREW, T. HOWES, & T. PEARCE, Creep Feed Grinding, Holt, Reinhart and Winston (1985), England.

7. J.E. FIELD, The Properties of Natural and Synthetic Diamond, Academic Press (1992), England.

8. J. WILKS and E.M. WILKS, Properties and Applications of Diamond, Butterworth-Heinemann (1991), Oxford, England.

9. D.R.F. WEST, Ternary Equilibrium Diagrams, Chapman and Hall (1982), 2nd Edition, London, England.

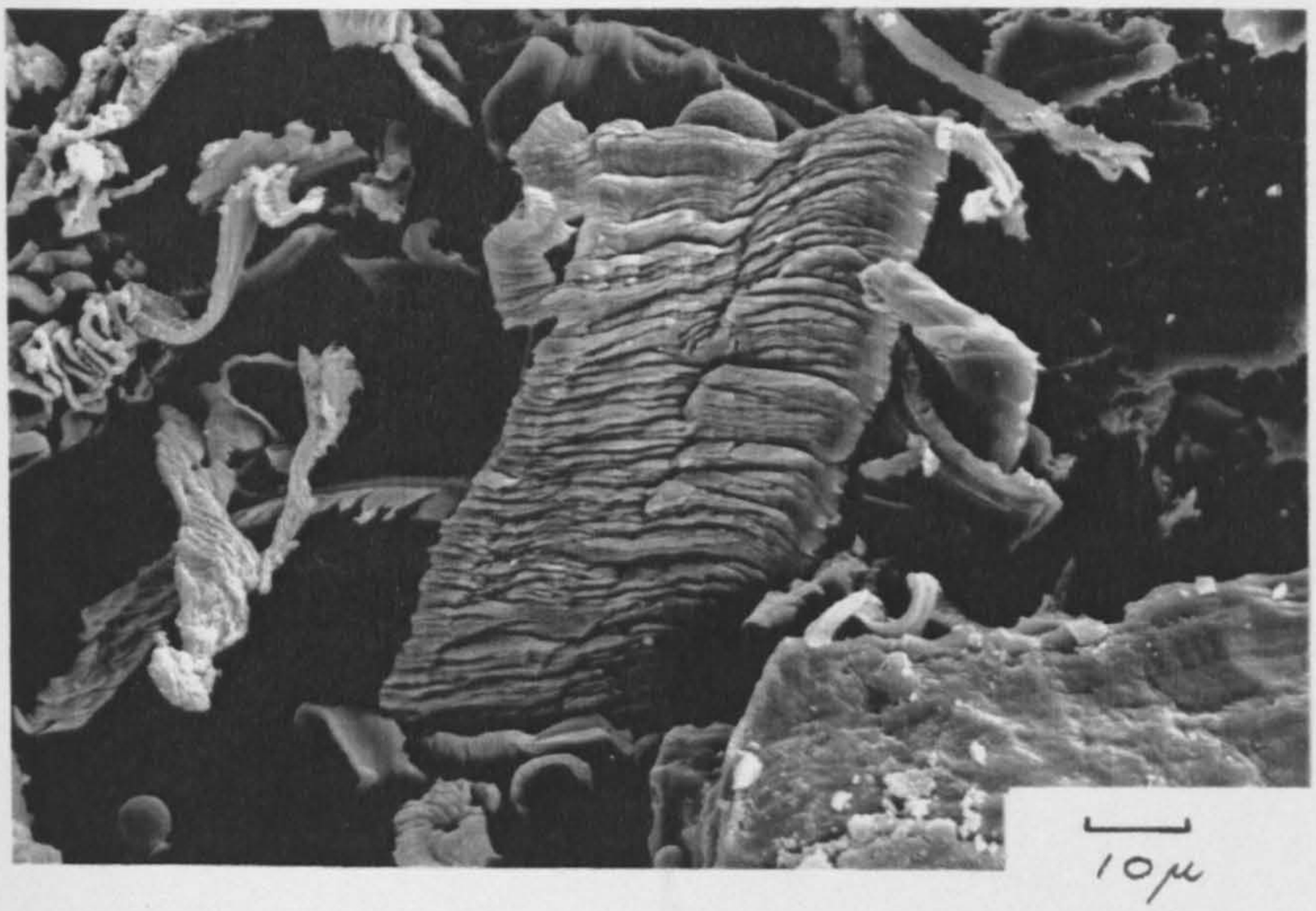

Figure 1.1 Electron micrograph showing a blocky-chip with a fine lamellar microstructure (lamellar spacing ~ 0.5μm), 800X magnification.

Figure 1.2 Electron micrograph showing a spherical grinding particle with fine dendritic microstructure. To the left of this sphere is a curled chip, 1800X magnification.

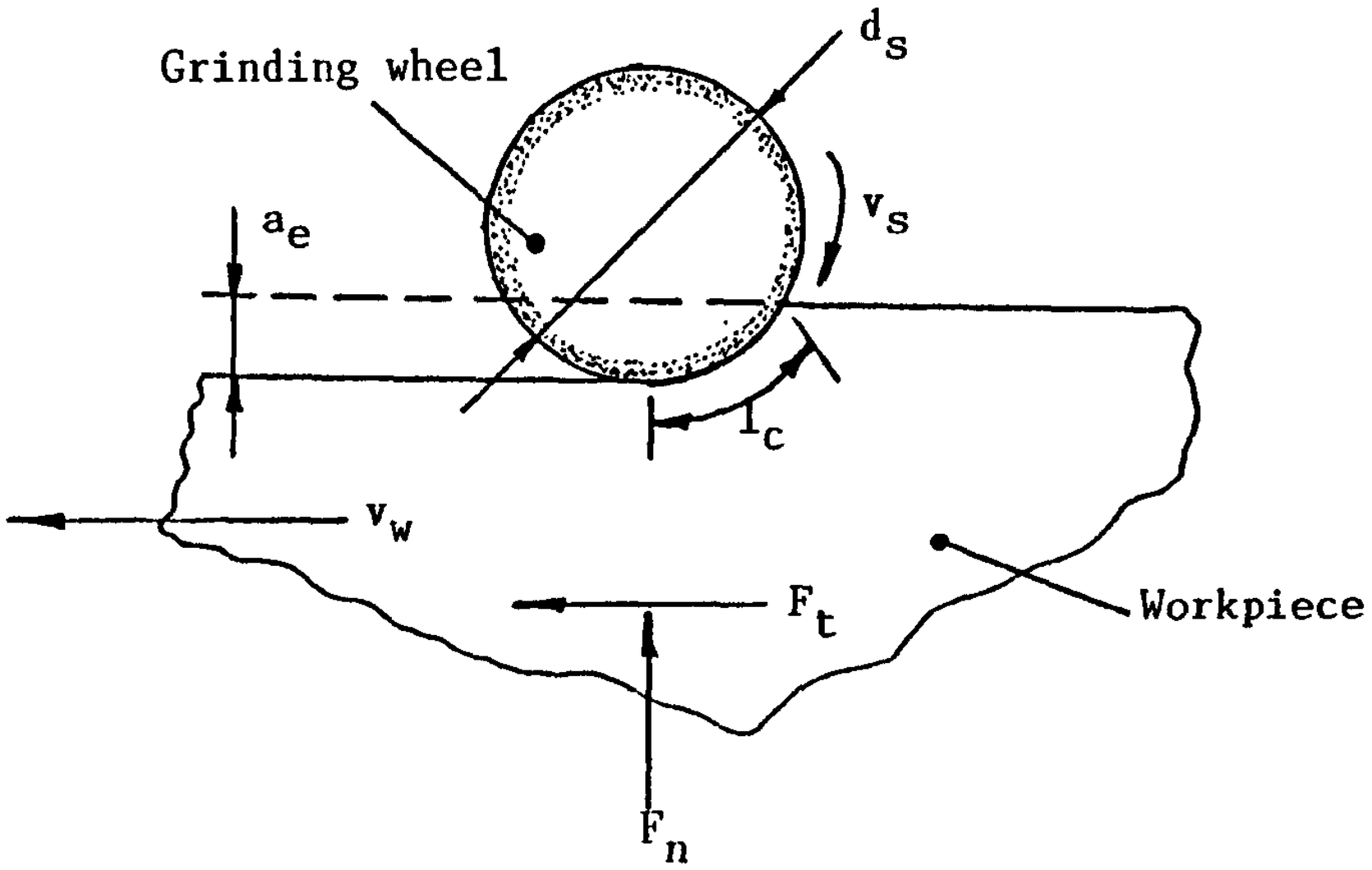

Figure 1.3 Illustration of grinding force components for surface grinding.

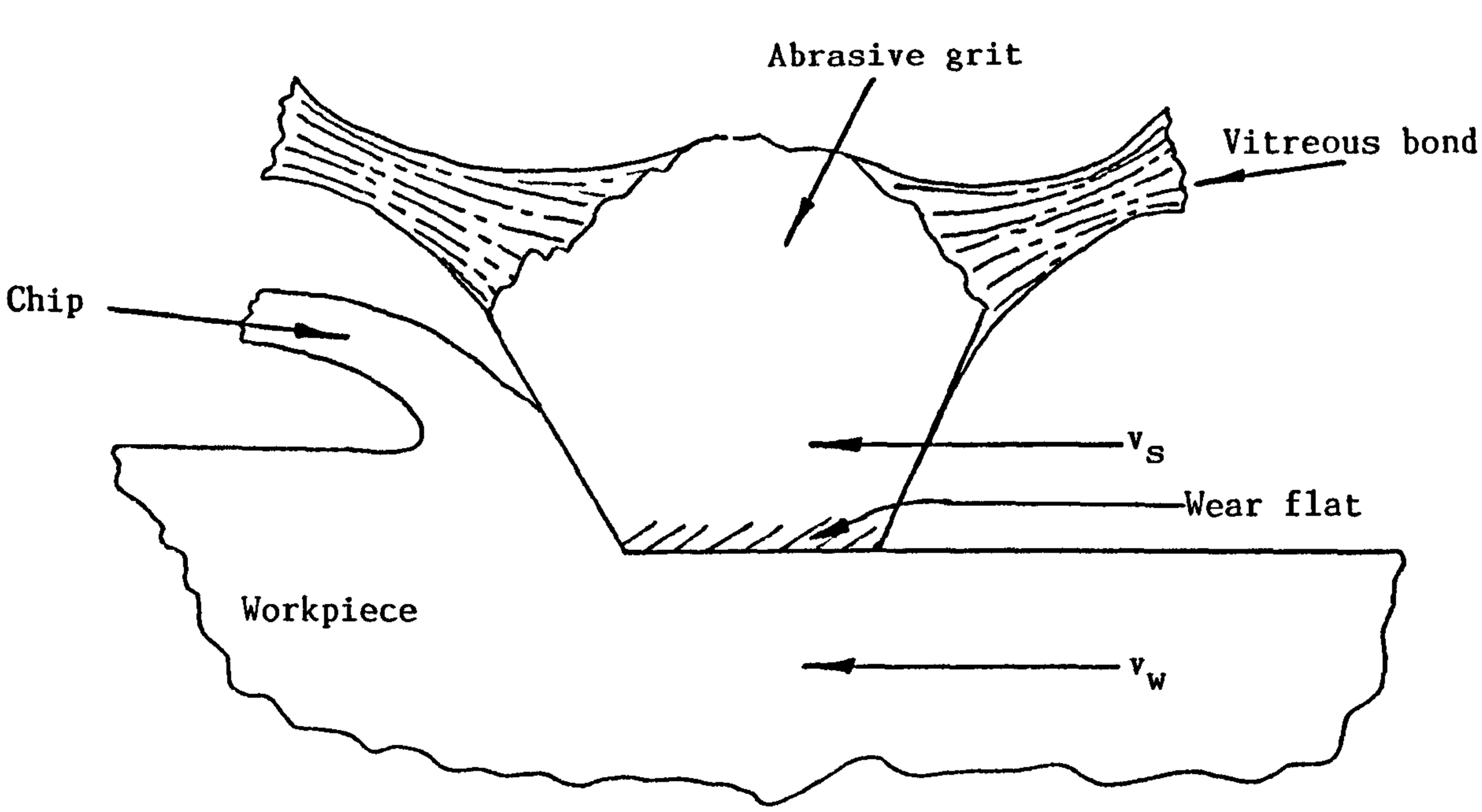

Figure 1.4 Abrasive grit cutting a chip with the dulled wear flat sliding against the newly-machined surface.

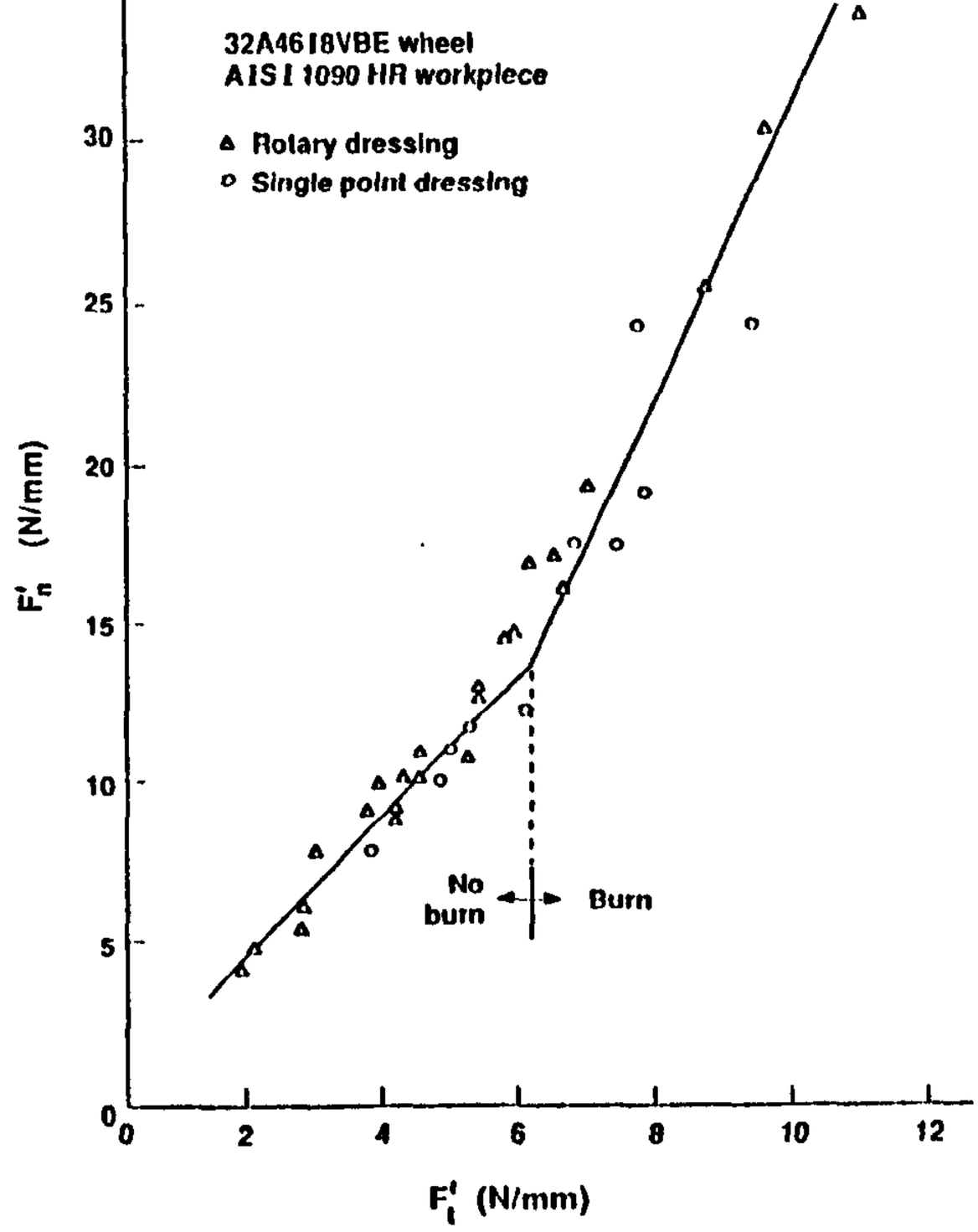

Figure 1.5 Normal versus tangential force per unit width for straight surface plunge grinding; v_s = 30m/s, d_s = 350mm, v_w = 8.6m/min, a = 25µm [11].

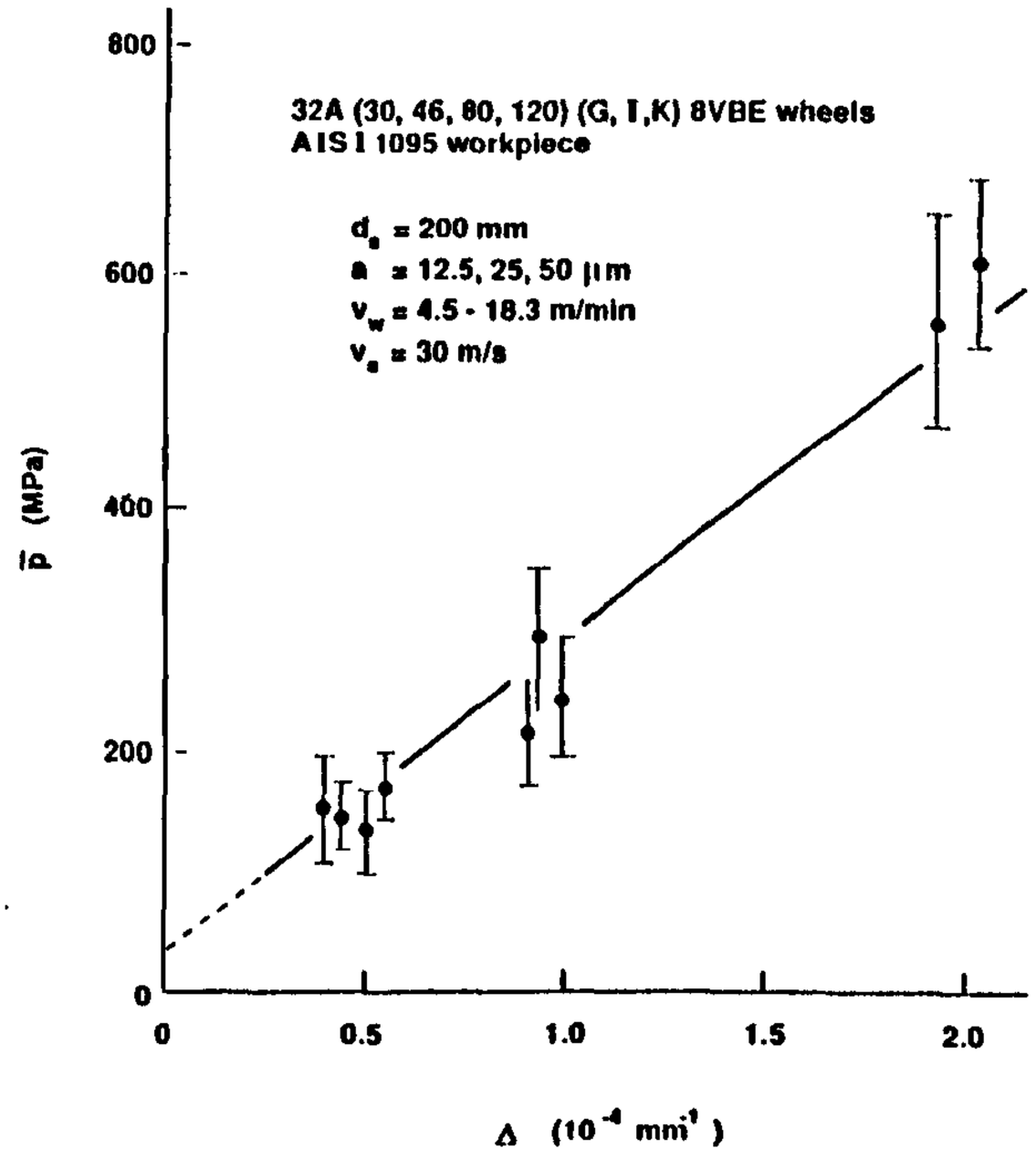

Figure 1.6 Average contact pressures versus curvature difference [12].

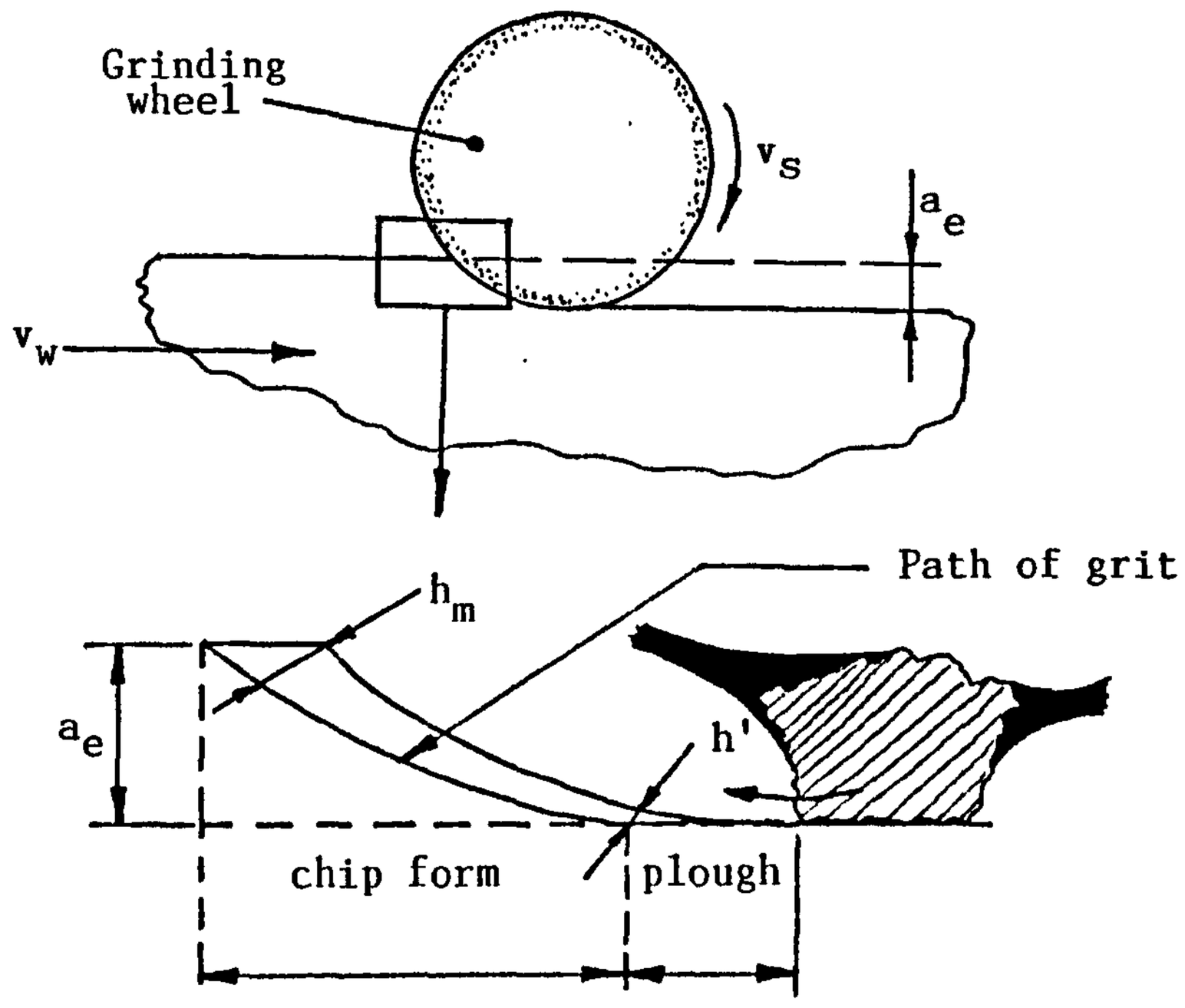

Figure 1.7 An illustration of ploughing followed by chip formation.

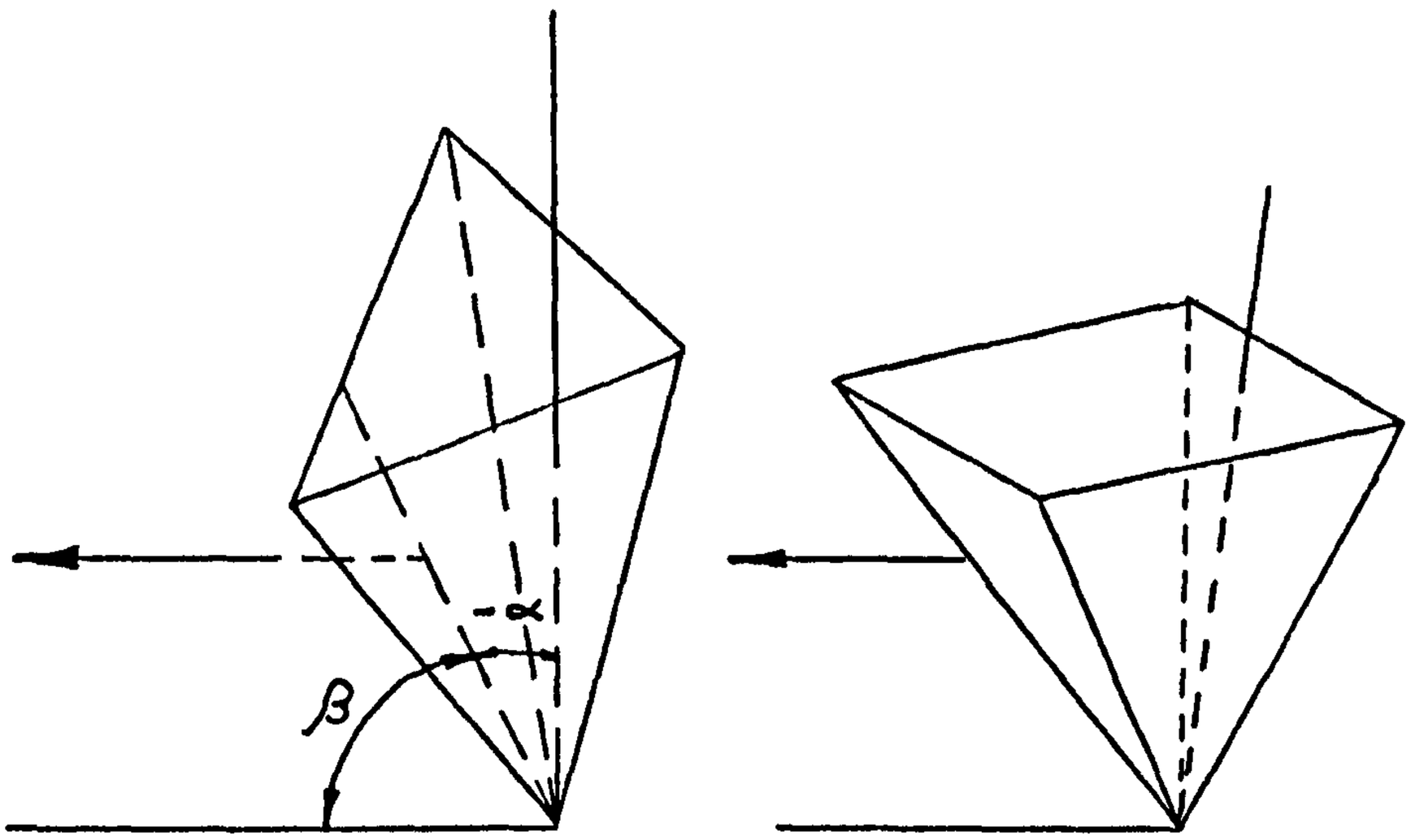

Figure 1.8 Orientation and shape of cutting tools used for cutting experiments which simulate abrasion; (a) triangular-based tool, (b) square-based pyramidal tool.

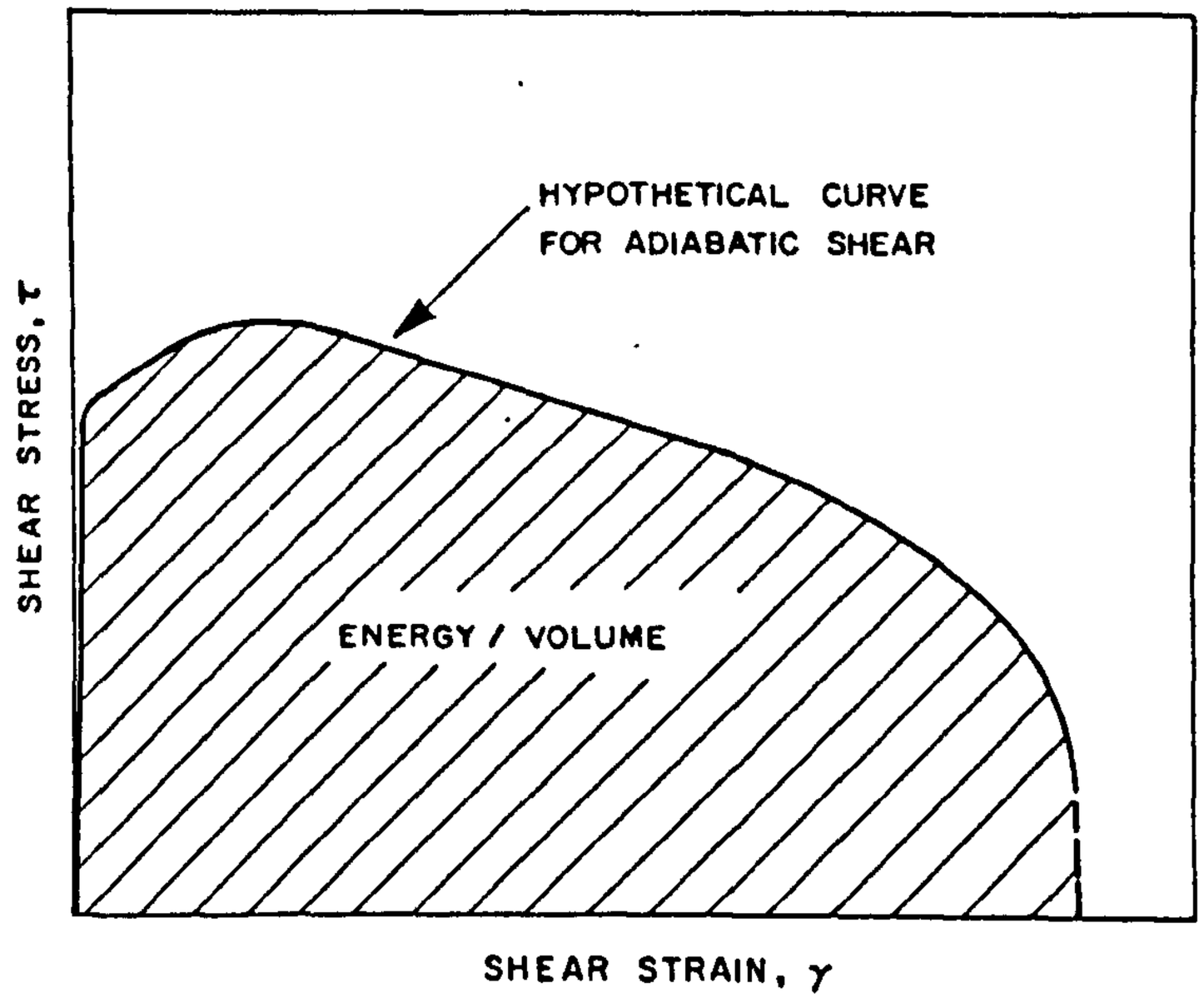

Figure 1.9 Hypothetical stress-strain behaviour for adiabatic shearing up to the melting point of the workpiece material [19,20].

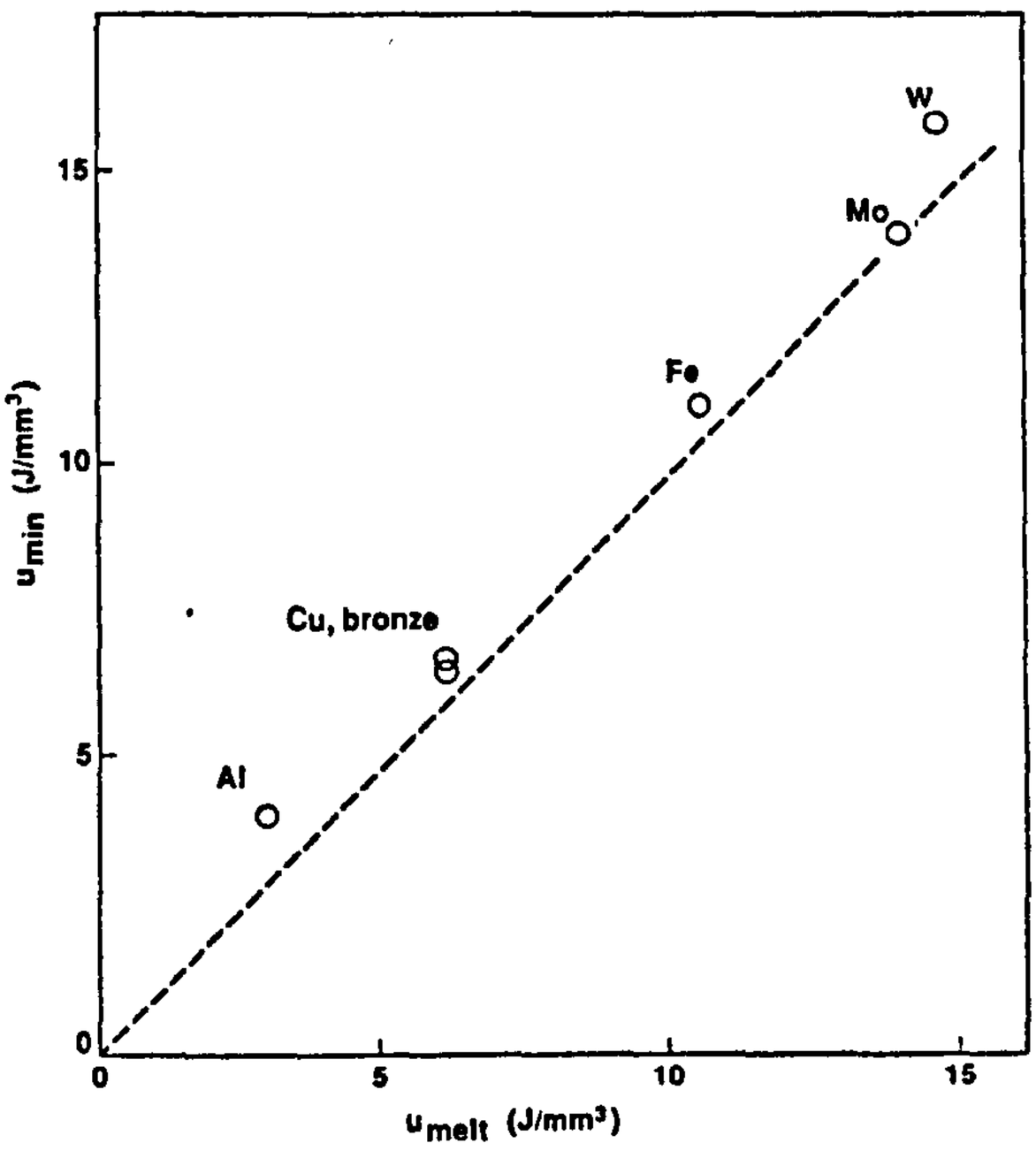

Figure 1.10 Minimum specific energy versus melting energy for various metallic materials [19,20].

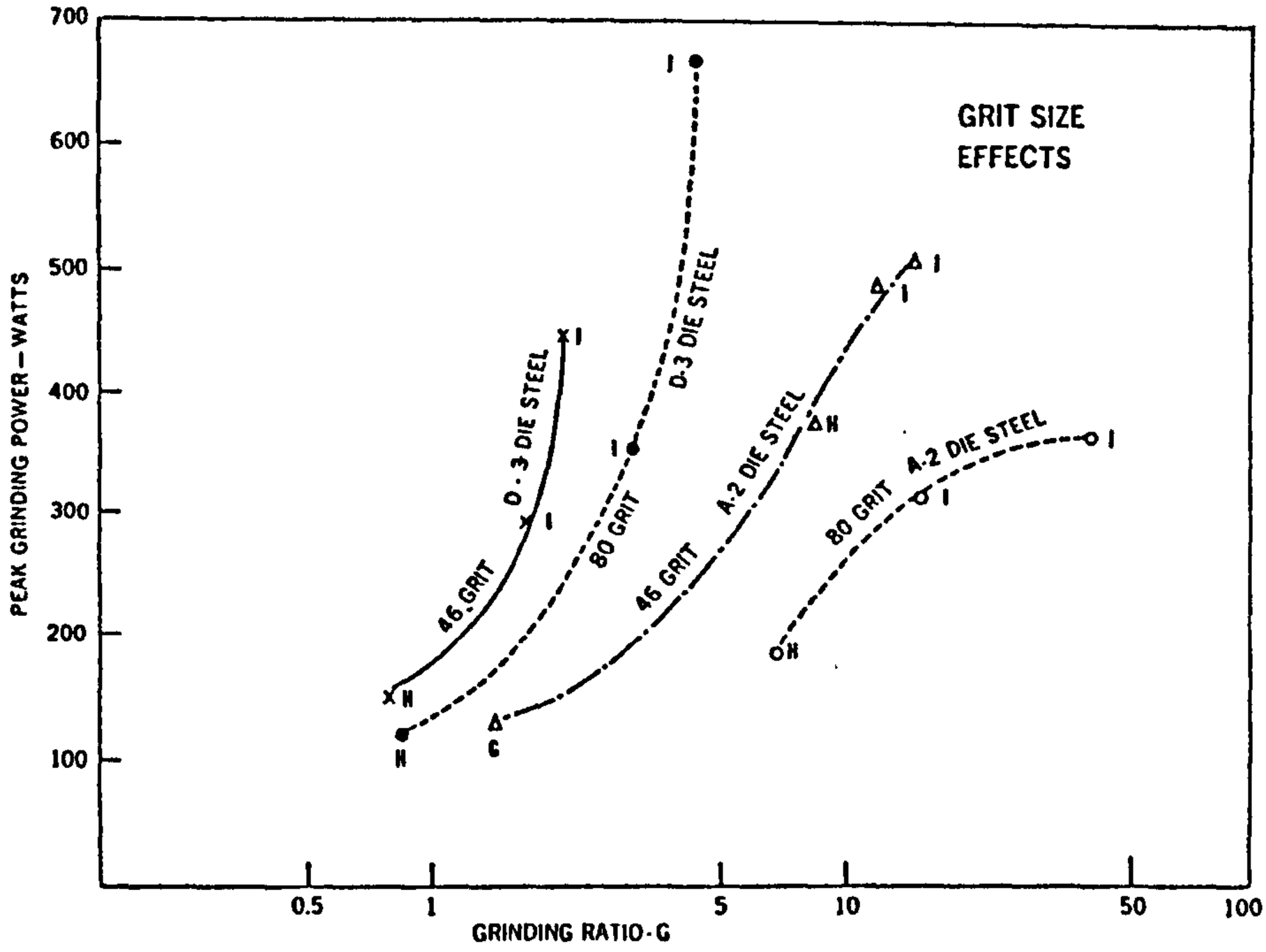

Figure 1.11a The effect of grit size on grinding wheel performance using a 38A-8VG vitrified grinding wheel. Wheel speed 6,000Ft/min, material hardness 61HRC [26].

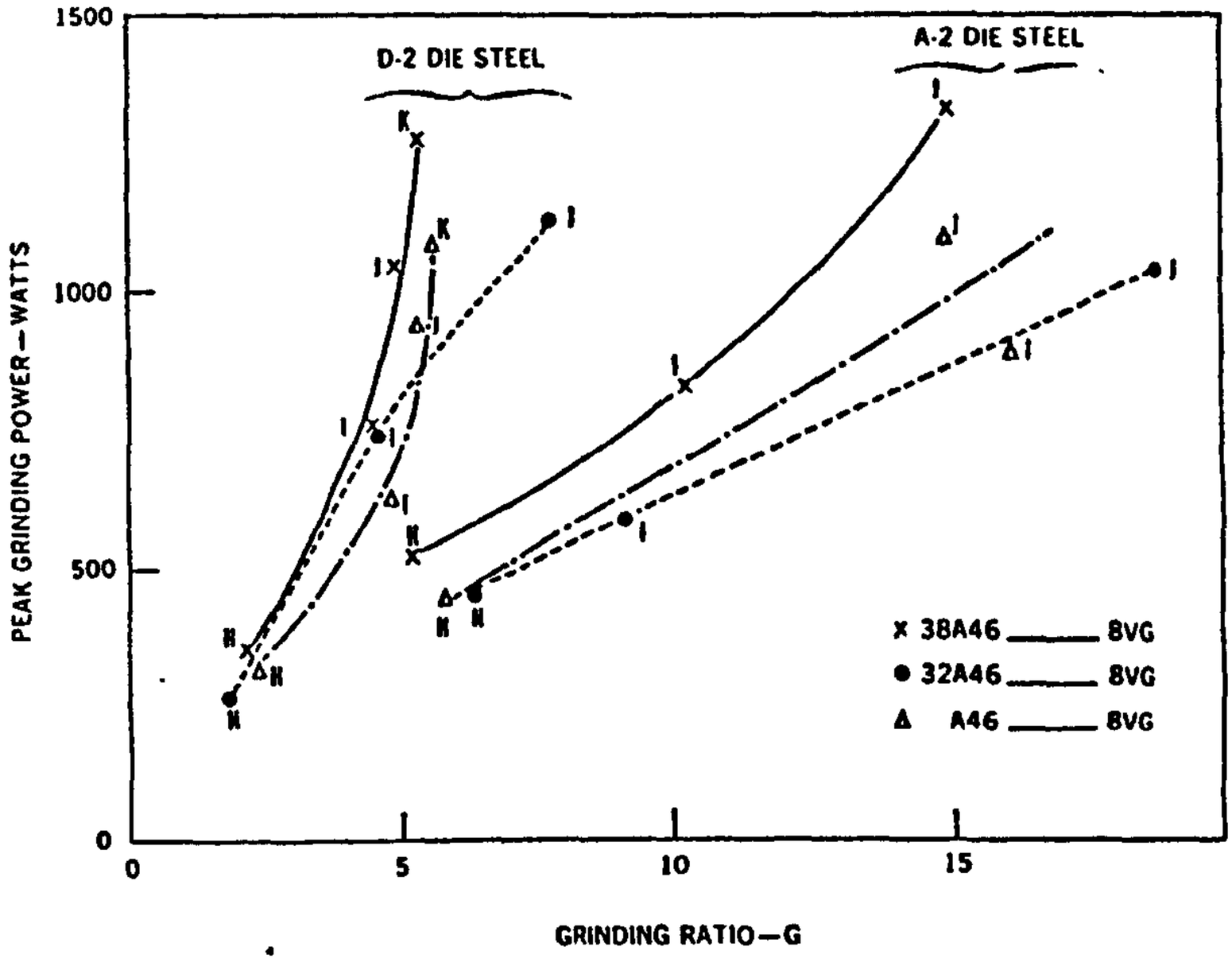

Figure 1.11b The effect of three different abrasive grits on grinding wheel performance. Wheel speed 6,000Ft/min. Workpiece materials: (1) D-2 die steel; A-2 die steel [26].

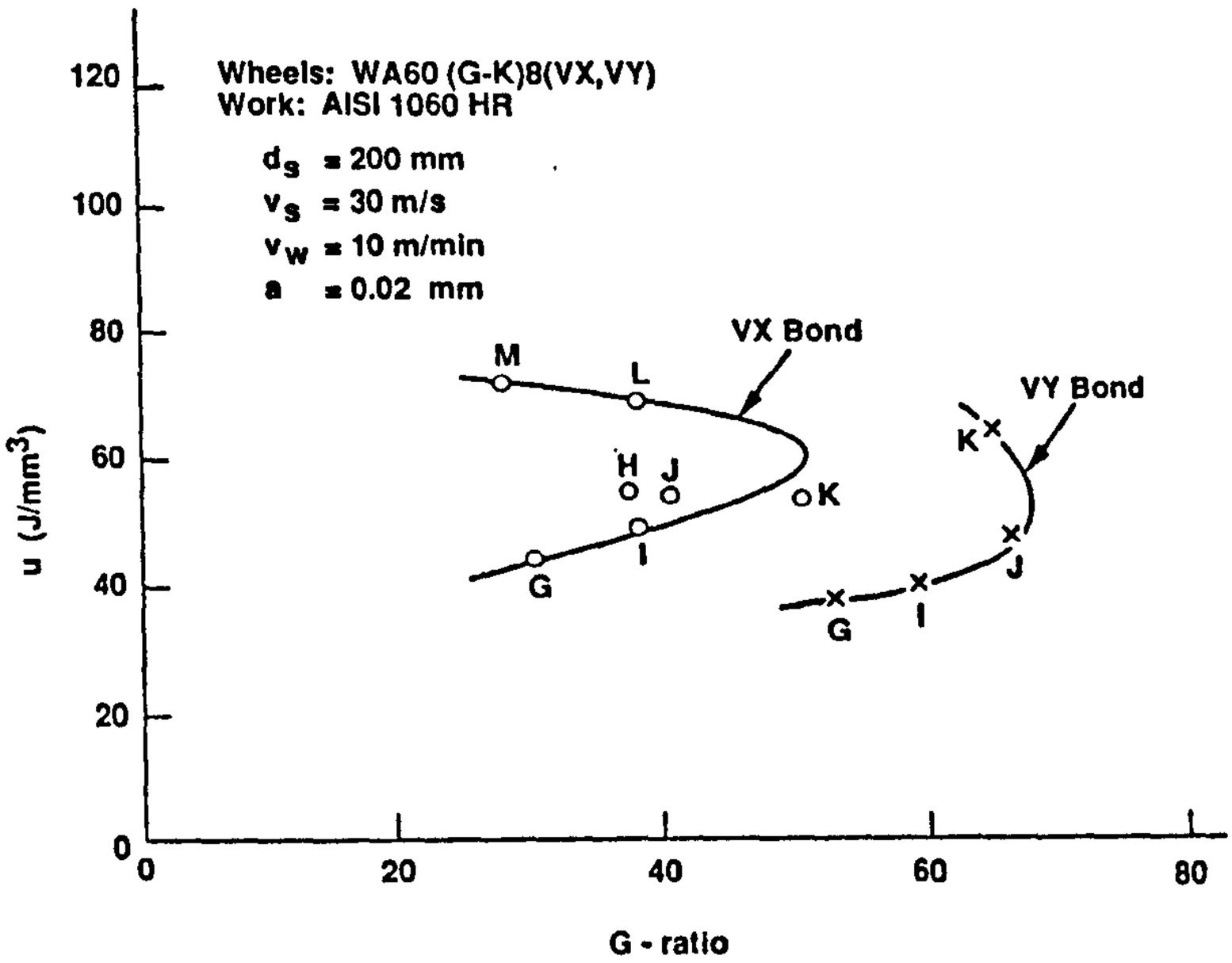

Figure 1.12 Grinding wheel performance evaluation of vitrified grinding wheels using two different bond materials. The letters on each curve refer to the wheel grade. Wheel types: WA60(G-K)8(VX,VY): Material ground: A1S1 1060HR: steel workpiece: [27]

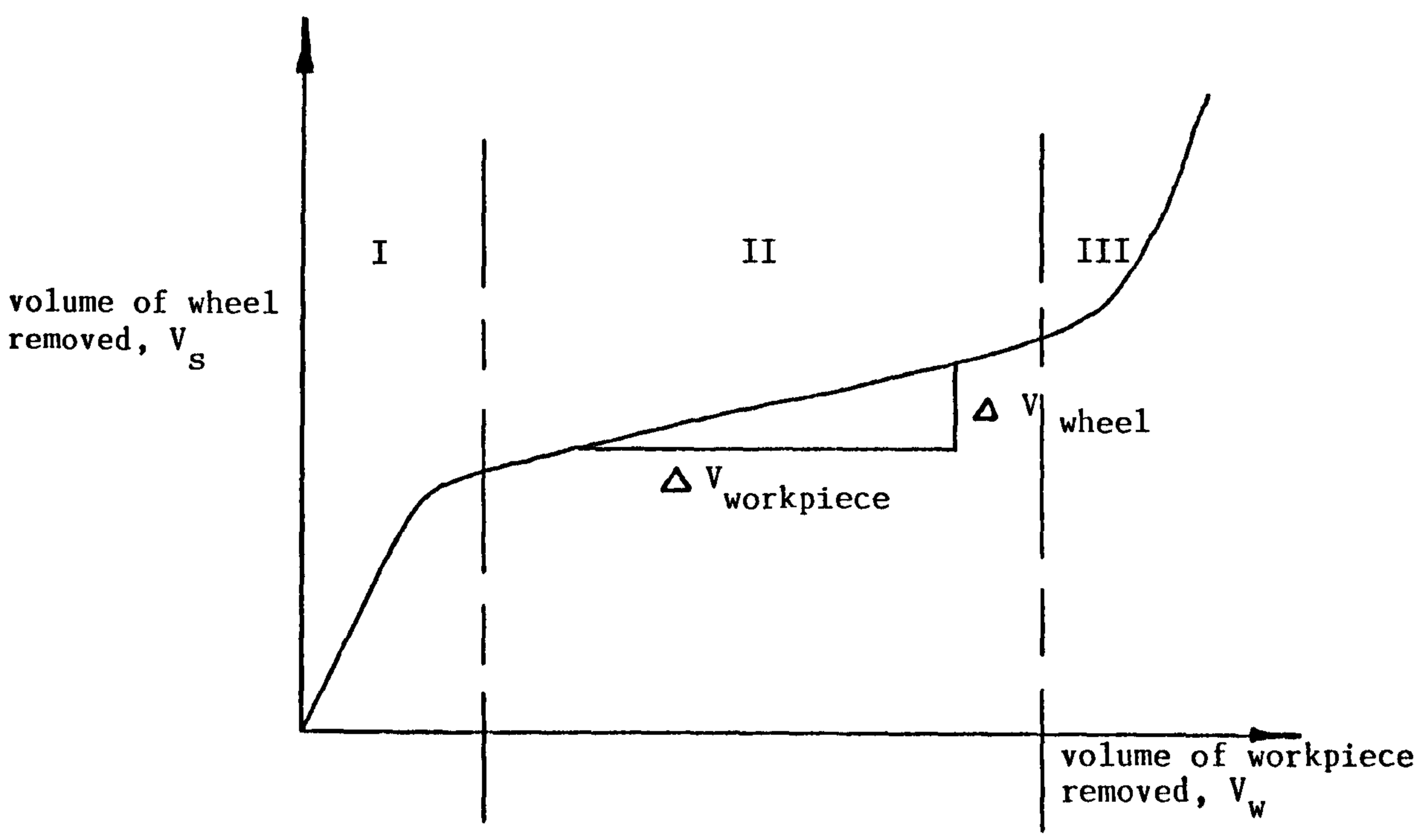

Figure 2.1. Volumetric wheel wear versus volumetric metal removed for a typical grinding operation. Region I indicates initial wheel wear due to release of cracked bond posts and grits, II - indicates steady-state wear due to attrition of grits, and III - accelerating wear due to forced pull-out of worn grits.

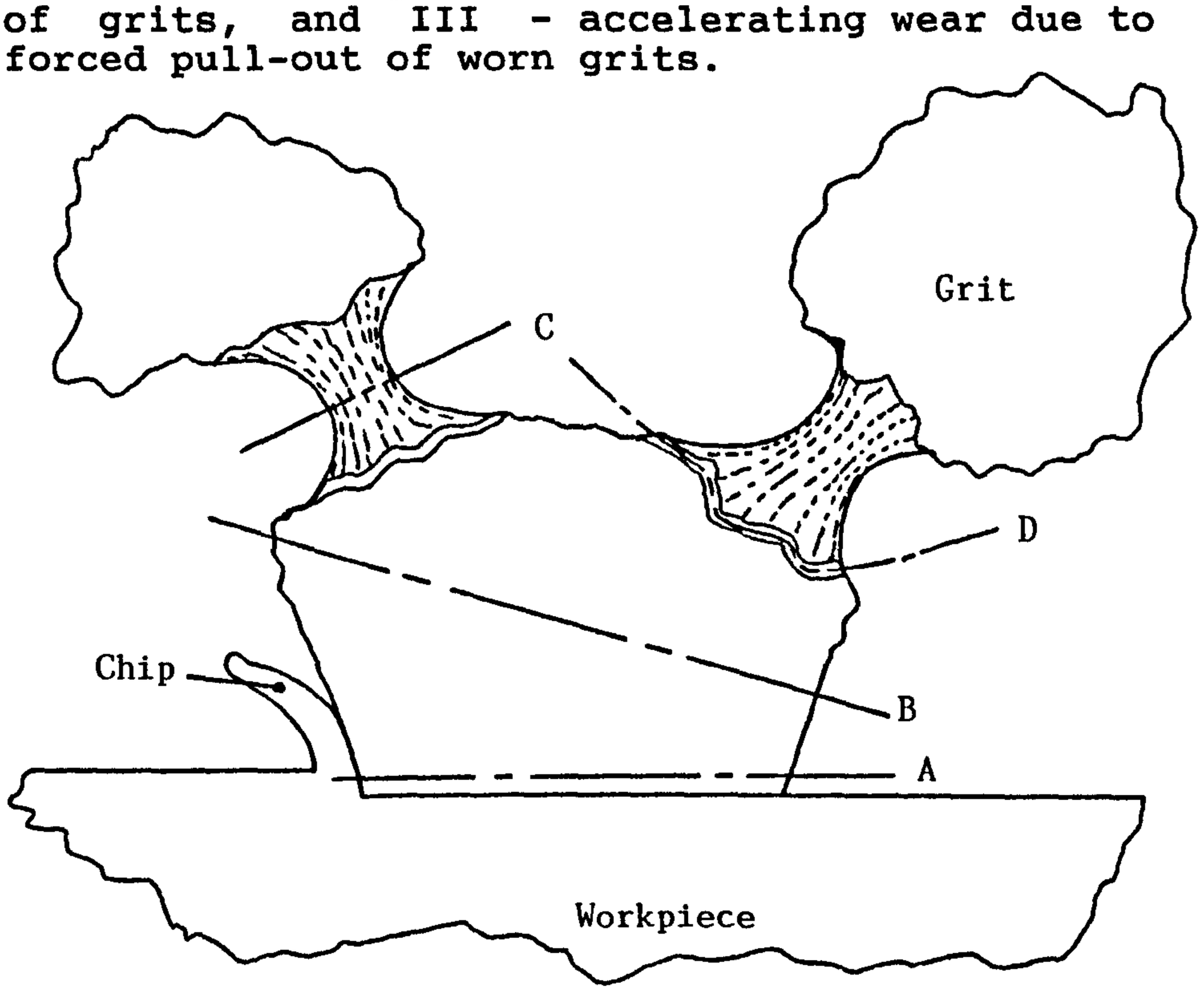

Figure 2.2 Illustration of principal wheel wear mechanisms: A - abrasive wear; B - grit fracture; C - bond fracture; D - fracture of reaction interface between grit and bond.

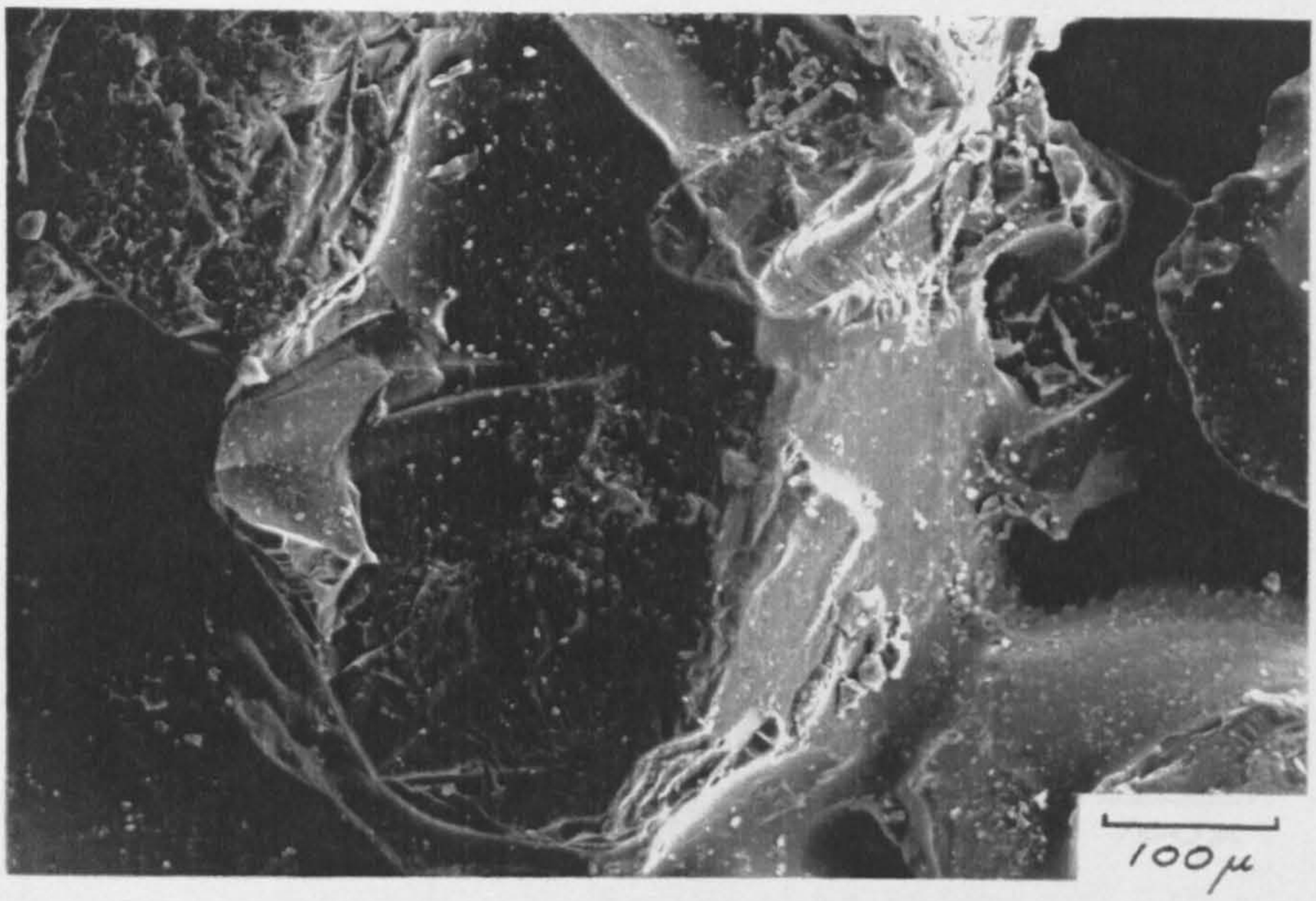

Figure 2.3 Illustration of attritious wear of a white alumina wheel due to mechanical friction acting between workpiece and abrasive.

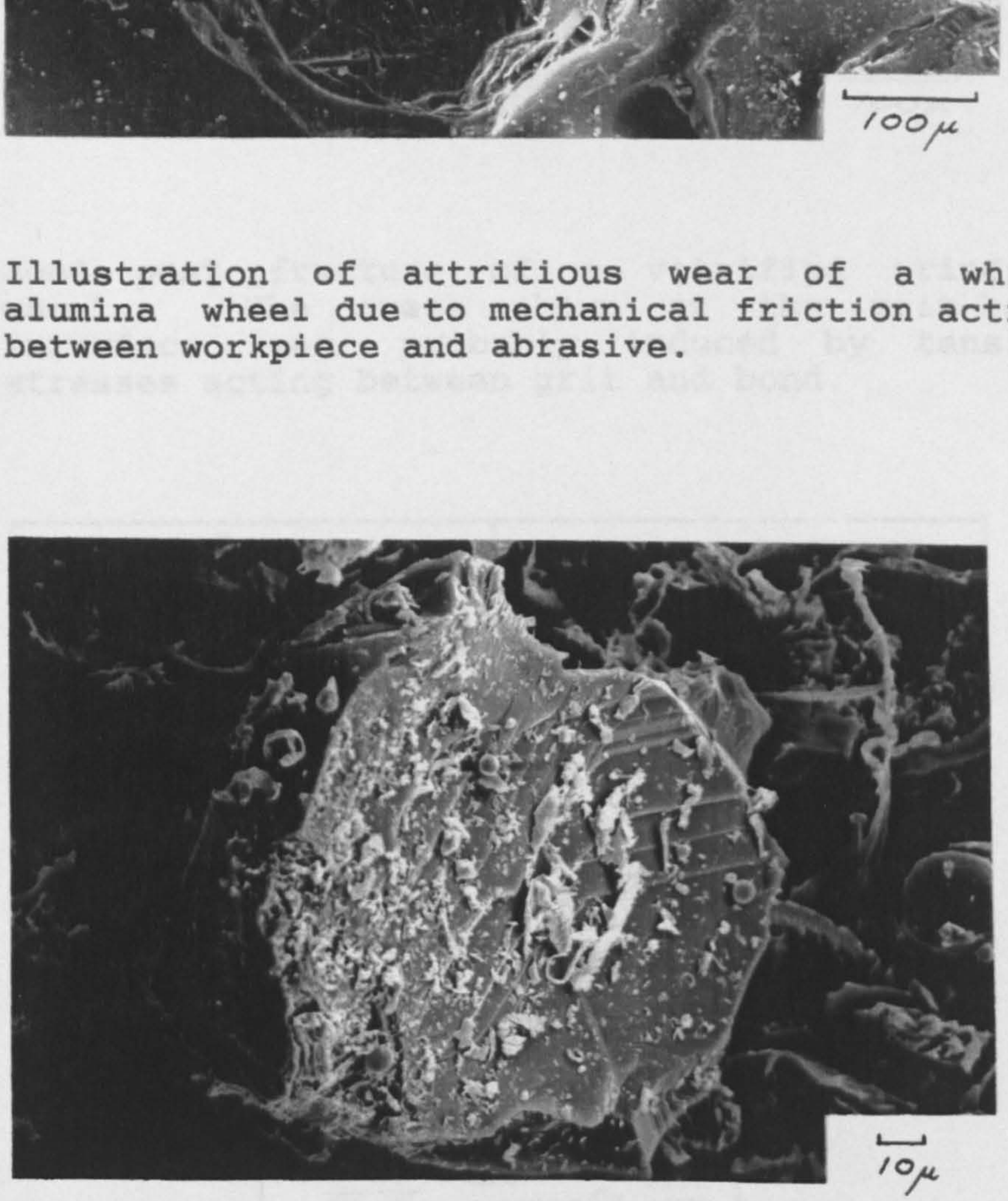

Figure 2.4 Illustration of grit fracture showing workpiece swarf attached to facets formed by cleavage of the grit along crystallographic planes.

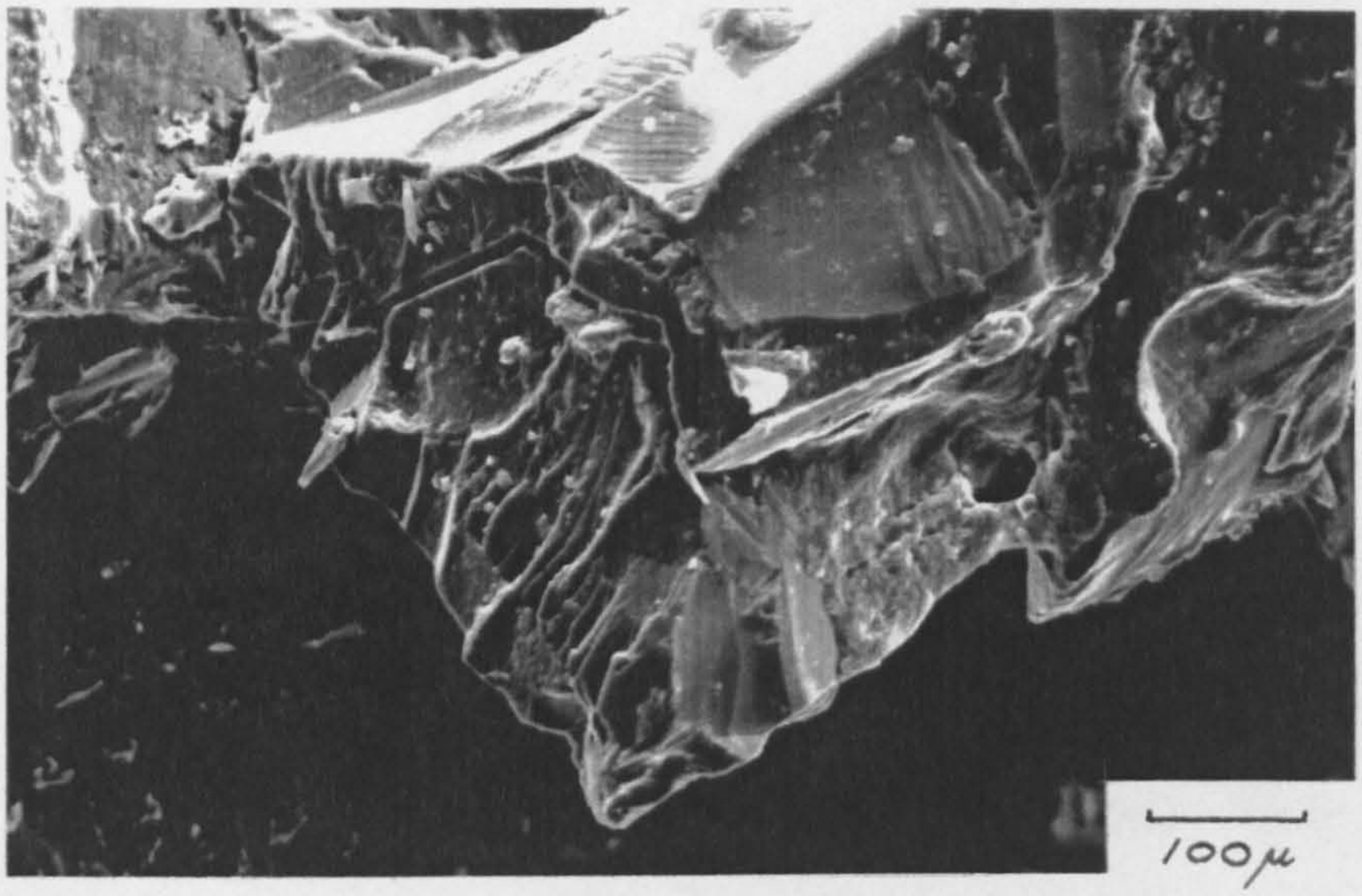

Figure 2.5. Bond post fracture of a vitrified grinding wheel. The crack shown at the grit-bond interface was probably induced by tensile stresses acting between grit and bond.

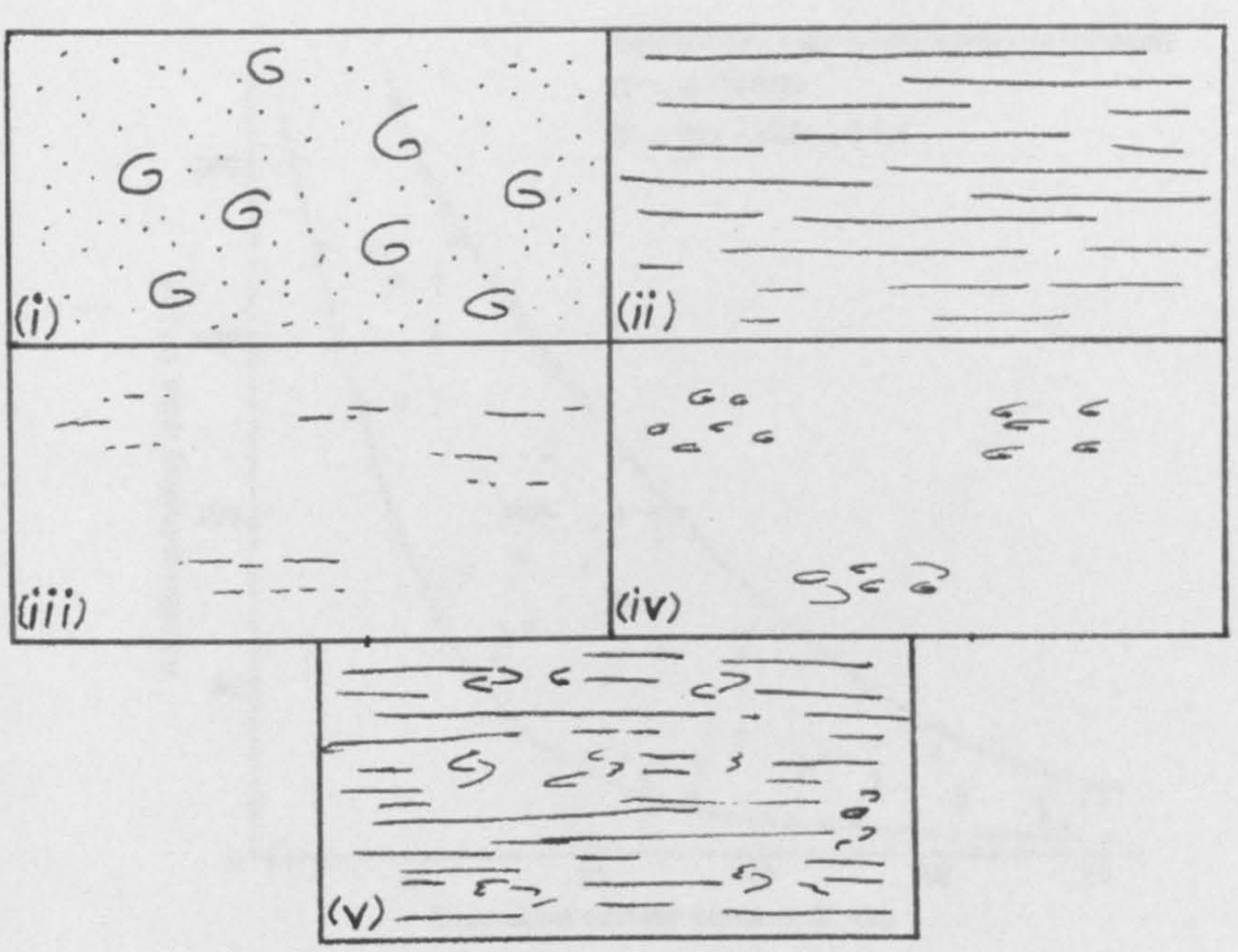

Figure 2.6. Types of wear in diamond grinding wheels, as observed using a scanning electron microscope (i) adhesion wear, (ii) abrasion wear, (iii) diffusion wear, (iv) diffusion and adhesion wear, (v) abrasion and adhesion wear [63].

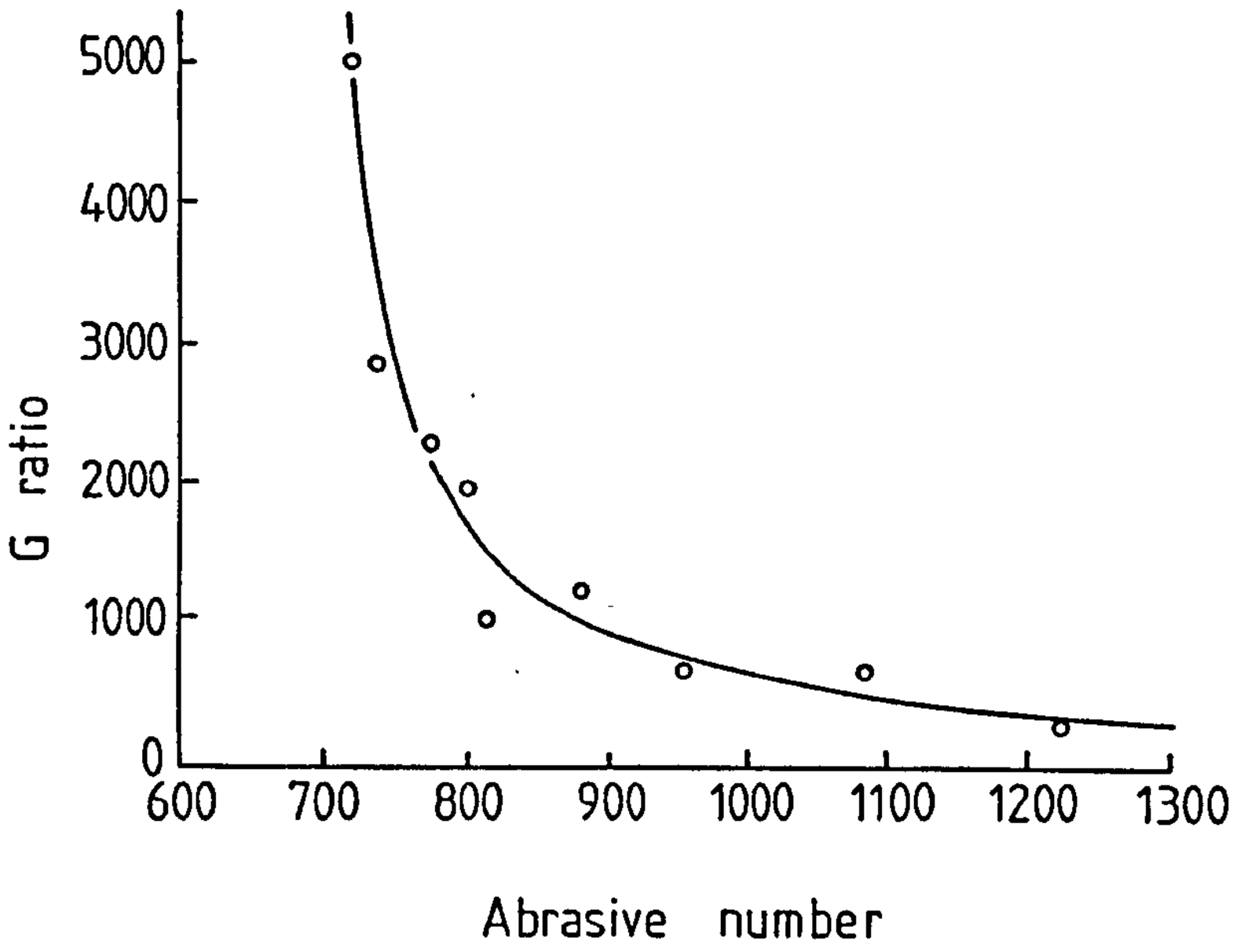

Figure 2.7 G-ratios for a C.B.N. grinding wheel grinding steels of different hardnesses, or abrasive number [64].

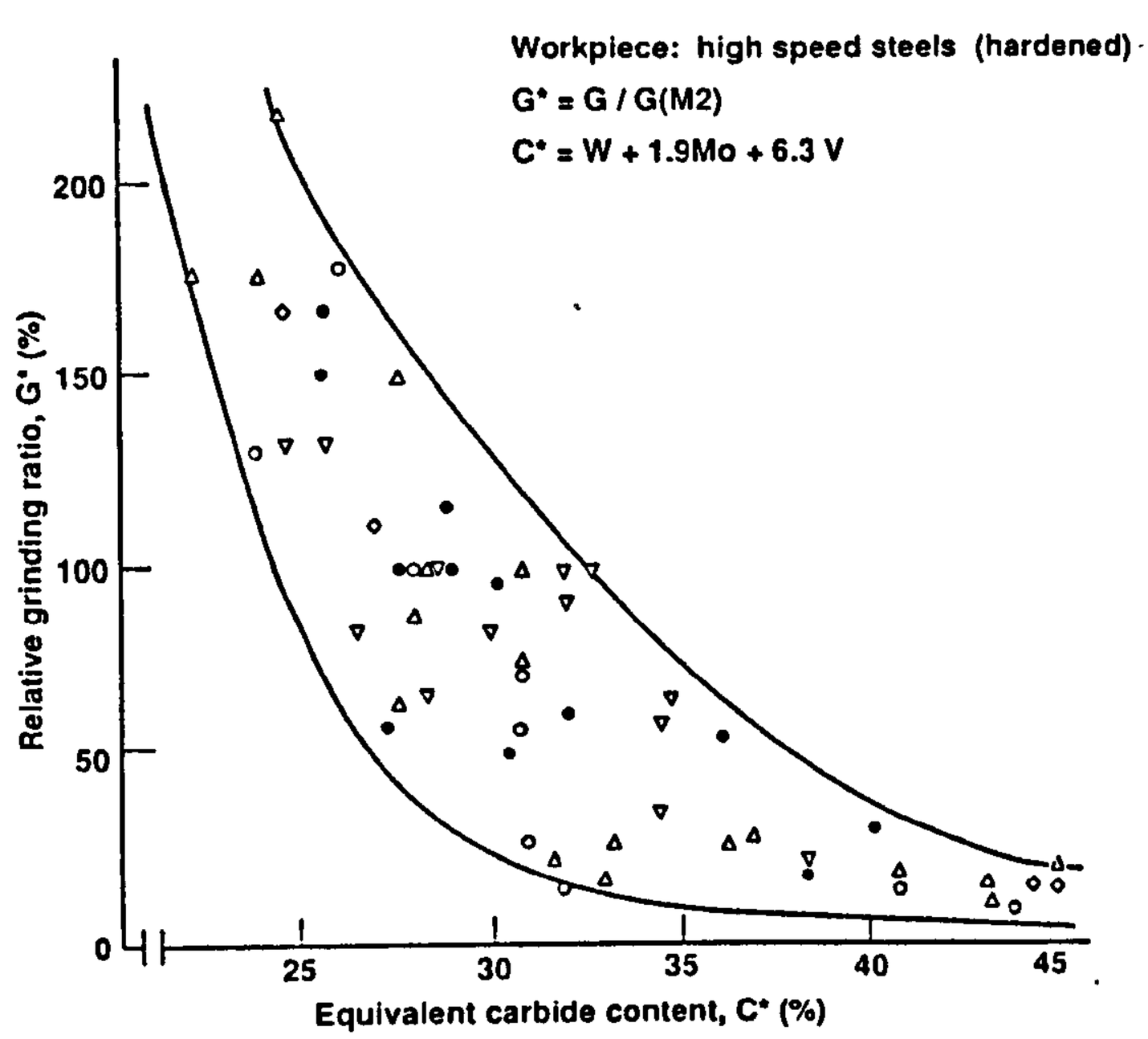

Figure 2.8. Effect of equivalent carbide content on the relative grinding ratio for hardened high-speed tool steels [70].

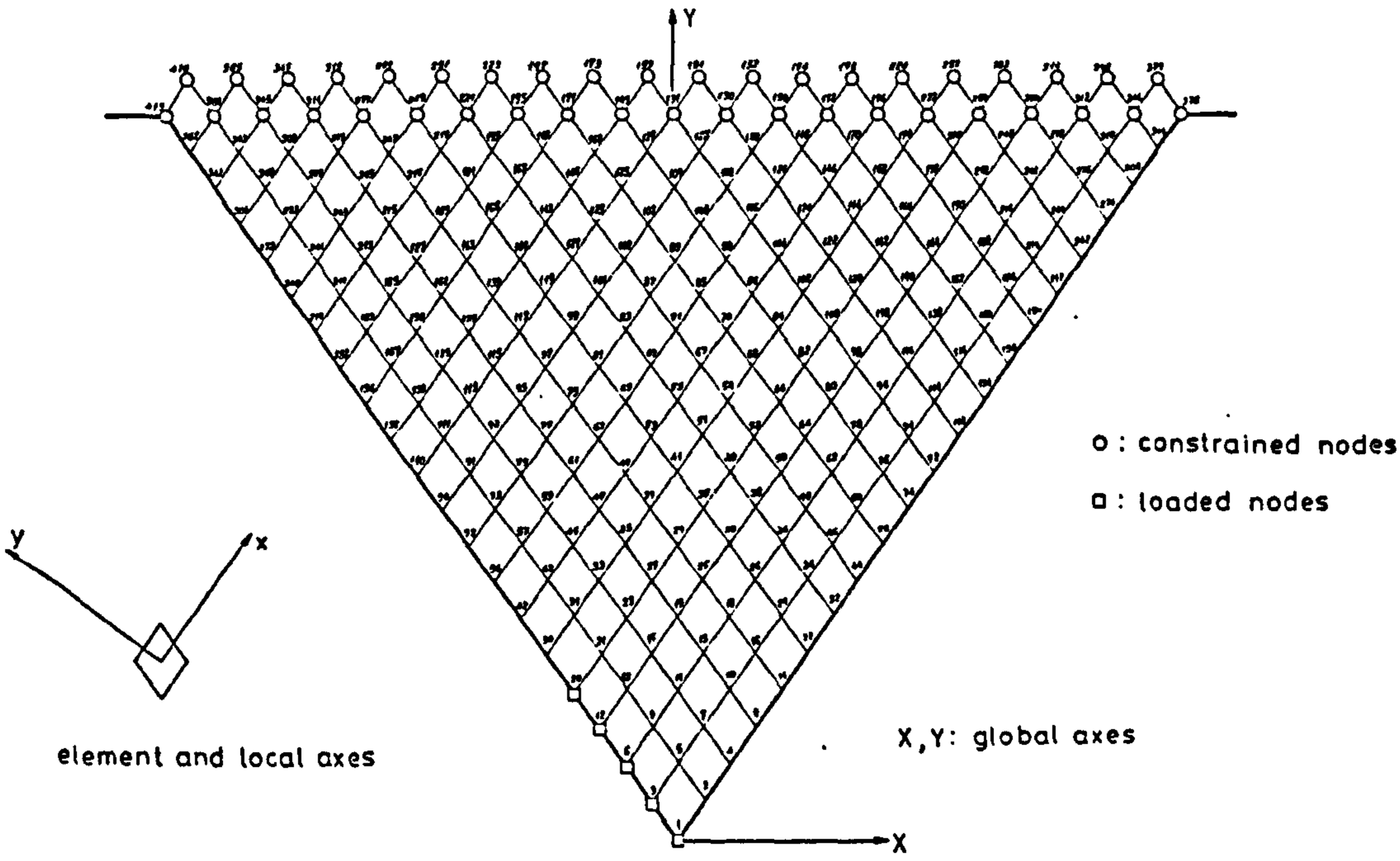

Figure 2.9. Finite element assemblage and boundary nodes for an idealised wedge simulating an abrasive grit particle [72].

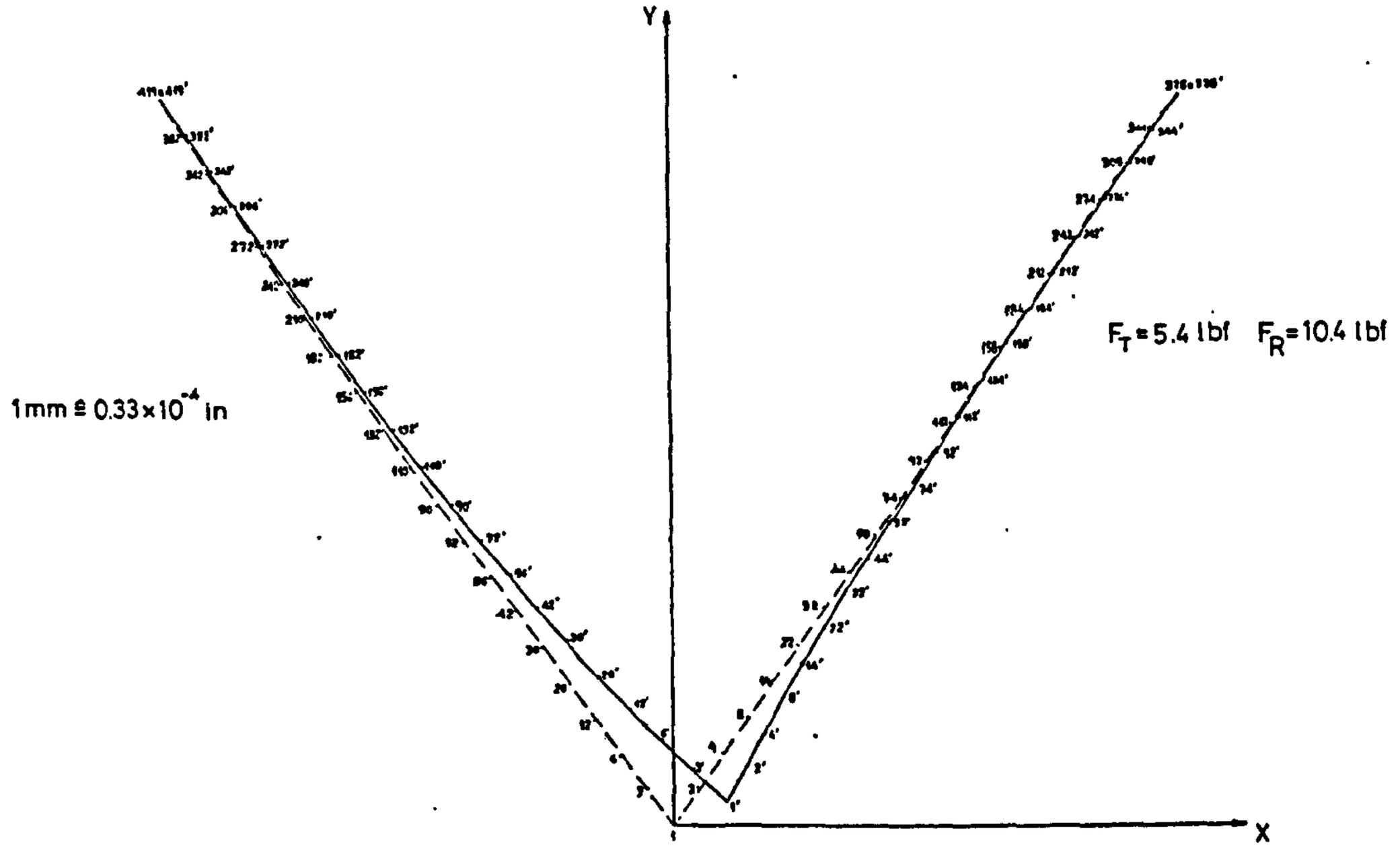

Figure 2.10 Model deflection pattern showing the reaction from nodes loaded tangentially and normally. F_t = 5.4lbf; F_n = 10.4lbf. Displacement Scale: 1mm ≡ 0.33 x 10^{-4} inch [72].

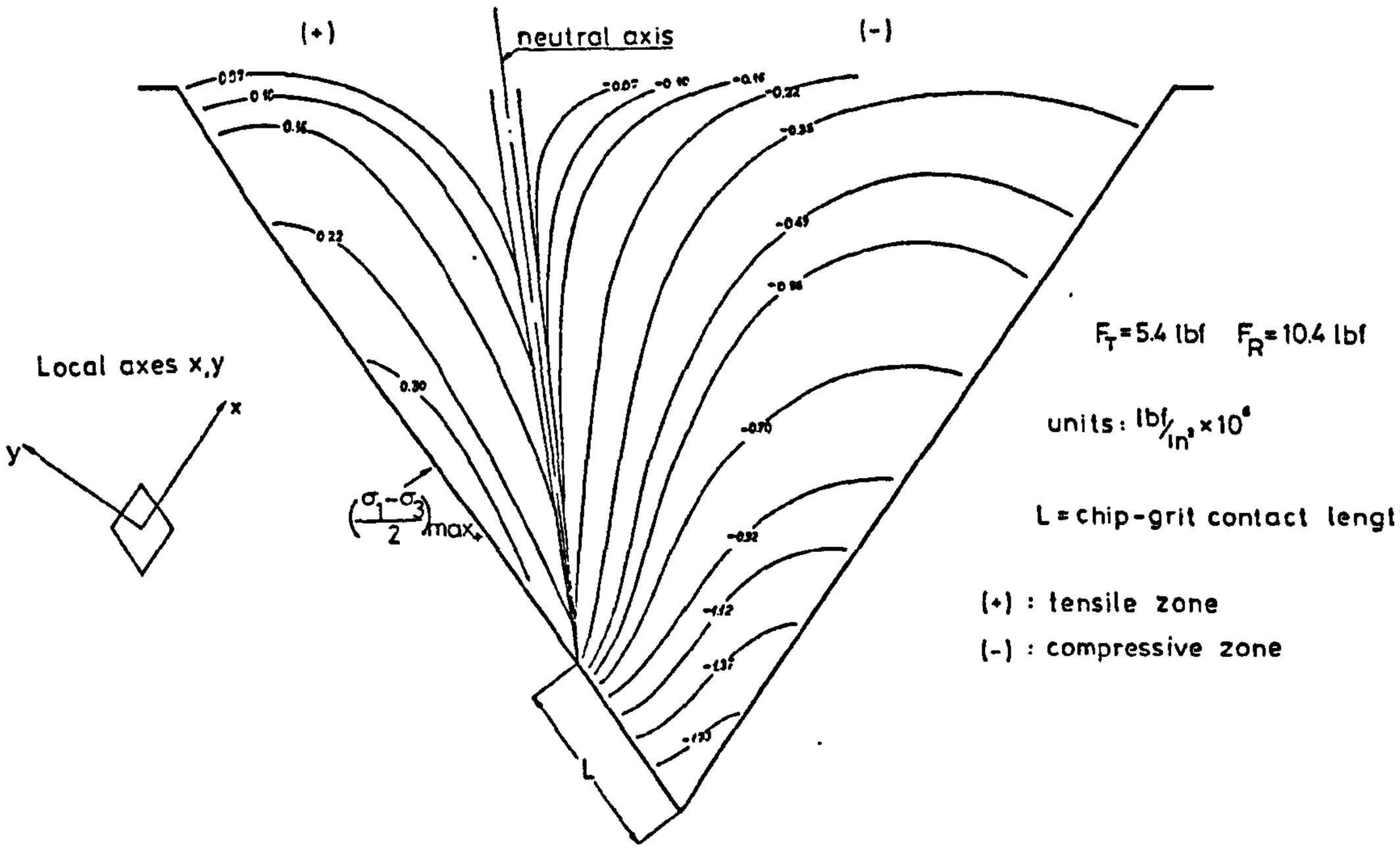

Figure 2.11 Lines of constant maximum shear stress showing areas of compressive, tensile and neutral stressing zones. [72].

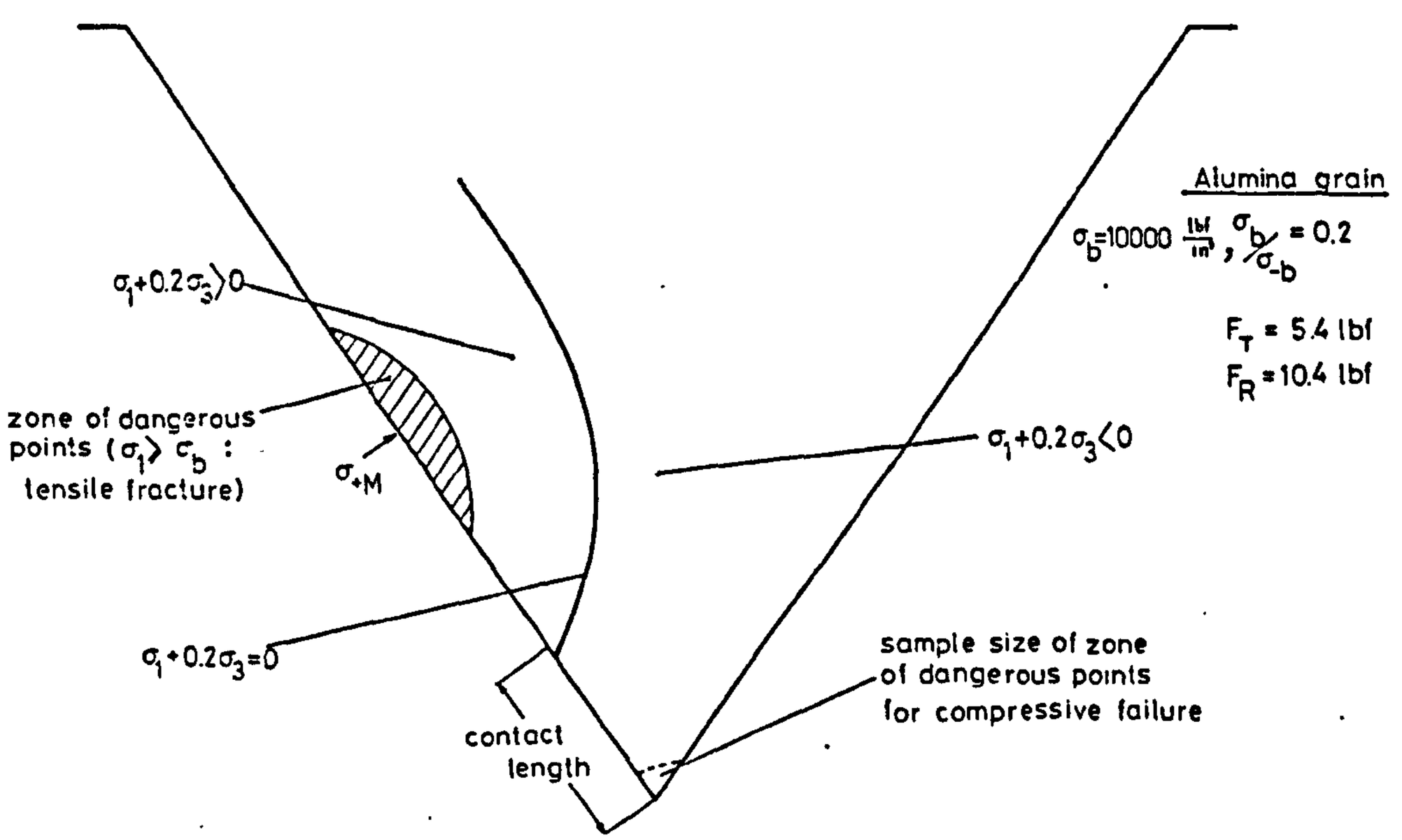

Figure 2.12 Illustration of brittle fracture in the idealised wedge using Griffith's criterion. The area of tensile brittle fracture is highlighted [72].

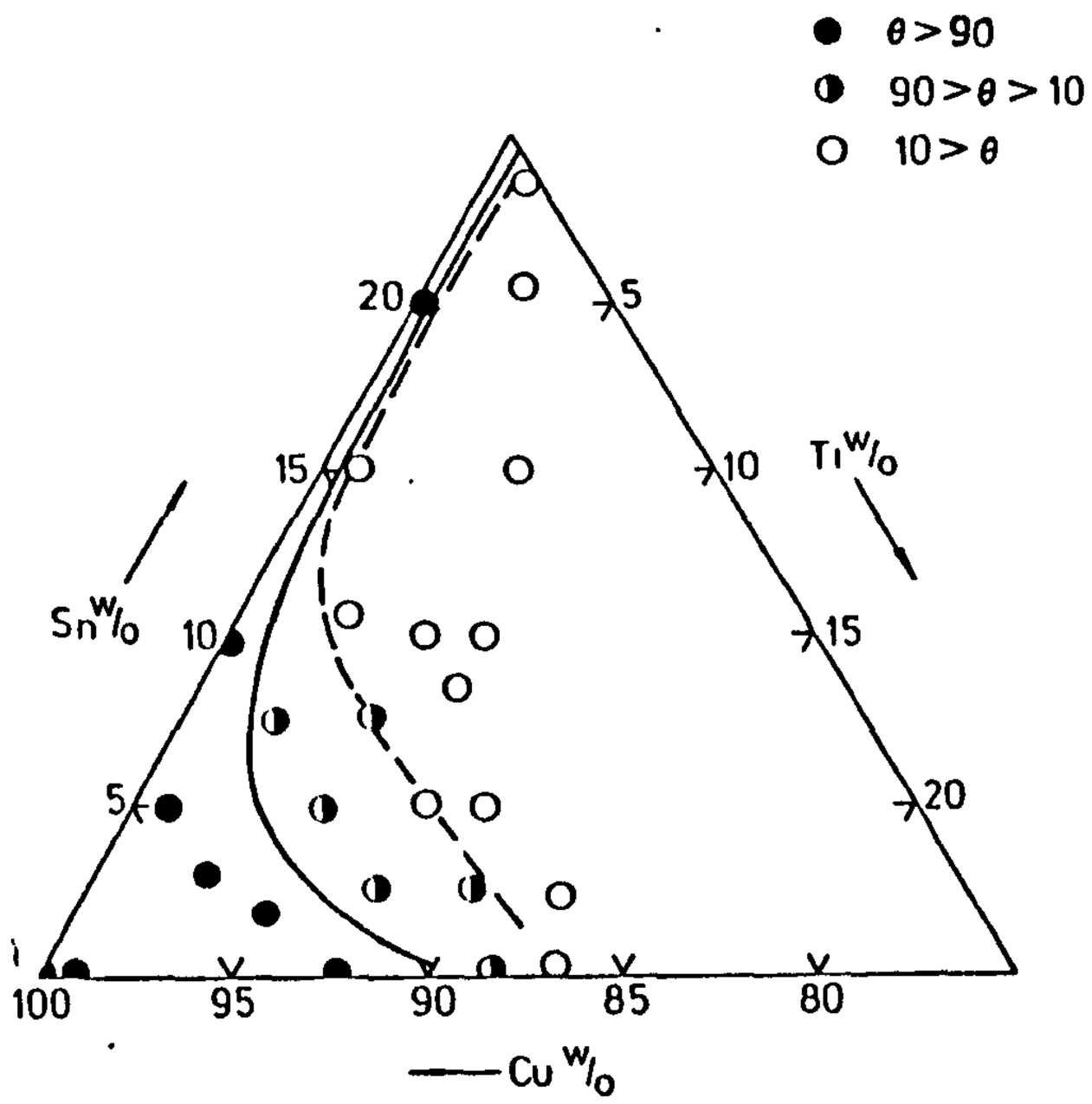

Figure 2.13 Wetting behaviour of copper-tin-titanium alloys on diamond at 1150°C [141,142].

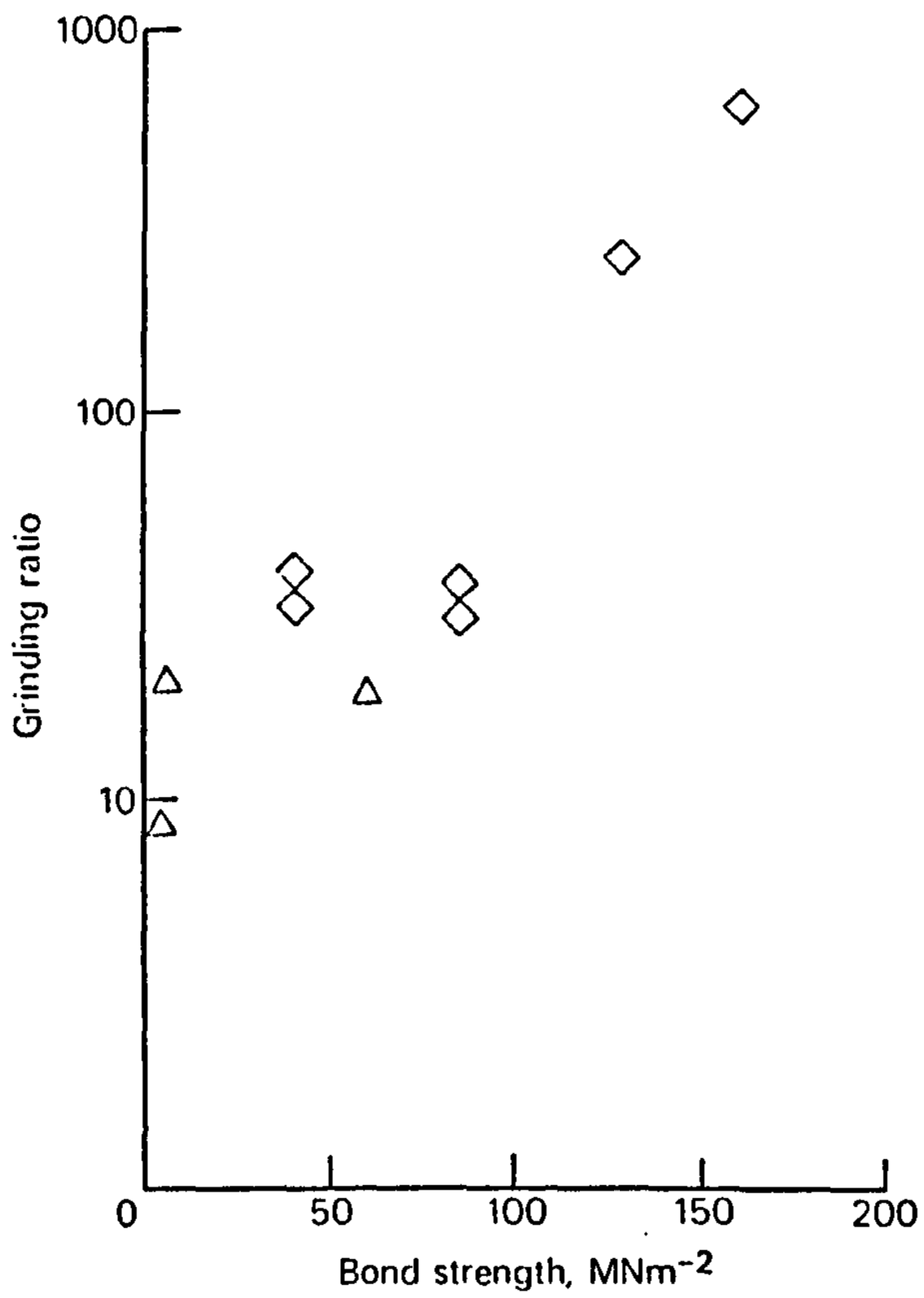

Figure 2.14 Correlation between bond strength and grinding ratio for copper-20% tin-10% titanium alloys (◇) and other copper-tin-titanium alloys (△) [142].

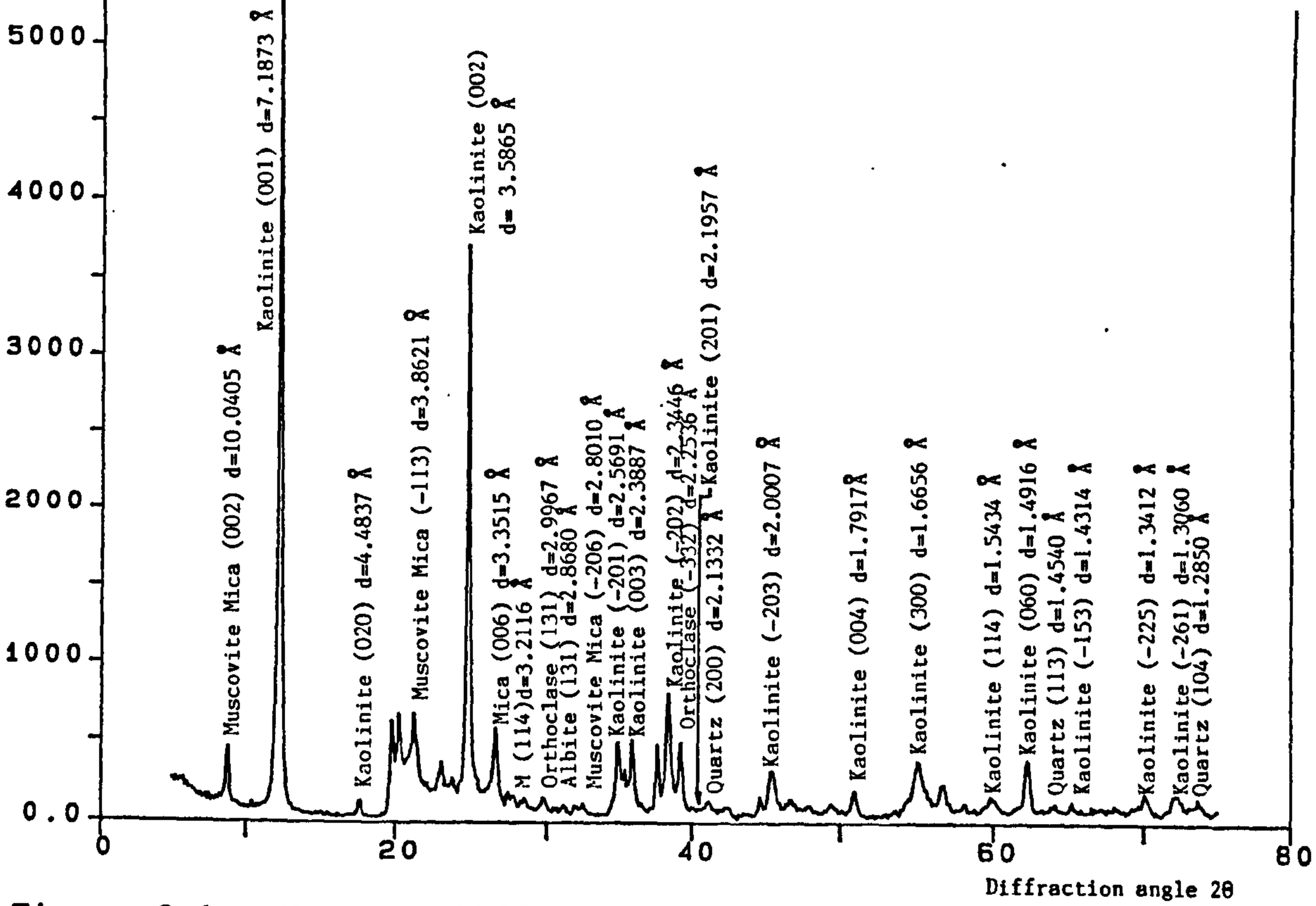

Figure 3.1. X-ray diffraction spectrum of China clay showing crystallographic planes and interplanar distances of various mineral phases in the clay.

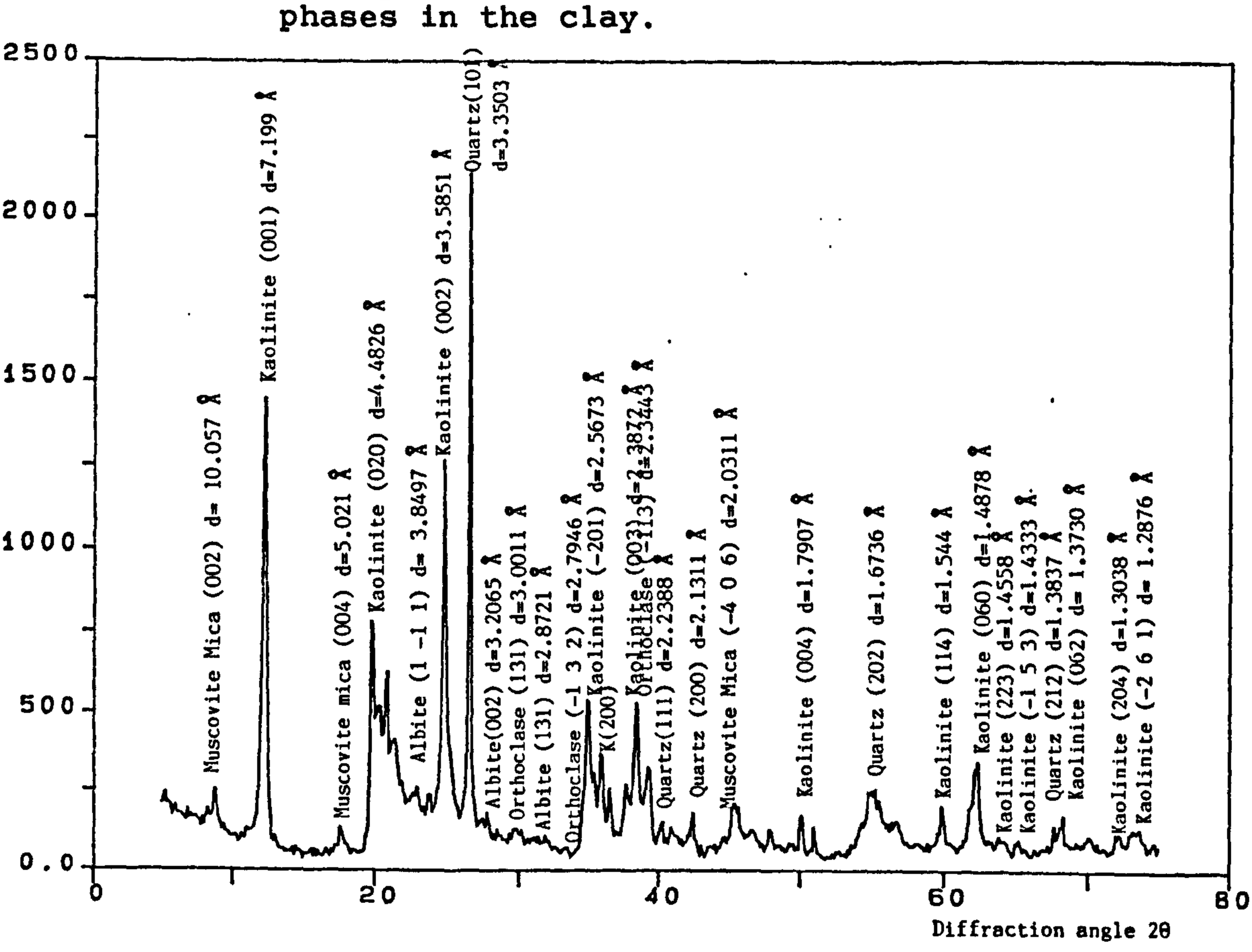

Figure 3.2. X-ray diffraction spectrum of ball clay showing crystallographic planes and interplanar distances of various mineral phases in the clay.

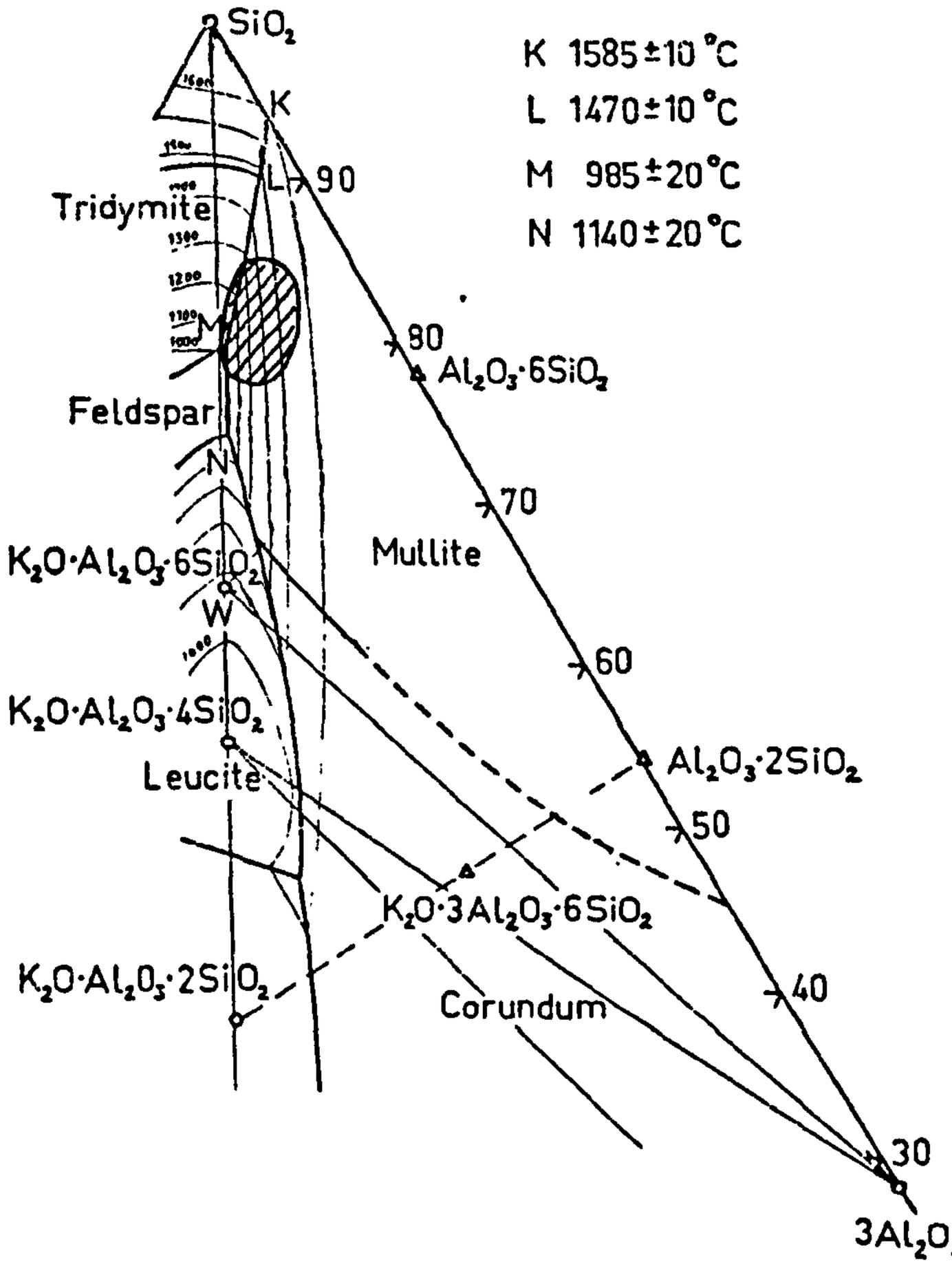

Figure 3.3. Portion of the K_2O-Al_2O_3-SiO_2 ternary equilibrium diagram applicable to sintering and fusible grinding wheel bonds.

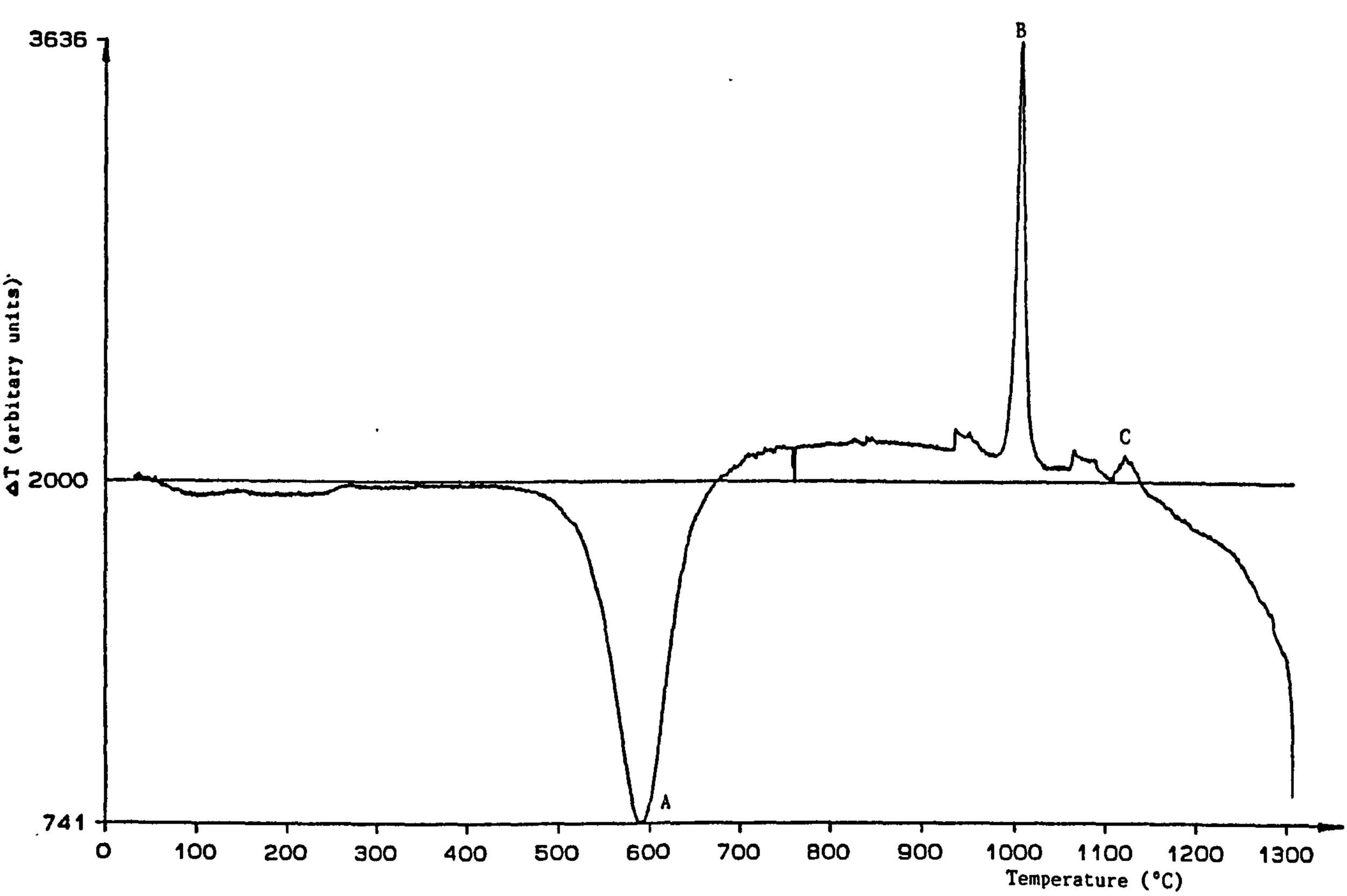

Figure 3.4. Differential thermal analysis trace of China clay. Notation : A - Endothermic trace due to dehydroxylation at 590°C, B = Exothermic peak due to formation of Al-Si spinel and amorphous silica at 1000°C; C - Formation of amorphous silica and melting at 1250°C.

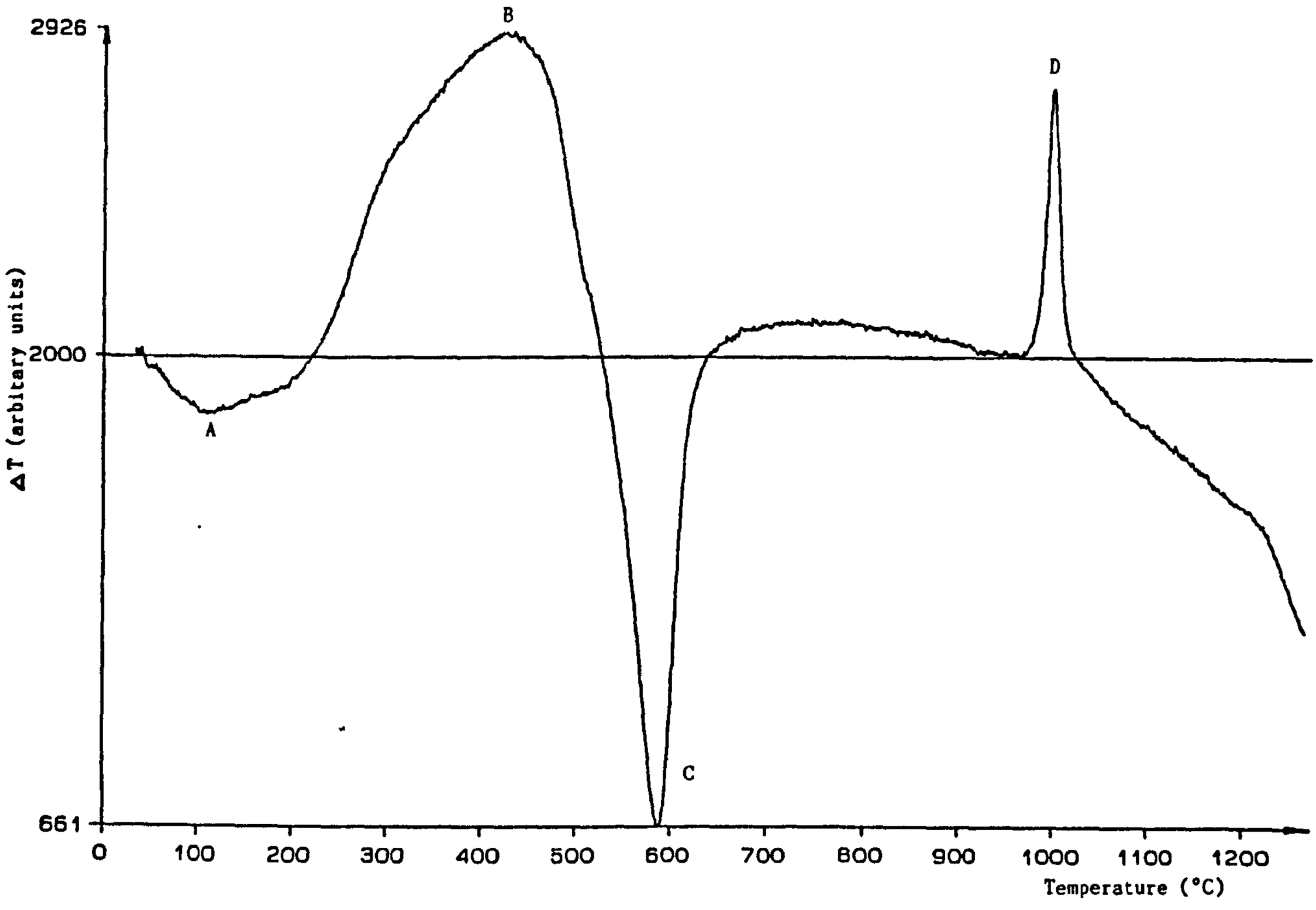

Figure 3.5 Differential thermal analysis trace of ball clay. Notation: A - Endothermic trough due to evolution of absorbed water; B - Exothermic peak due to breakdown of carbonaceous matter; C - Formation of meta-kaolin (bond water released) at 580°C; D - Formation of Al-Si spinel and some amorphous silica at 980°C. Melt formation at 1220°C.

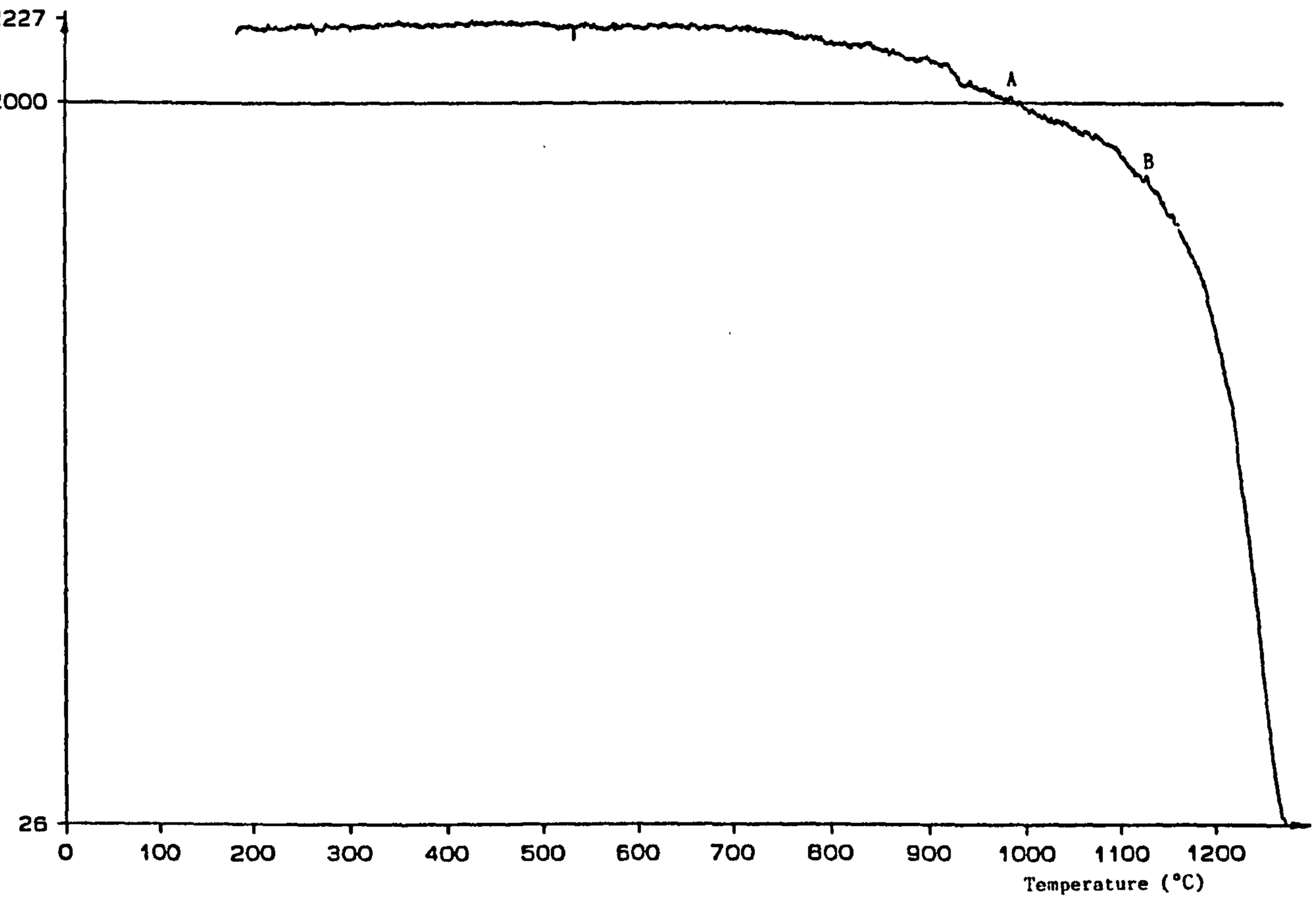

Figure 3.6. Differential thermal analysis of potash feldspar. Notation: A - breakdown of sanidine at 950°C; B-melting occurs at 1170°C.

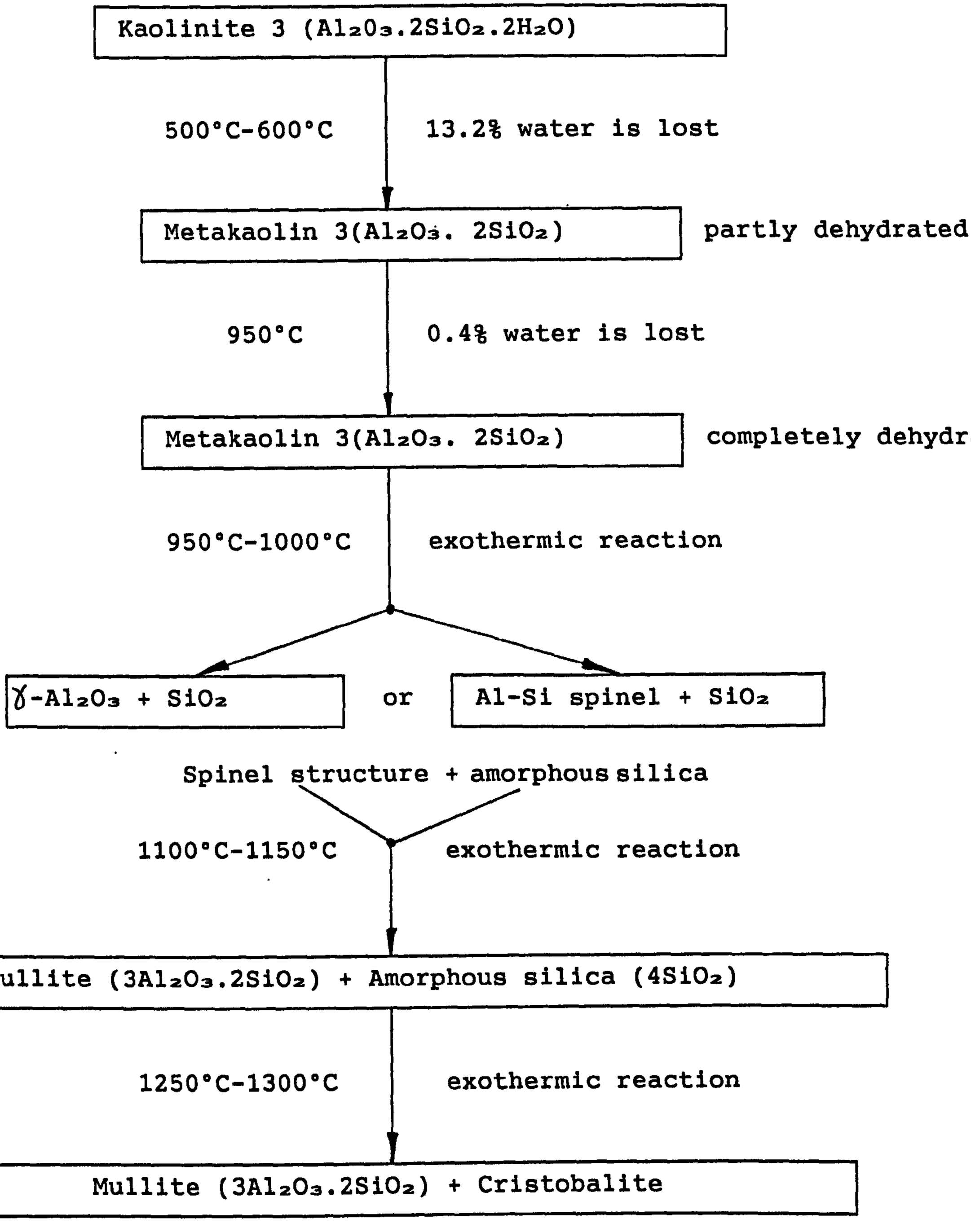

Figure 3.7 - Kaolinite-Mullite phase transformation sequence [162]

Mechanism Number	Transport Path	Source of Matter	Sink of Matter
1	Surface diffusion	Surface	Neck
2	Lattice diffusion	Volume	Neck
3	Vapor transport	Surface	Neck
4	Boundary diffusion	Grain boundary	Neck
5	Lattice diffusion	Grain boundary	Neck
6	Lattice diffusion	Dislocations	Neck

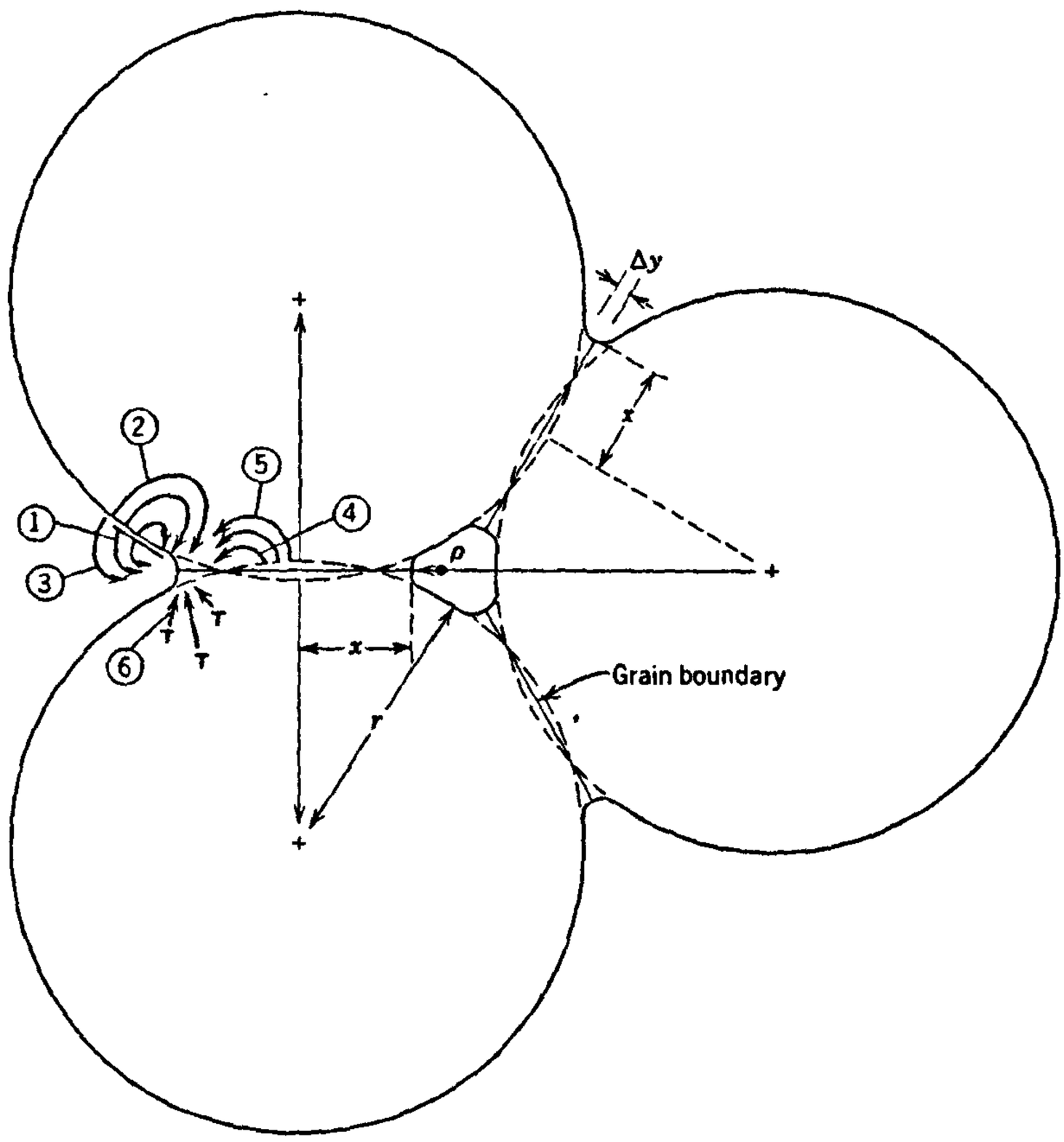

Figure 3.8 Model for the initial stage of sintering of spherical particles in contact showing alternate paths for matter transport [81].

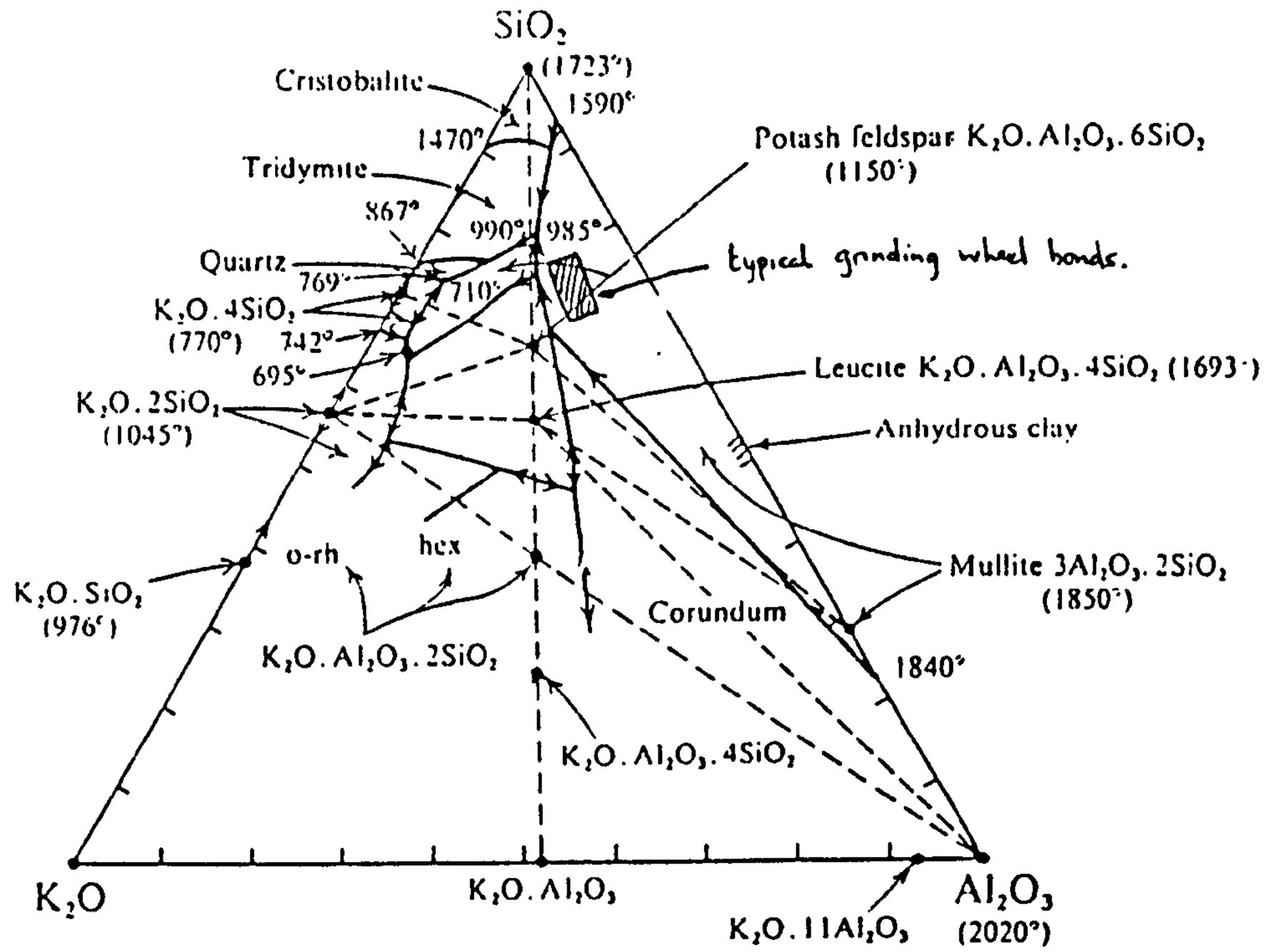

Figure 4.1 K_2O-Al_2O_3-SiO_2 ternary equilibrium diagram.

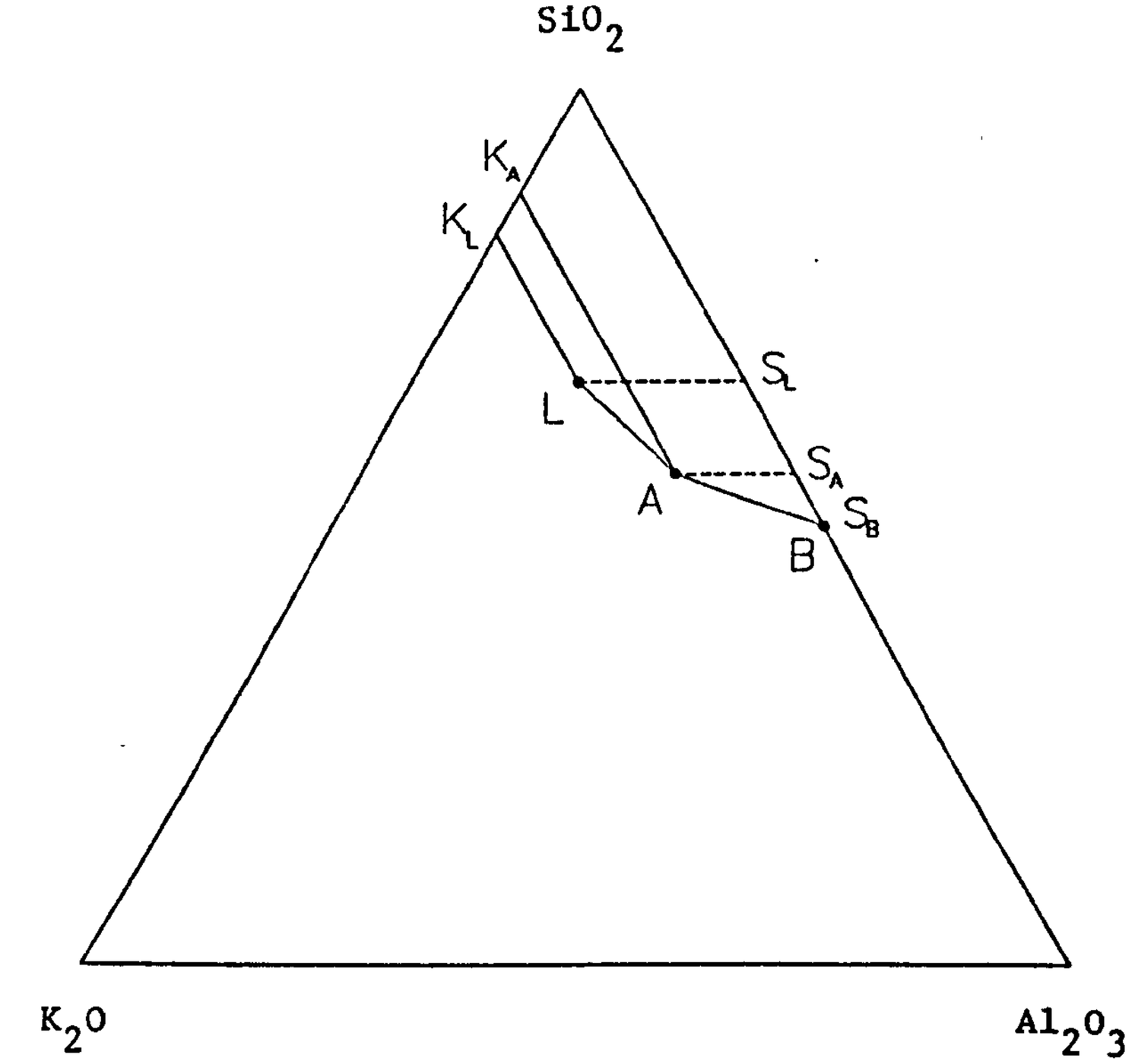

Figure 4.2. Calculation of constitutions from the K_2O-Al_2O_3-SiO_2 phase diagram.

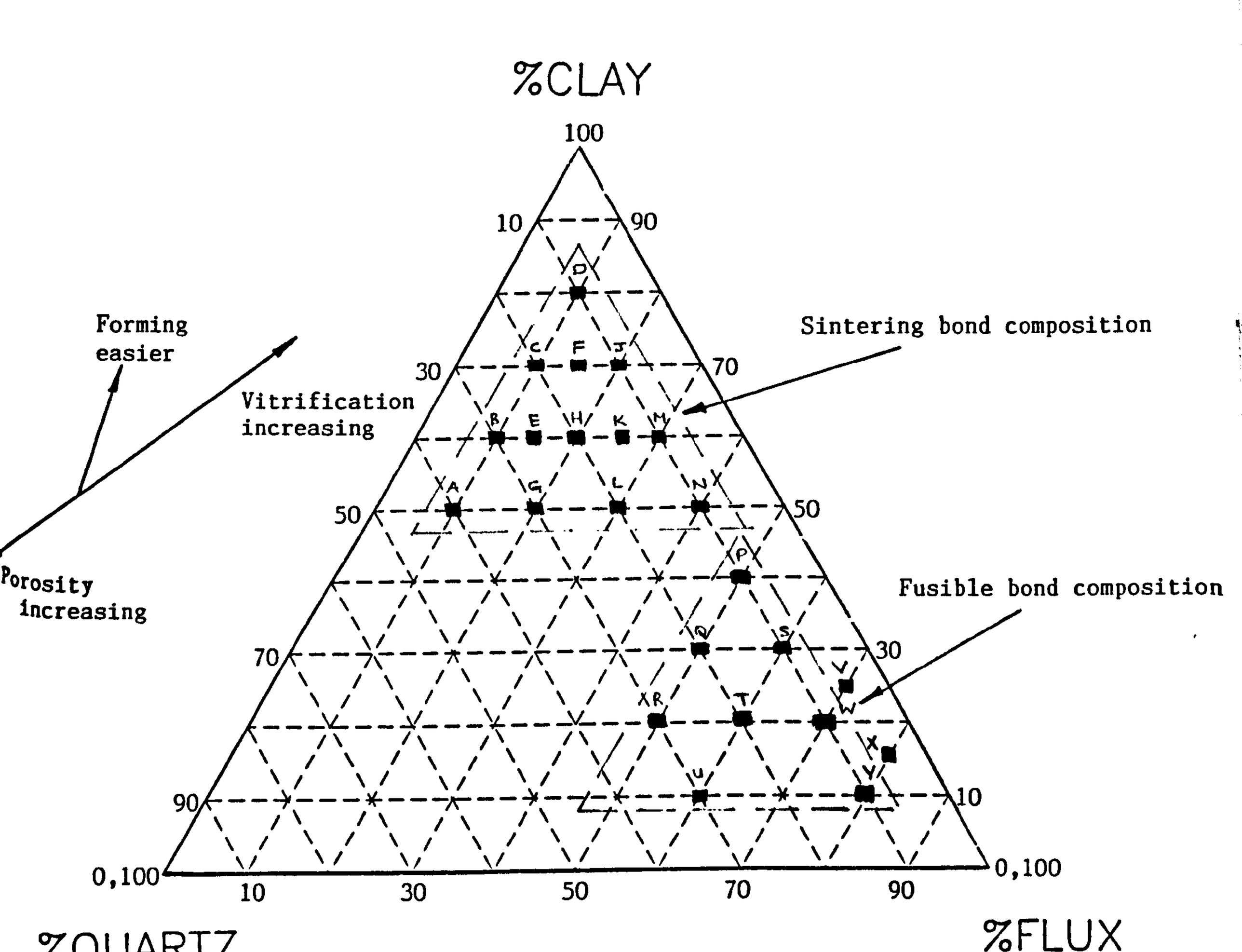

Figure 4.3. Compositions of bonds chosen for experimental work.

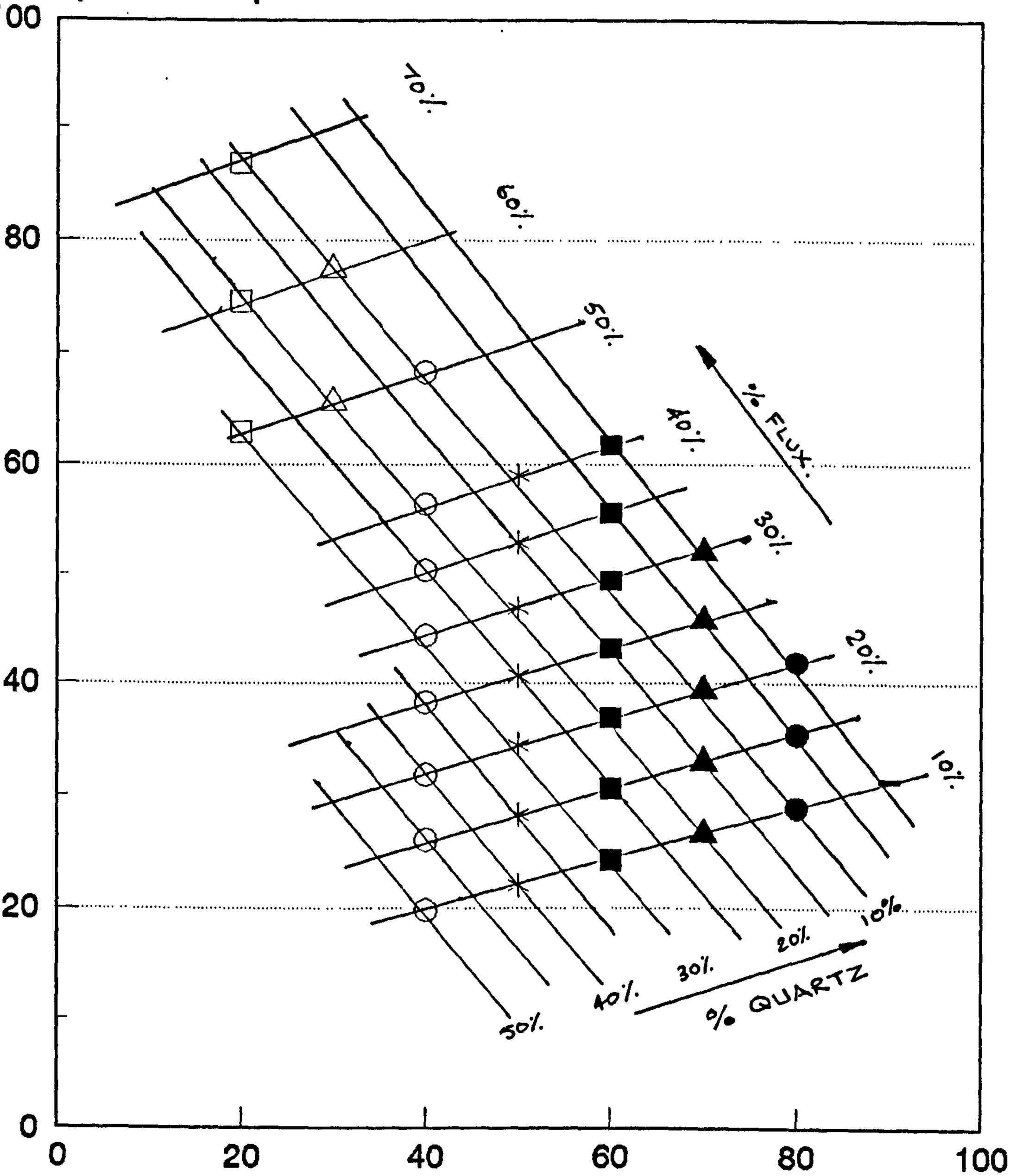

Figure 4.4 Equilibrium liquid content as a function of bond composition.

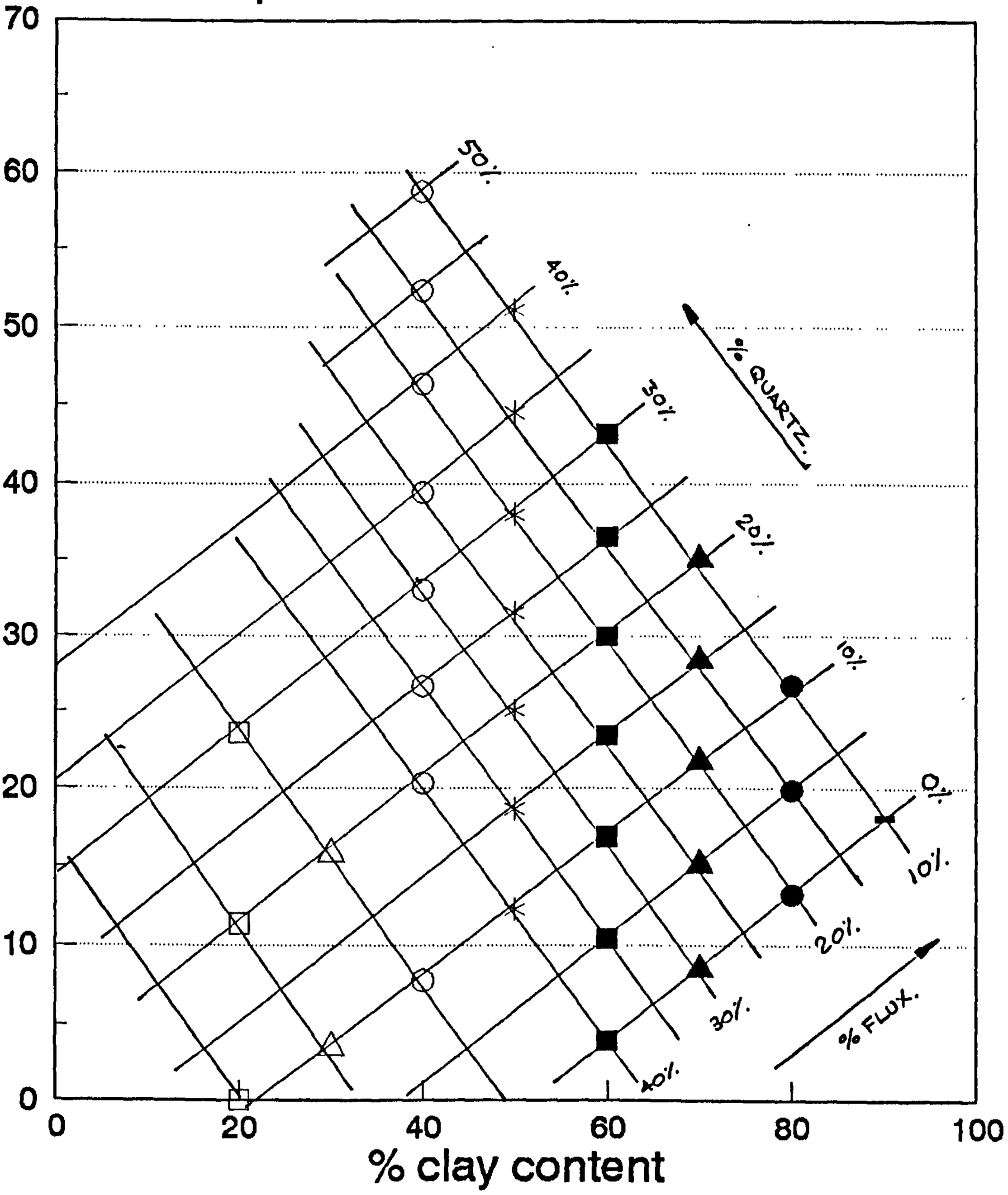

Figure 4.5 Equilibrium silica content as a function of bond composition.

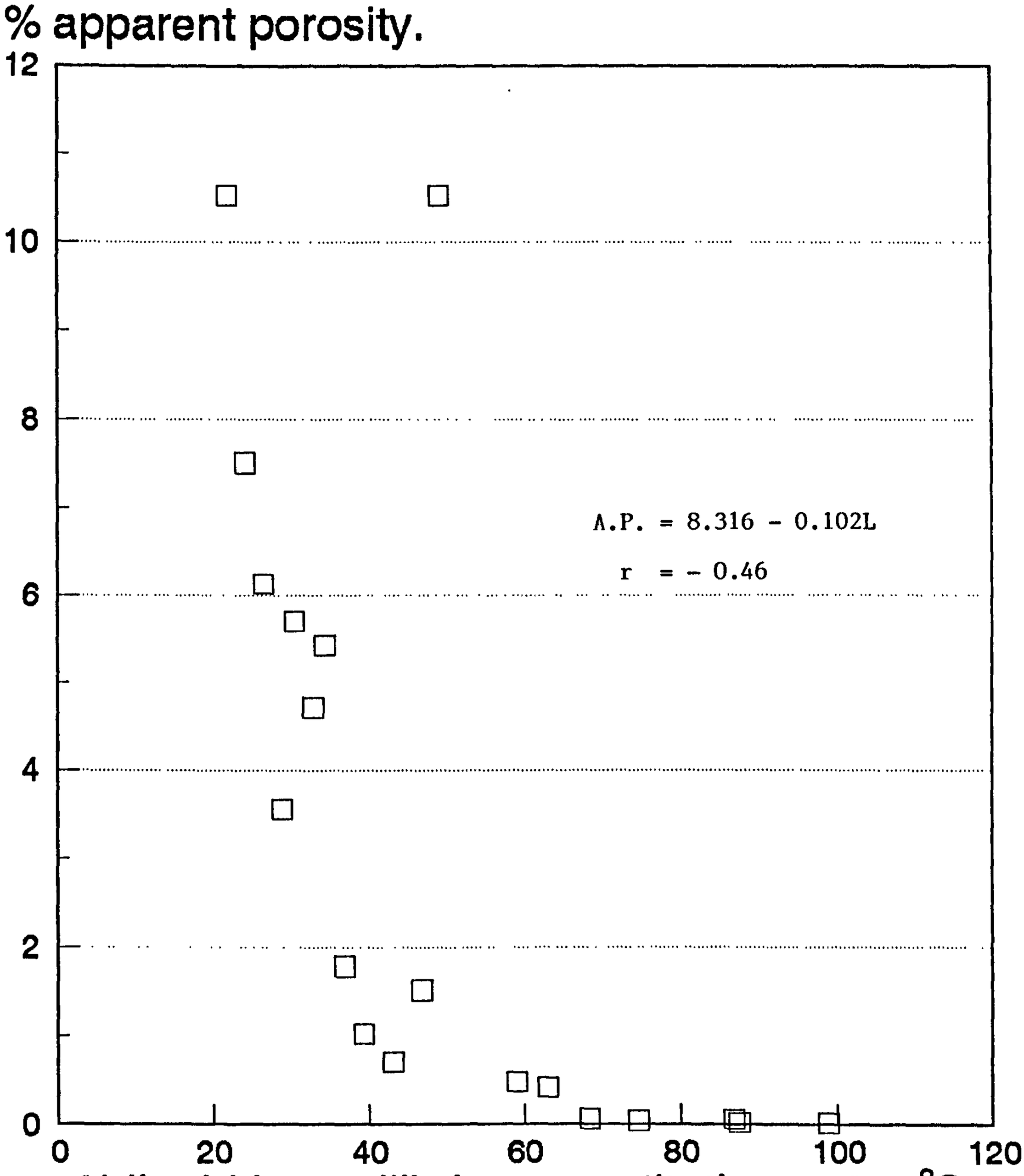

Figure 4.6 Statistical relationship between % apparent porosity and equilibrium constitution at a soaking temperature of 1150°C

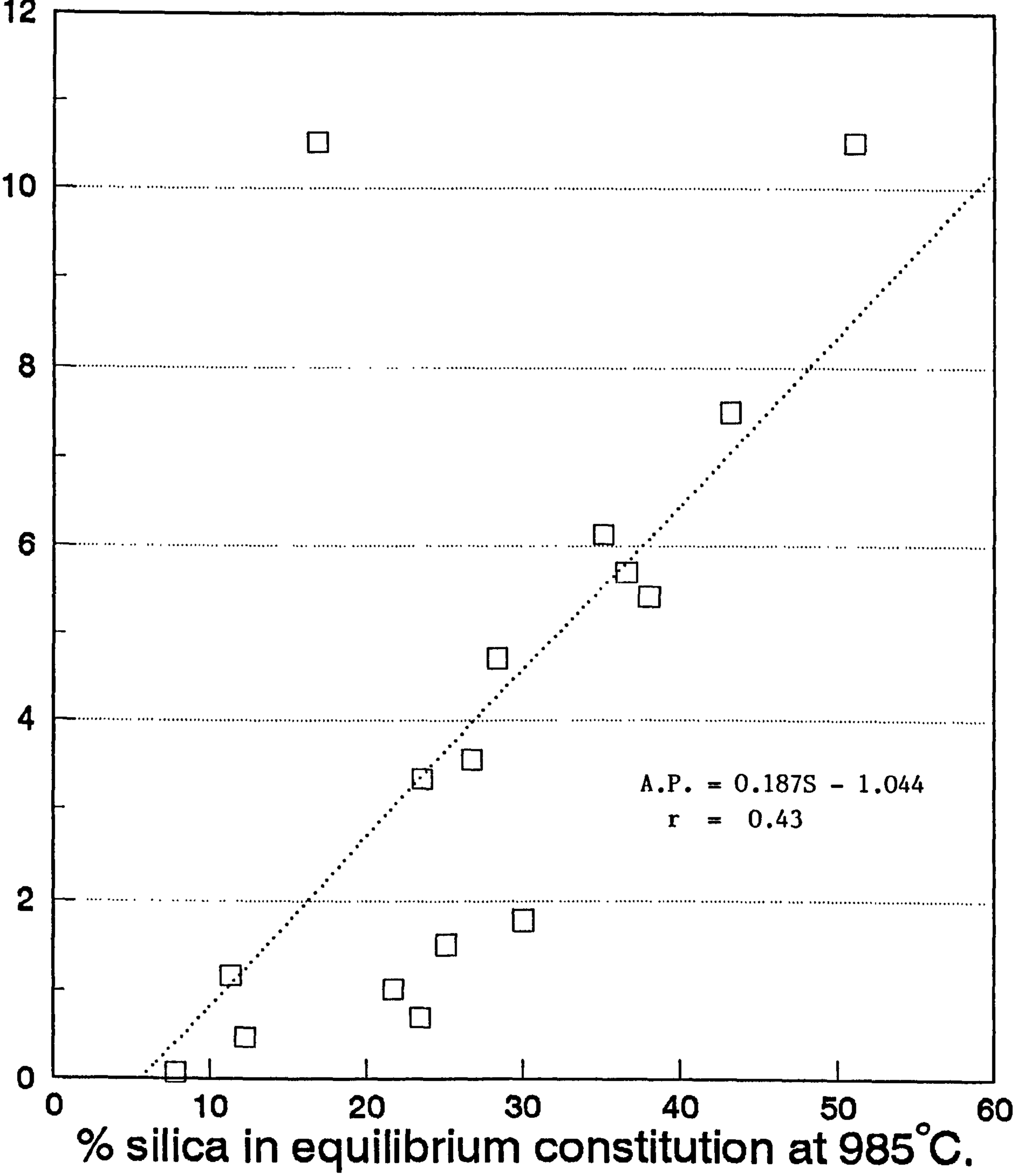

Figure 4.7 Statistical relationship between apparent porosity and equilibrium constitution at a soaking temperature of 1150°C.

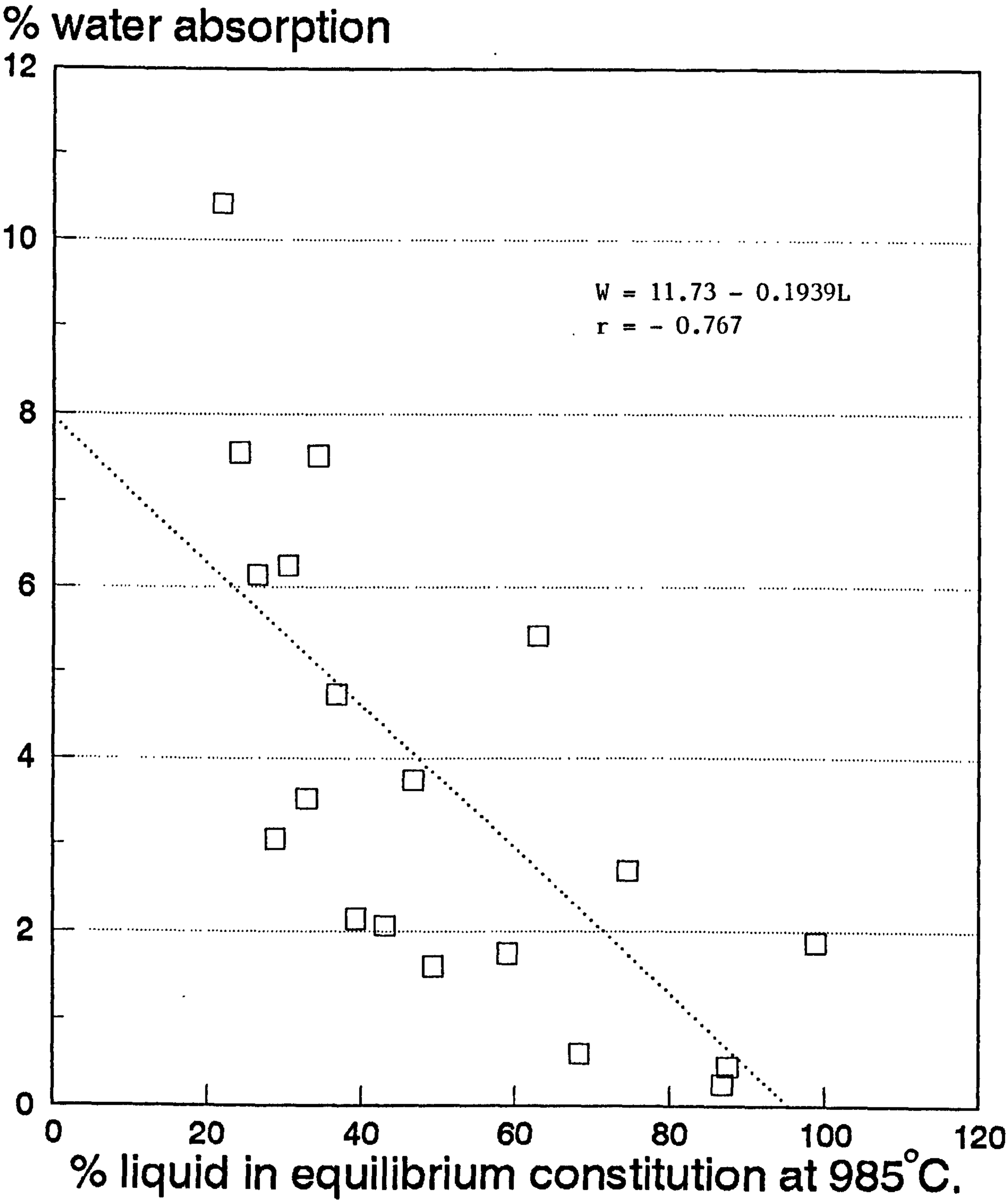

Figure 4.8 Statistical relationship between water absorption and equilibrium constitution at a soaking temperature of 1150°C.

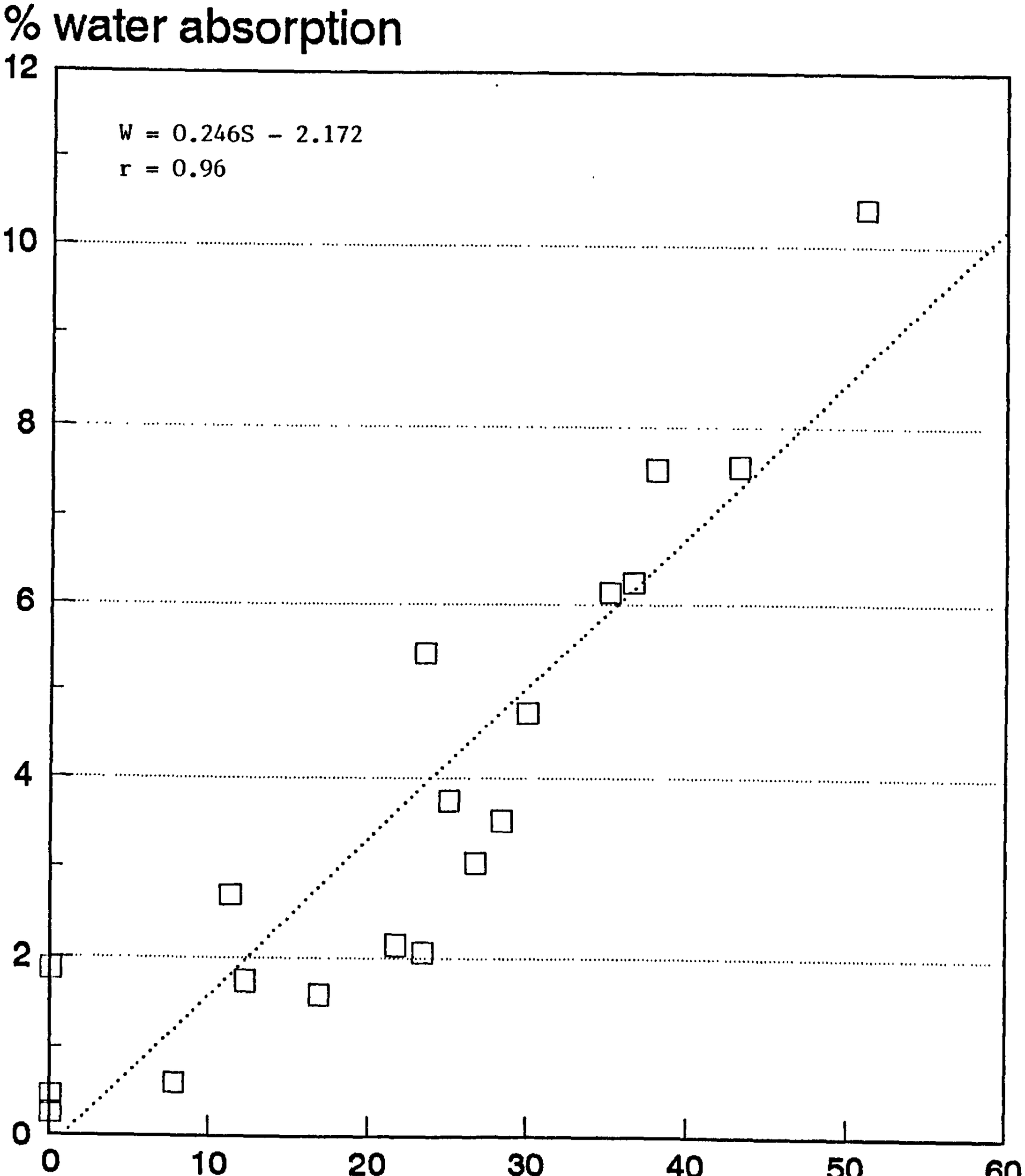

Figure 4.9 Statistical relationship between water absorption and equilibrium constitution at a soaking temperature of 1150°C.

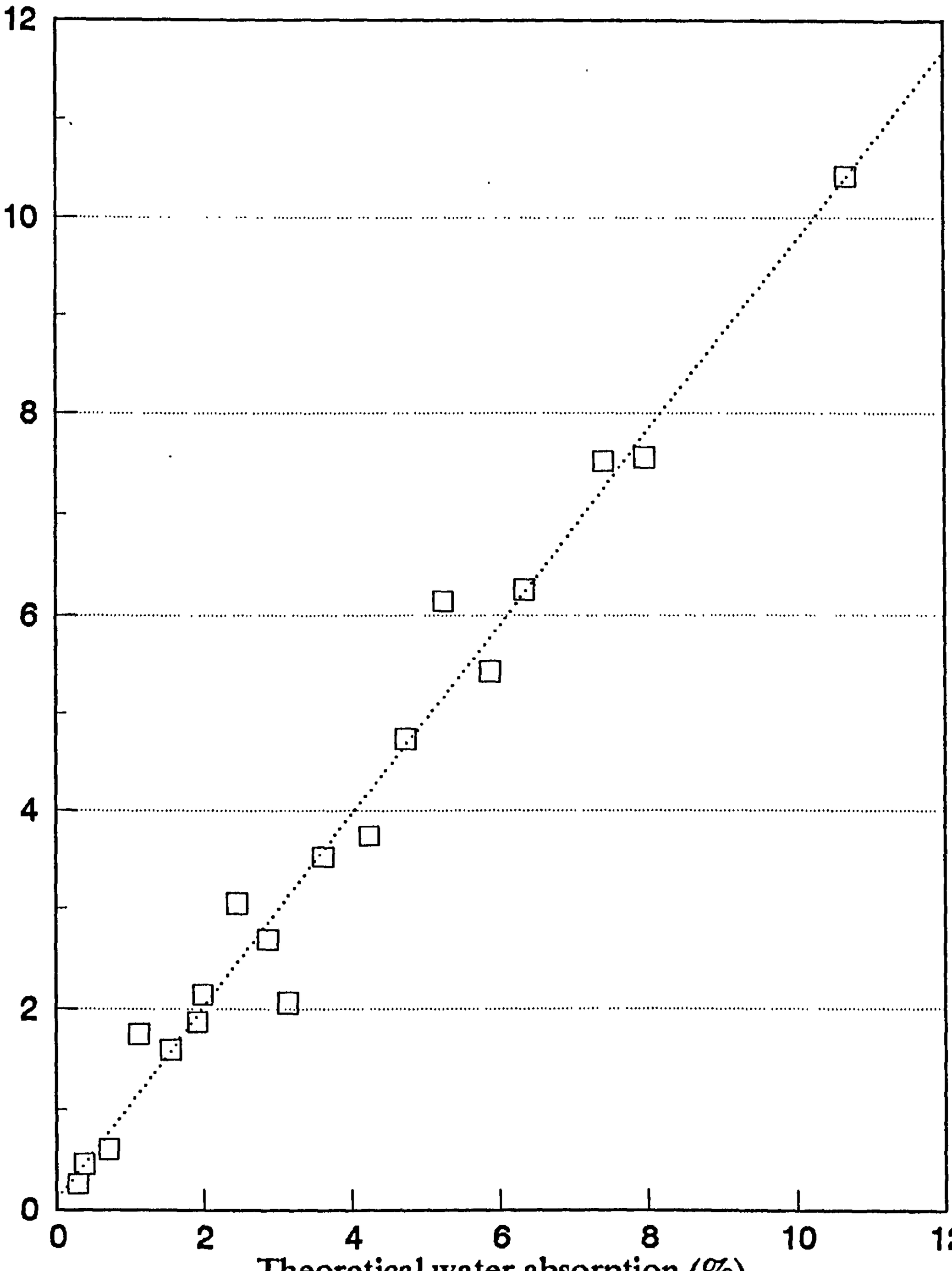

Figure 4.10 Experimental and theoretical water absorption values.

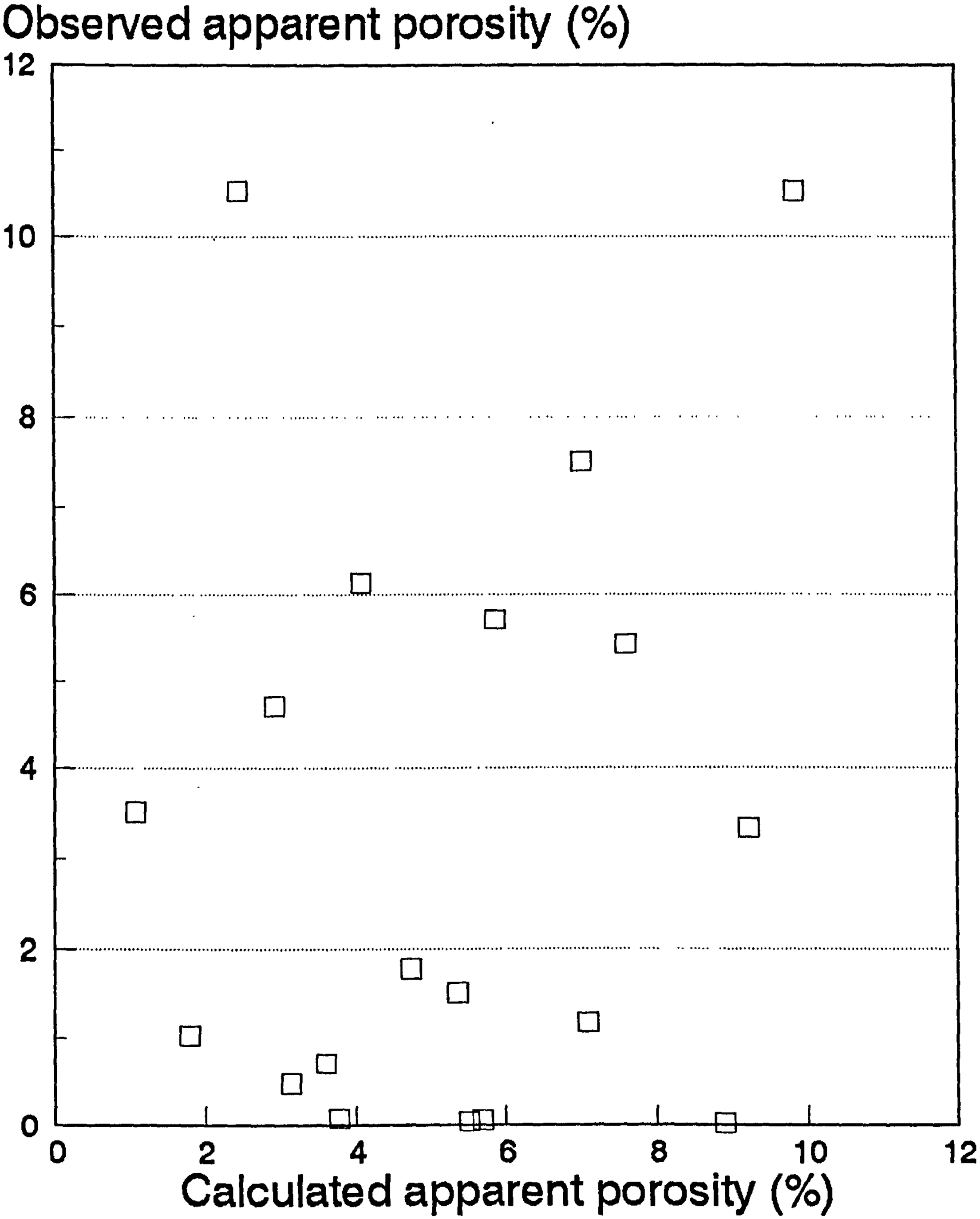

Figure 4.11 Experimental and theoretical apparent porosity values.

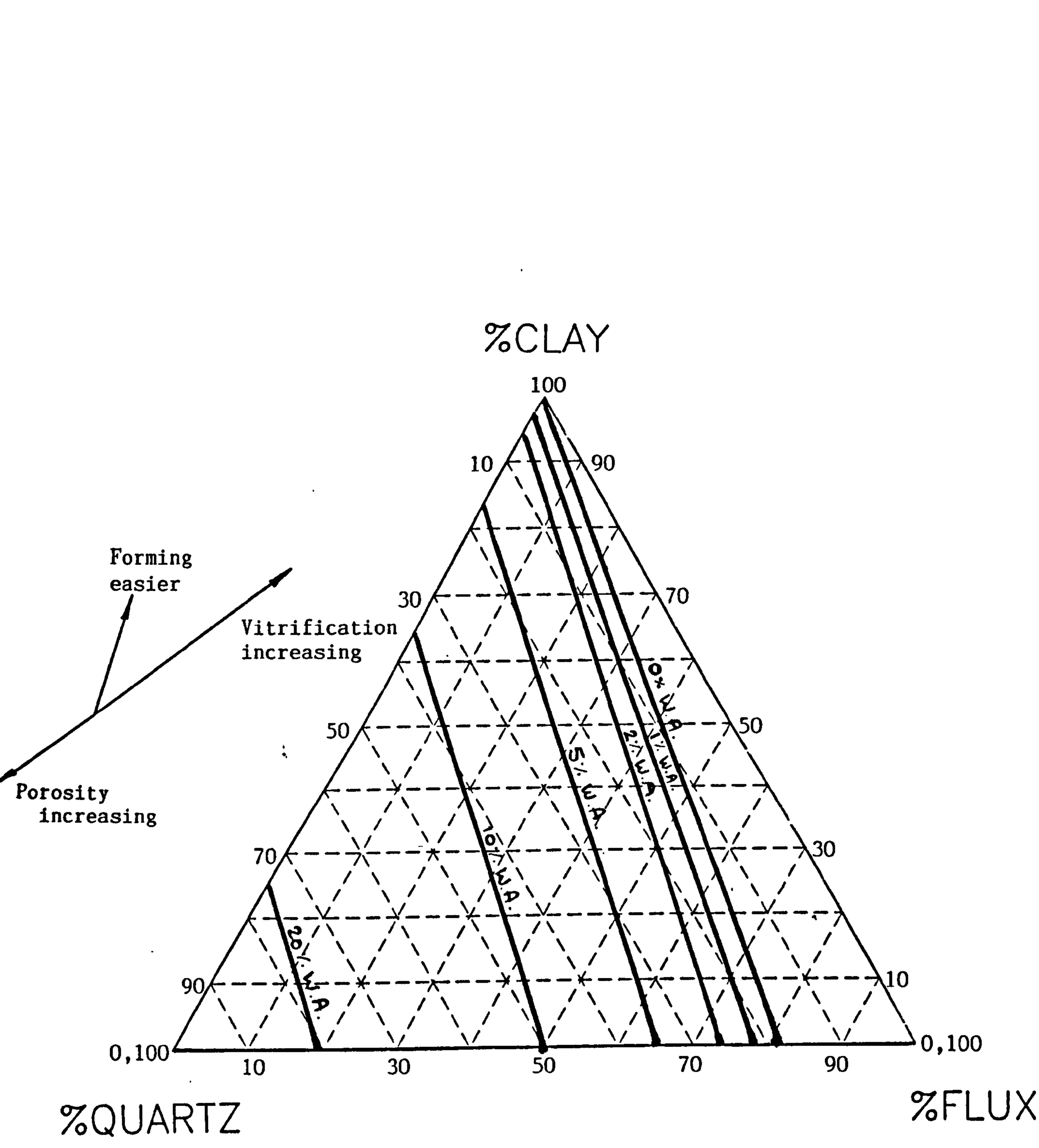

Figure 4.12 Vitrification map derived from water absorption results for a bond mixture fired at 1150°C - heating and cooling rate was 2.9°C/min: test pieces 36mm diameter.

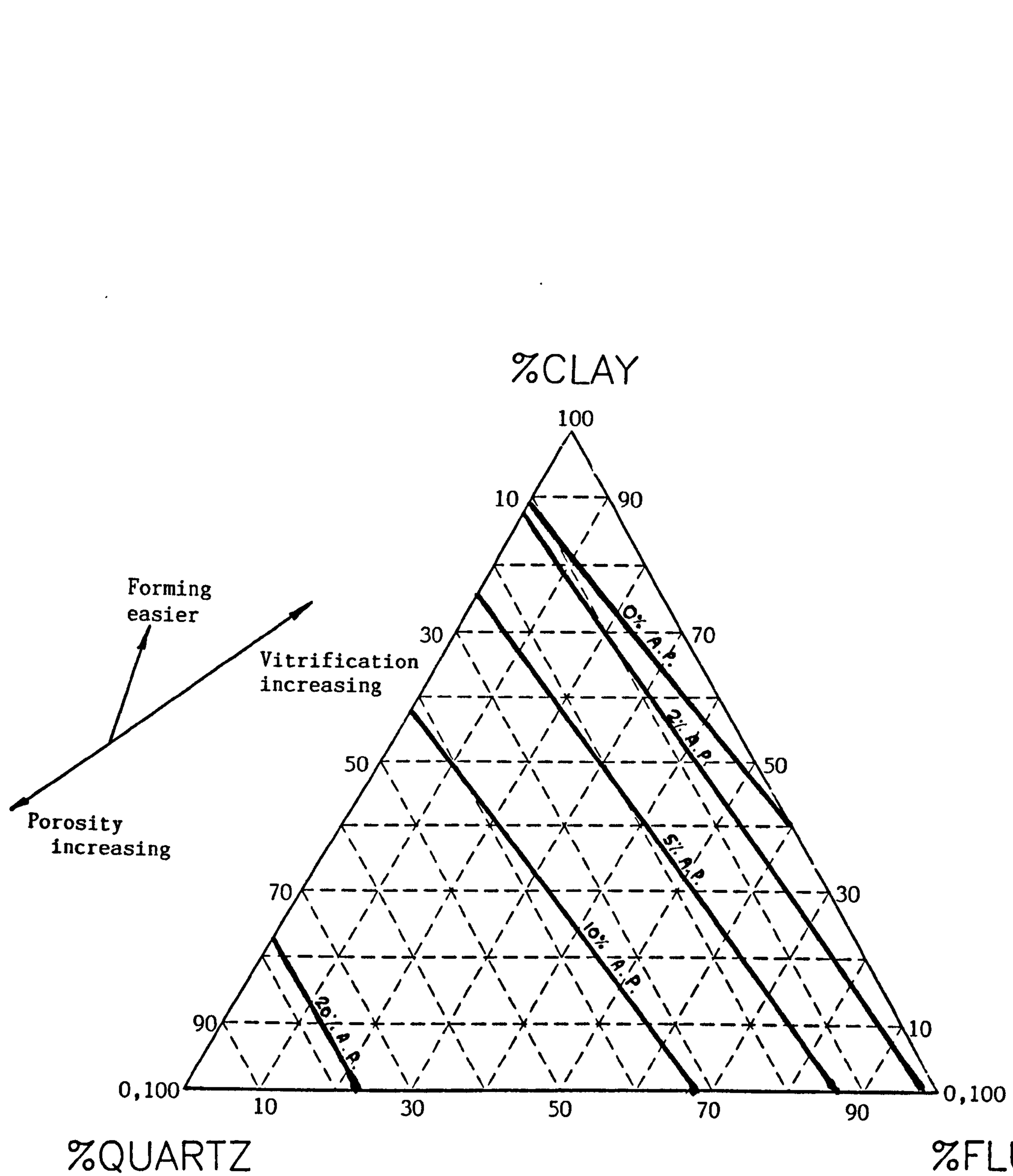

Figure 4.13 Vitrification map derived from apparent porosity results for a bond mixture fired at 1150°C - heating and cooling rate was 2.9°C/min: test pieces 36mm diameter.

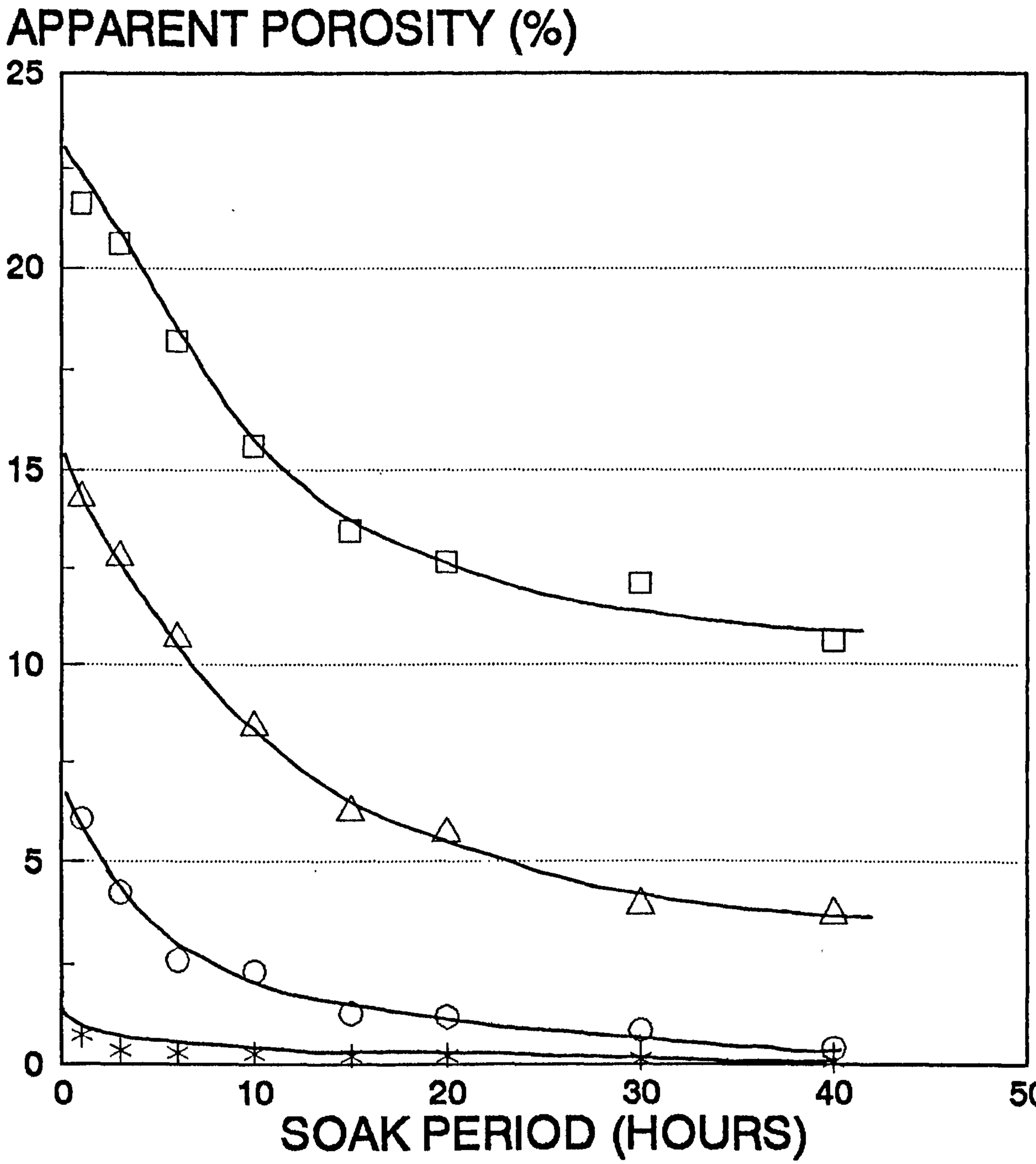

Figure 4.14 Apparent porosity as a function of soaking time at 1200°C for bond mixtures containing 50% clay. (□) 10% feldspar, (△) 20% feldspar, (o) 30% feldspar, (*) 40% feldspar.

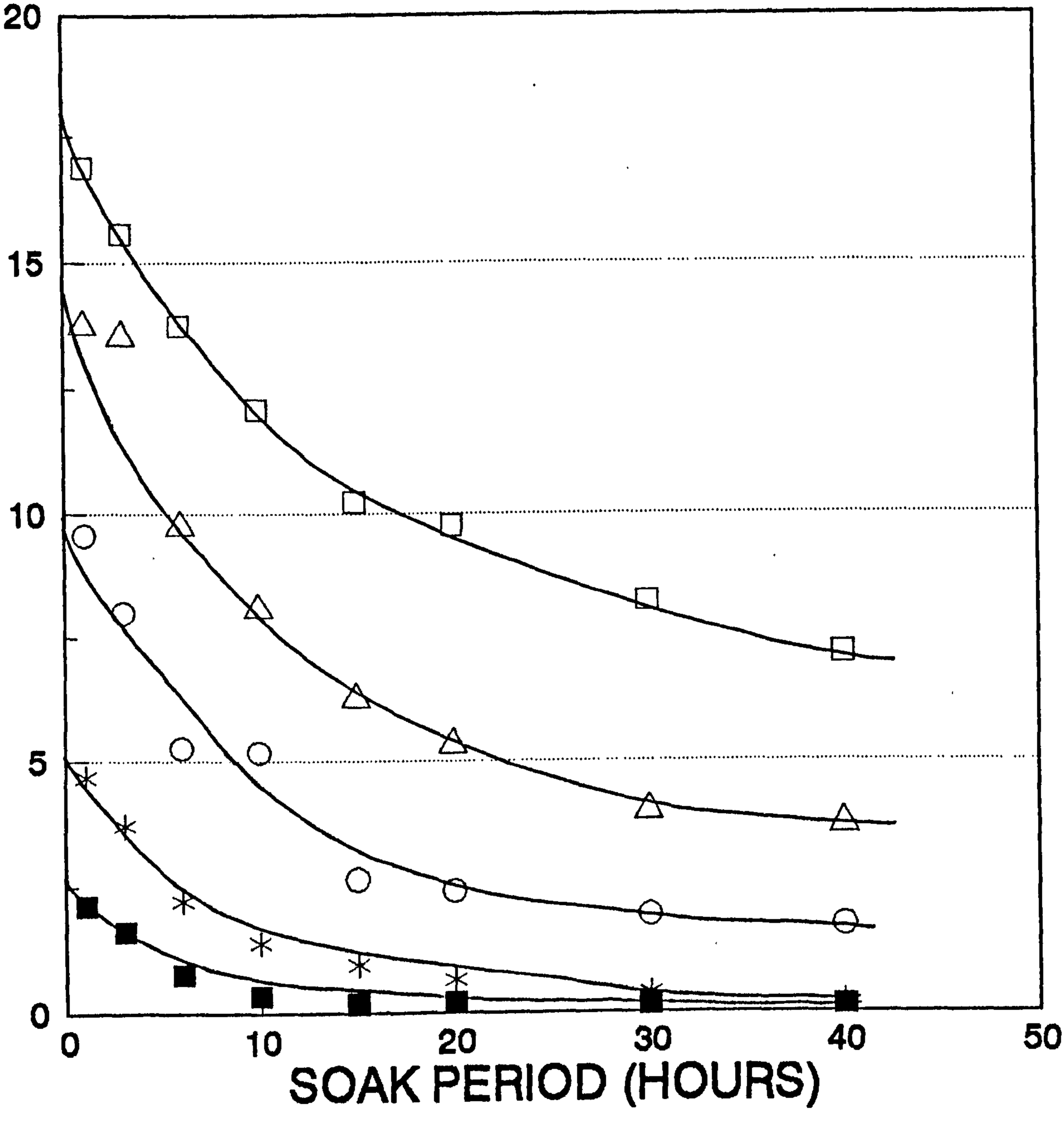

Figure 4.15 Apparent porosity as a function of soaking time at 1200°C for bond mixtures containing 60% clay. (□) 10% feldspar, (Δ) 15% feldspar, (o) 20% feldspar, (*) 25% feldspar, (■) 30% feldspar.

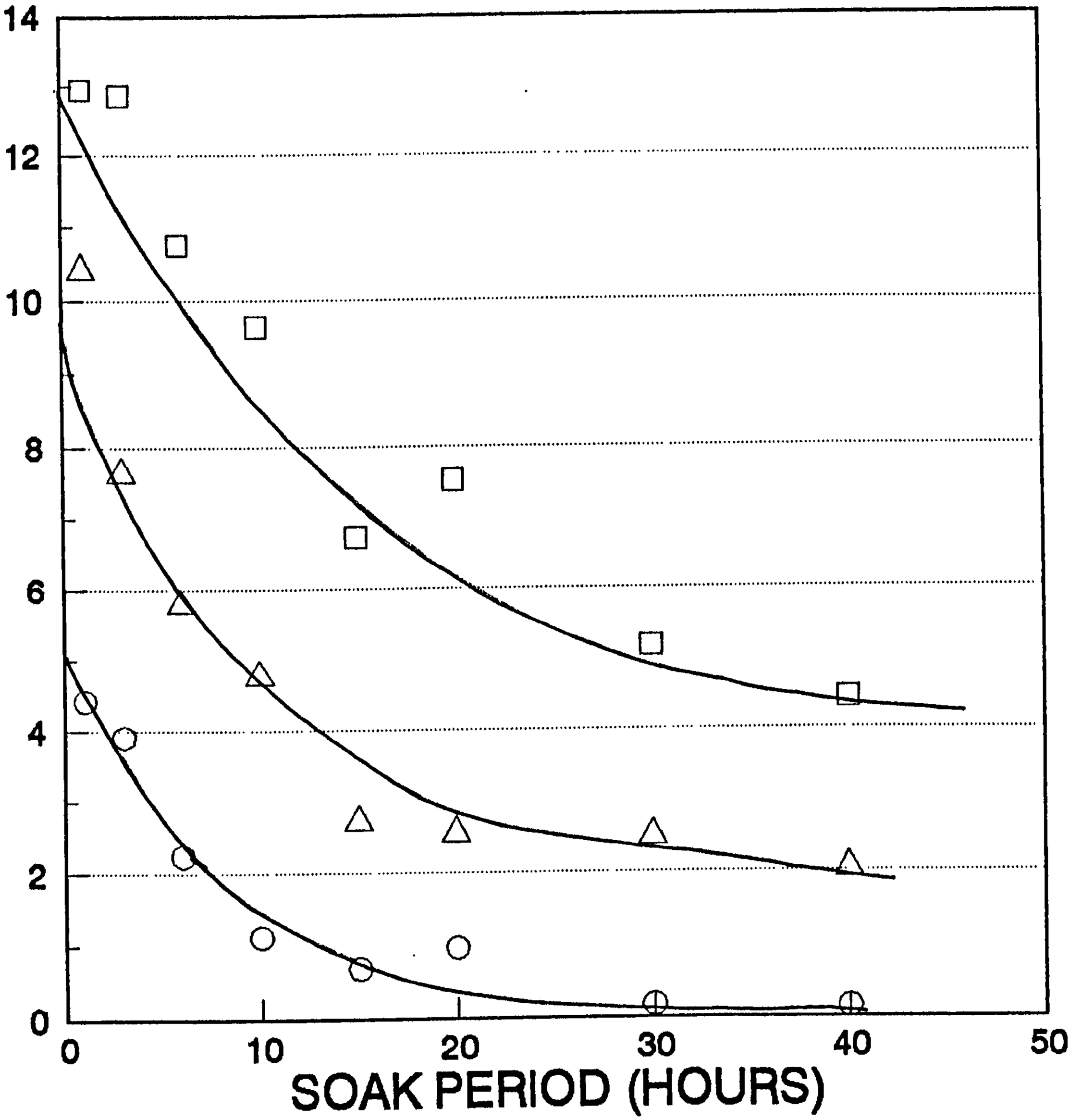

Figure 4.16 Apparent porosity as a function of soaking time at 1200°C for bond mixtures containing 70% clay. (□) 10% feldspar, (△) 15% feldspar, (o) 20% feldspar.

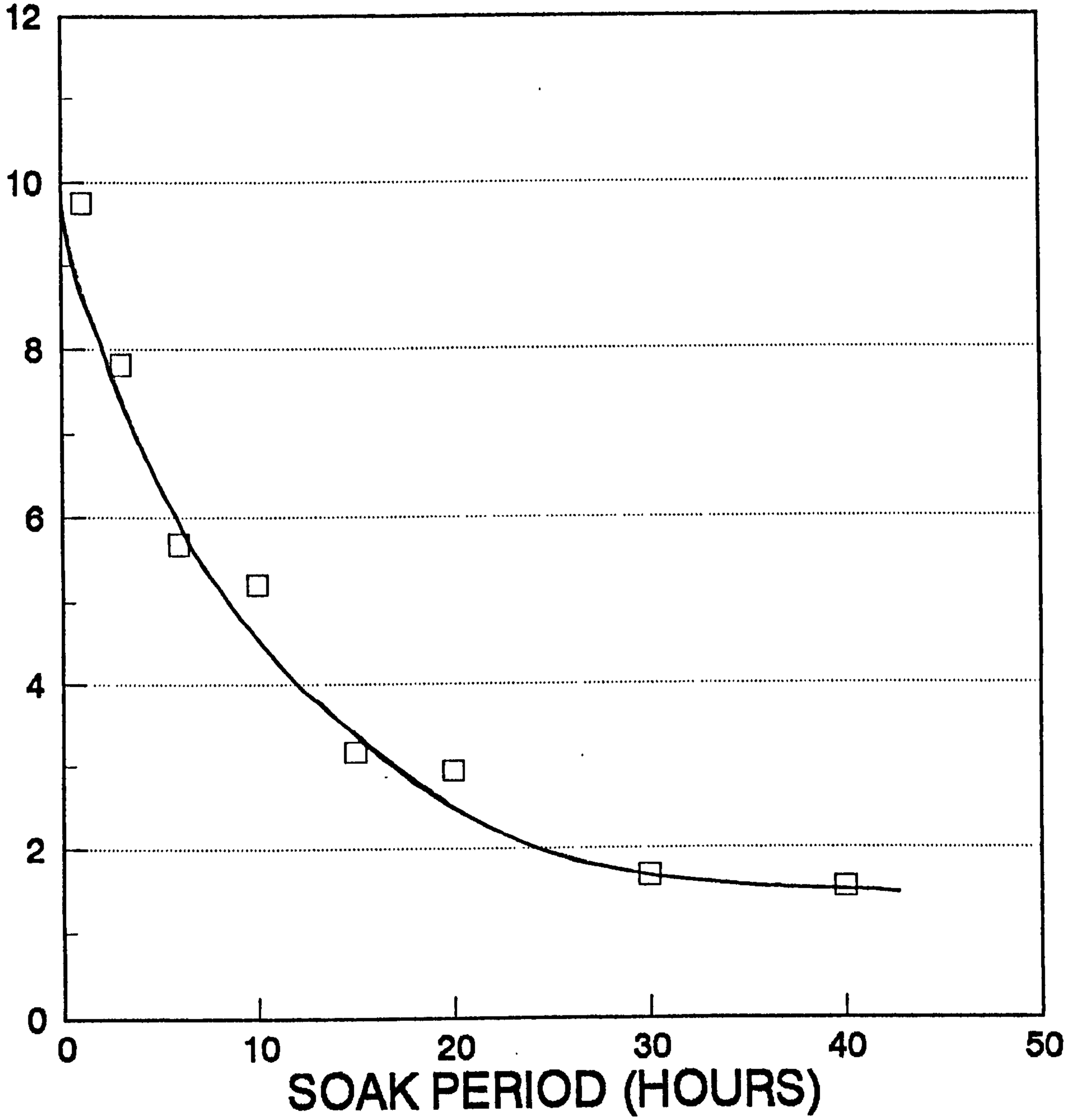

Figure 4.17 Apparent porosity as a function of soaking time at 1200°C for bond mixtures containing 80% clay. (□) 10% feldspar.

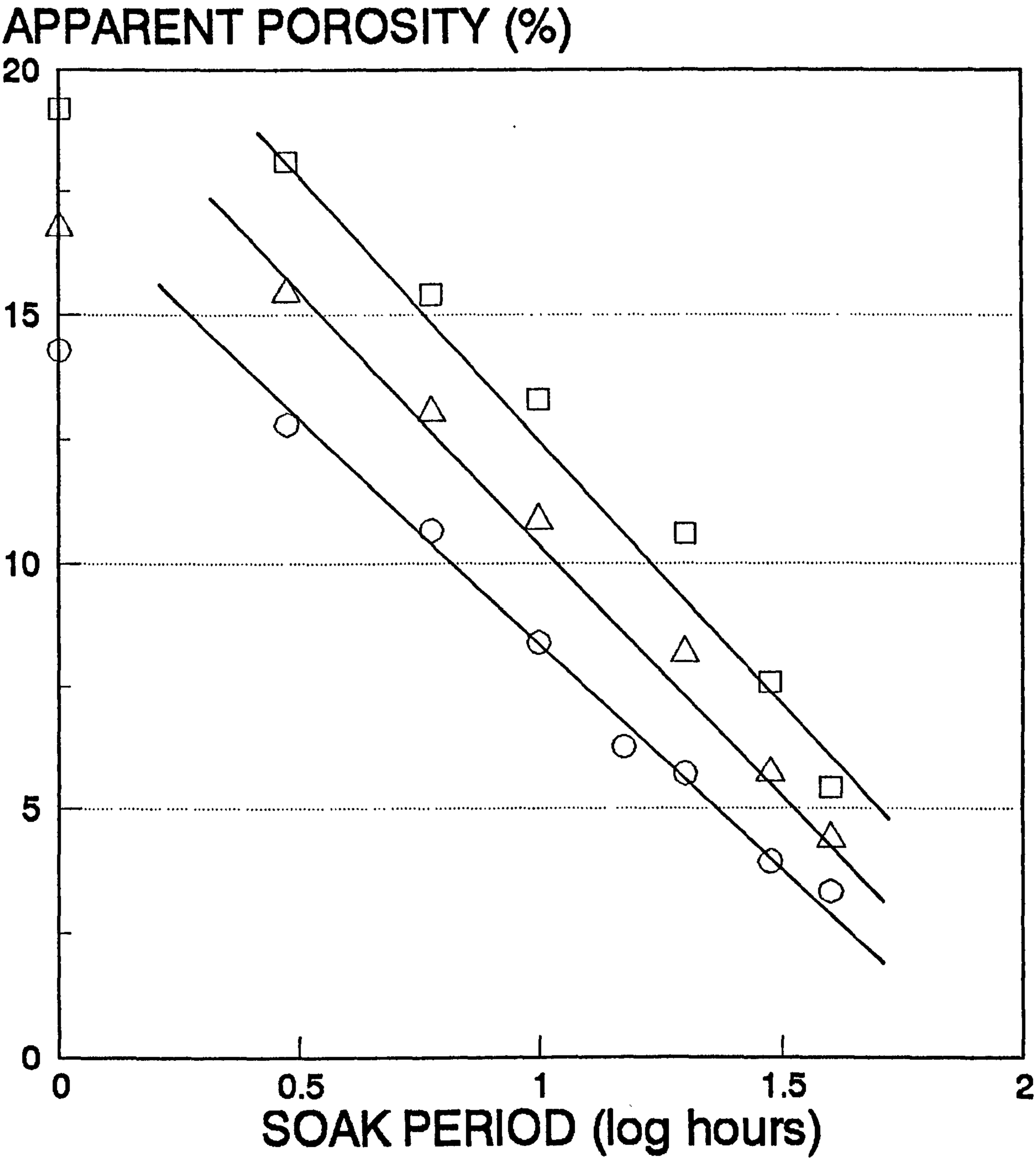

Figure 4.18 Apparent porosity as a function of log soaking time at 1150°C - 1200°C for bond mixture G (□) 1150°C, (△) 1175°C, (o) 1200°C.

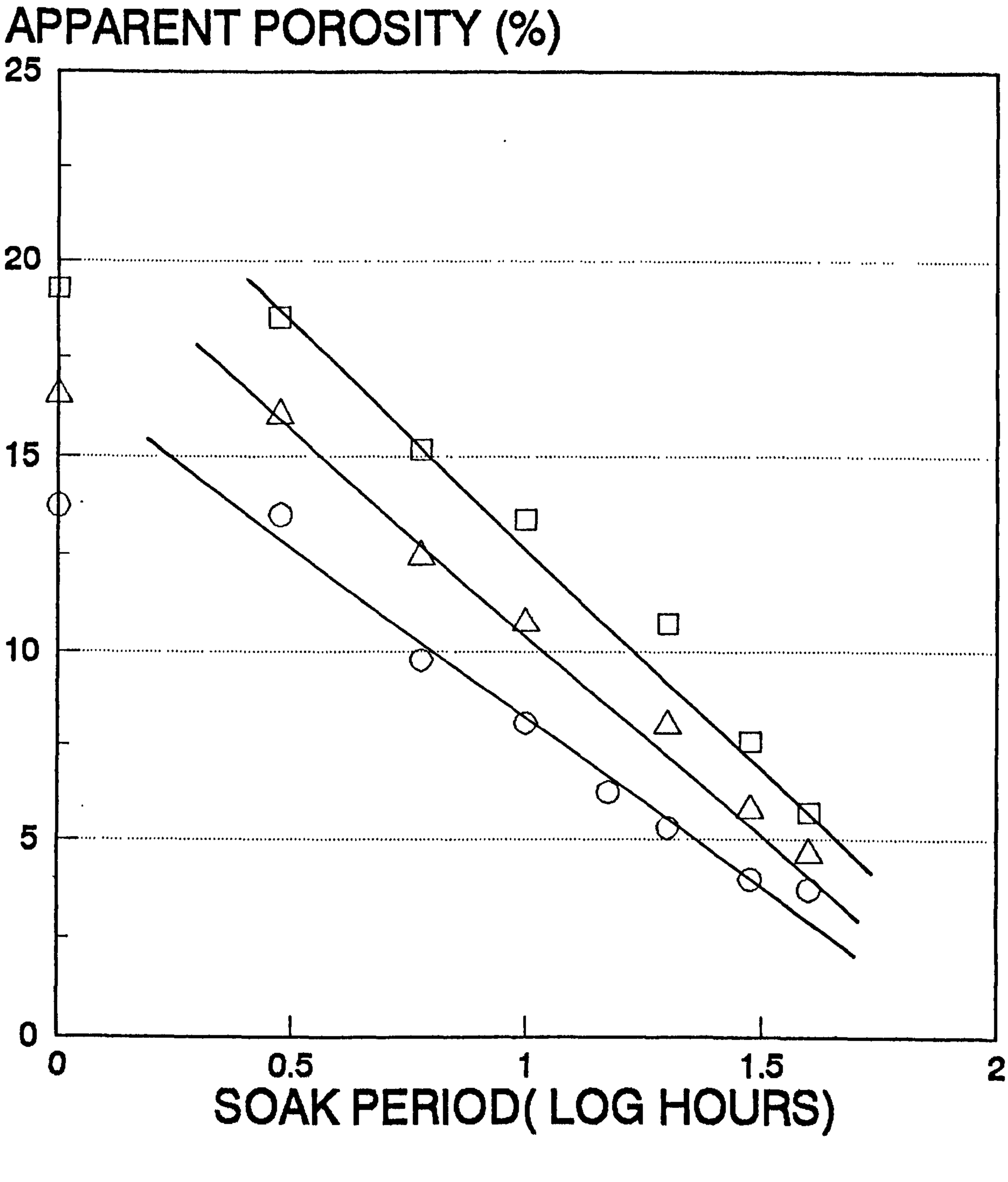

Figure 4.19 Apparent porosity as a function of log soaking time at 1150°C-1200°C for bond mixture E. (□) 1150°C, (△) 1175°C, (o) 1200°C.

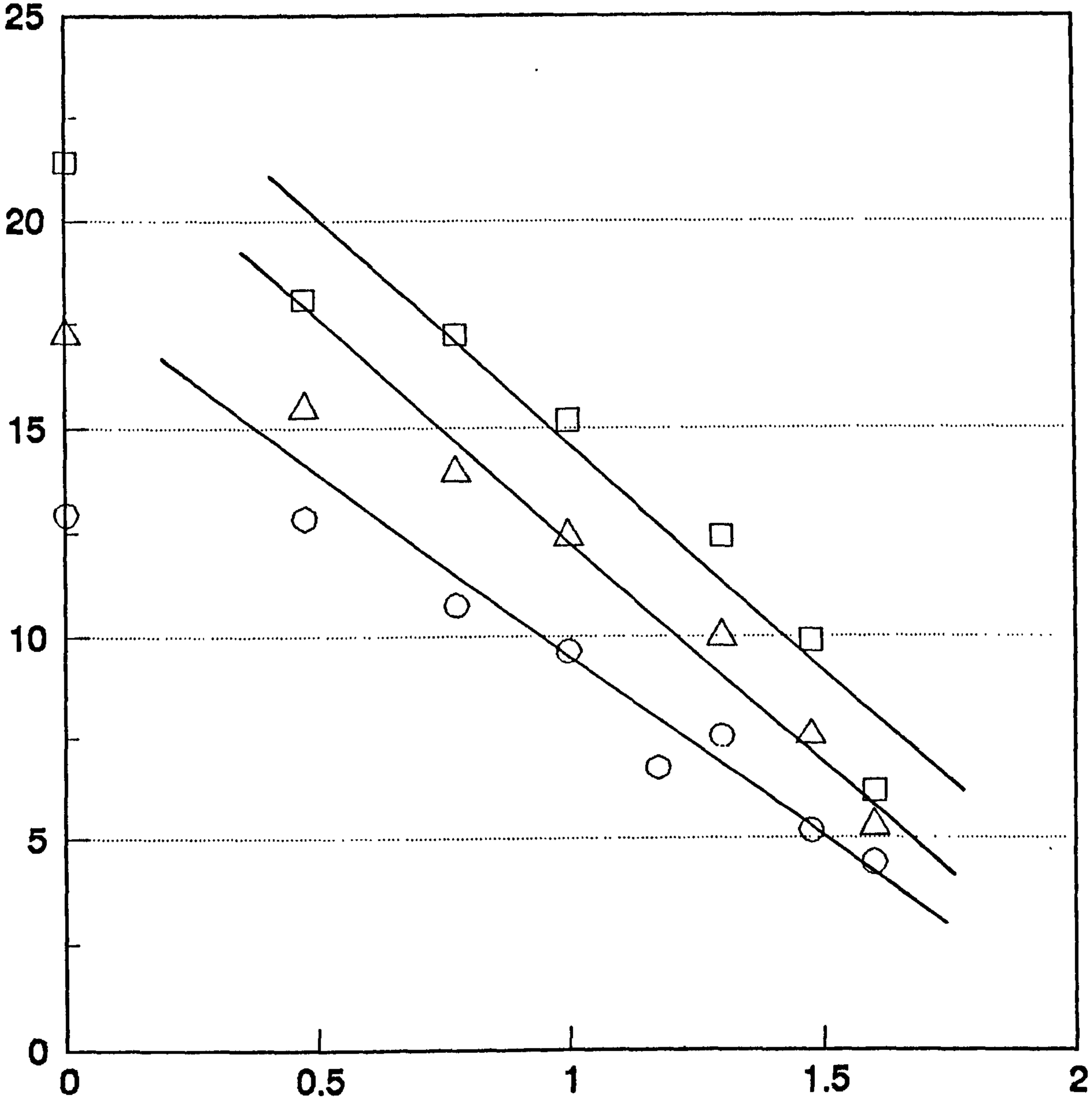

Figure 4.20 Apparent porosity as a function of log soaking time at 1150°C-1200°C for bond mixture C. (□) 1150°C, (△) 1175°C, (o) 1200°C.

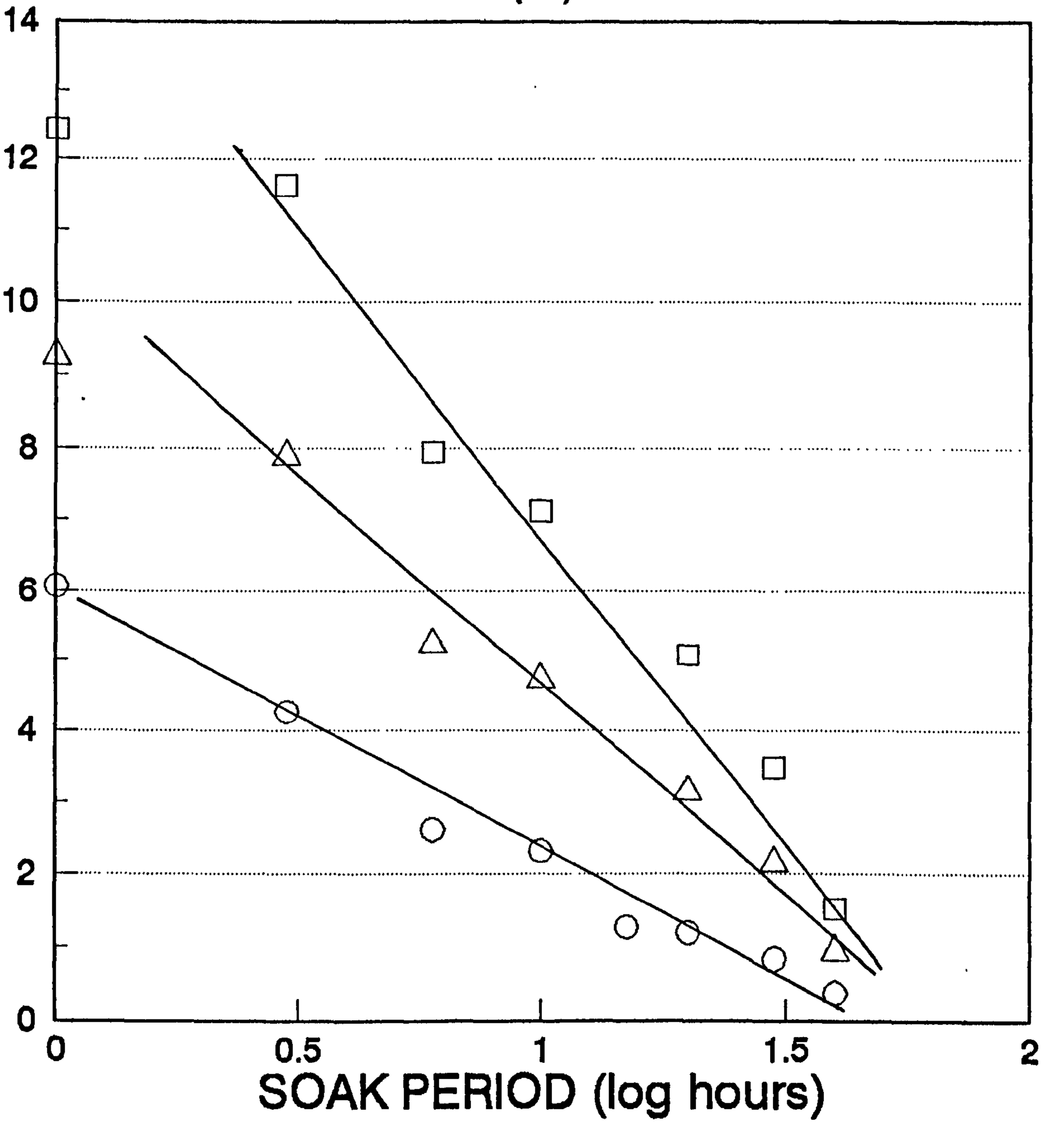

Figure 4.21 Apparent porosity as a function of log soaking time at 1150°C-1200°C for bond mixture L. (□) 1150°C, (△) 1175°C, (o) 1200°C.

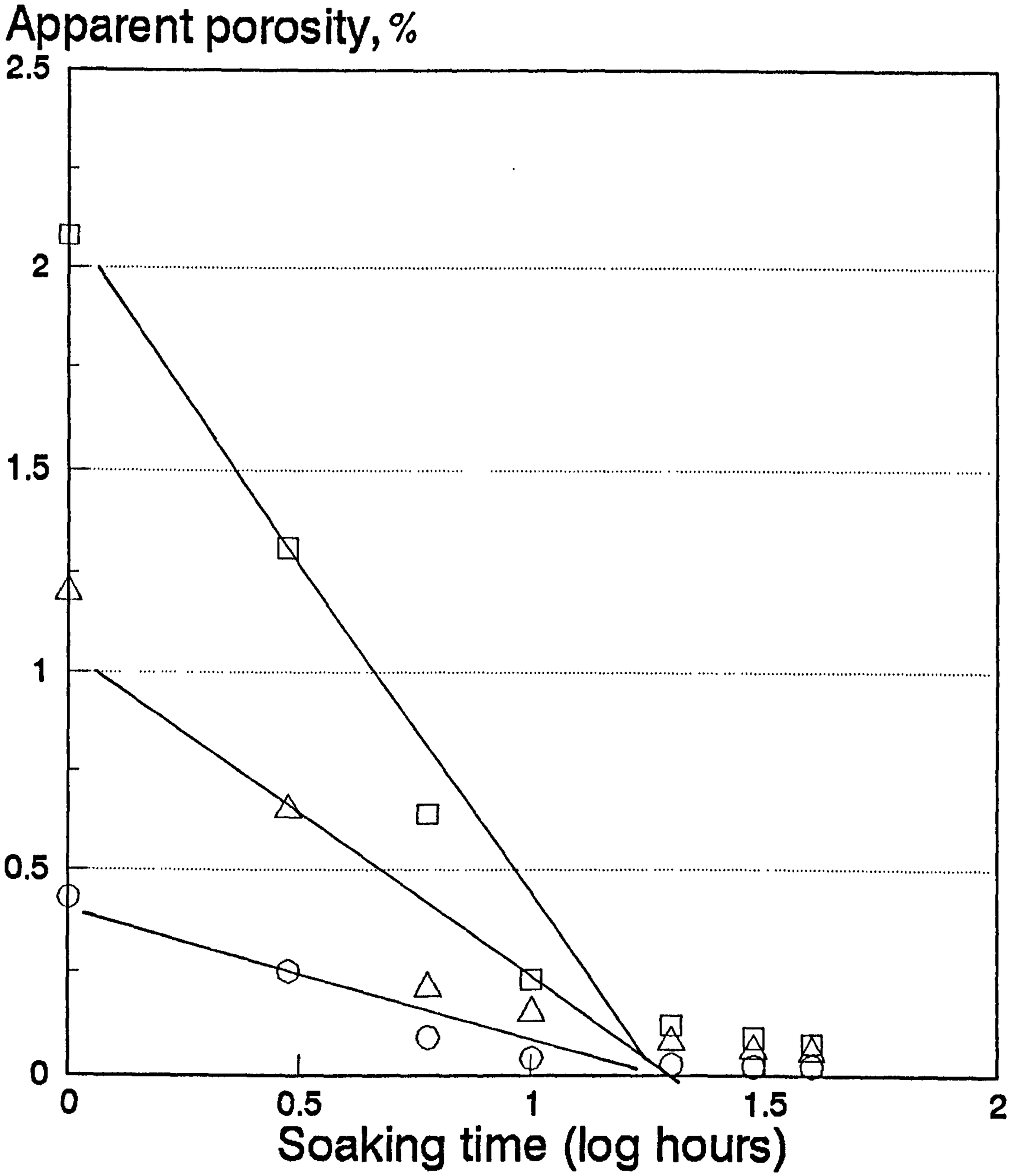

Figure 4.22 Apparent porosity as a function of log soaking time at 1150°C-1200°C for bond mixture P. (□) 1150°C, (△) 1200°C, (o) 1250°C.

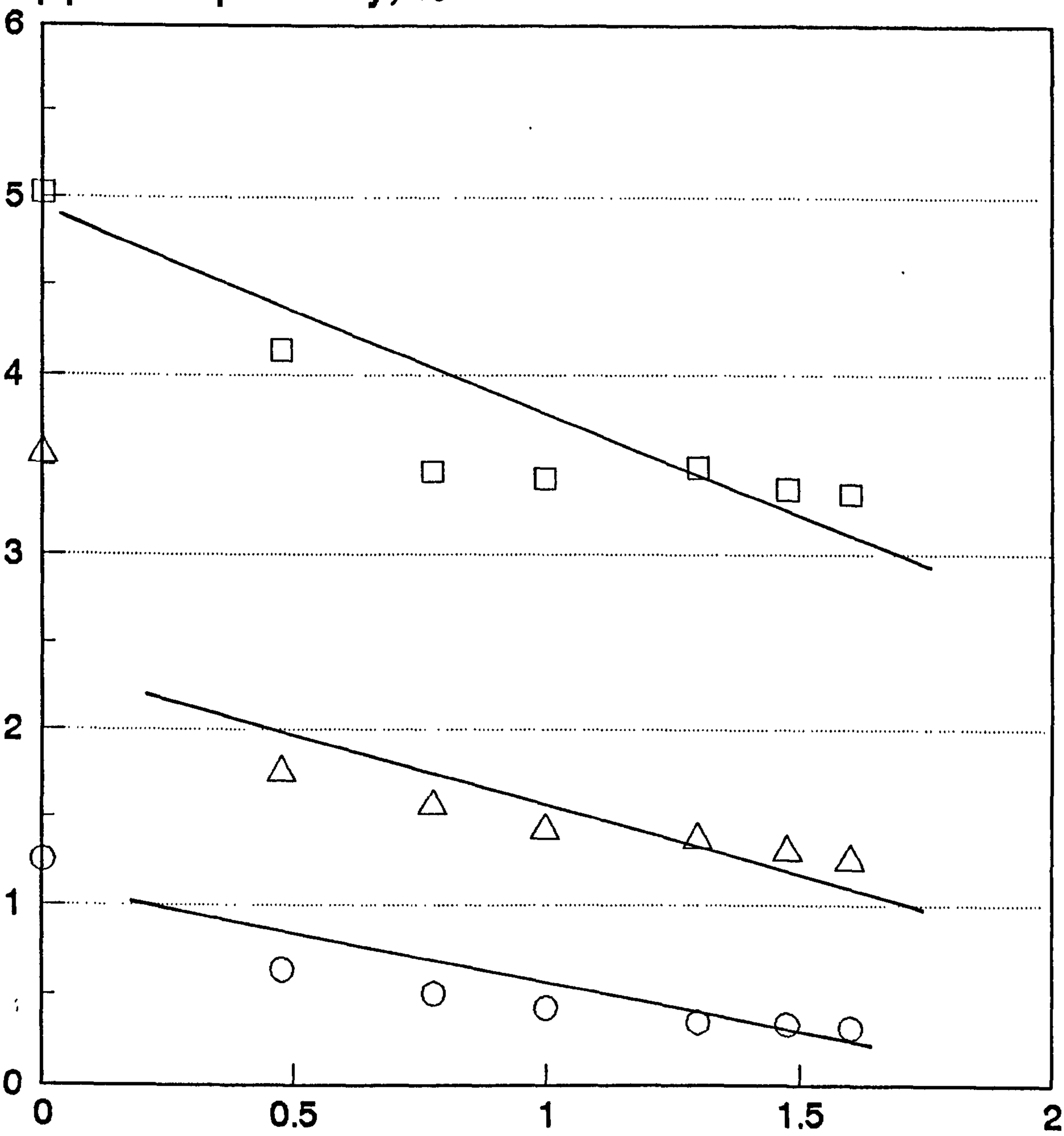

Figure 4.23 Apparent porosity as a function of log soaking time at 1150°C-1200°C for bond mixture R. (□) 1150°C, (△) 1200°C, (o) 1250°C.

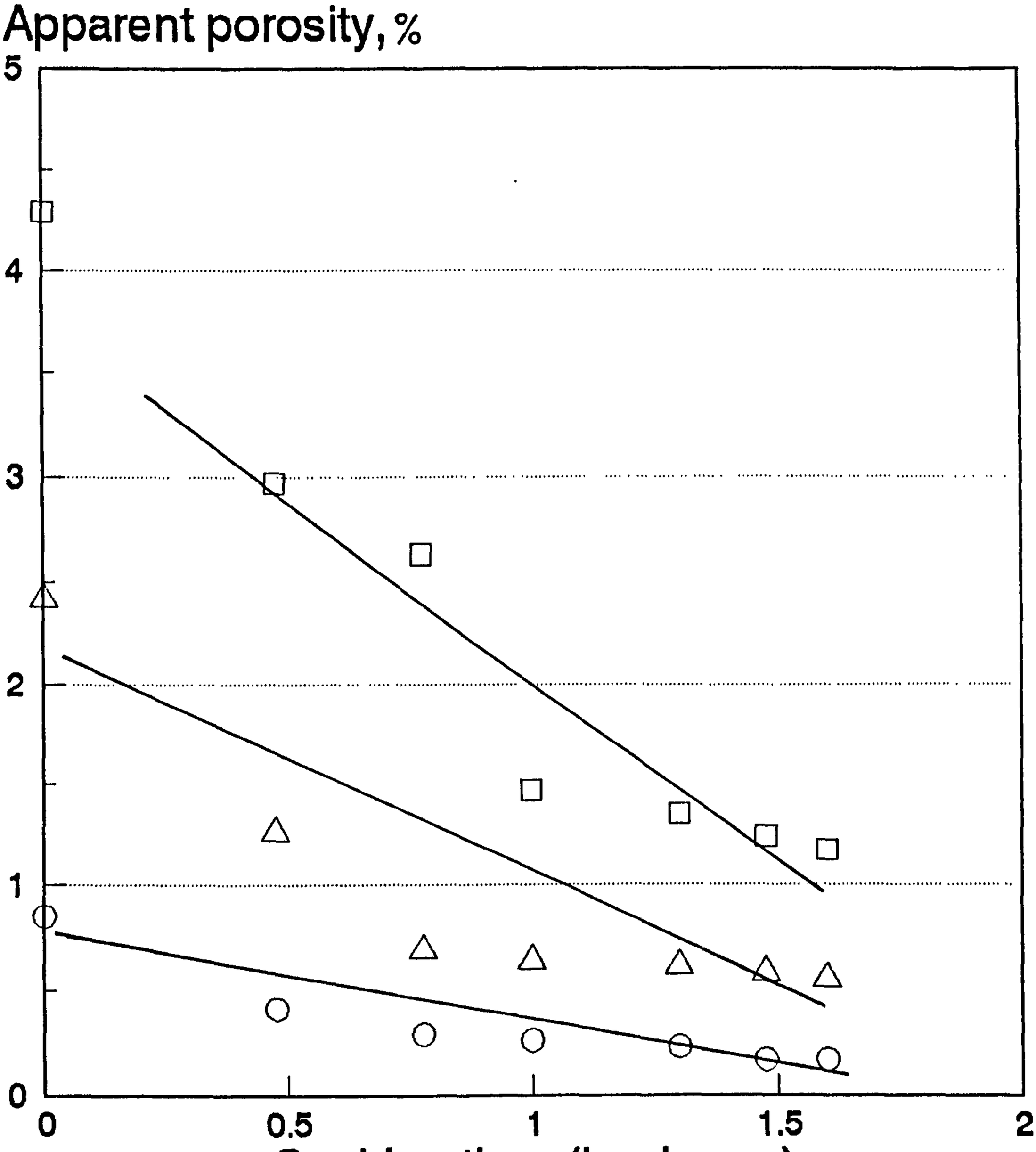

Figure 4.24 Apparent porosity as a function of log soaking time at 1150°C-1200°C for bond mixture T. (□) 1150°C, (△) 1200°C, (o) 1250°C.

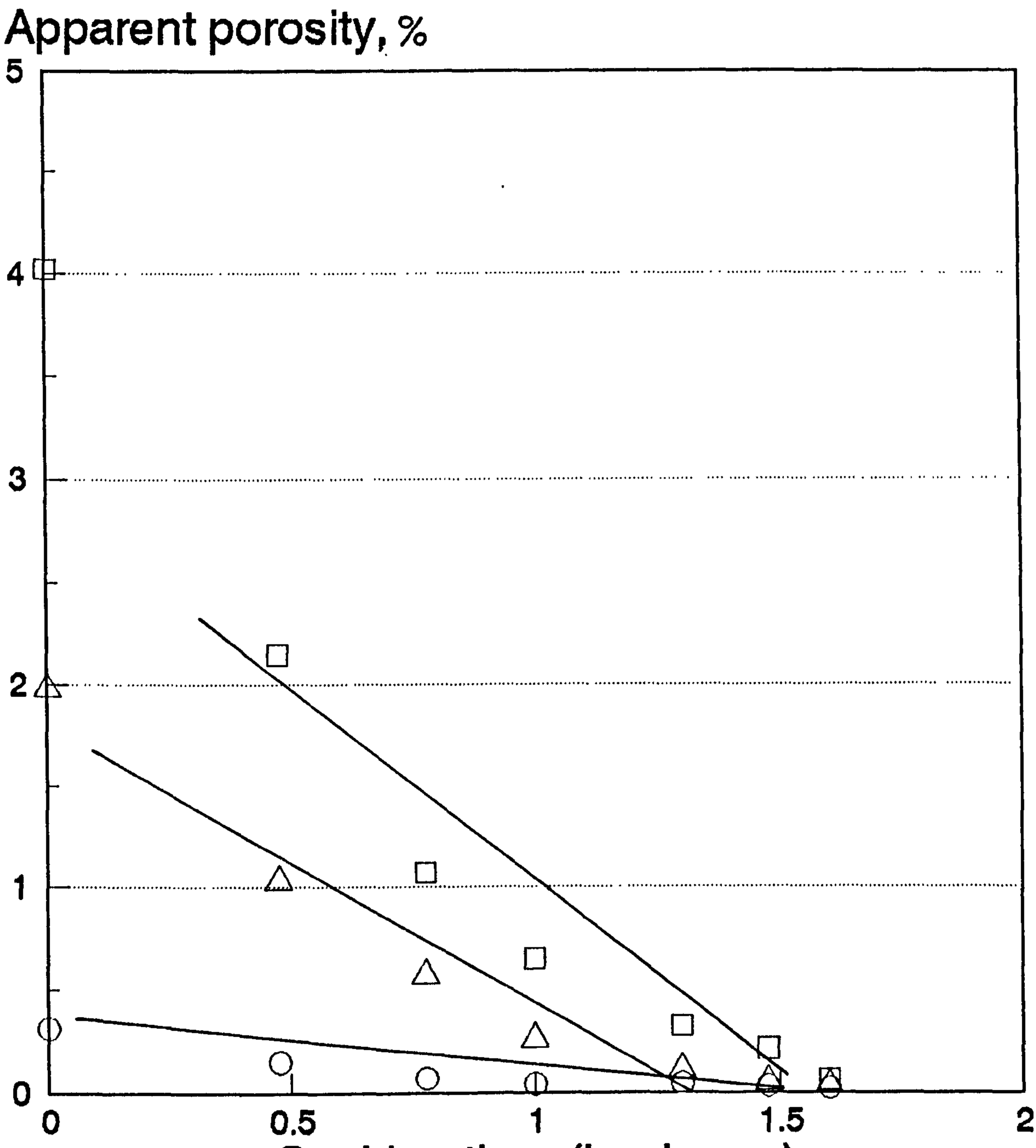

Figure 4.25 Apparent porosity as a function of log soaking time at 1150°C-1200°C for bond mixture V. (□) 1150°C, (△) 1200°C, (o) 1250°C.

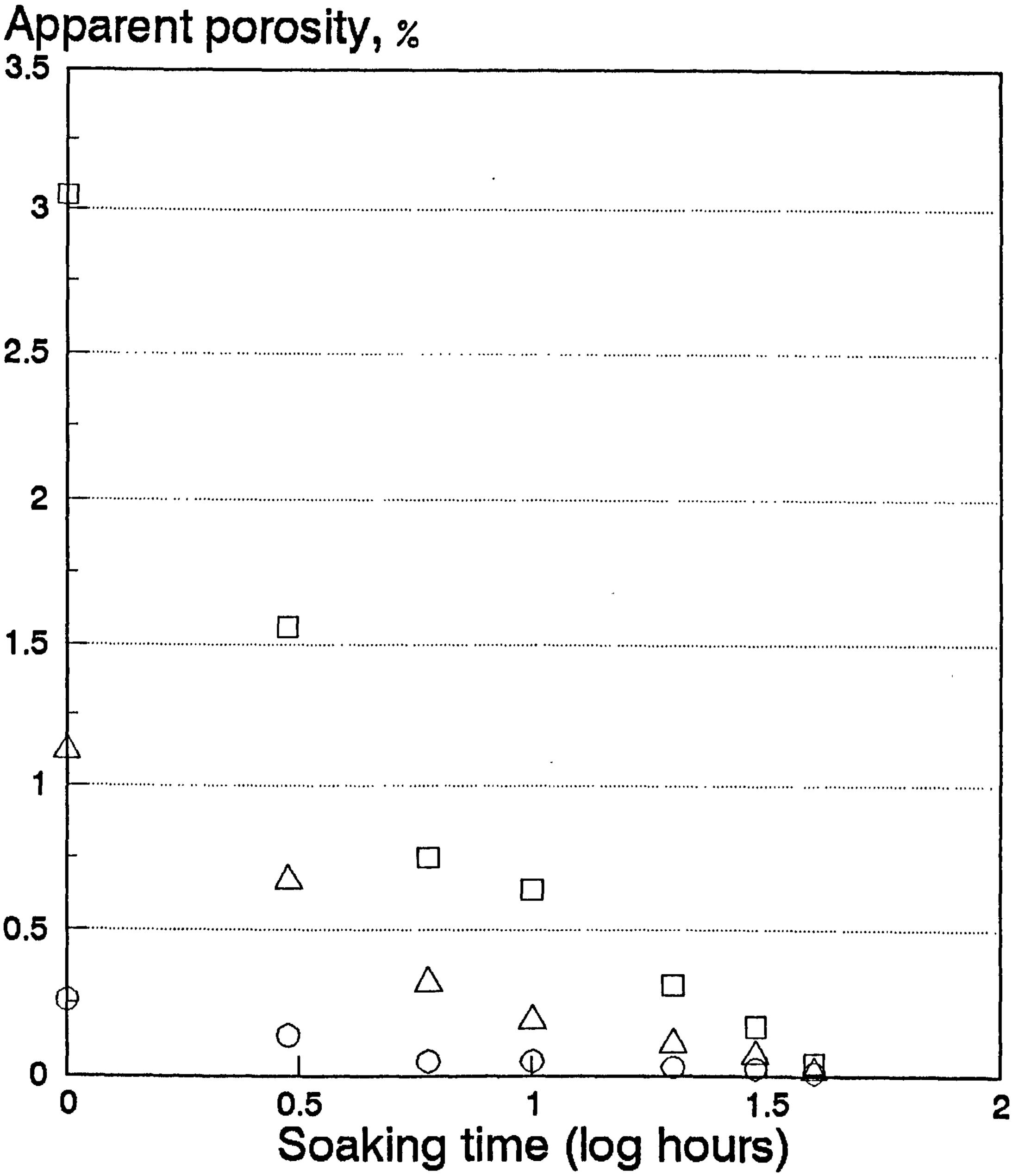

Figure 4.26 Apparent porosity as a function of log soaking time at 1150°C-1200°C for bond mixture W. (□) 1150°C, (△) 1200°C, (o) 1250°C.

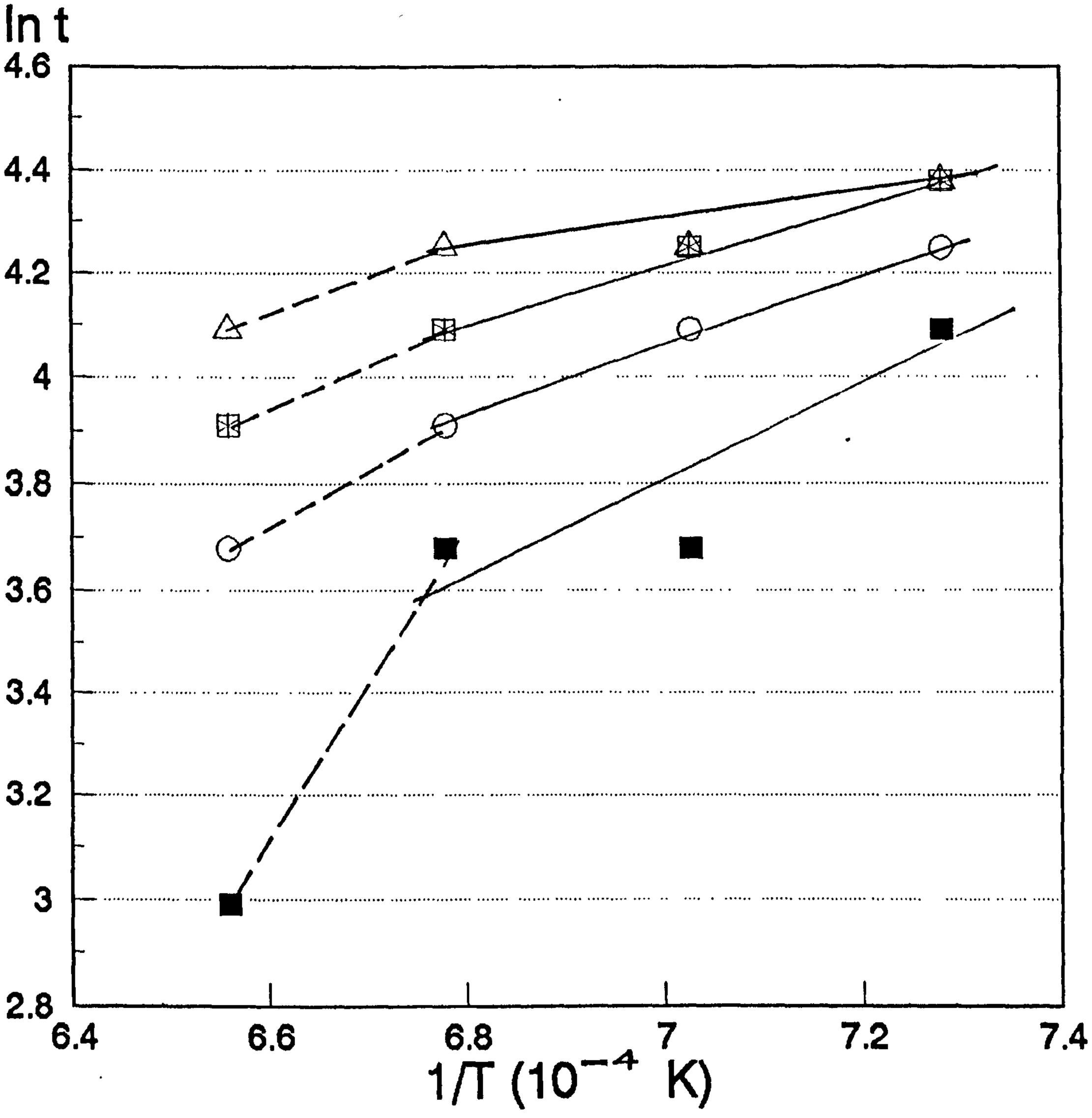

Figure 4.27a Temperature-time curves for isothermal firing of sintering wheel bond compositions (□) H, (△) J, (o) K, (✳) L and (■) N.

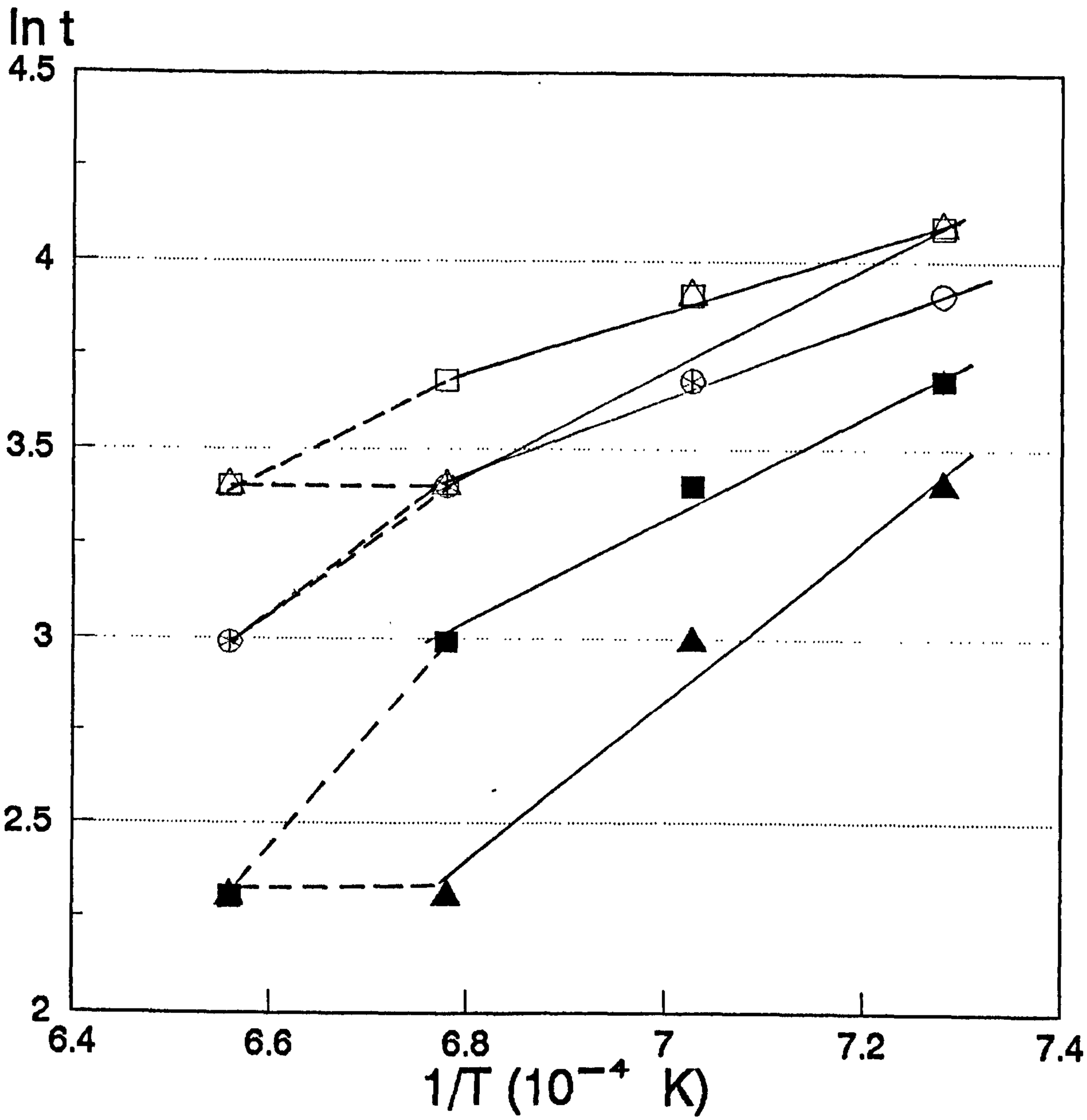

Figure 4.27b Temperature-time curves for isothermal firing of fusible wheel bond compositions (□) P, (△) R, (o) T, (✳) V, (■) W and (▲) X.

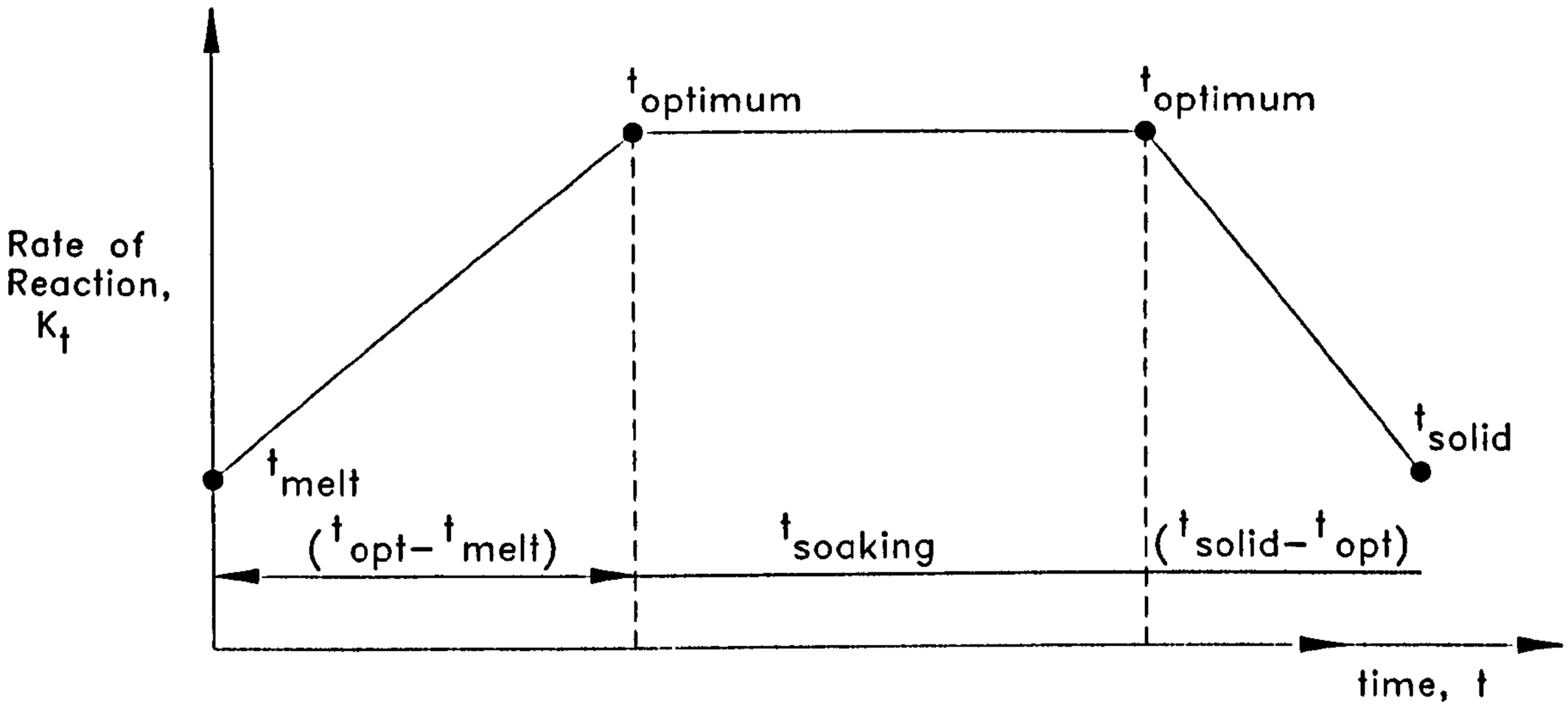

Figure 4.28 Schematic diagram of the reaction rate-time of firing dependence for grinding wheel bonds.

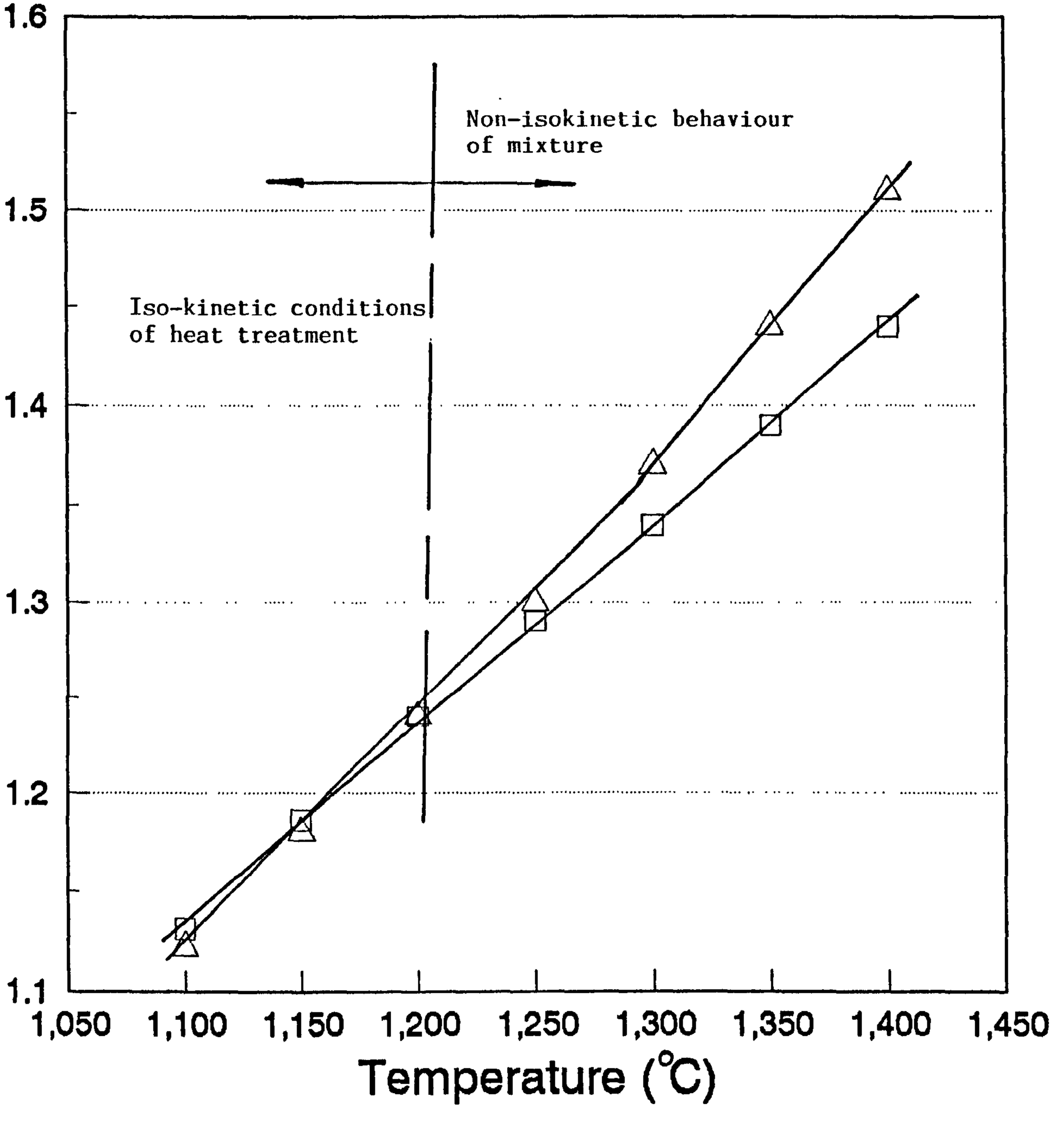

Figure 4.29a Rate of vitrification-temperature diagram bond mixture H showing theoretical and empirical data at various soaking temperatures. (□) K_t theoretical, (△) K_t empirical.

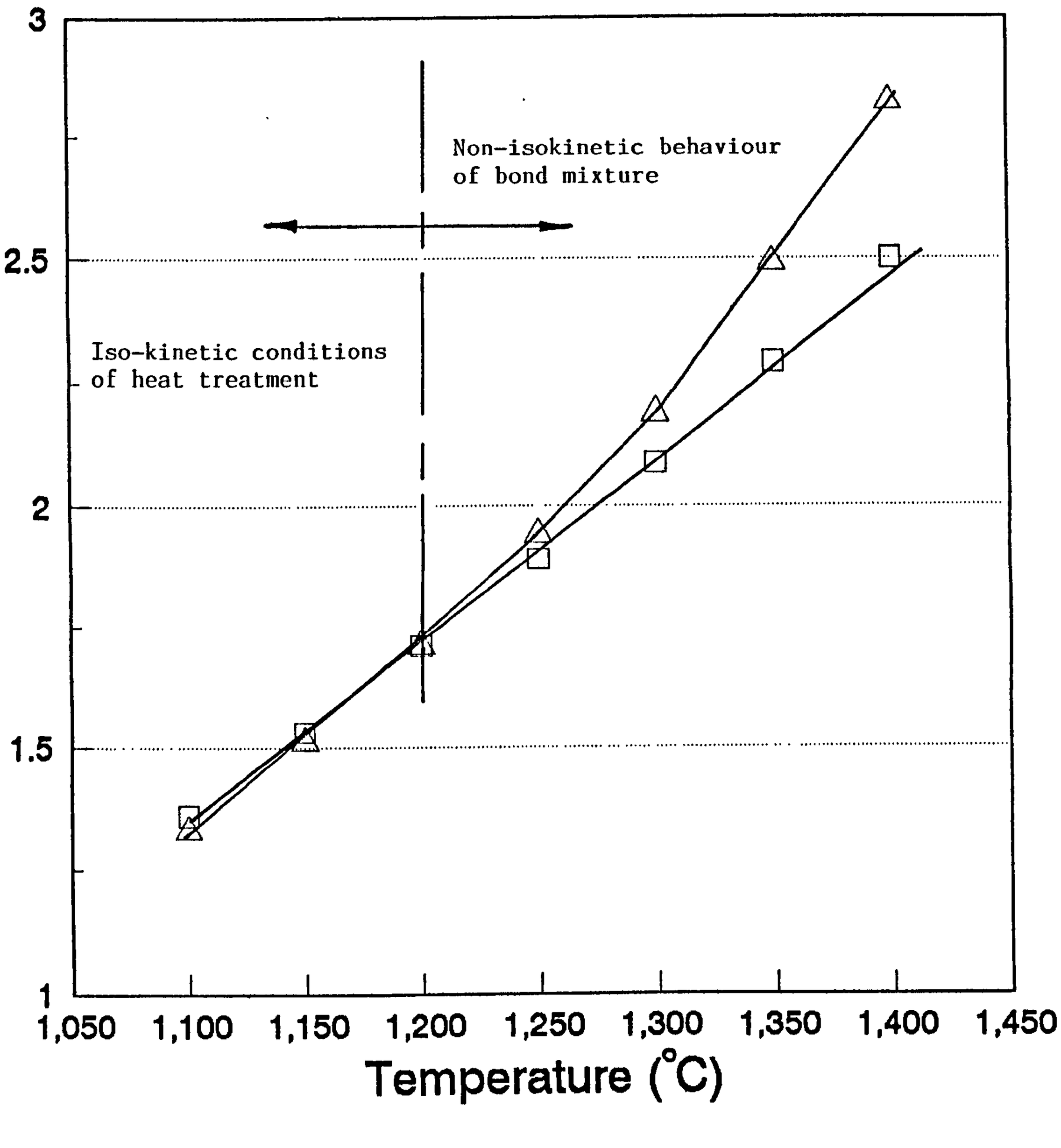

Figure 4.29b Rate of vitrification-temperature diagram for bond mixture K showing theoretical and empirical data at various soaking temperatures. (□) K_t theoretical, (△) K_t empirical.

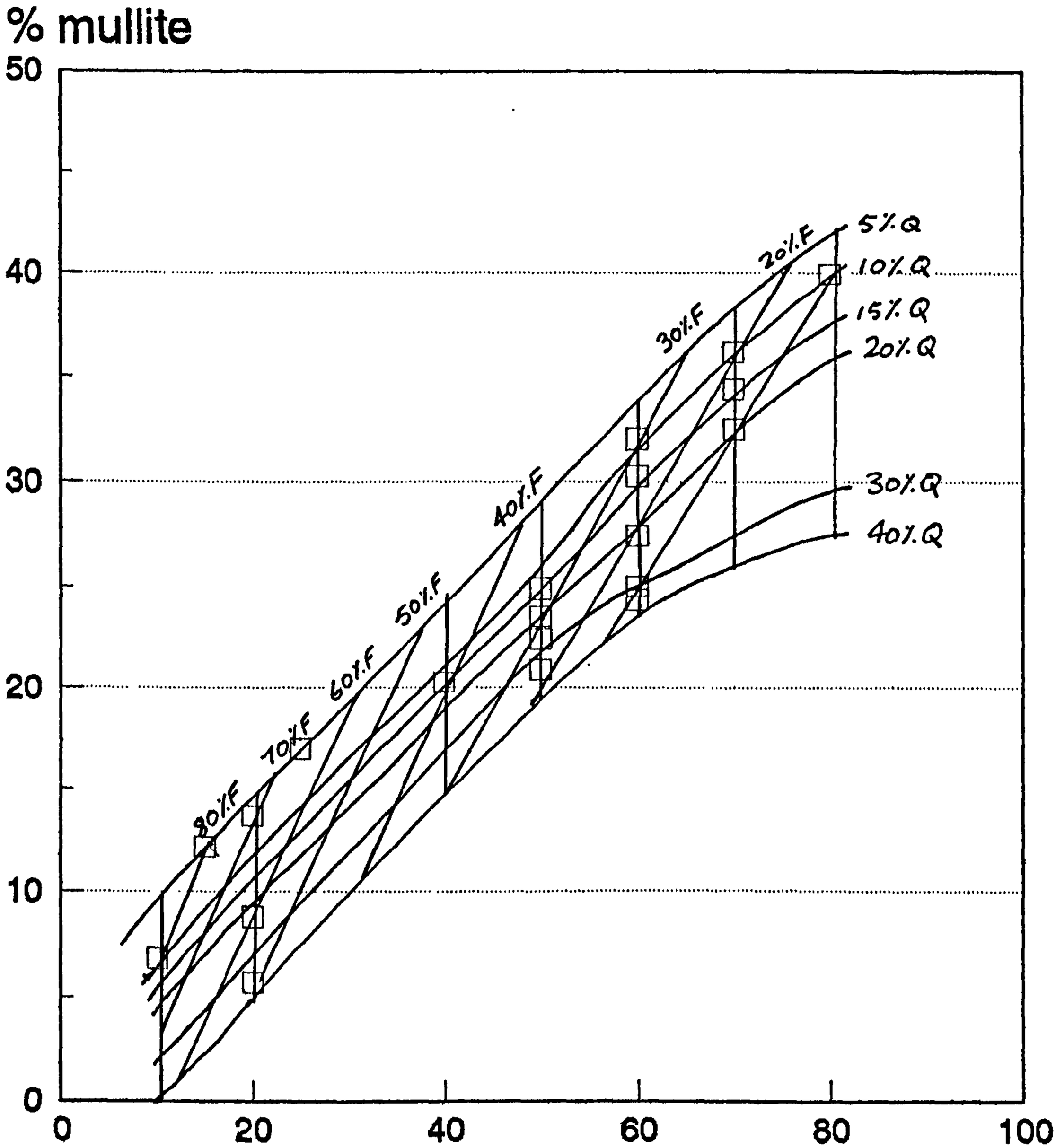

Figure 5.1 Experimentally-determined mullite content as a function of clay content for mixtures fired at 1200°C for 40 hours.

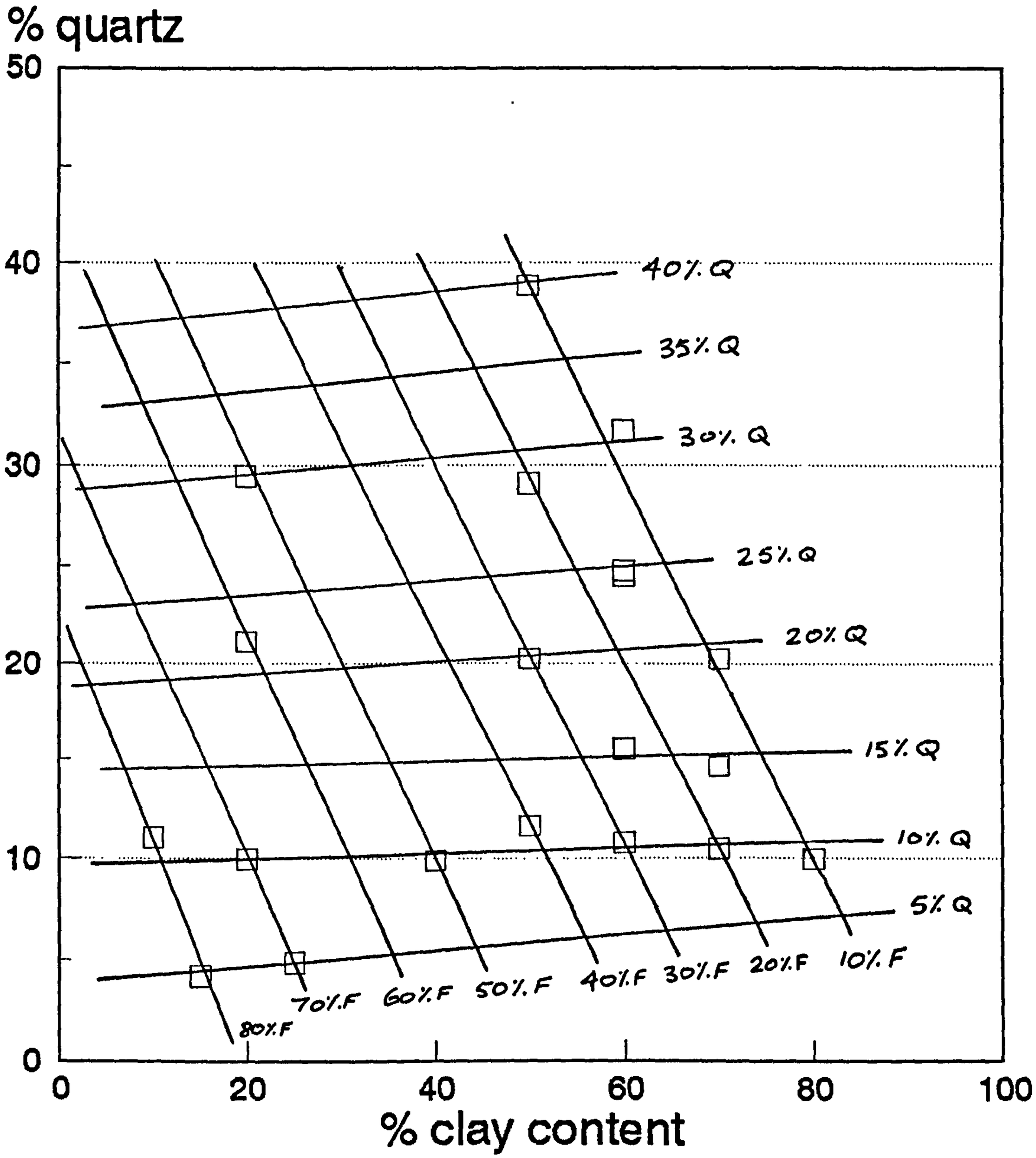

Figure 5.2 Experimentally-determined quartz content as a function of clay content for mixtures fired at 1200°C for 40 hours.

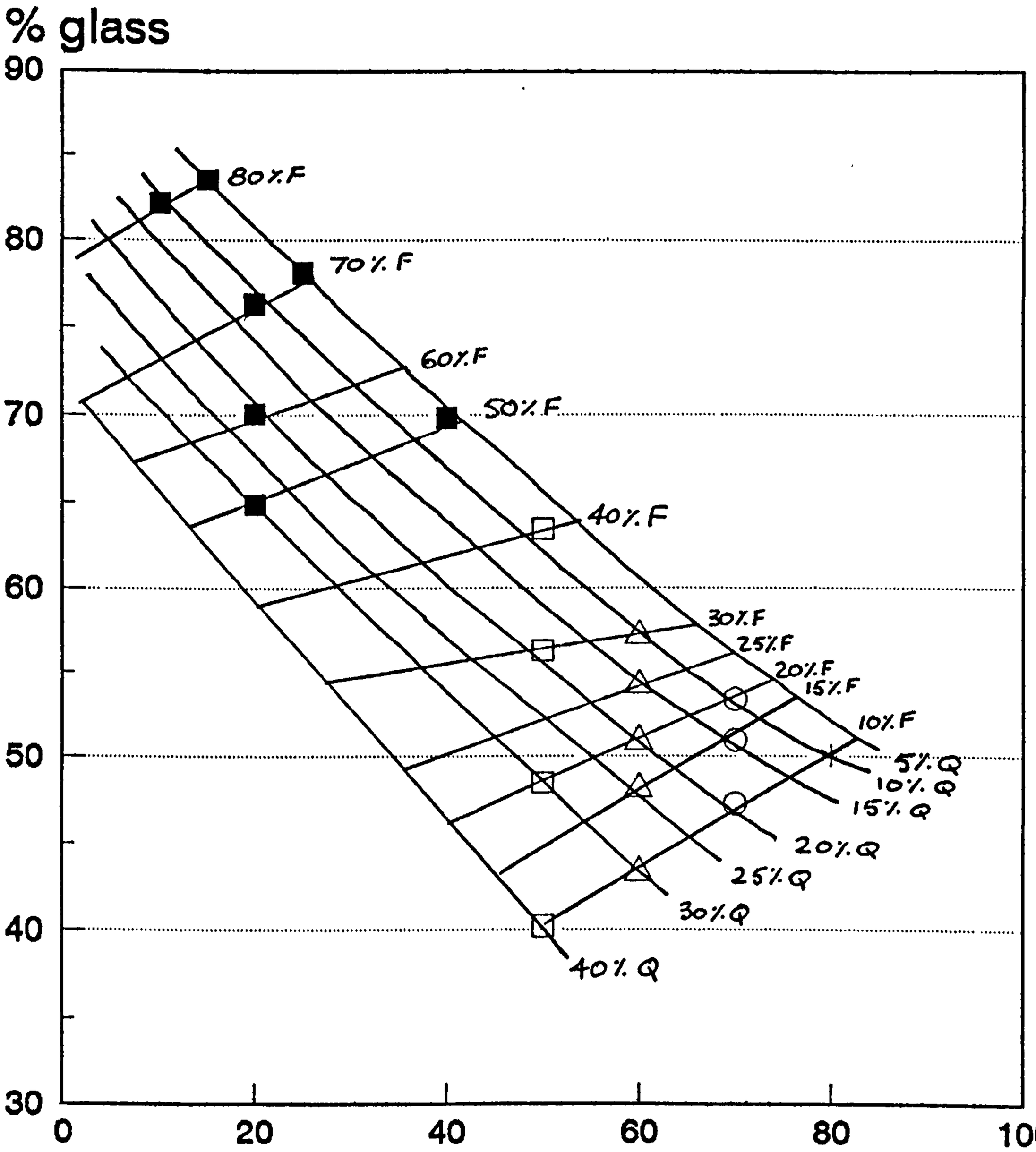

Figure 5.3 Experimentally-determined glass content as a function of clay content for mixtures fired at 1200°C for 40 hours.

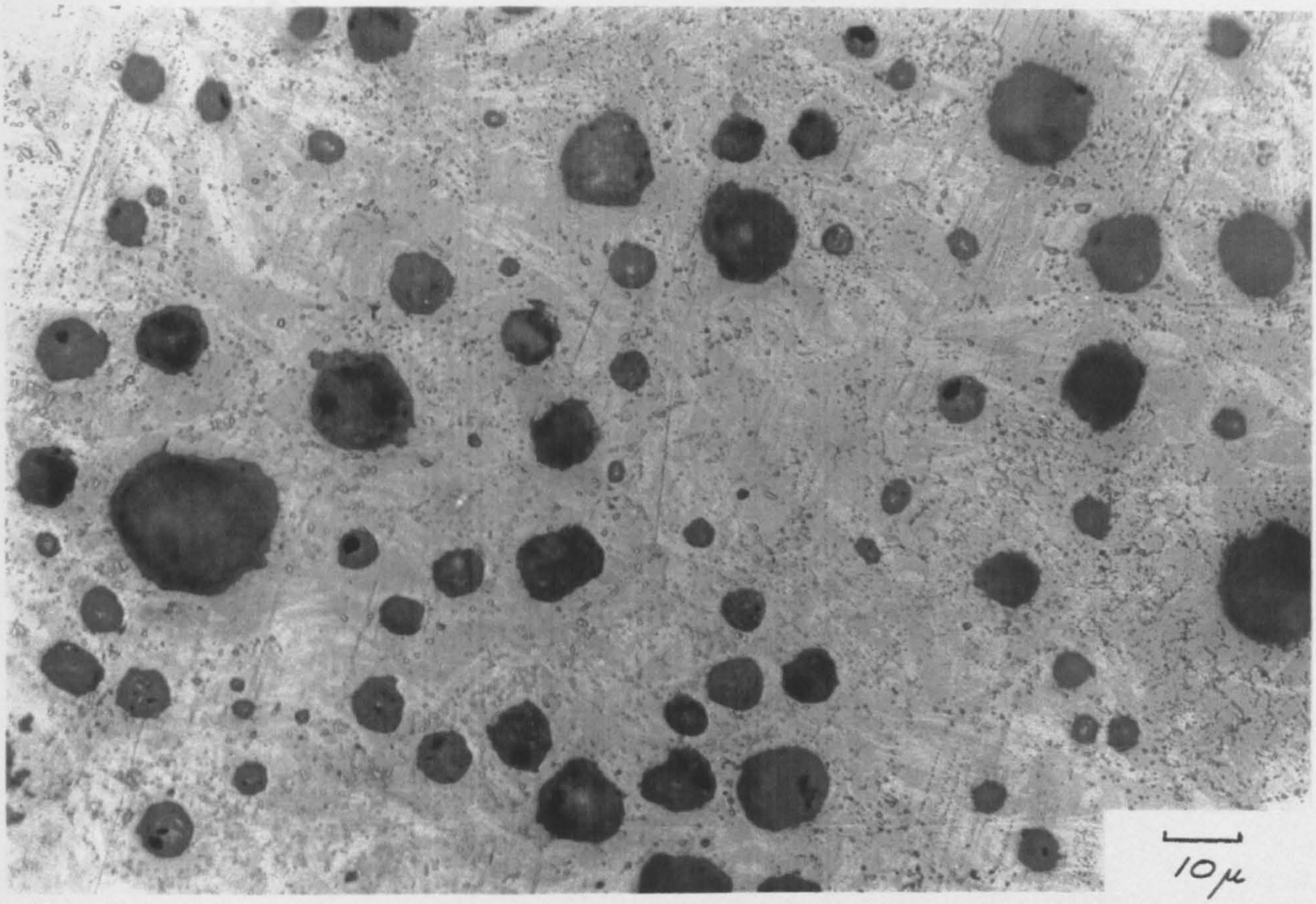

Figure 5.4 Optical micrograph of bond mixture P showing ∝-alumina (white elongated grains), glass matrix, plus a fine distribution of mullite crystals originating from the clay relicts. Black areas are pores in the structure. Etched in 10% H.F. for 10s.

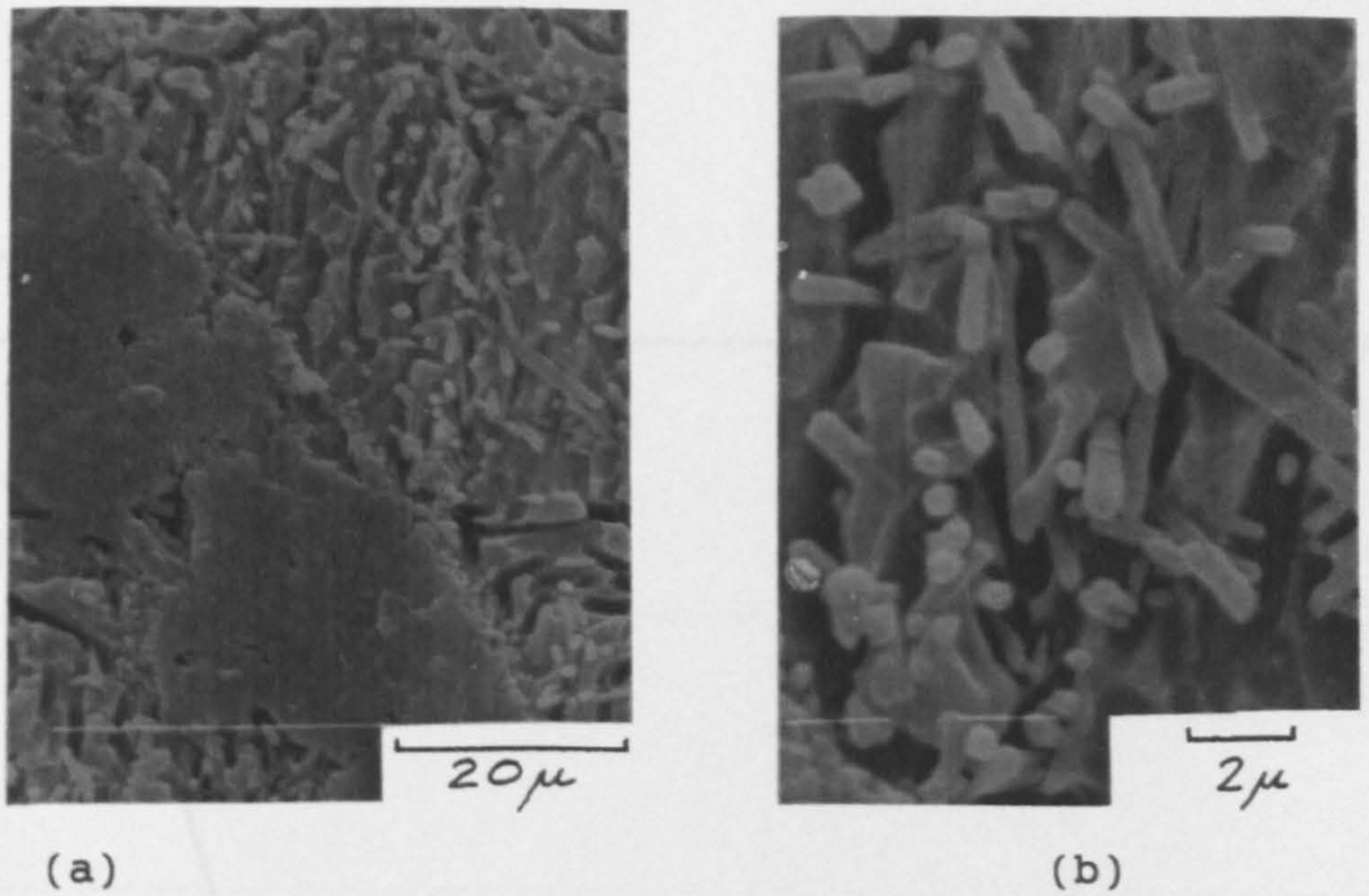

(a) (b)

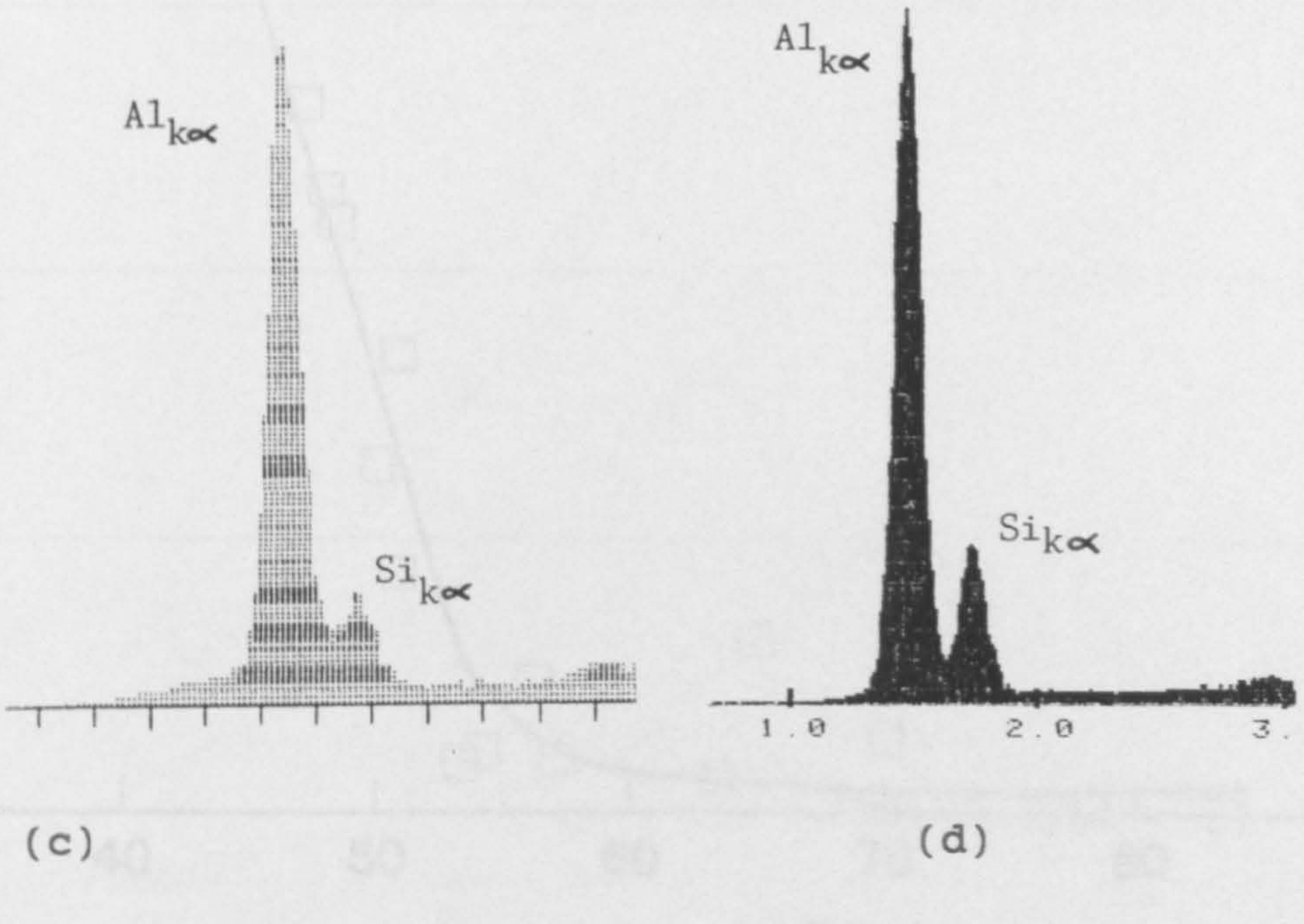

(c) (d)

Figure 5.5 Secondary electron image of etched bond sample (bond mixture P). (a) primary and secondary mullite formations; (b) magnified view of secondary mullite (re-crystallised from the melt); (c) electron probe microanalysis of primary mullite phases showing normalised % wt for Al and Si (81.34% wt and 18.66% wt respectively); (d) electron probe microanalysis of the secondary mullite phase showing normalised % wt of Al and Si (67.22% wt and 32.78% wt respectively).

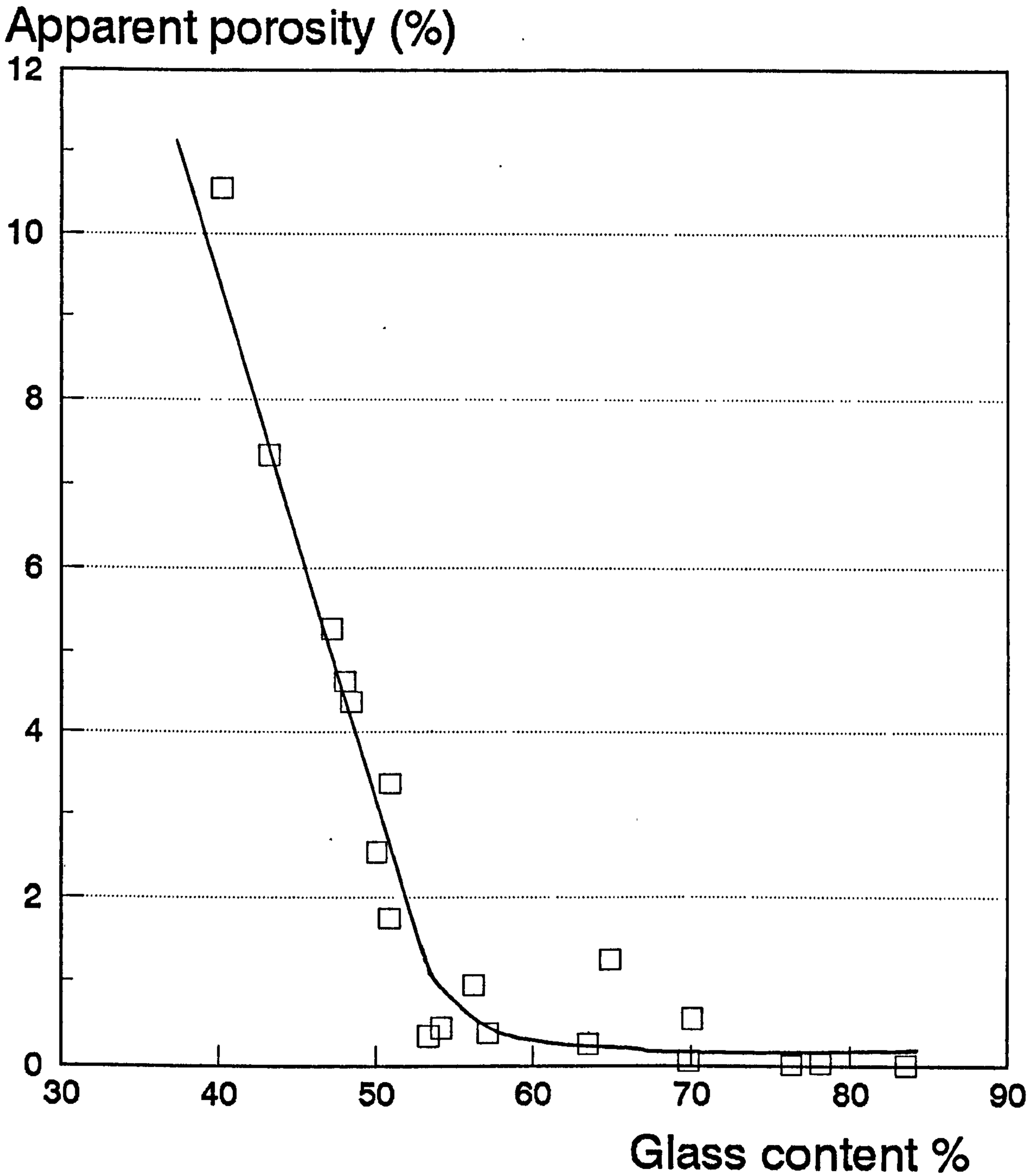

Figure 5.6 Apparent porosity data as a function of x-ray determined glass content for bond mixtures fired at 1200°C for 40 hours.

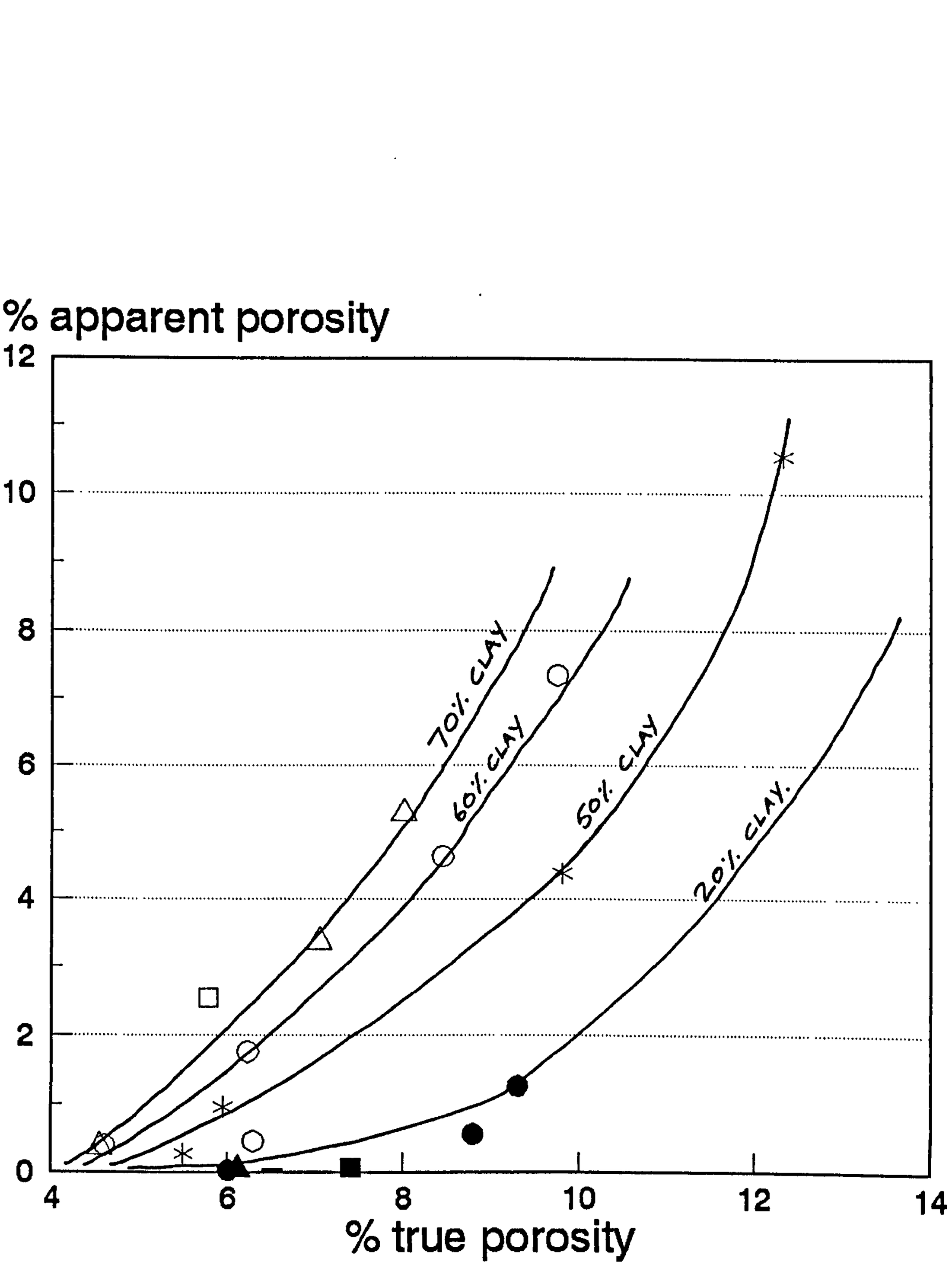

Figure 5.7 Apparent porosity as a function of true porosity and clay content . Note: (□) 80% clay; (△) 70% clay; (o) 60% clay; (*) 50% clay; (■) 40% clay; (▲) clay; (●) 20% clay; (—) 15% clay.

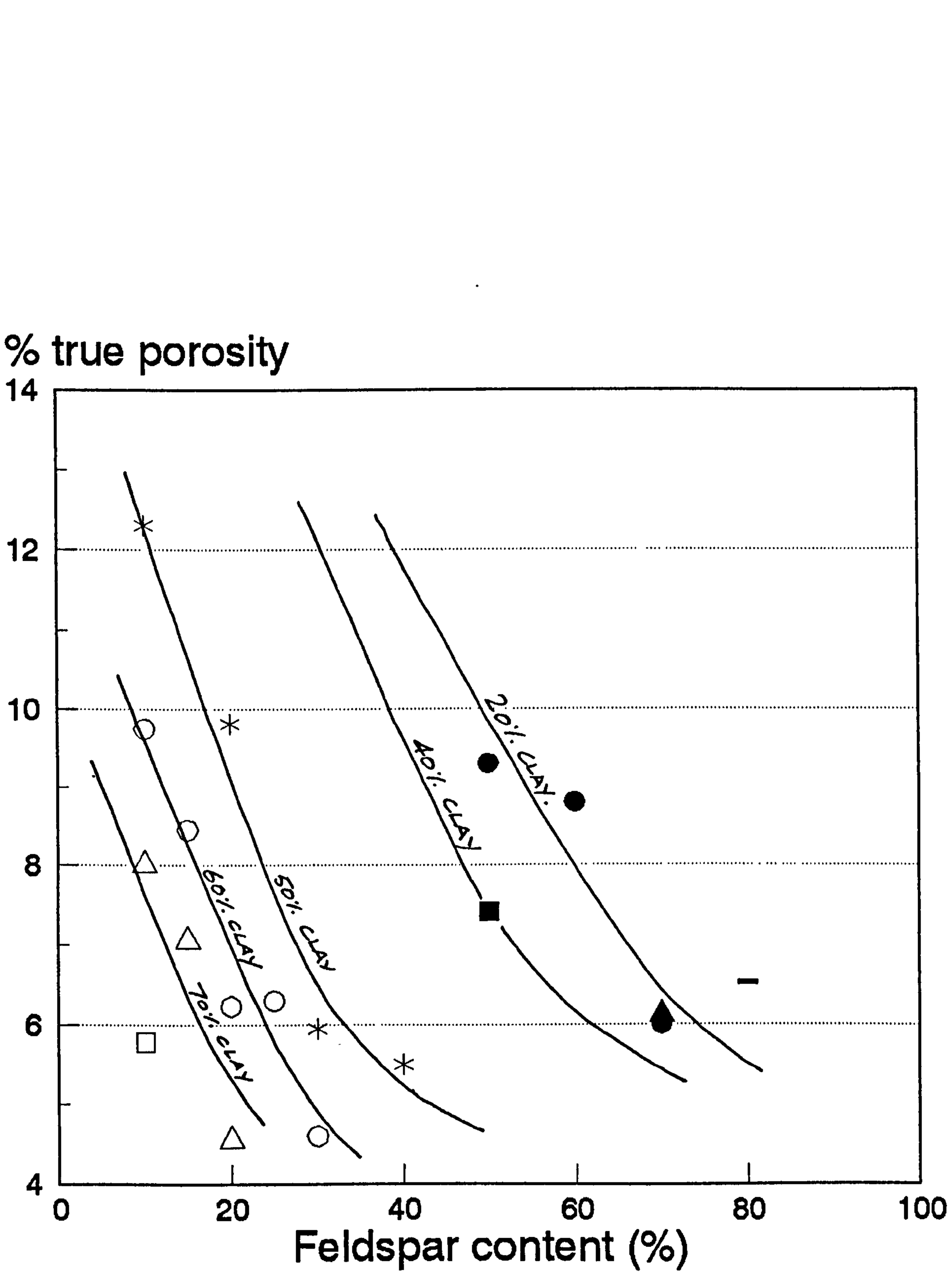

Figure 5.8 The effect of feldspar content on the true porosity of samples fired at 1200°C for 40 hours as a function of clay content. Note: (□) 80% clay; (△) 70% clay; (o) 60% clay; (*) 50% clay; (■) 40% clay; (▲) 25% clay; (●) 20% clay; (▬) 15% clay.

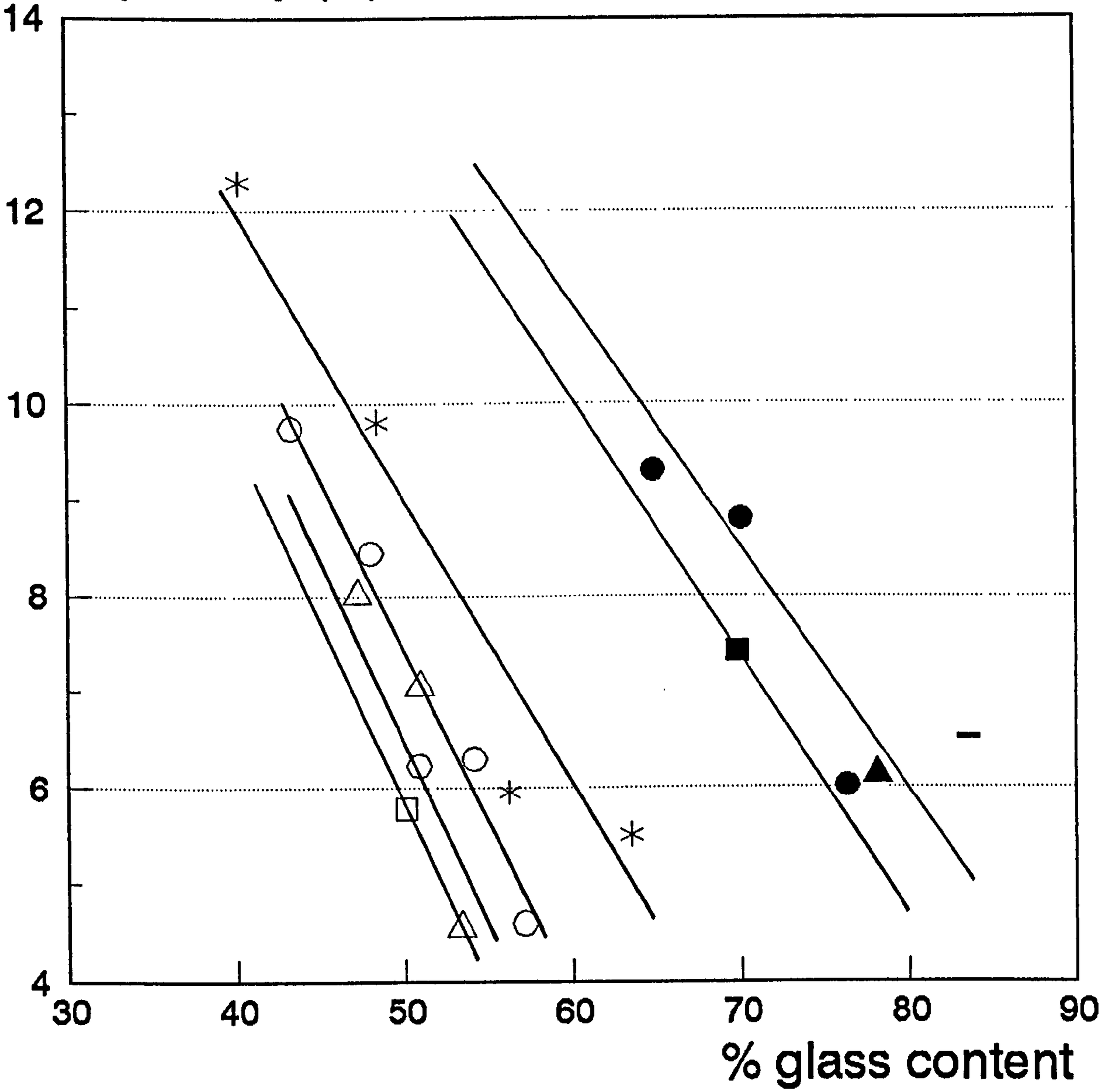

Figure 5.9 Effect of experimentally-determined glass content on the level of true porosity in bond samples fired at 1200°C for 40 hours. Note: (□) 80% clay; (△) 70% clay; (o) 60% clay; (*) 50% clay; (■) 40% clay; (▲) 25% clay; (●) 20% clay; (▬) 15% clay.

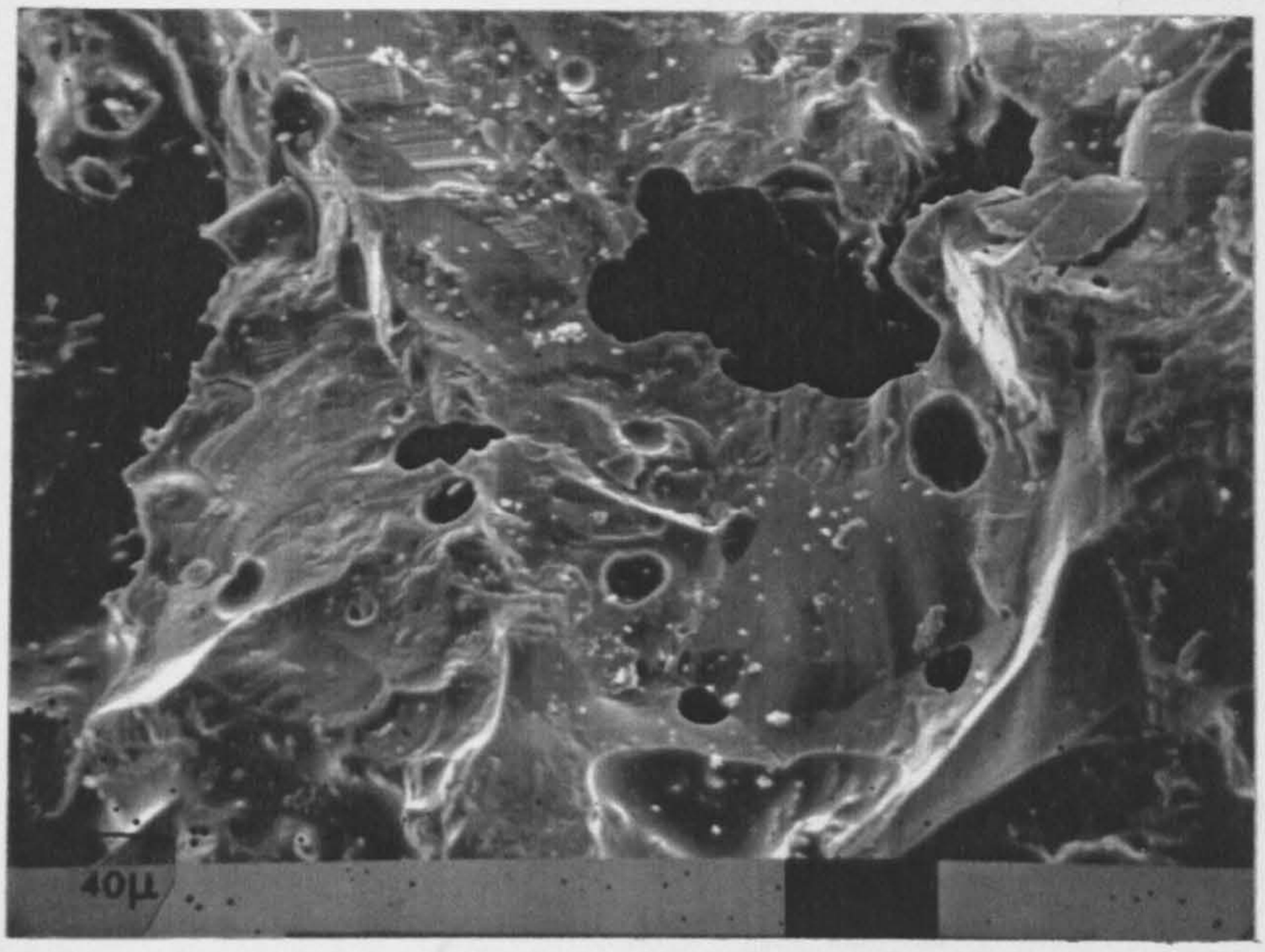

Figure 5.10 Secondary electron image of a grinding wheel containing bond mixture X (15% wt. clay/80%wt. flux/5% wt. quartz) showing large closed pores on the fracture face. The post-fired composition of the bond is 83.56% wt. glass, 12.2% wt. mullite, and 4.24% wt. quartz.

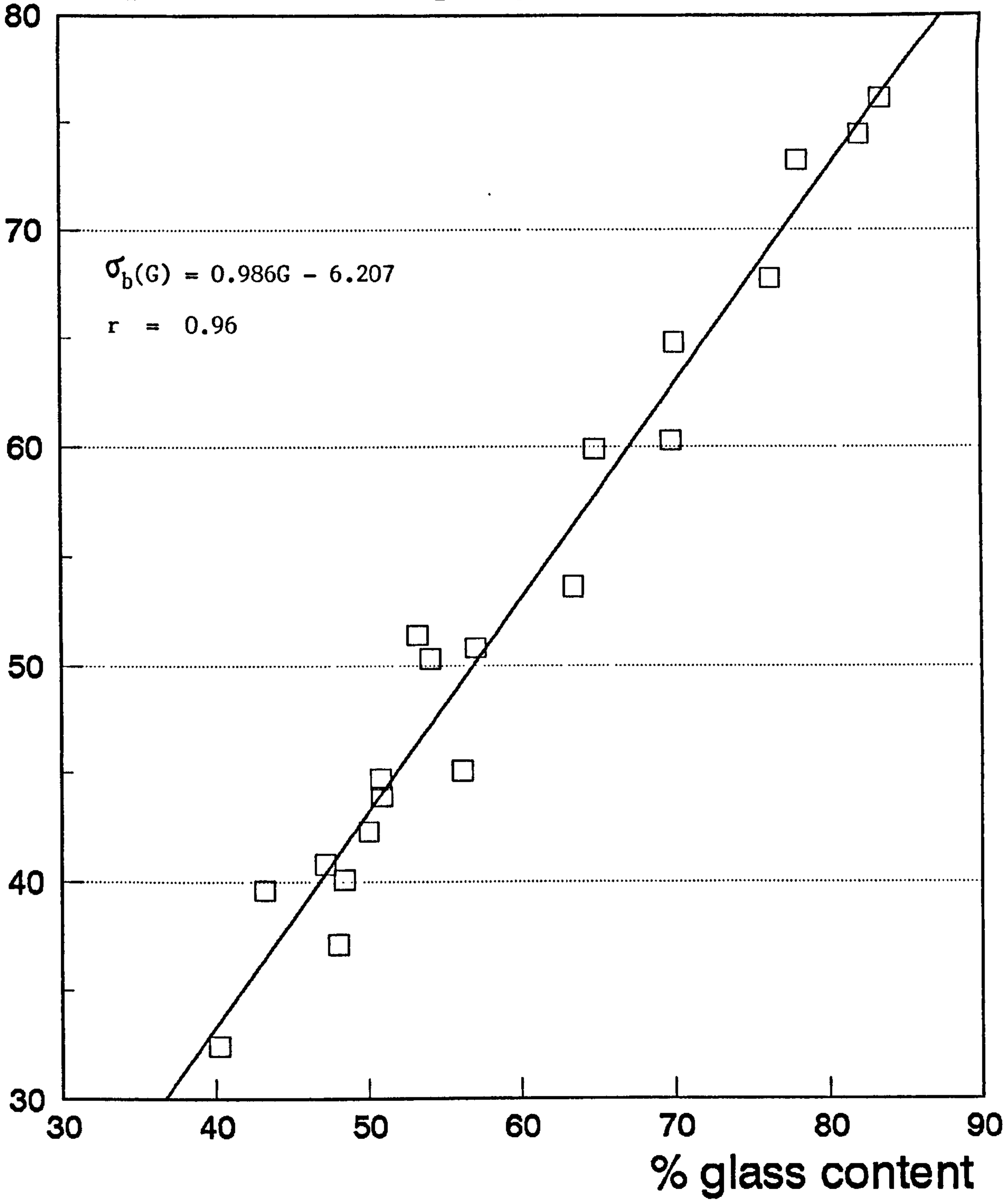

Figure 5.11 Average flexure strength of test pieces fired at 1200°C for 40 hours as a function of glass content.

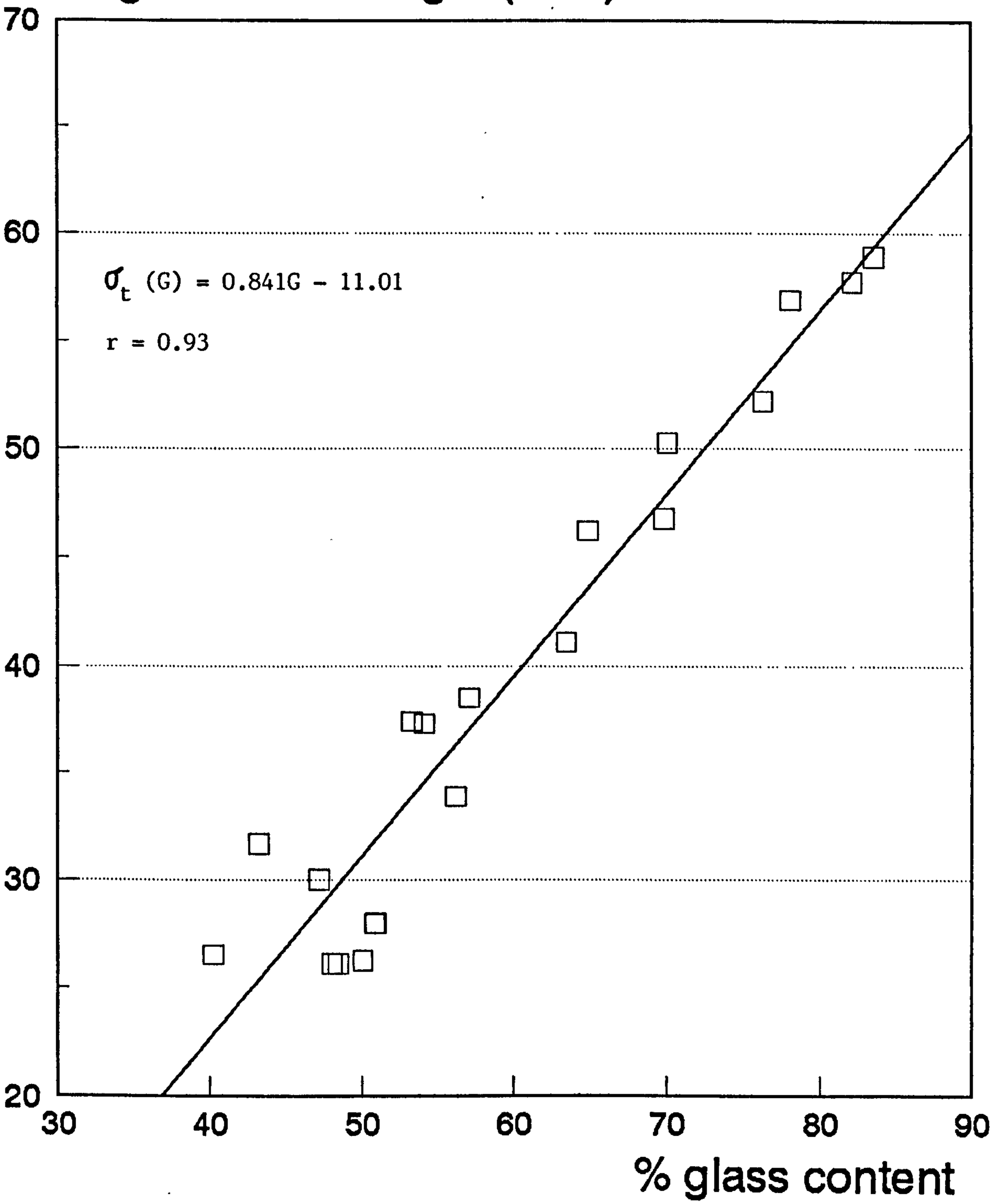

Figure 5.12 Average tensile strength of test pieces as a function of glass content. The strength of the test pieces has been calculated considering the difference in stress field distribution in geometrically-similar test bars.

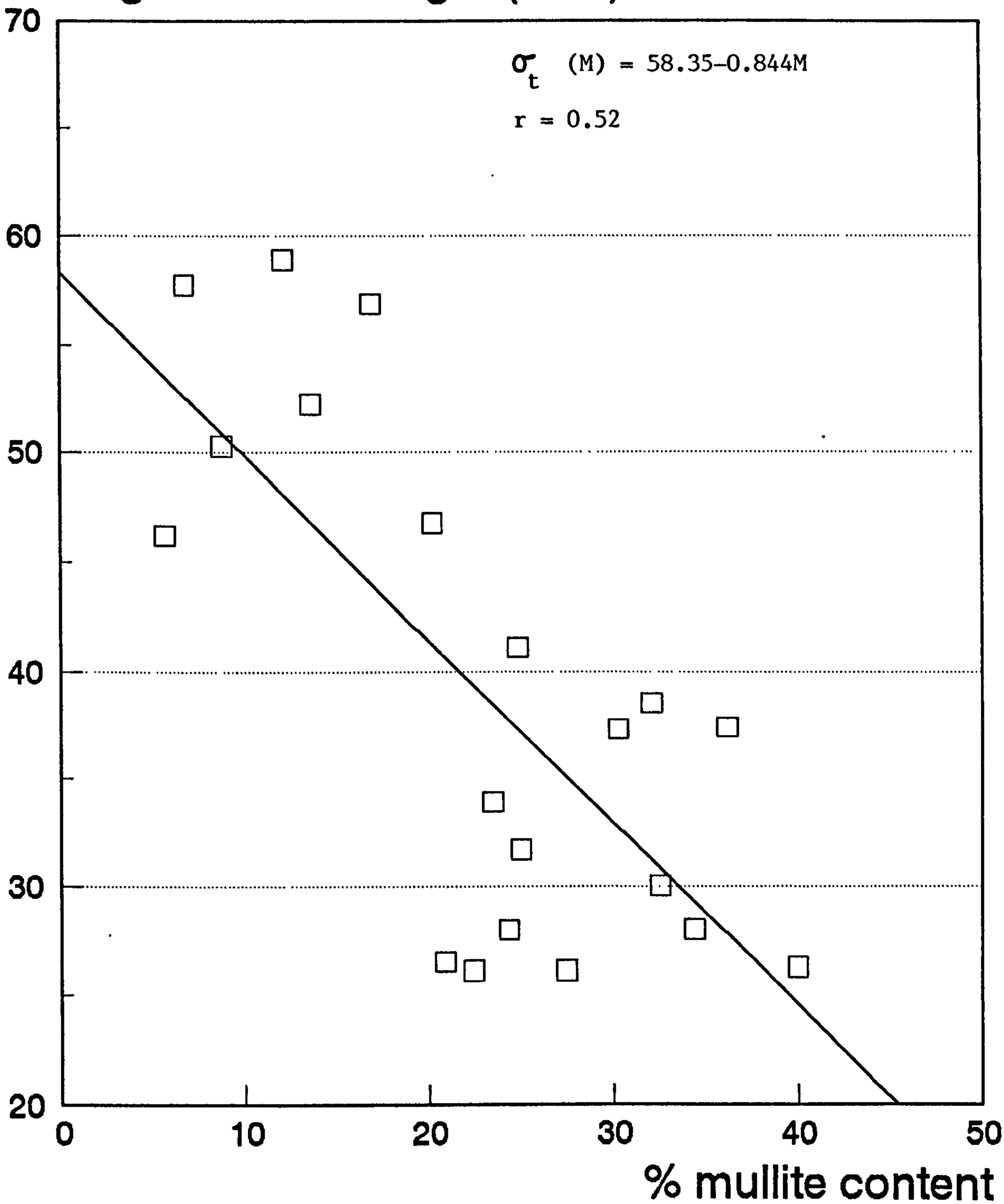

Figure 5.13 Average tensile strength of bond specimens asa function of mullite content fired at 1200°C for 40 hours.

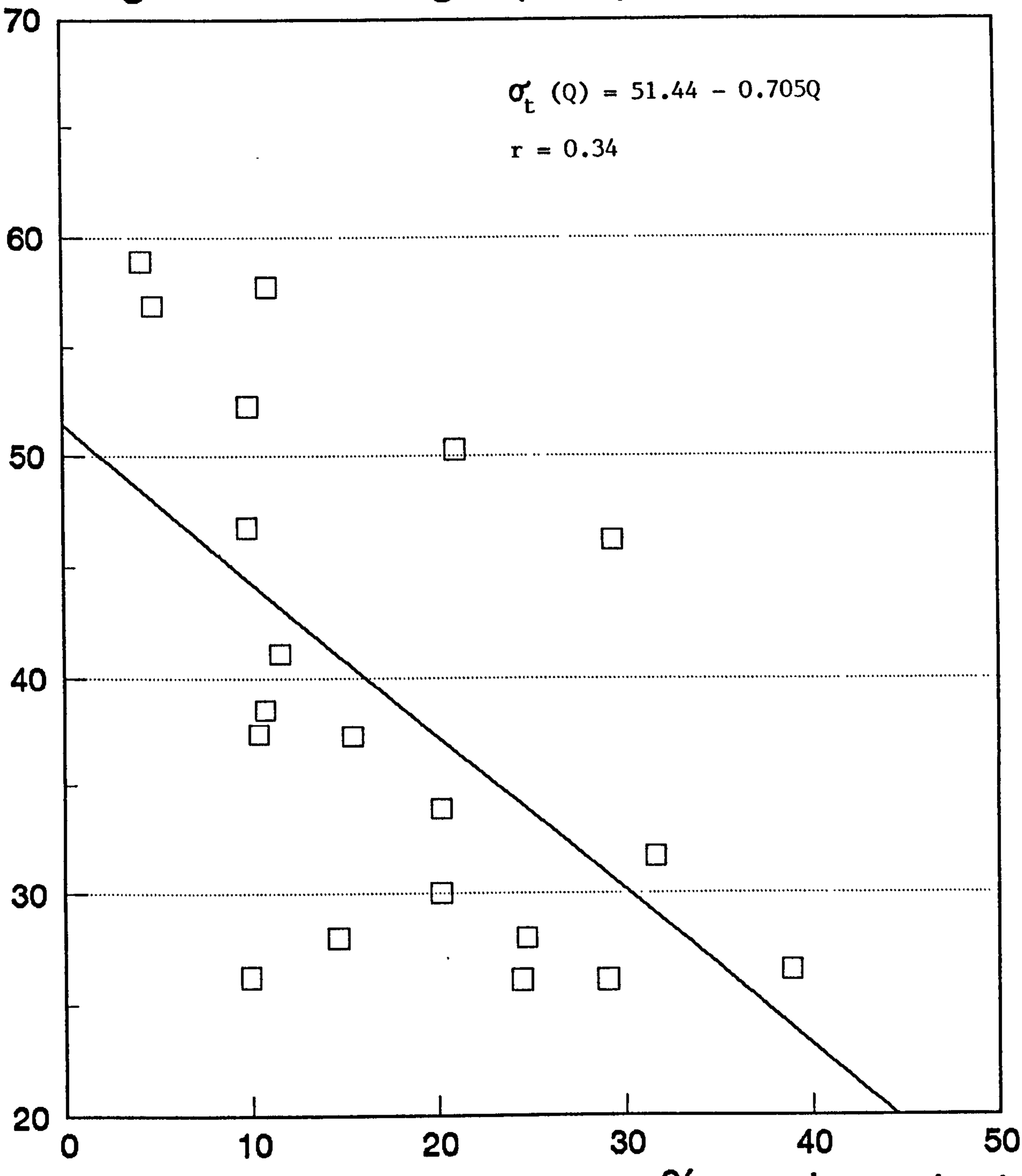

Figure 5.14 Average tensile strength of bond specimens as a function of quartz content.

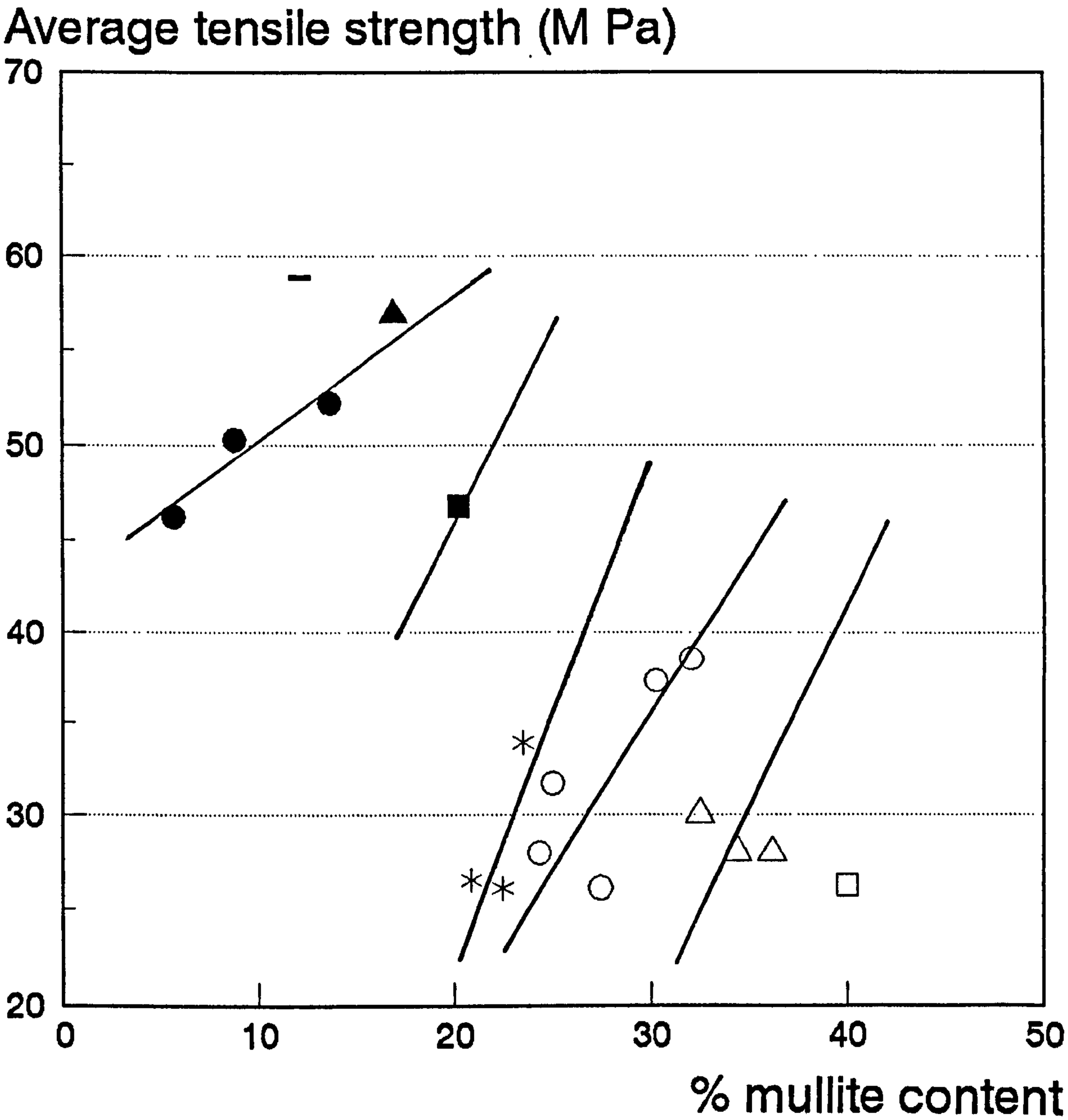

Figure 5.15 Effect of x-ray determined mullite content on average tensile strength of bond mixtures as a function of clay content. Note: (□) 80% clay; (△) 70% clay; (o) 60% clay; (*) 50 % clay; (■) 40% clay; (▲) 25% clay; (●) 20% clay; (▬) 15% clay.

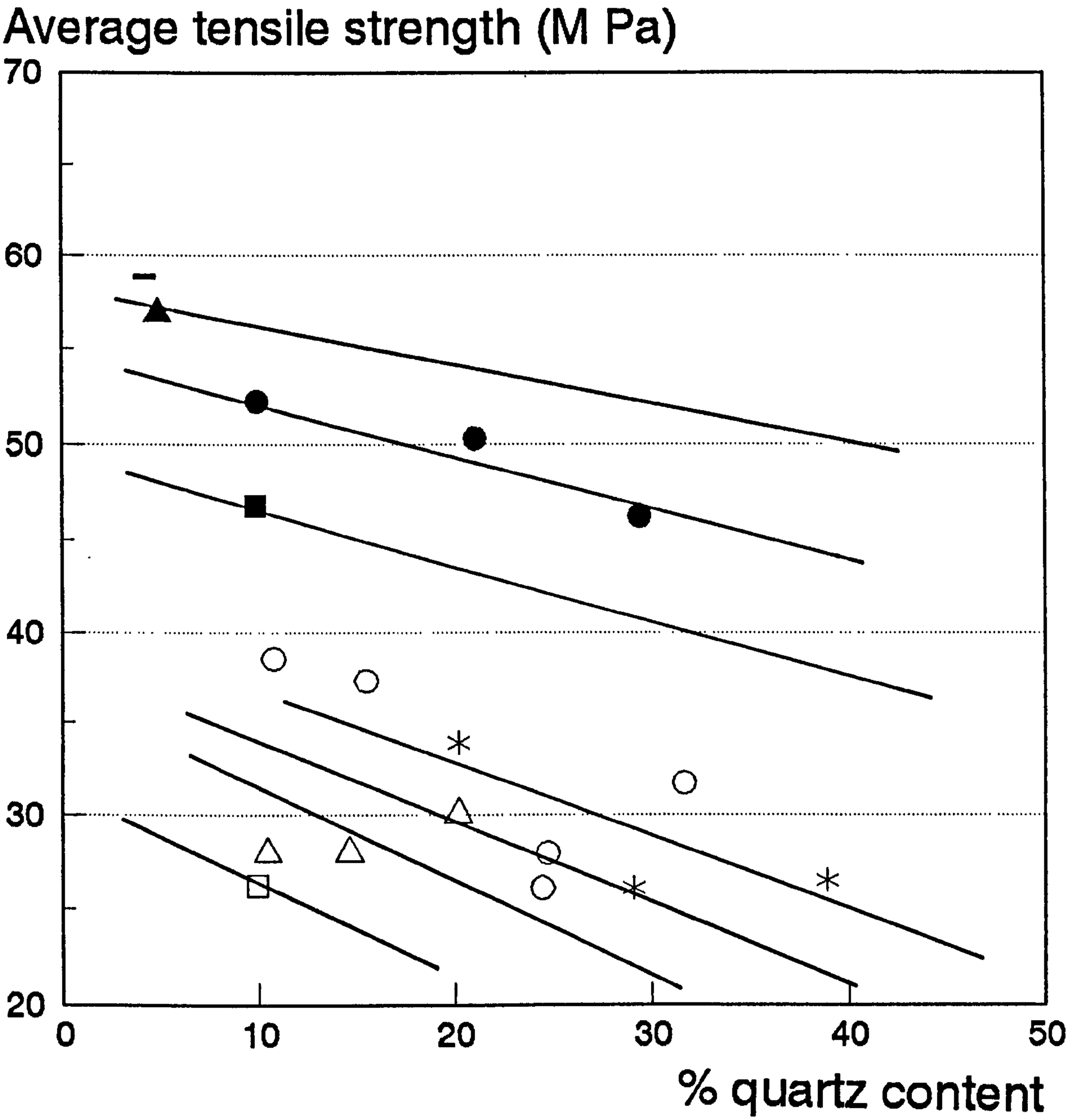

Figure 5.16 Effect of x-ray determined quartz content on the average tensile strength of bond mixtures as a function of clay content. Note: (□) 80% clay; (△) 70% clay; (o) 60% clay; (*) 50% clay; (■) 40% clay; (▲) 25% clay; (●) 20% clay; (▬) 15% clay.

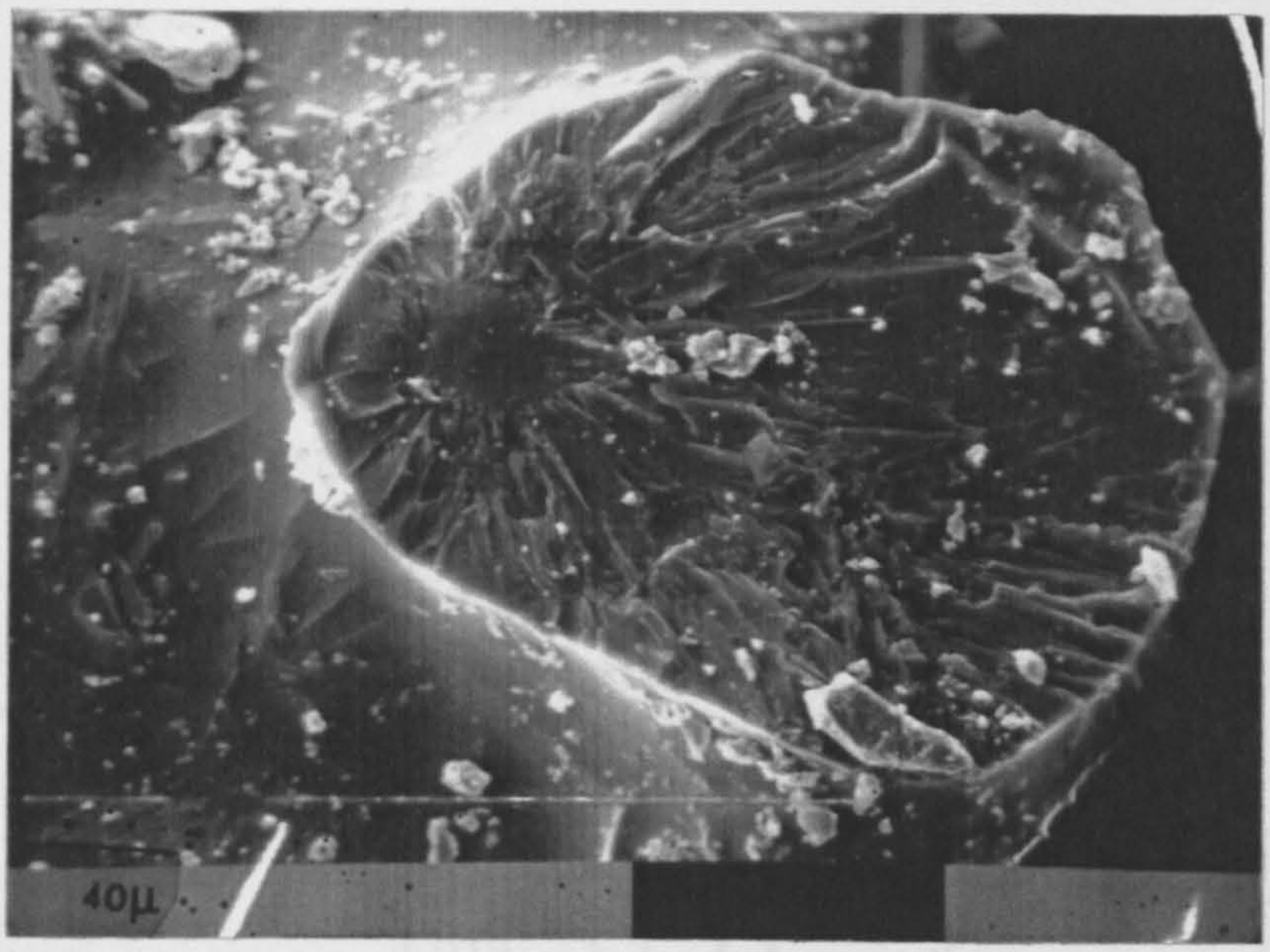

Figure 5.17 Secondary electron image of a fractured bond bridge made with bond type X(83.56 wt.% glass, 12.2 % wt. mullite and 4.24 wt.% quartz) showing mirror, mist and hackle regions indicating fracture origin.

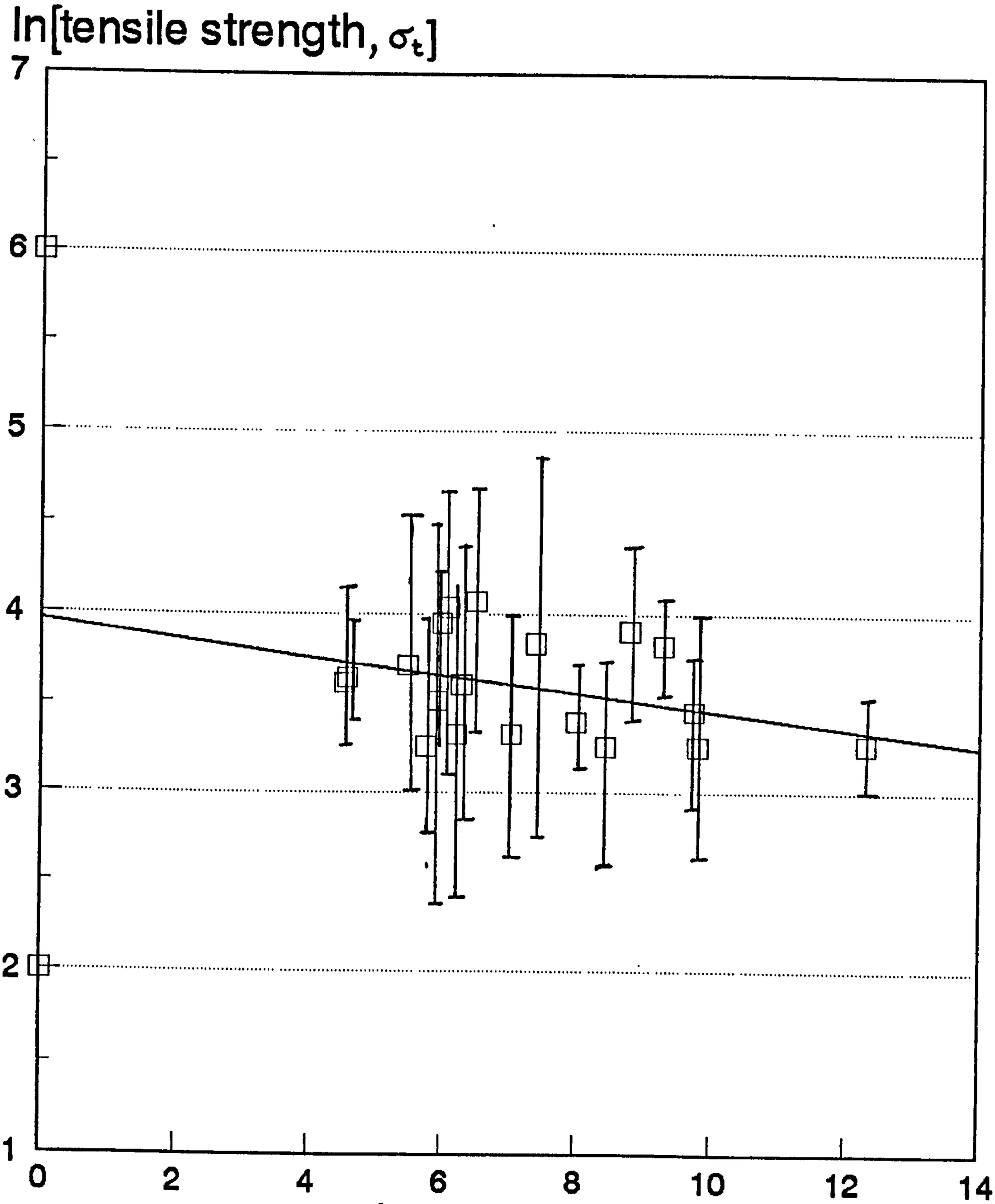

Figure 5.18 Ryshkewitch-Duckworth relationship between log$_e$ failure strength (tensile) and true porosity for the bond compositions fired at 1200°C for 40 hours.

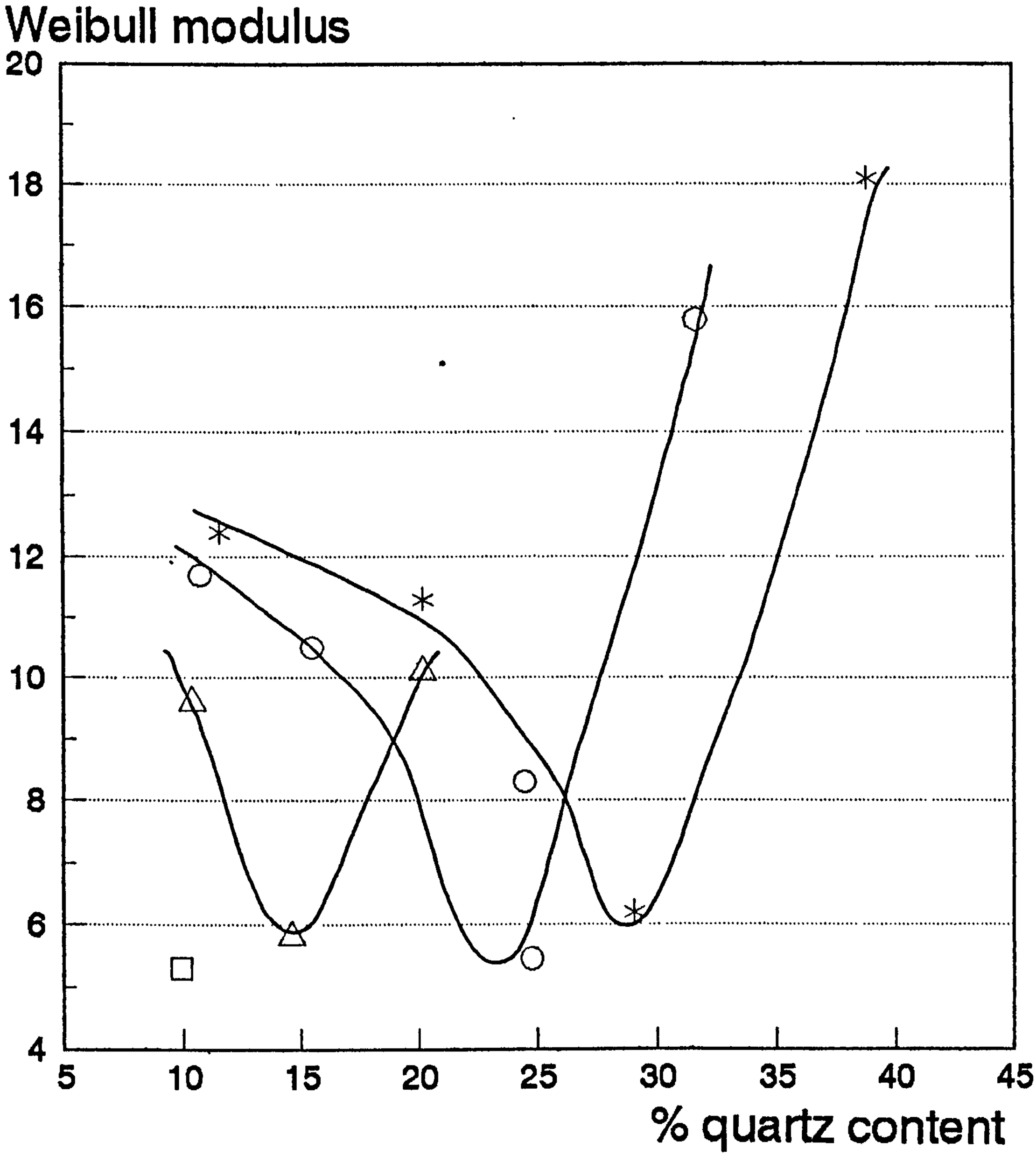

Figure 5.19 The effect of quartz content (x-ray determined) on the Weibull modulus of test pieces fired at 1200°C for 40 hours as a function of clay content. Note: (□) 80% clay; (△) 70% clay; (o) 60% clay; (*) 50% clay.

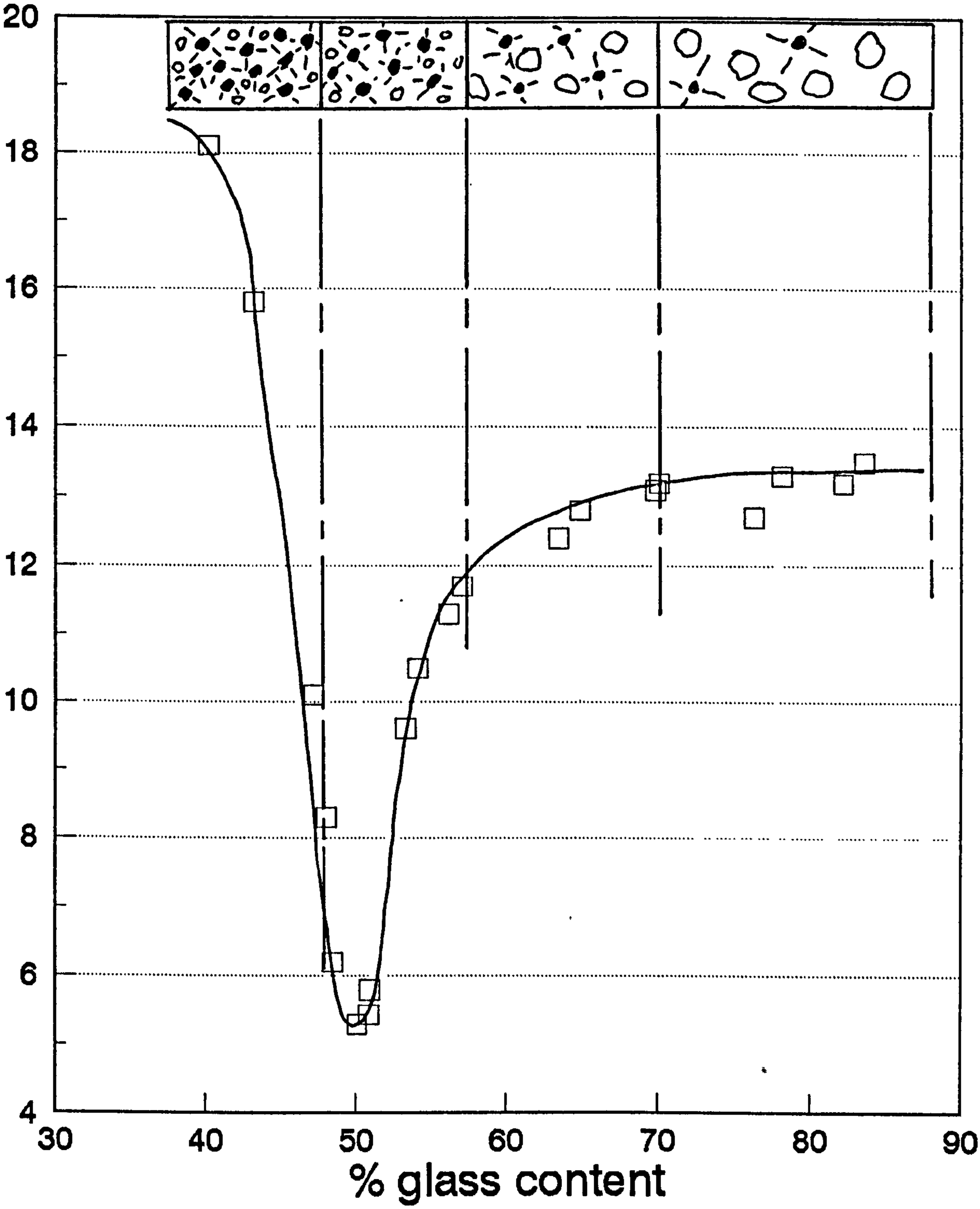

Figure 5.20 The effect of glass content (x-ray determined) on the Weibull modulus of test pieces fired at 1200°C for 40 hours.

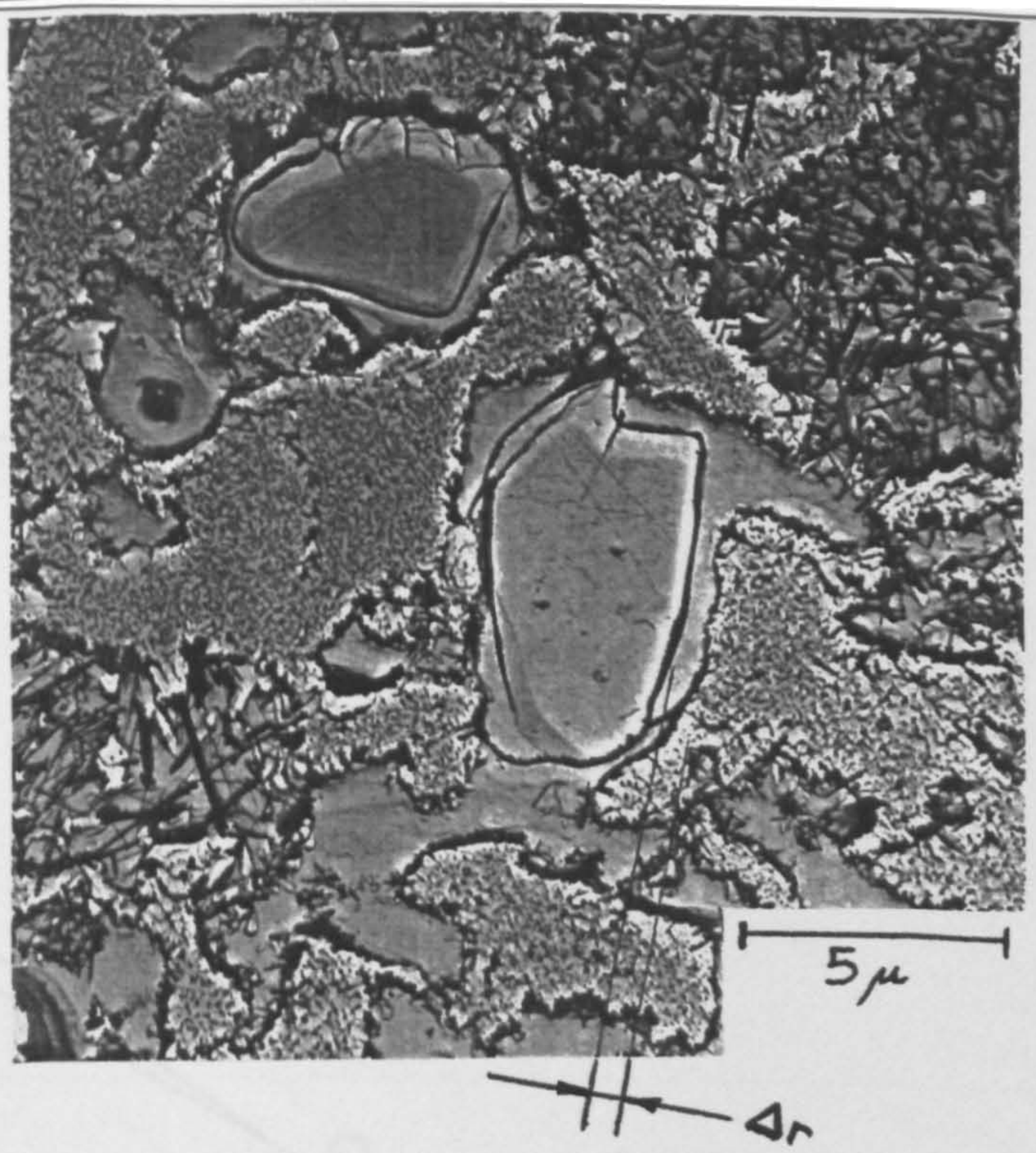

Figure 6.1a Scanning electron micrograph of a bond of composition: 50% wt clay: 25% wt quartz: 25% wt flux - etched 10sec. 0°C - 40% H.F. Solution (Silica replica) [167]. Mag. 2800X, Δ r= penetration depth.

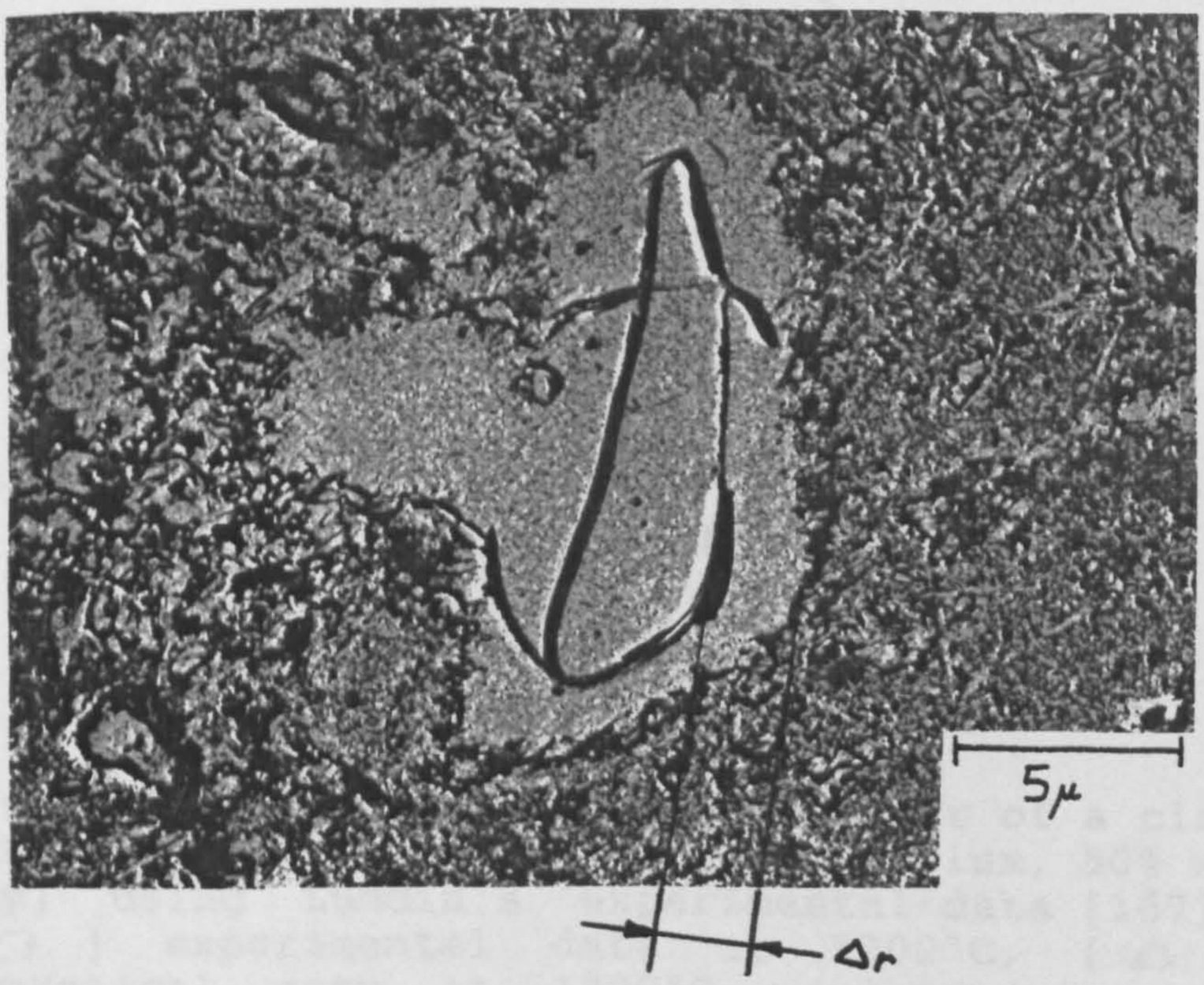

Figure 6.1b Partly dissolved quartz particle present in a bond of composition specified above. (etched 10sec. 0°C, 40% H.F. Solution - (aluminium replica) [167]. Mag. 2800X. Δ r = penetration depth.

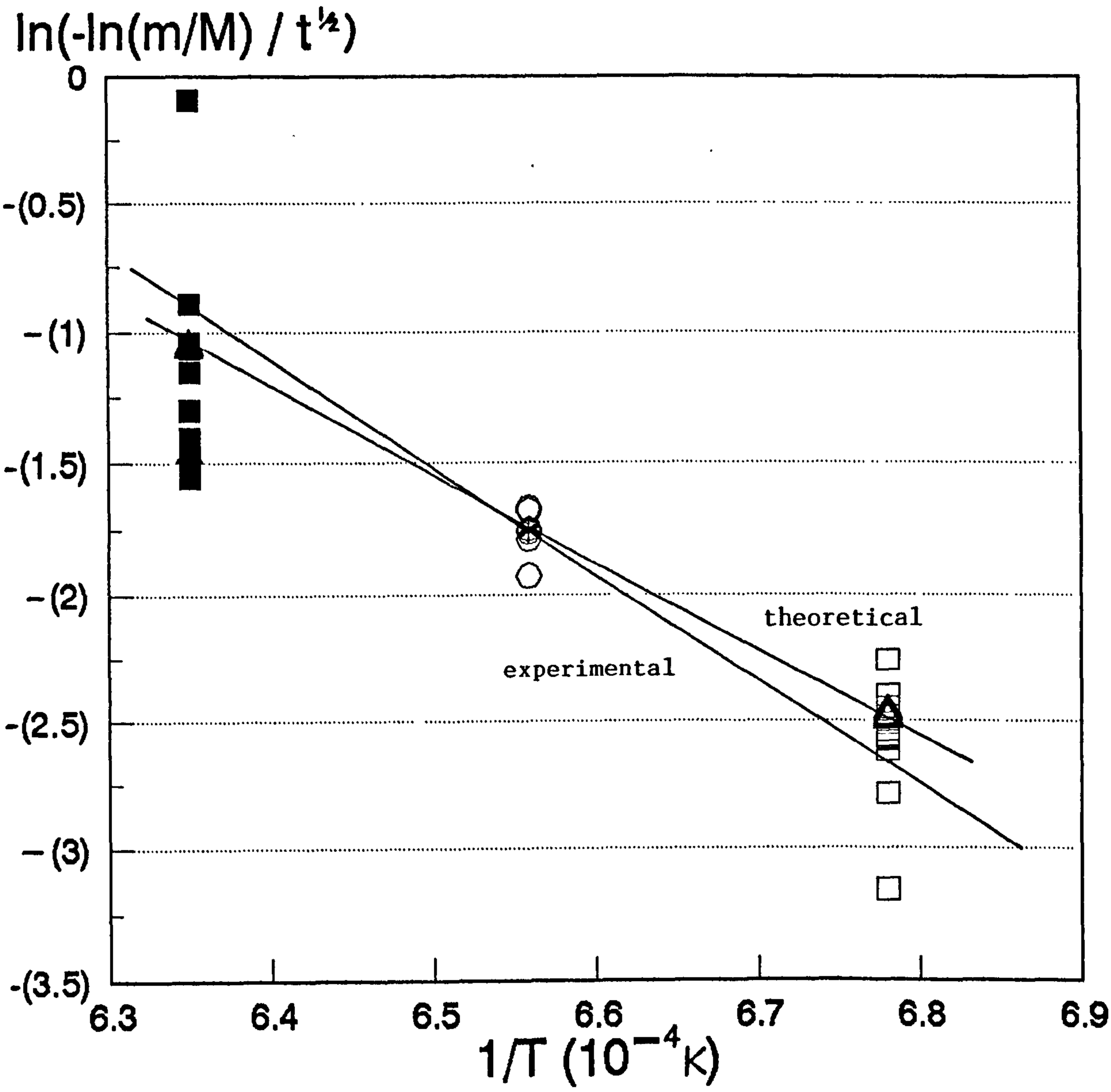

Figure 6.2 Illustration of dissolution behaviour of a clay mixture (25% wt. quartz. 25% wt flux, 50% wt clay) using Lundin's experimental data [167]. (□) experimental data at 1200°C, (△) theoretical data at 1200°C, (o) experimental data at 1250°C, (*) theoretical data at 1250°C, (■) experimental data at 1300°C, and (▲) theoretical data at 1300°C.

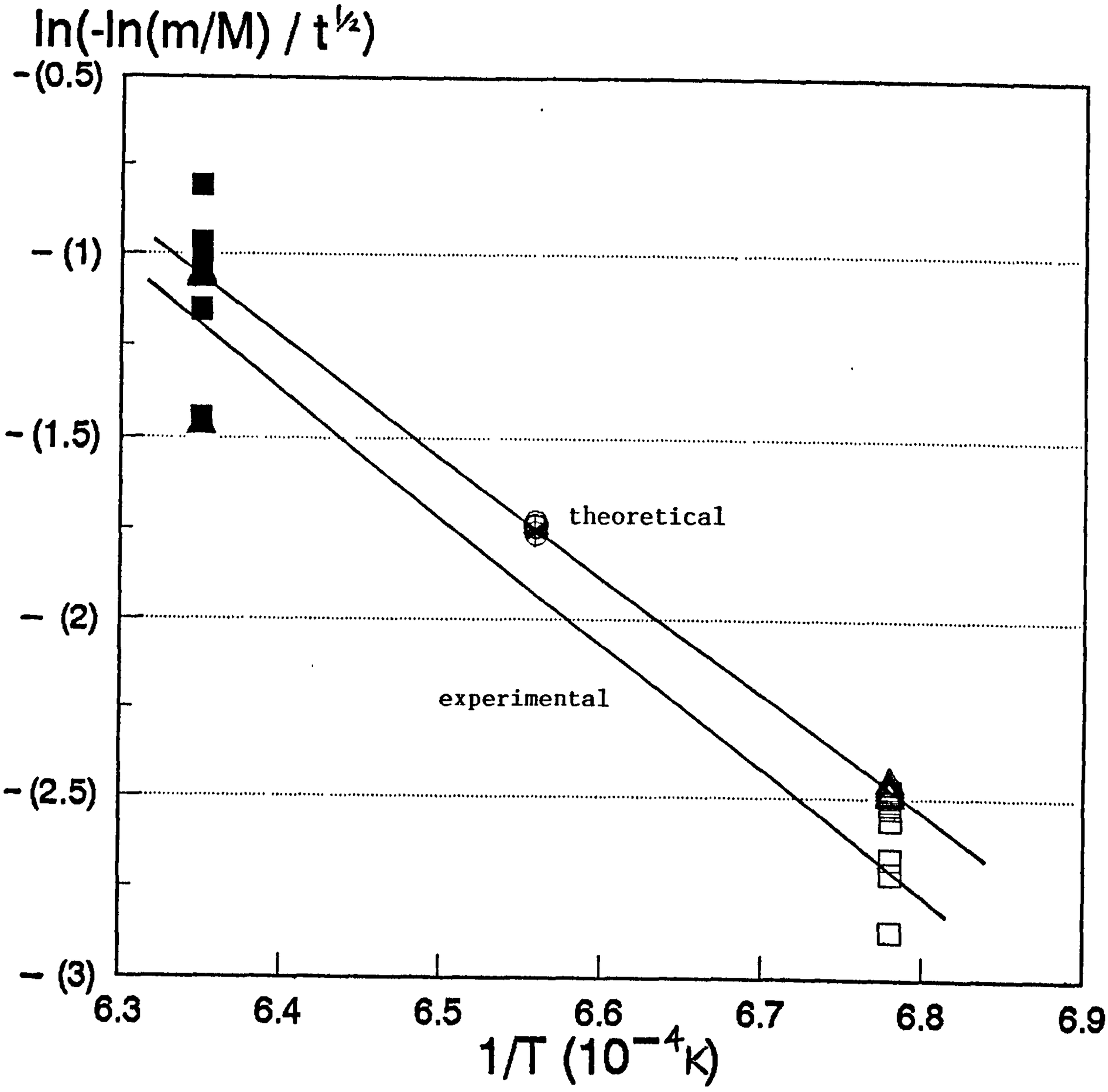

Figure 6.3 Dissolution behaviour of a clay mixture (25% wt. quartz, 25% wt. flux, 50% wt. clay) using Jackson's experimental data. (□) experimental data at 1200°C, (△) theoretical data at 1200°C, (o) experimental data at 1250°C, (*) theoretical data at 1250°C, (■) experimental data at 1300°C, (▲) theoretical data at 1300°C.

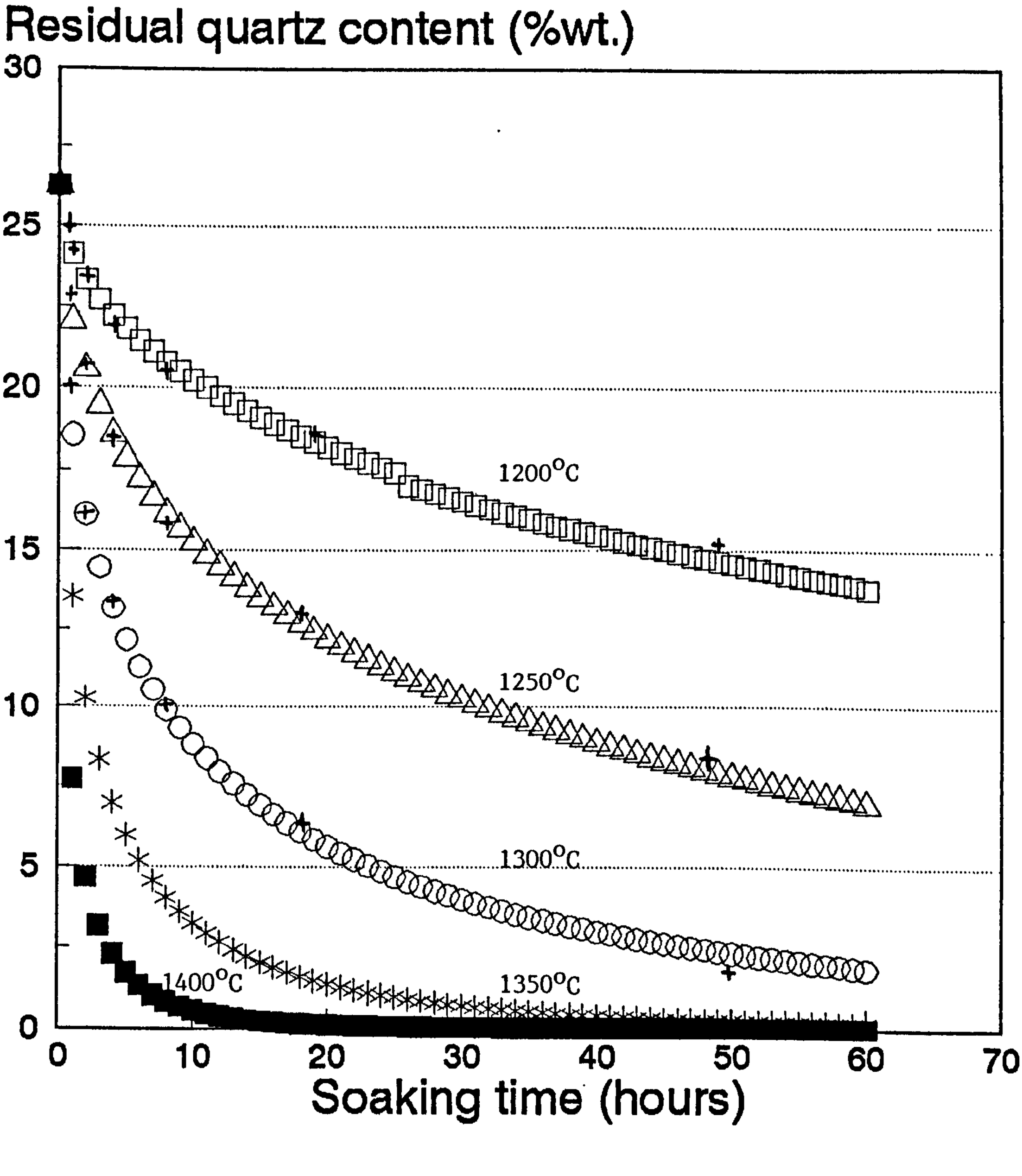

Figure 6.4 Effect of time on residual quartz content according to the theoretical model and compared with Lundin's experimental data. (□) 1200°C, (△) 1250°C, (o) 1300°C, (*) 1350°C, (■) 1400°C, (+) Lundin's experimental data.

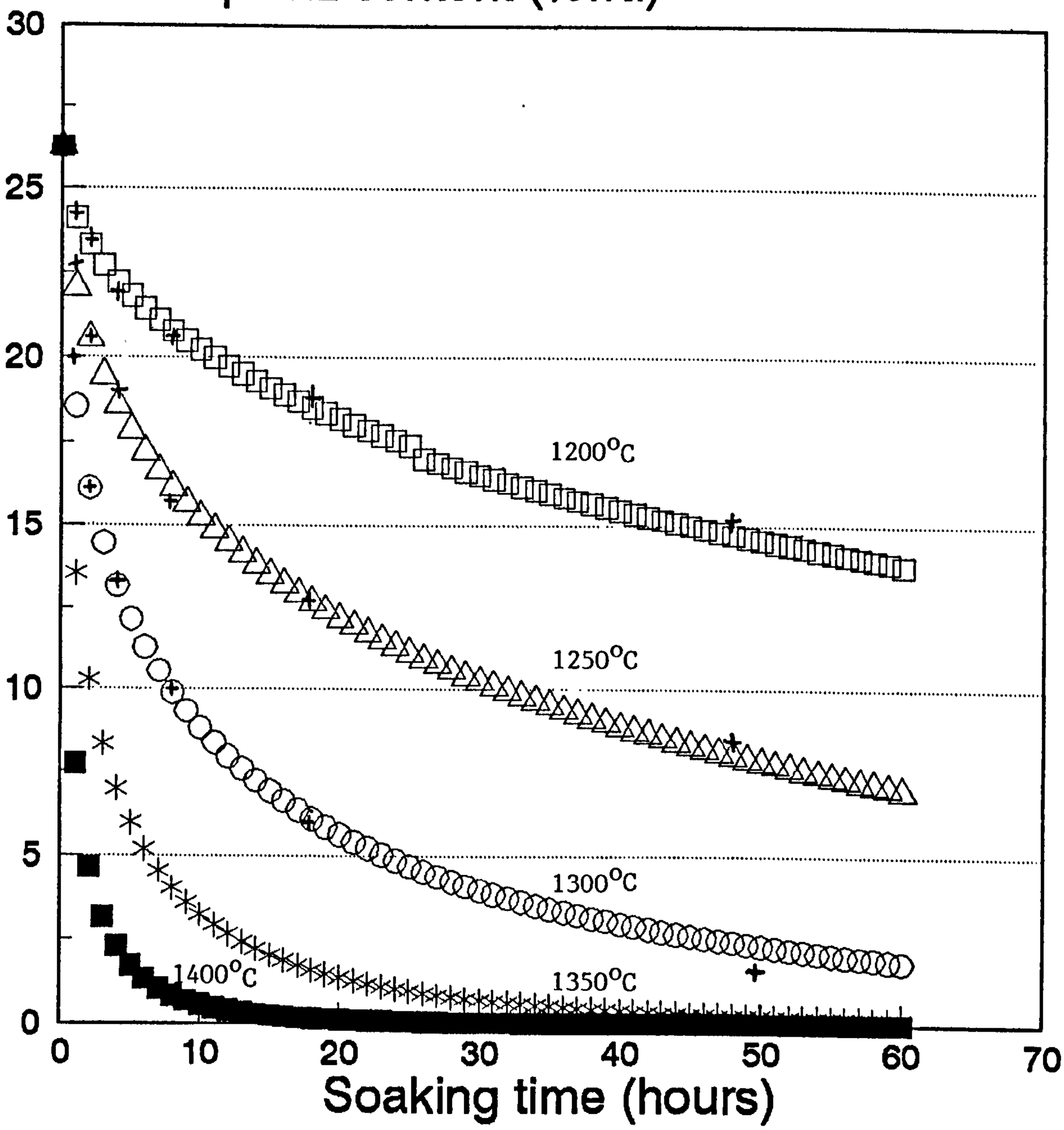

Figure 6.5 Effect of time on residual quartz content according to the theoretical model and compared with the current experimental data. (□) 1200°C, (△) 1250°C, (o) 1300°C, (*) 1350°C, (■) 1400°C, (+) Jackson's experimental data.

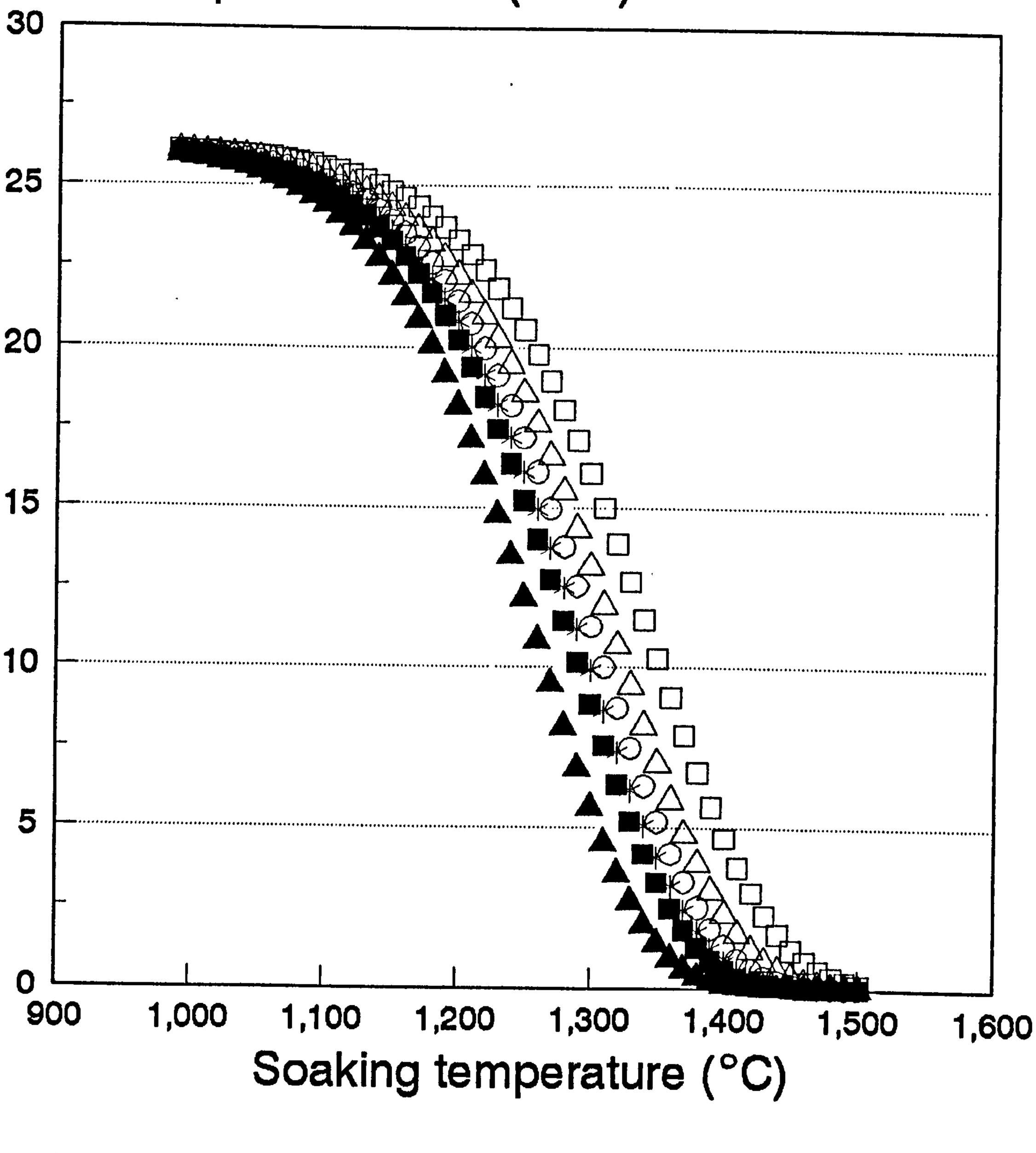

Figure 6.6 Effect of temperature on residual quartz content according to the theoretical model. (□) 2 hours, (△) 4 hours, (o) 6 hours, (*) 8 hours, (■) 10 hours, (▲) 20 hours.

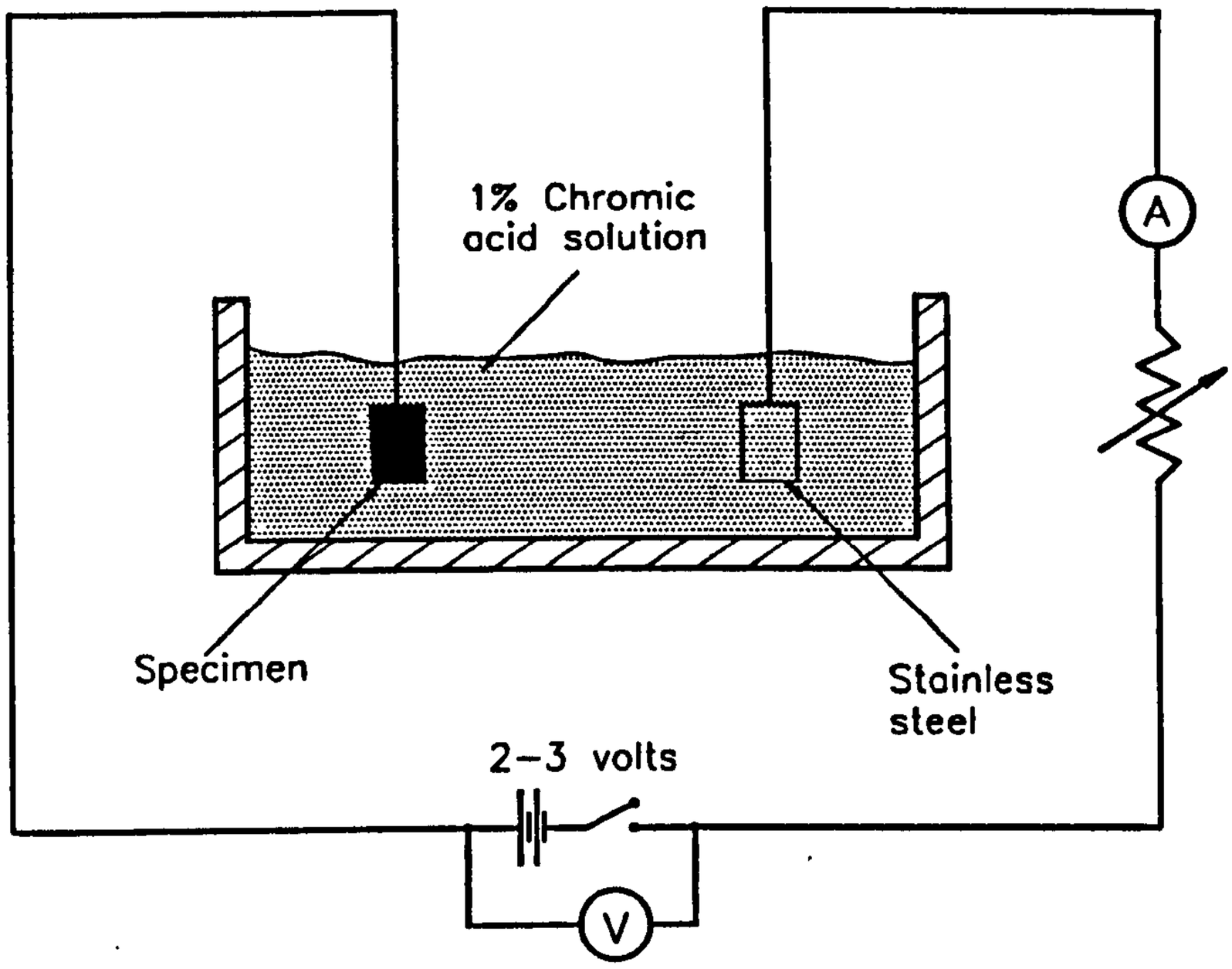

Figure 7.1 - A schematic diagram illustrating the etching rig used for revealing complex carbides in tool steels.

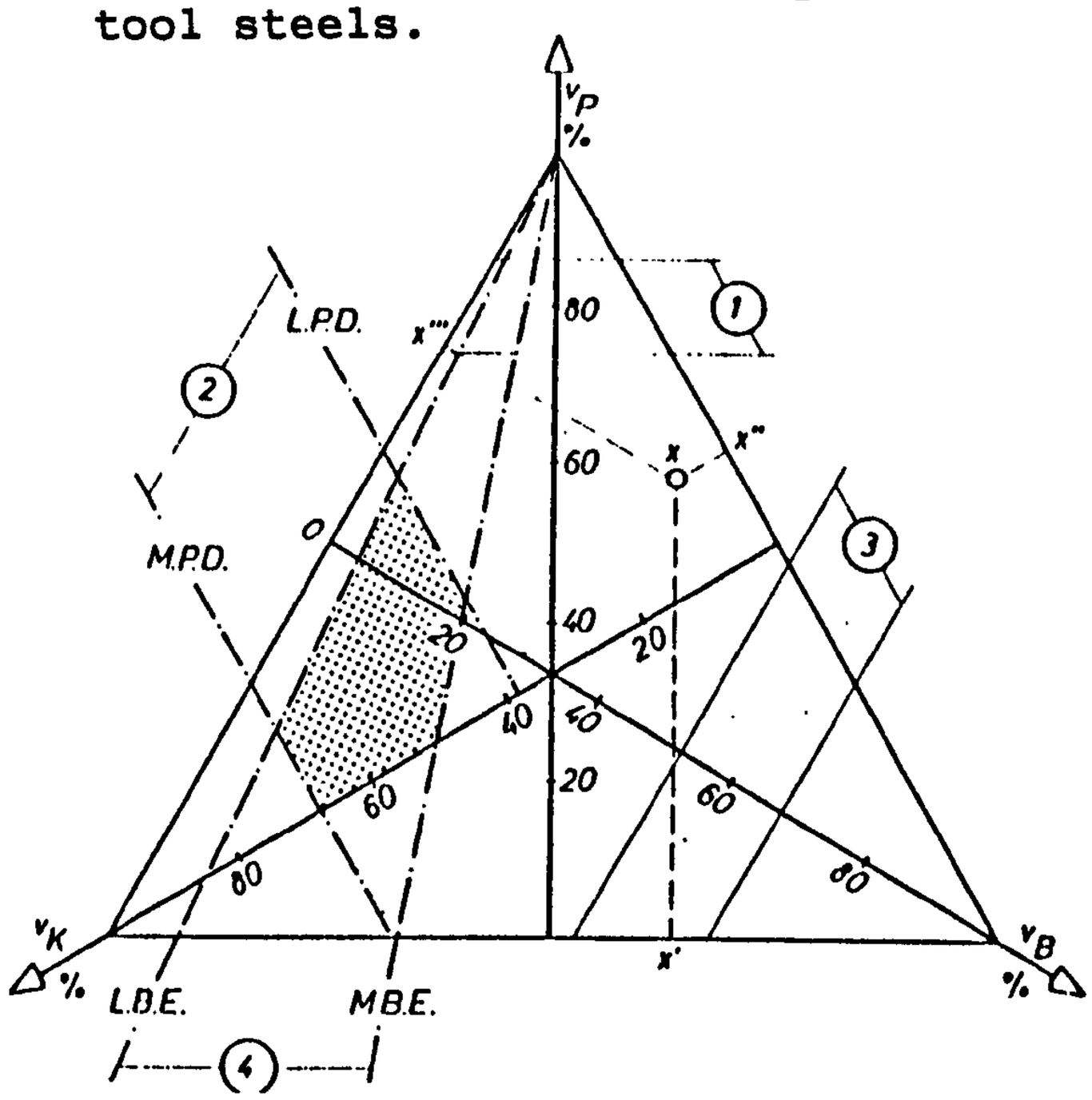

Figure 7.2 - Ternary Composition Diagram. Iso-lines in the ternary diagram: (1) Iso-porosity lines; (2) Iso-grit volume lines (Iso-structure lines); (3) Iso-bond volume lines; (4) Lines of constant ratio of grit volume to bond volume. M.B.E. is the maximum bond equivalent, L.B.E. is the lowest bond equivalent, M.P.D. is the maximum packing density, and L.P.D. is the lowest packing density.

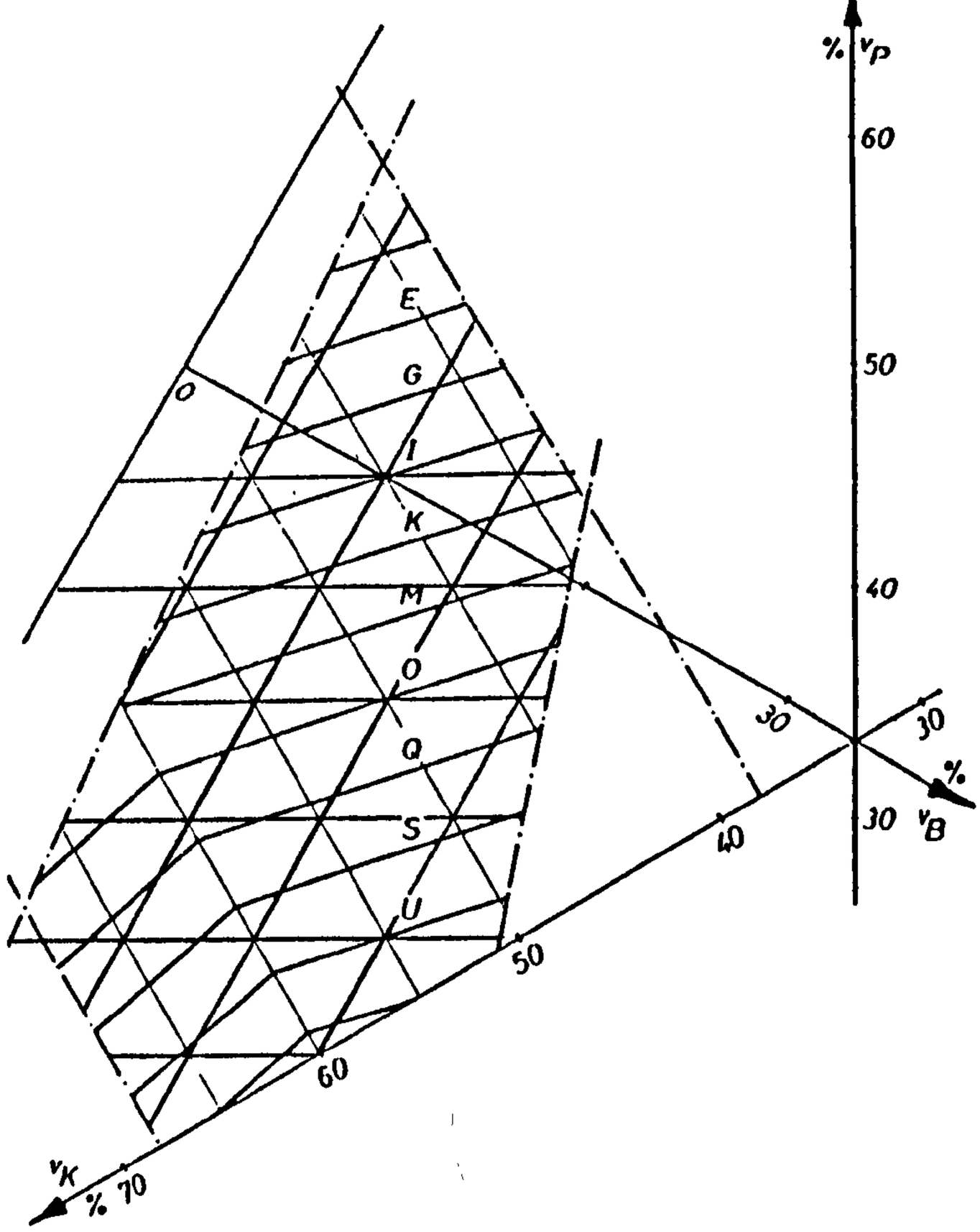

Figure 7.3 - Useful area of the ternary phase diagram showing iso-grade loci.

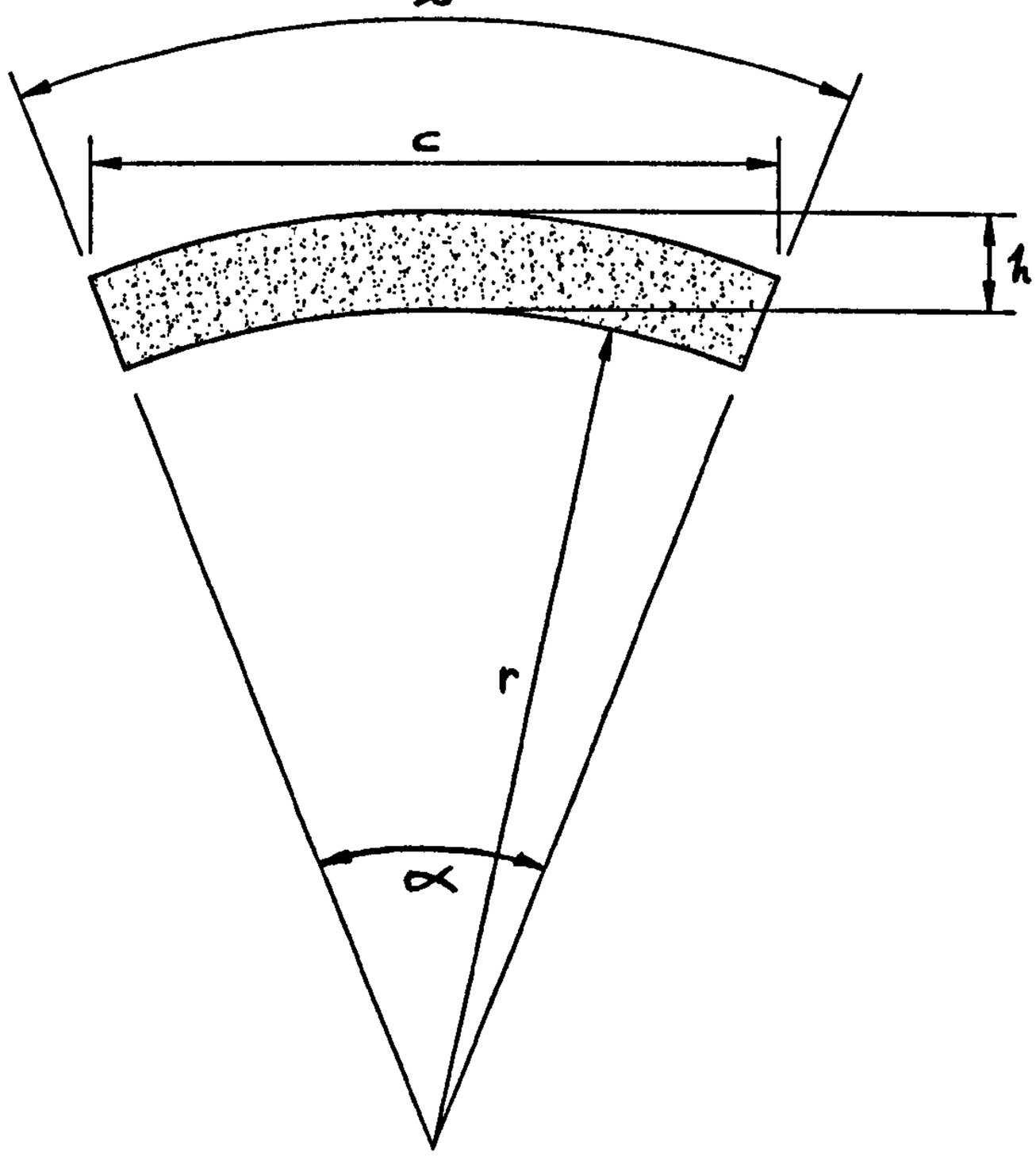

Figure 7.4. - Geometry of an abrasive segment. ℓ is the arc length, h is the segment width mid-way, r is the radius and α is the angle subtended by the segment.

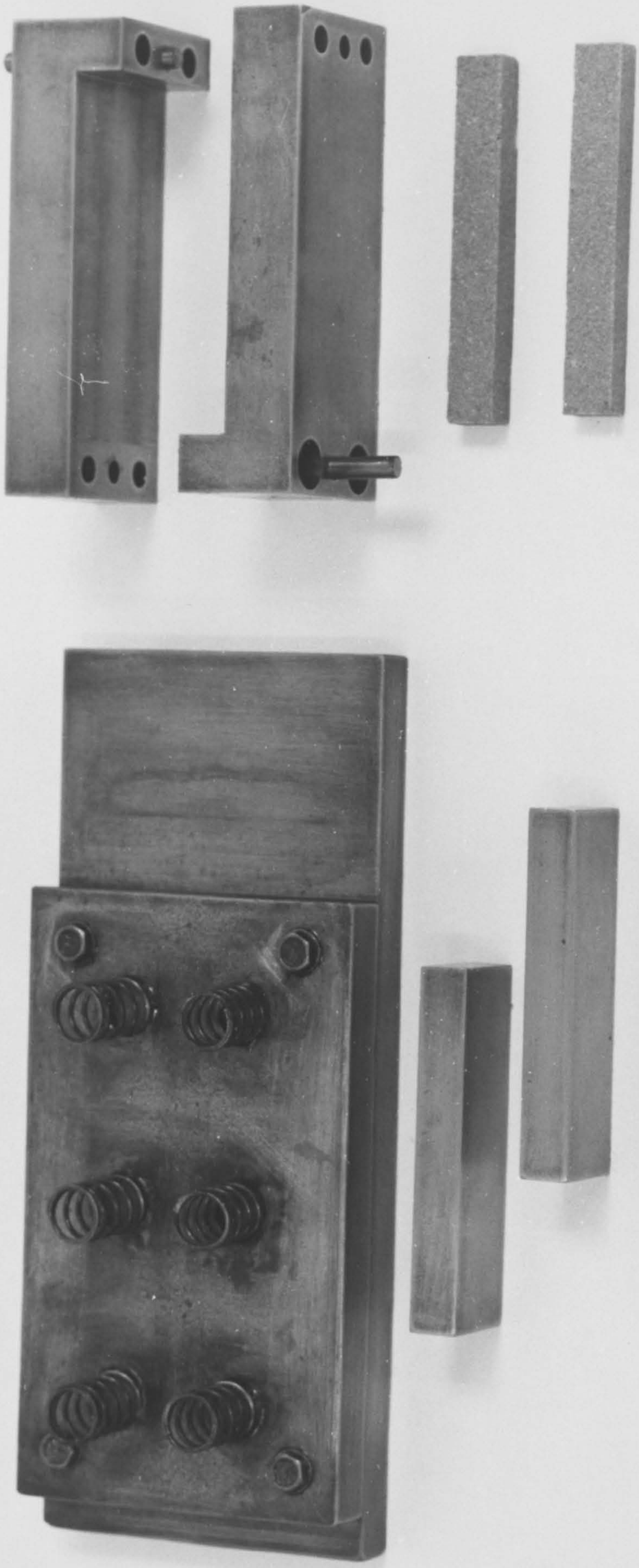

Figure 7.5 - Grading bar mould and compression platen.

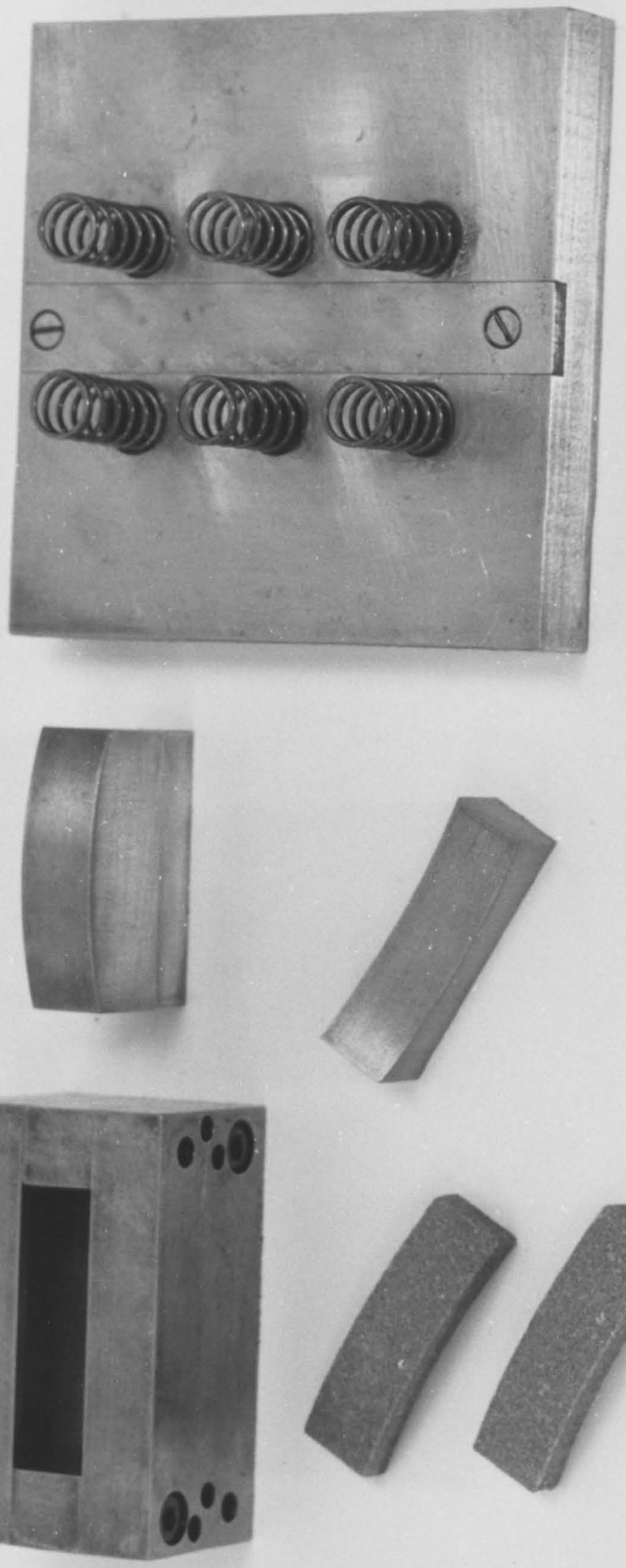

Figure 7.6 - Abrasive segment mould and compression platen.

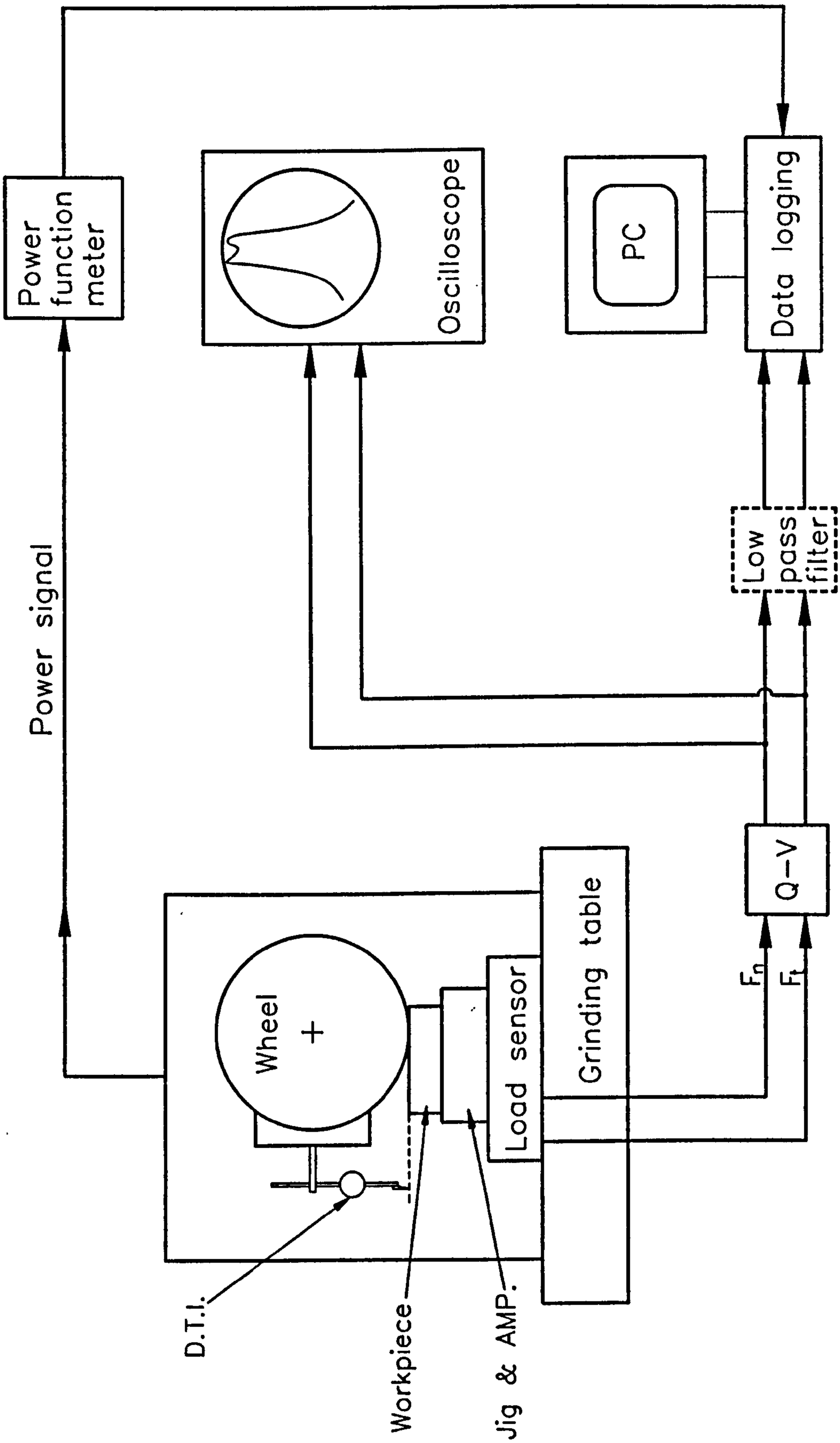

Figure 7.7 - System for measuring grinding forces, power and real depth of cut.

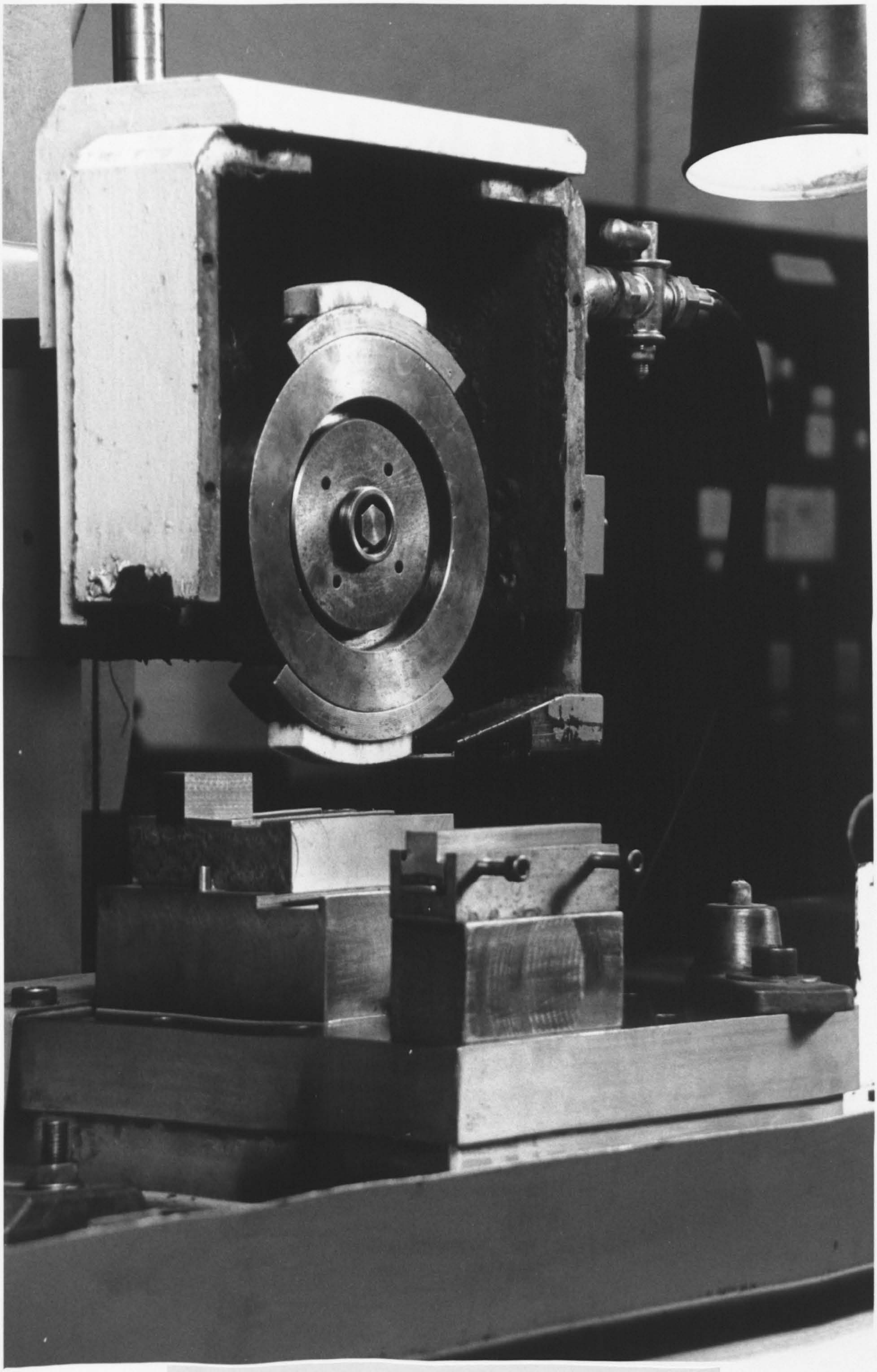

Figure 7.8 - Experimental apparatus showing grinding wheel, dresser and block.

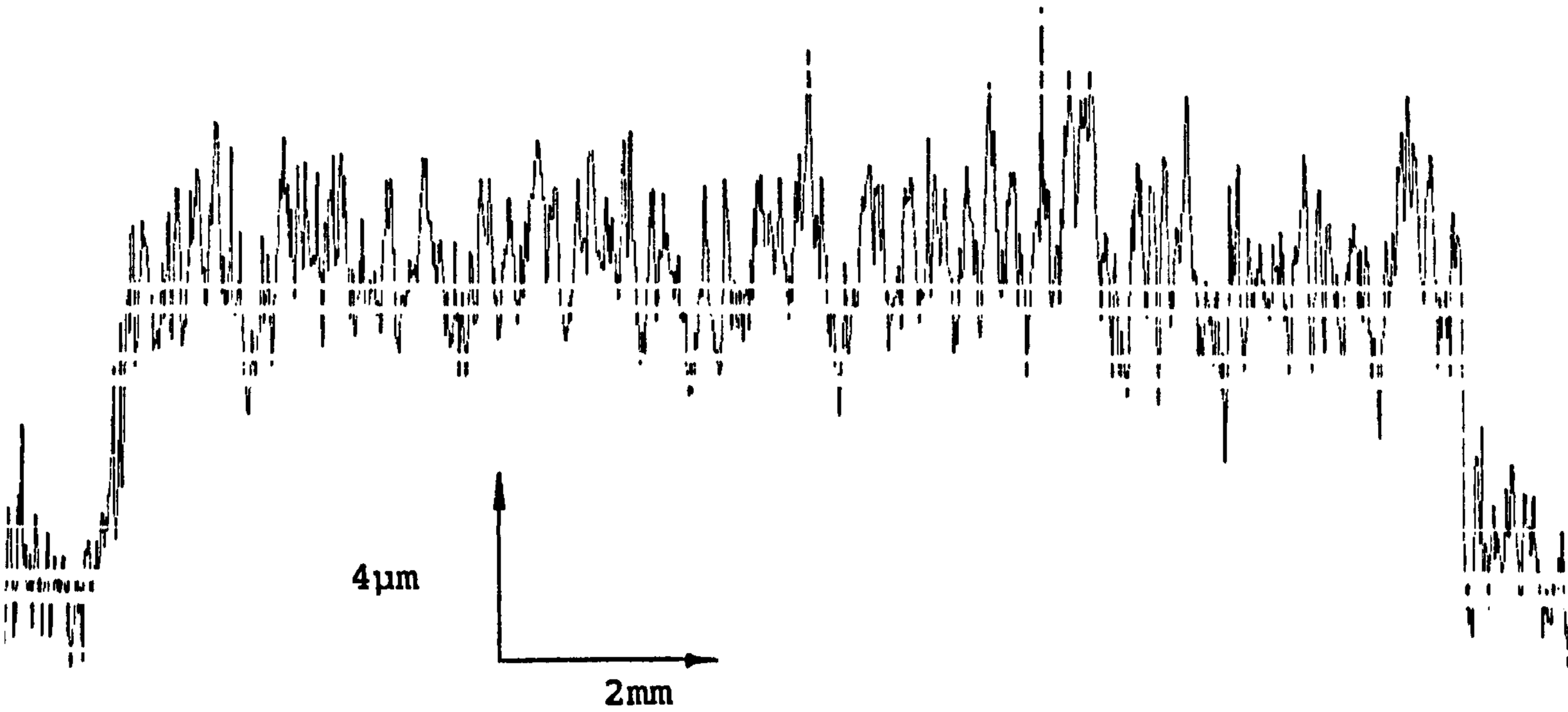

Figure 7.9 - Wheel wear trace generated by traversing the Talysurf stylus along a ground razor blade.

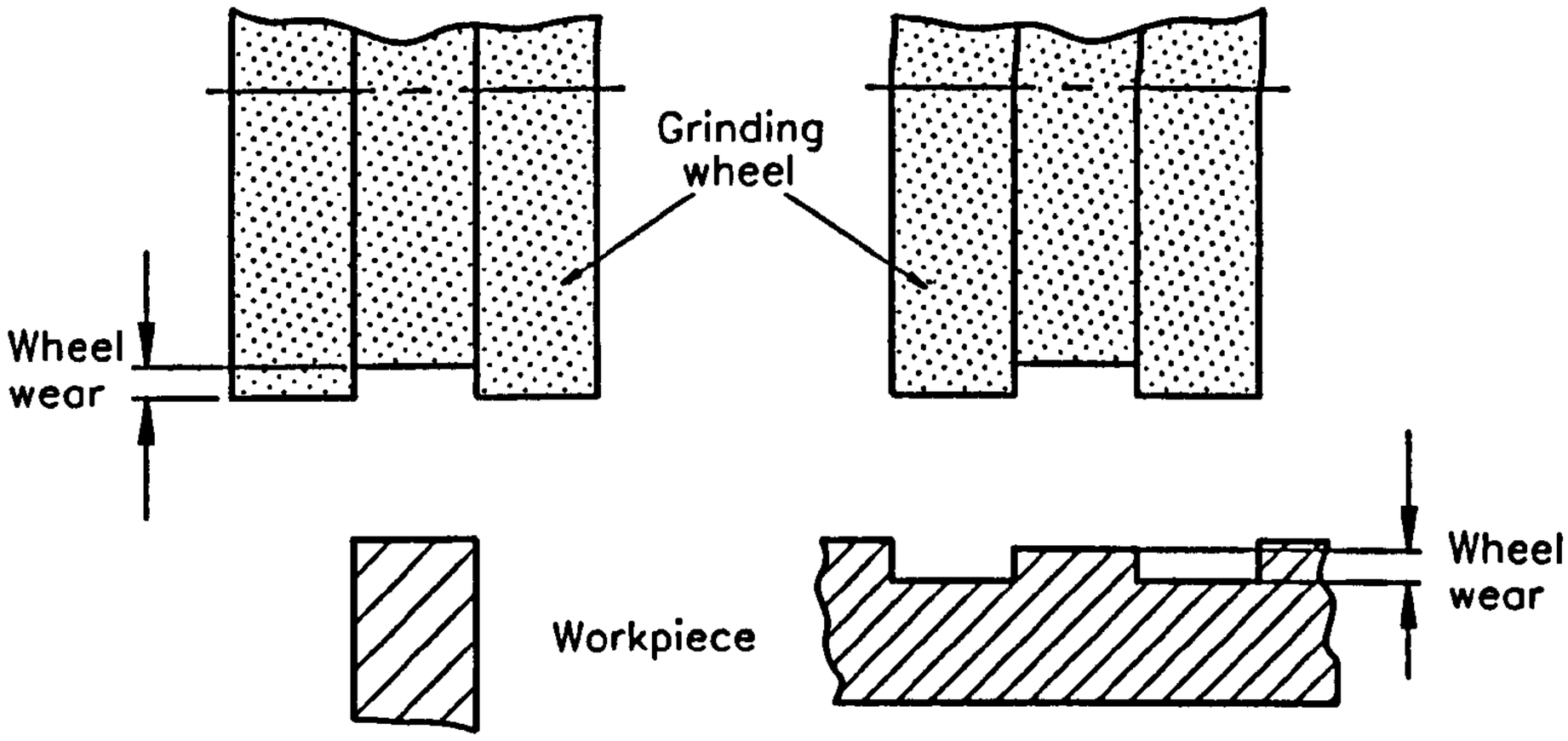

Figure 7.10 - Schematic diagram for measuring wheel wear using the 'razor-blade' technique.

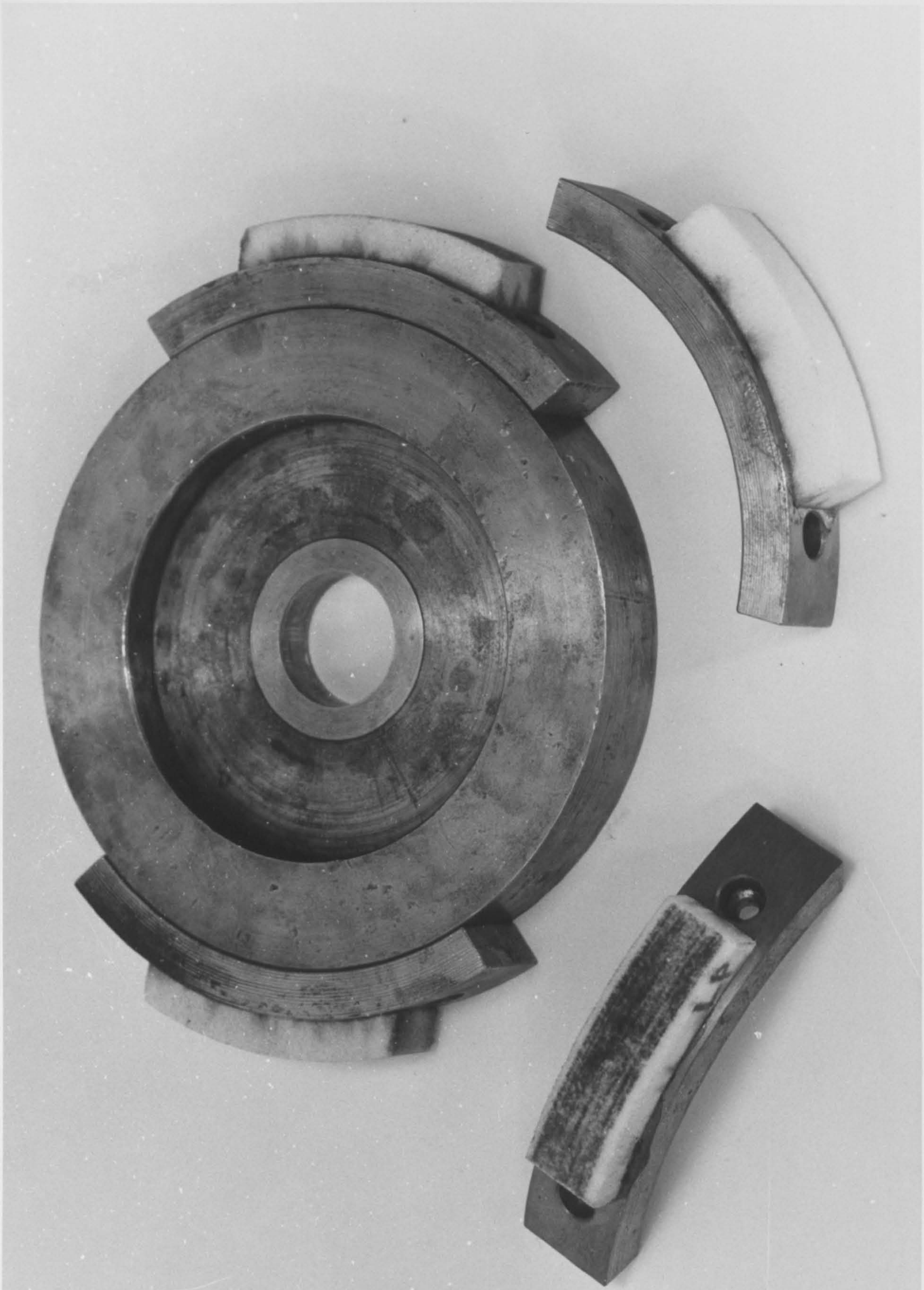

Figure 7.11 - Segmented grinding wheel with detachable segments.

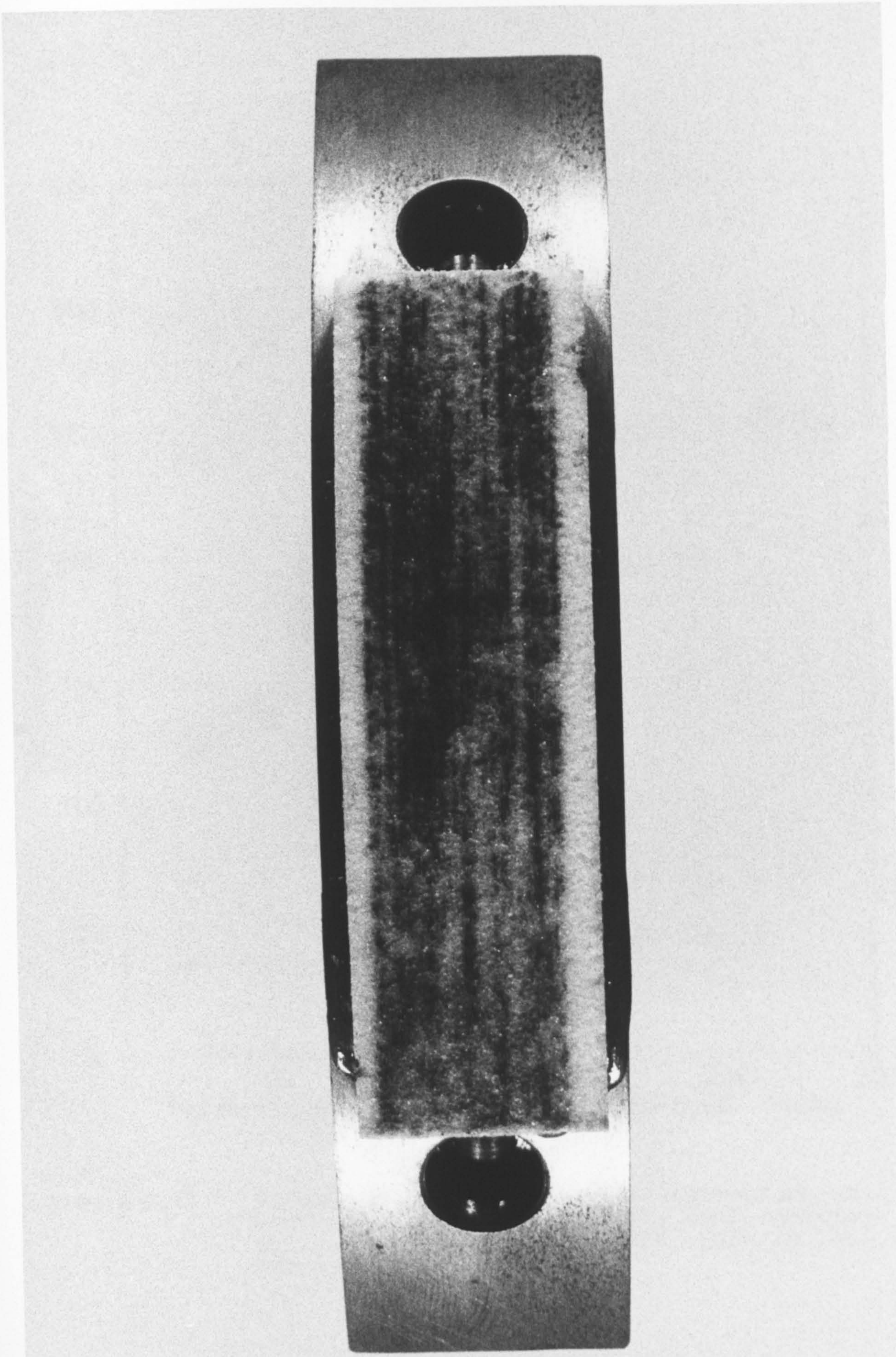

Figure 7.12 - Worn abrasive segment showing uneven wheel wear.

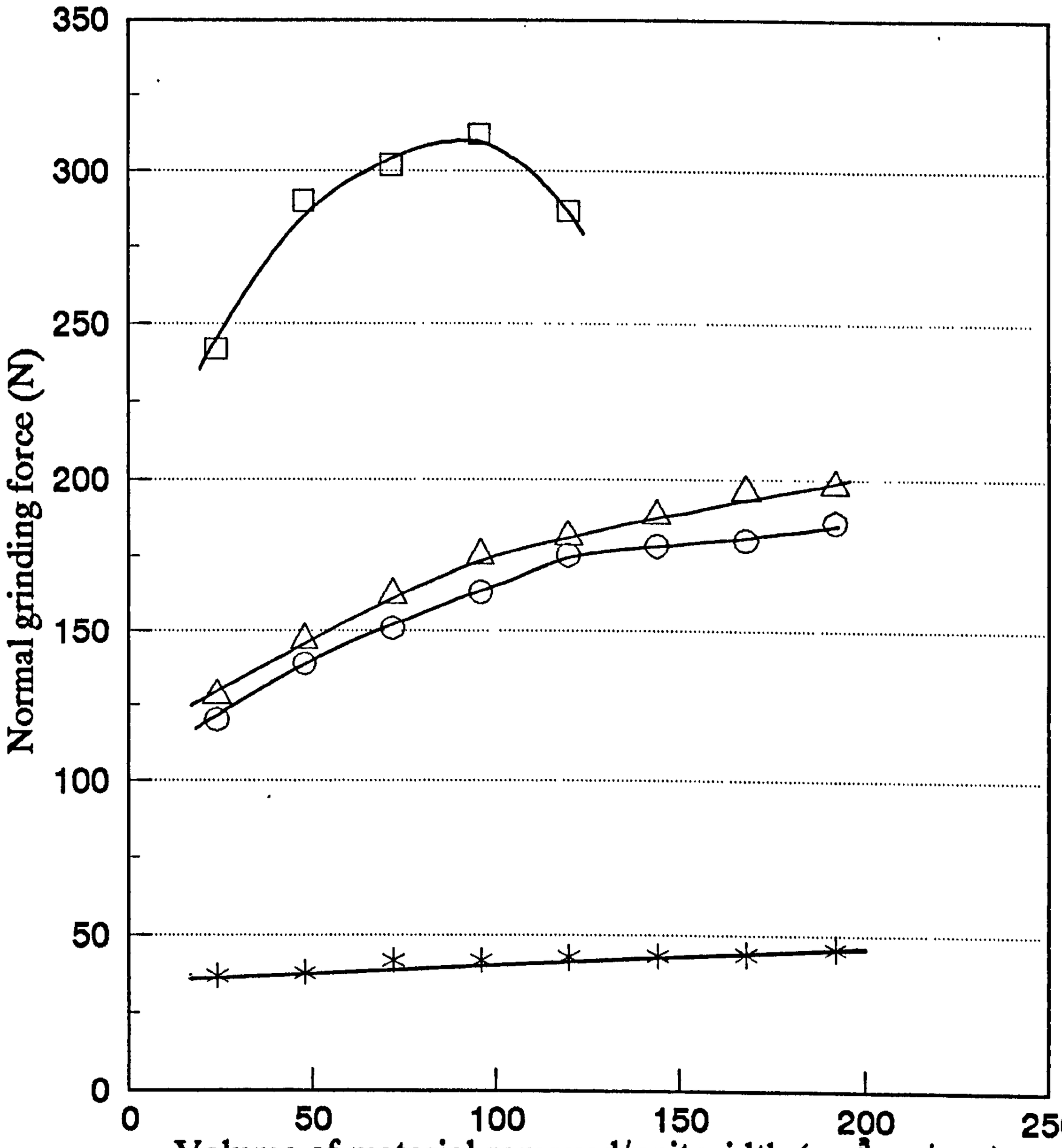

Figure 7.13 - Effect of volume of material removed per unit width on the normal grinding force component for workpiece materials M15 (□), M2 (△), ASP23 (O) and 01 (*).

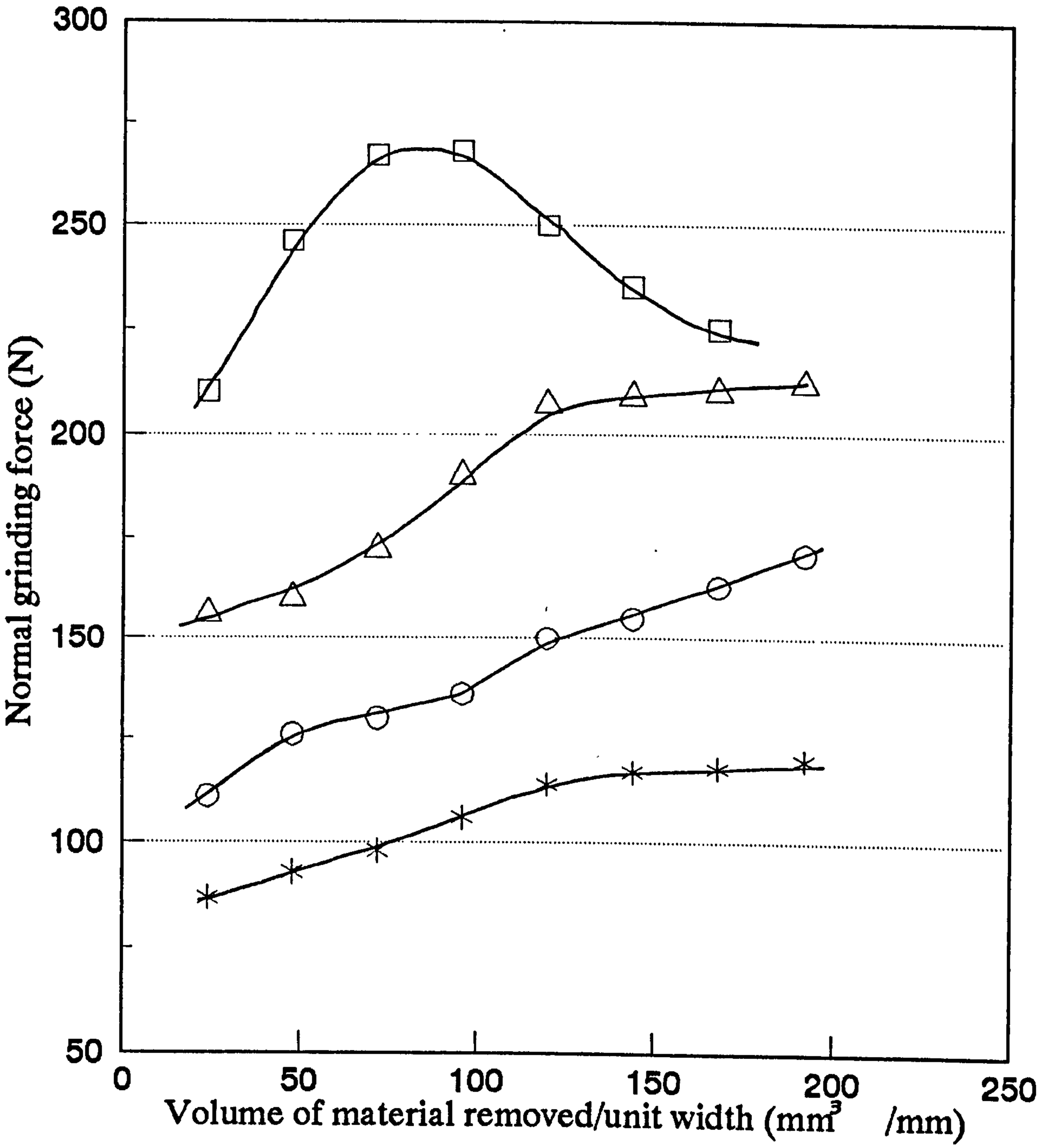

Figure 7.14 - Effect of volume of material removed per unit width on the normal grinding force component for workpiece materials T4 (□), M42 (△), T1 (O) and M1 (*).

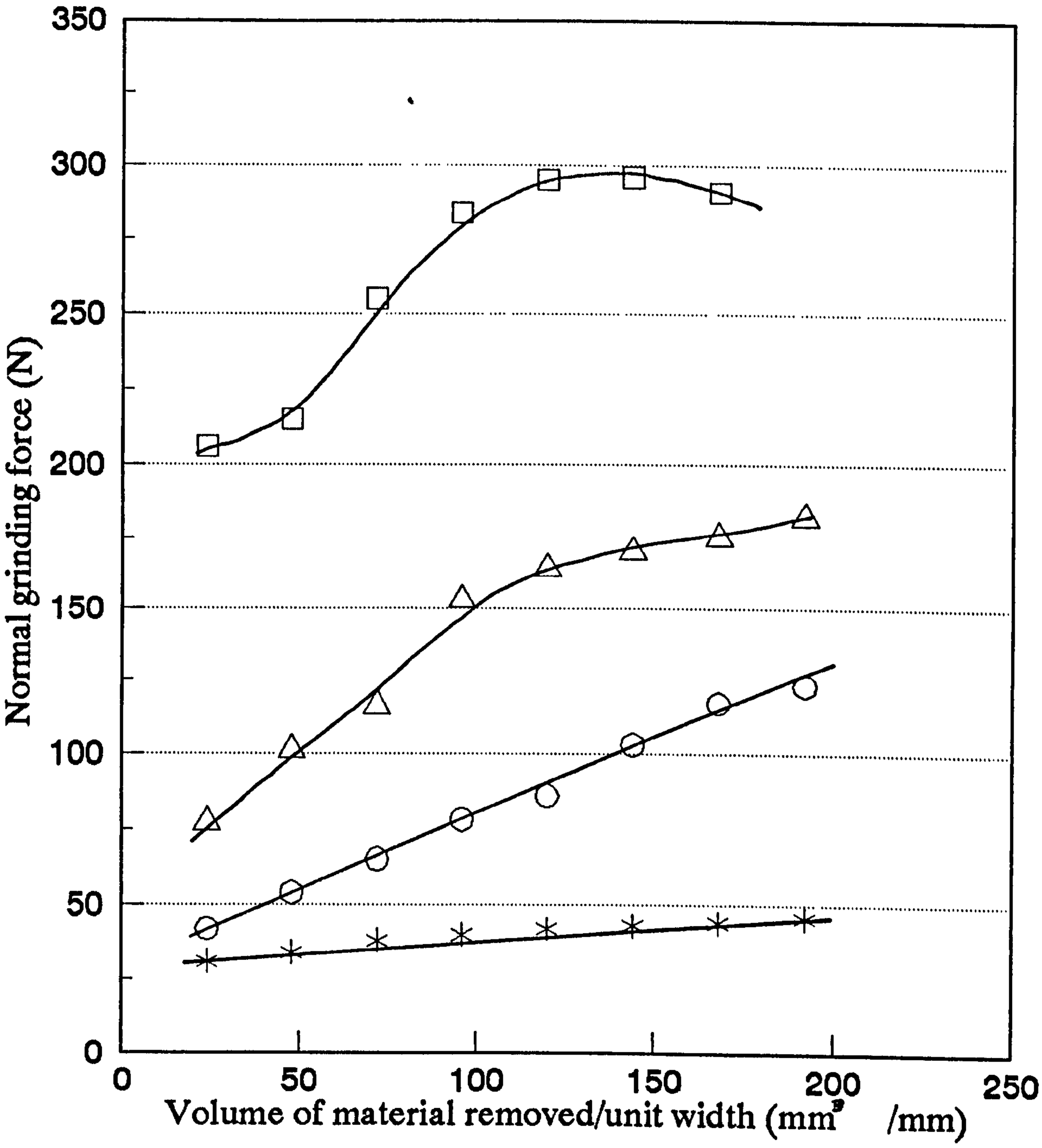

Figure 7.15 - Effect of volume of material removed per unit width on the normal grinding force component for workpiece materials T15 (□), D3 (△), D2 (O) and 01 (*).

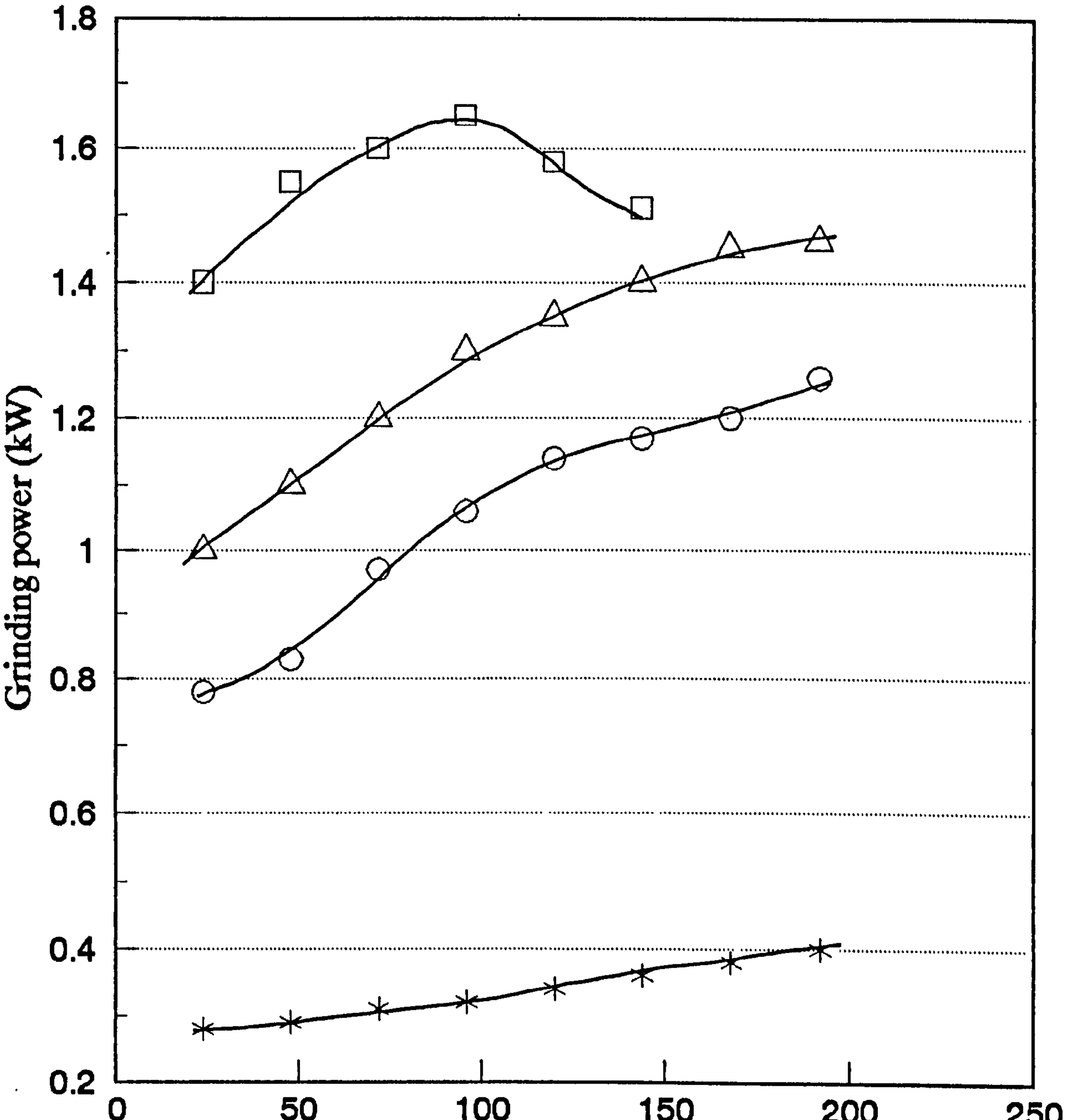

Figure 7.16 - Effect of volume of material removed per unit width on the net grinding power required to grind workpiece materials M15 (□), M2 (△), ASP23 (O) and 01 (*).

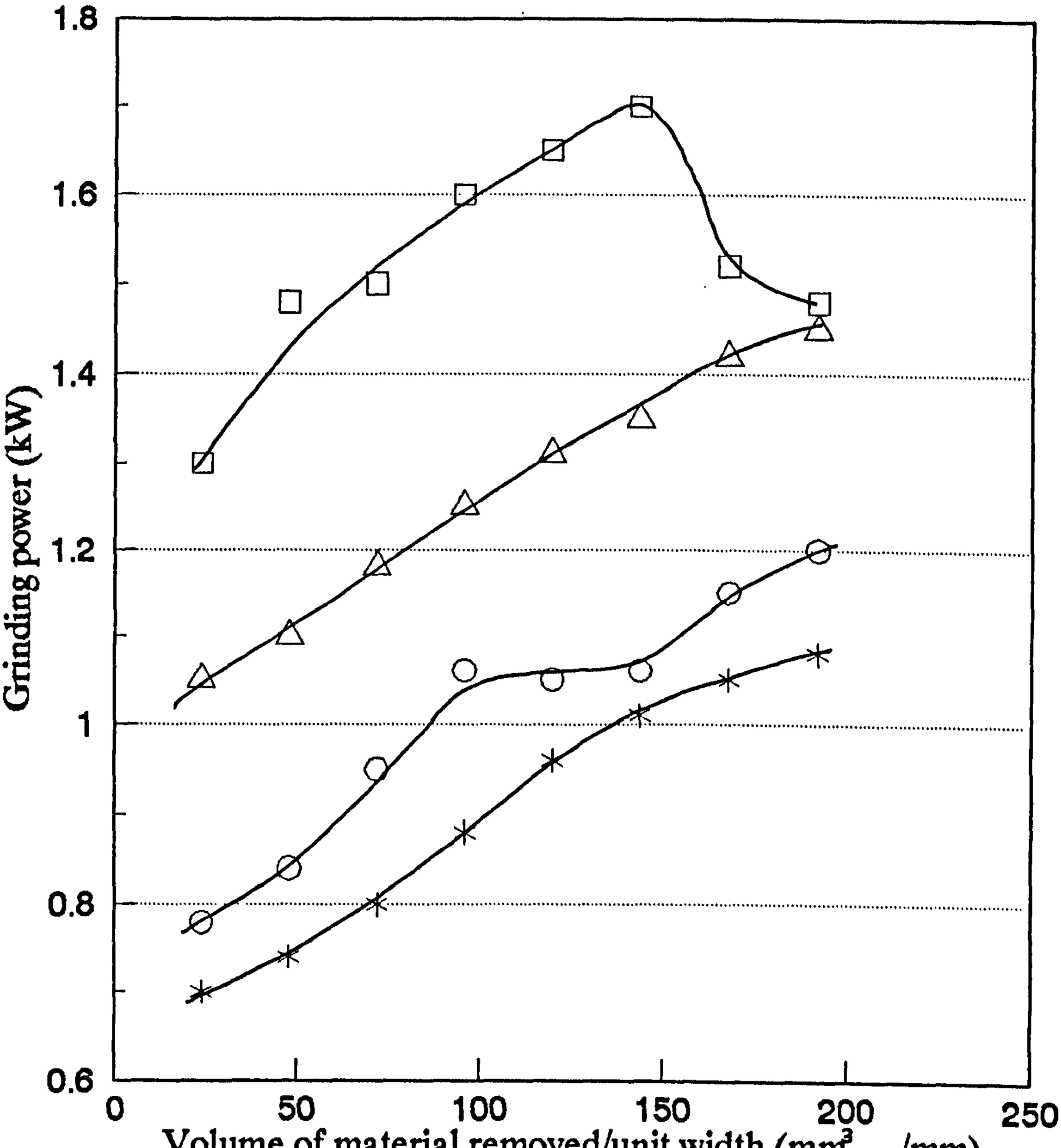

Figure 7.17 - Effect of volume of material removed per unit width on the net grinding power required to grind workpiece materials T4 (□), M42 (△), T1 (o) and M1 (*).

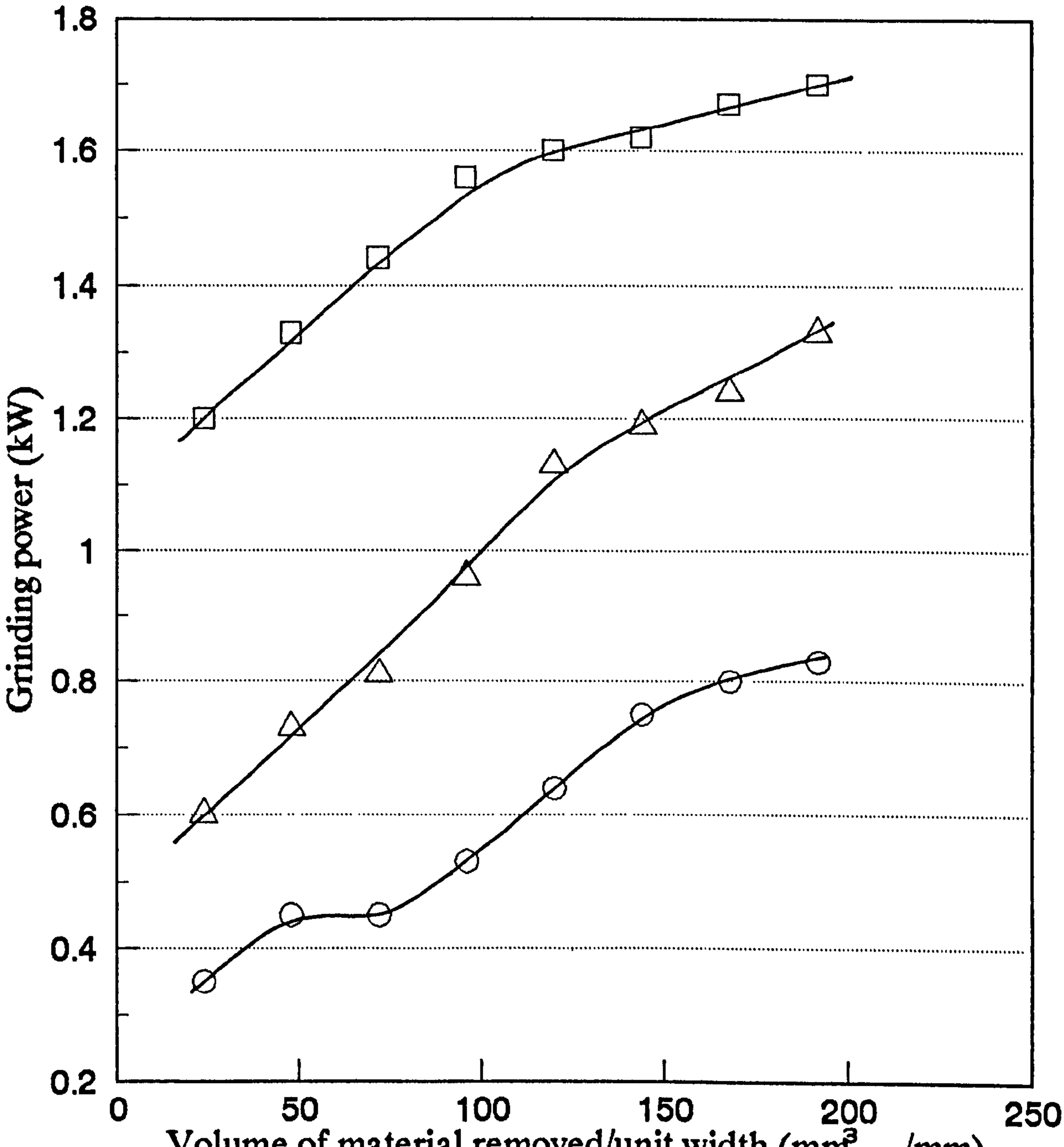

Figure 7.18 - Effect of volume of material removed per unit width on the net grinding power required to grind workpiece materials T15 (□), D3 (△) and D2 (o).

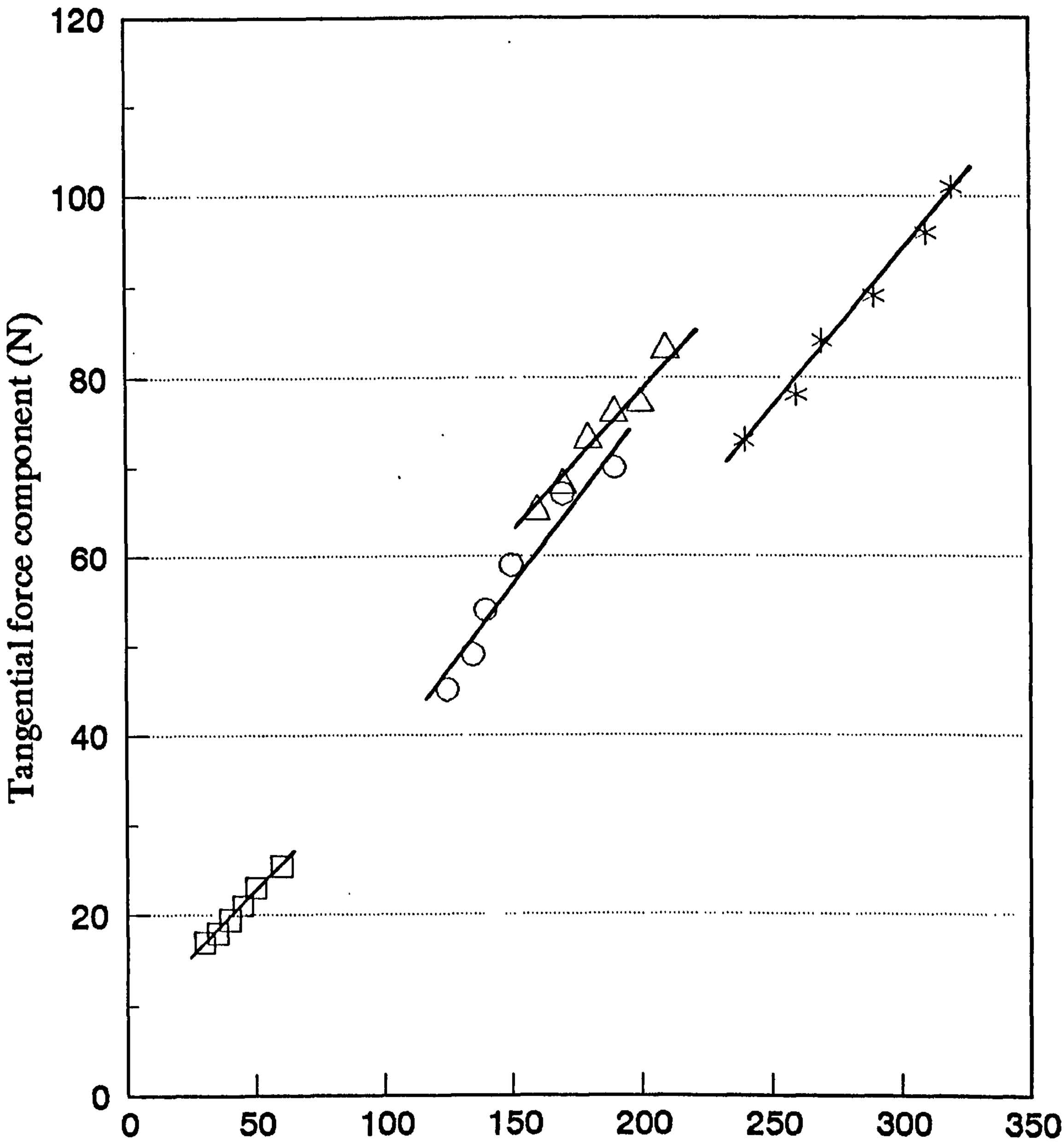

Figure 7.19 - Relationship between tangential and normal grinding force components for workpiece materials 01 (□), M2 (△), ASP23 (o) and M15 (*).

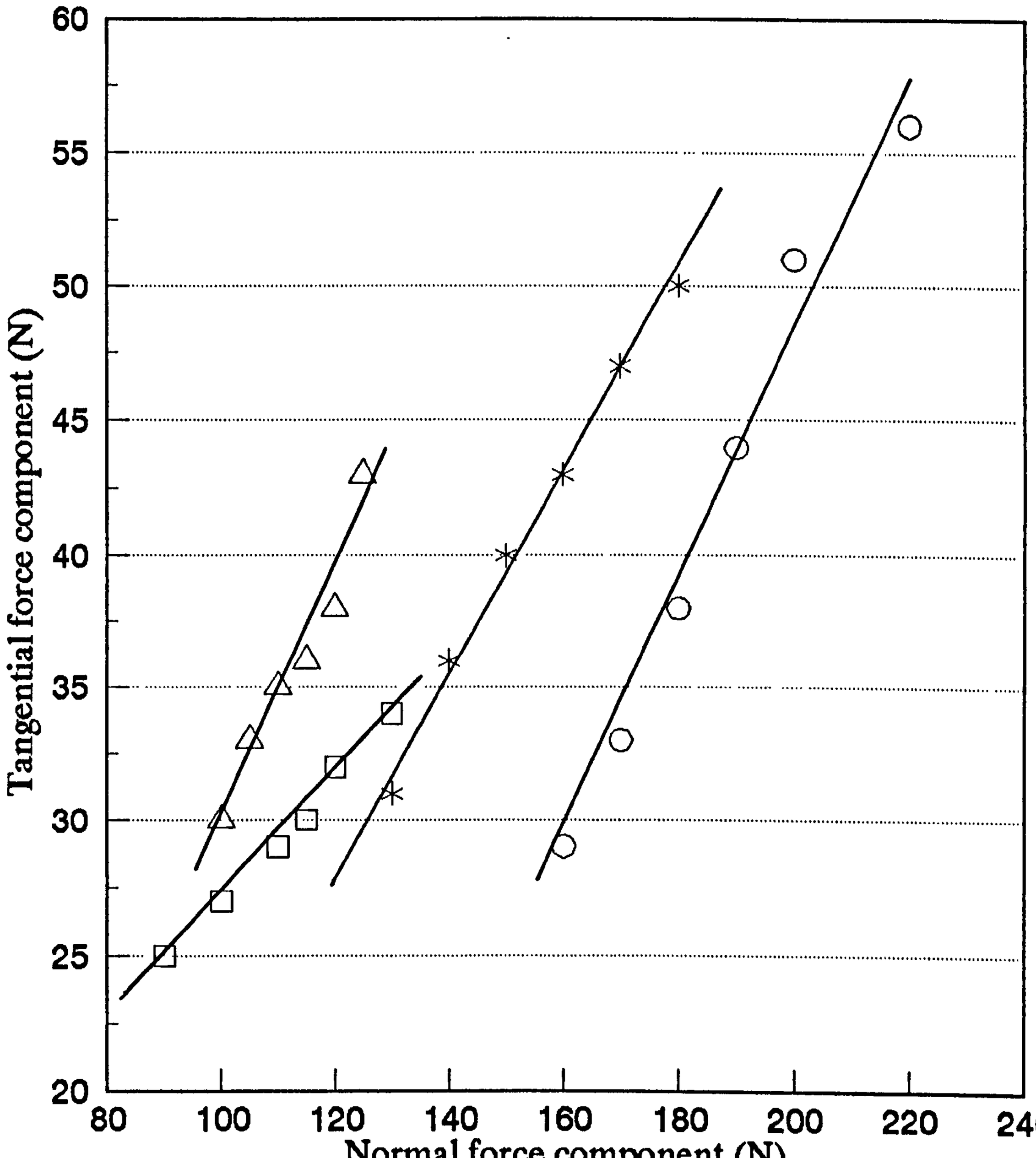

Figure 7.20 - Relationship between tangential and normal grinding force components for workpiece materials M1 (□), T1 (△), M42 (o) and T4 (*).

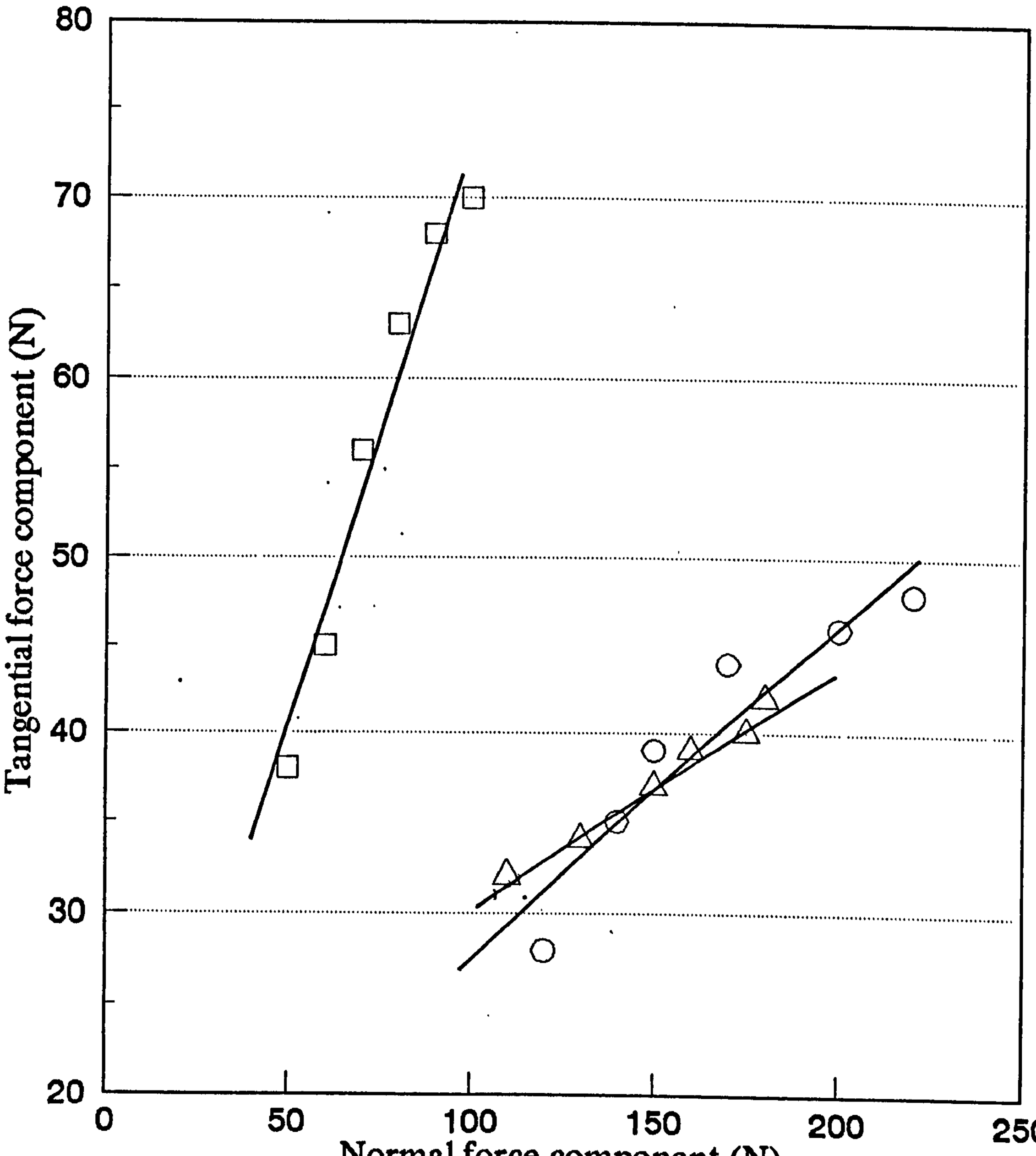

Figure 7.21 - Relationship between tangential and normal grinding force components for workpiece materials T15 (□), D3 (△) and D2 (o).

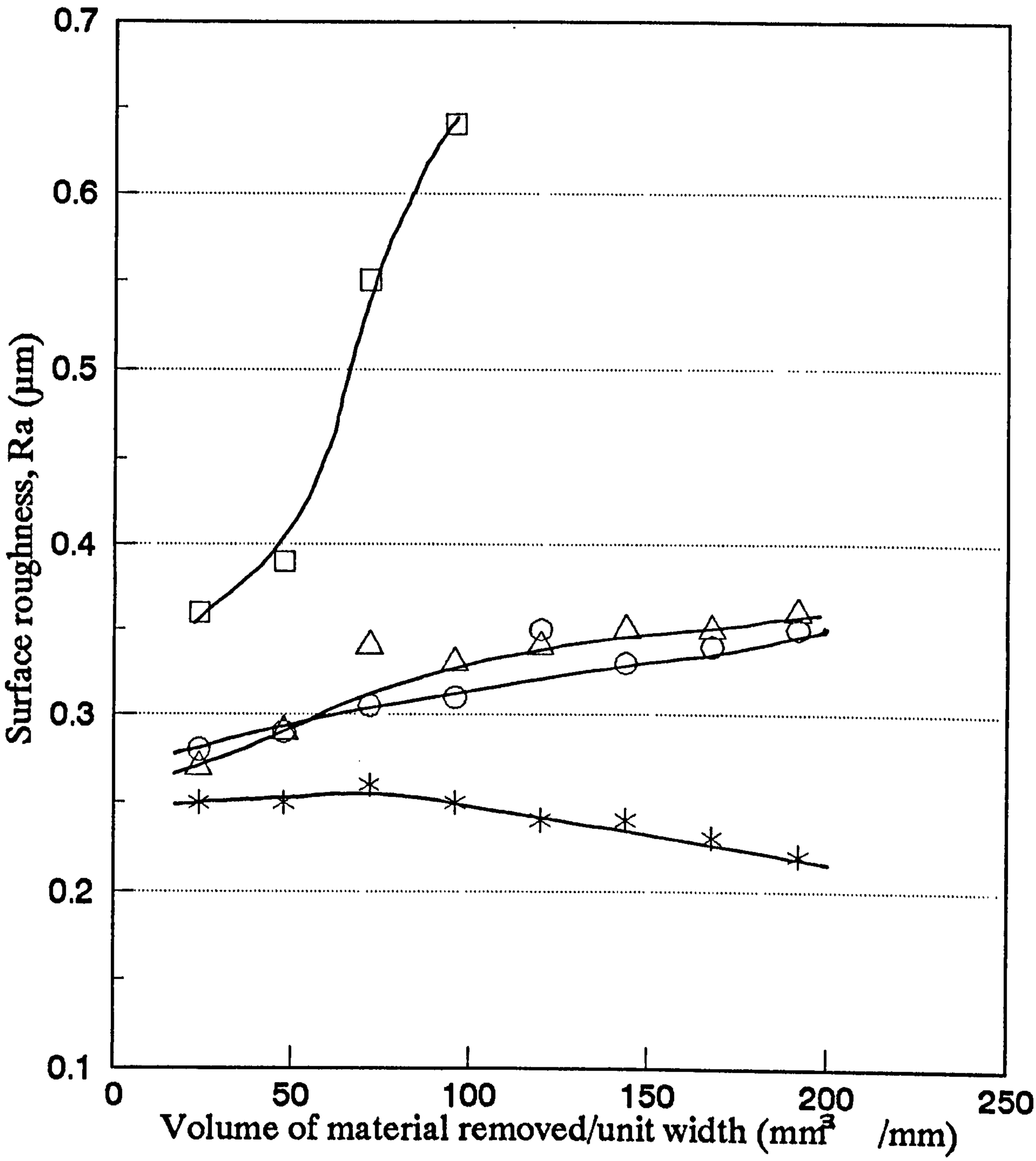

Figure 7.22 - Effect of volume of material removed per unit width on the surface roughness of workpiece materials M15 (□), ASP23 (△), M2 (o) and 01 (*).

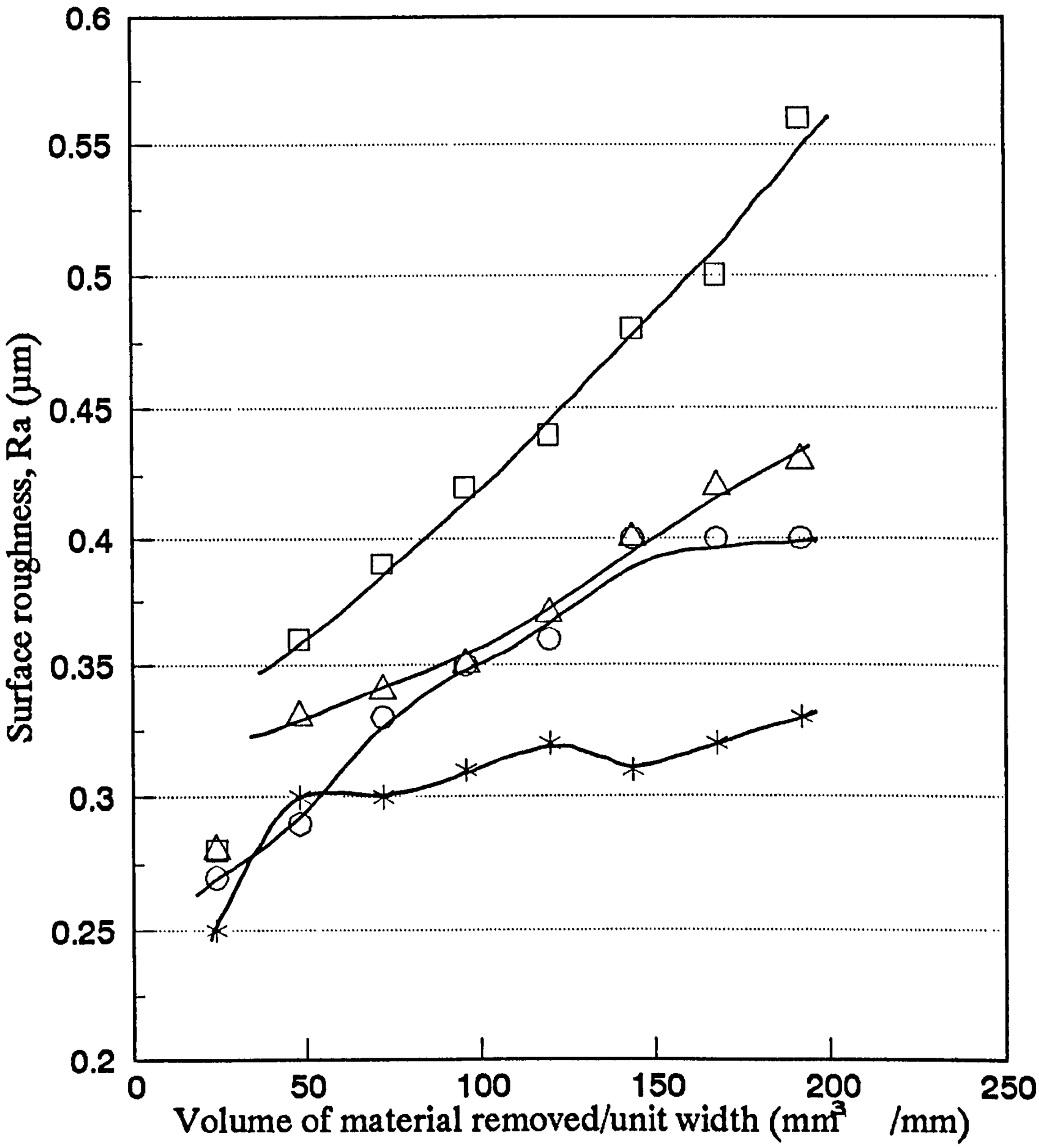

Figure 7.23 - Effect of volume of material removed per unit width on the surface roughness of workpiece materials T4 (□), M42 (△), T1 (o) and M1 (*).

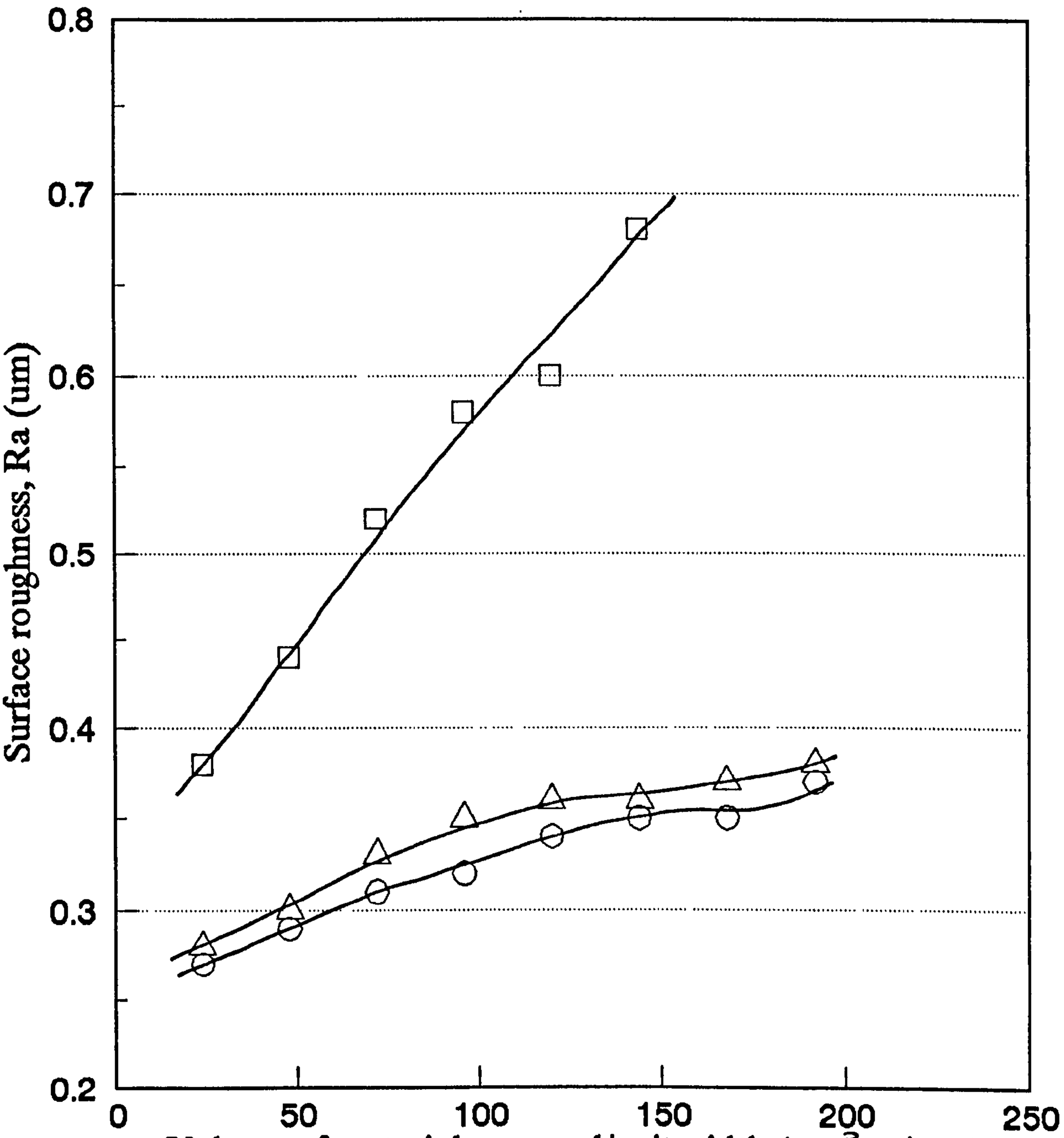

Figure 7.24 - Effect of volume of material removed per unit width on the surface roughness of workpiece materials T15 (□), D3 (△) and D2 (o).

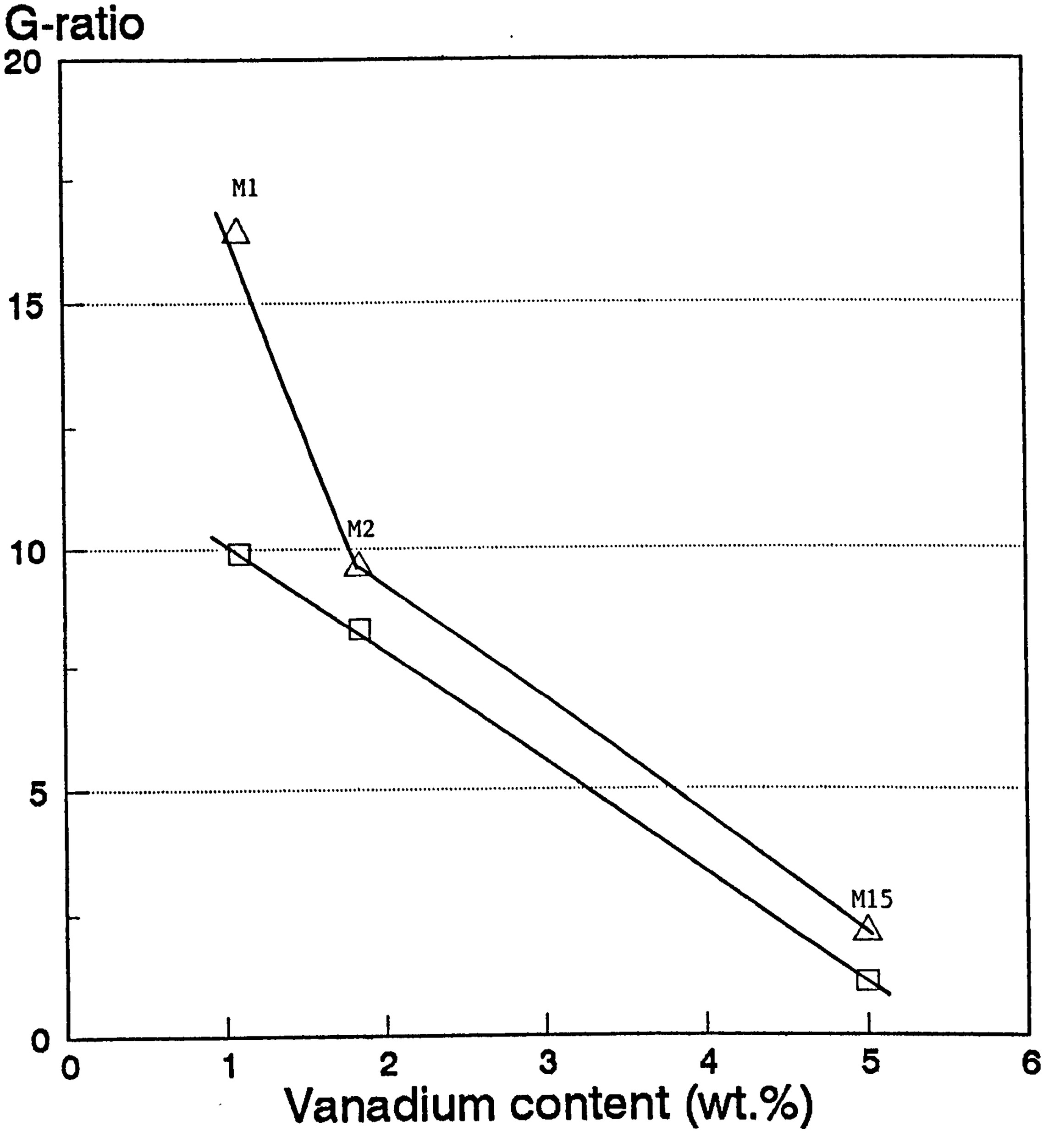

Figure 7.25 - Effect of vanadium content on the wheel wear parameter (G-ratio) when grinding workpiece materials M1, M2 and M15. The results are also dependent on the bond composition used in the abrasive structure. In this work bond type R (□) and X (△) are compared.

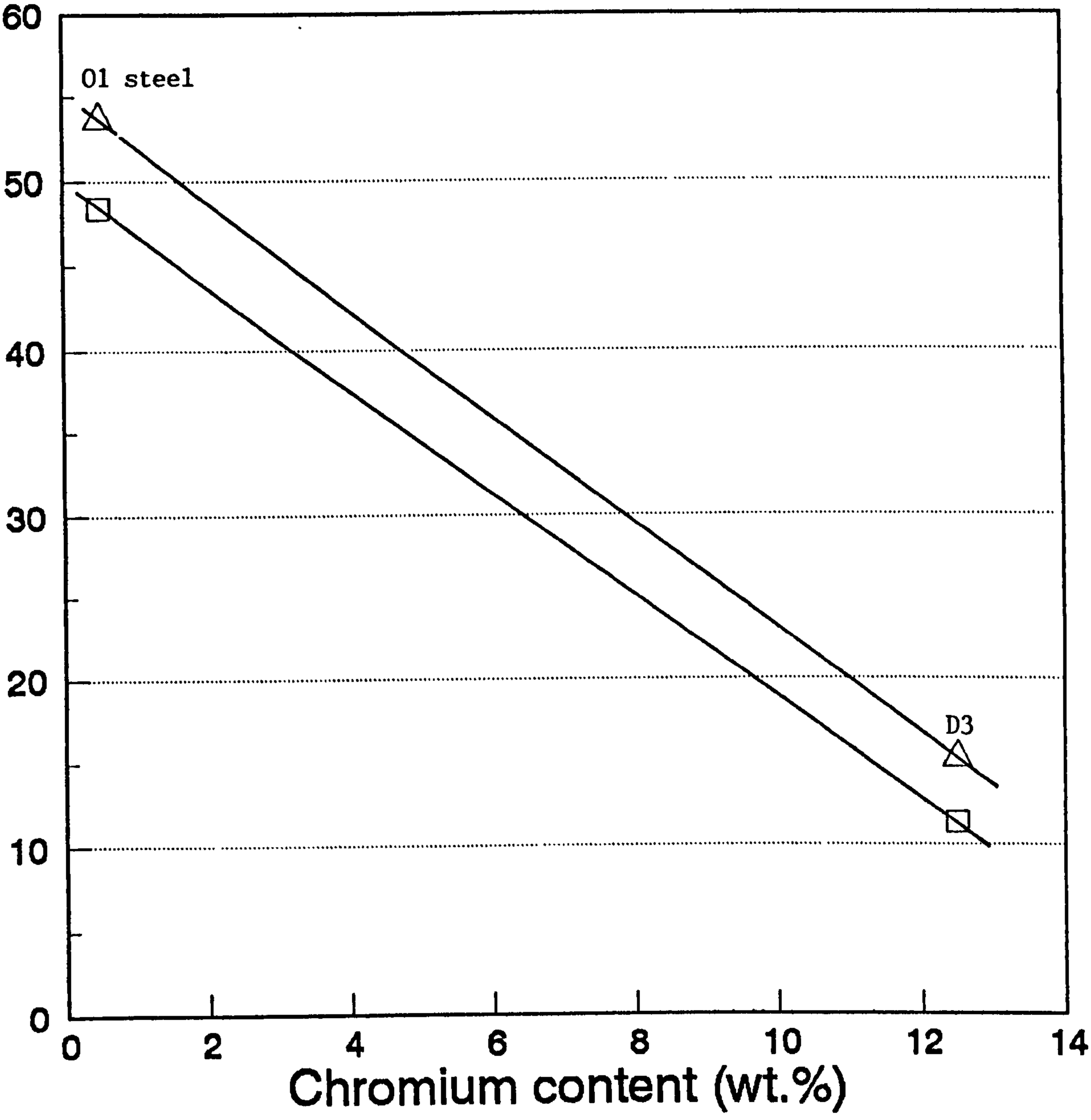

Figure 7.26 - Effect of chromium content on the wheel wear parameter when grinding workpiece materials 01 and D3 die steel. The results are also dependent on the bond composition used in the abrasive structure. In this work, bond type R (□) and X (△) are compared.

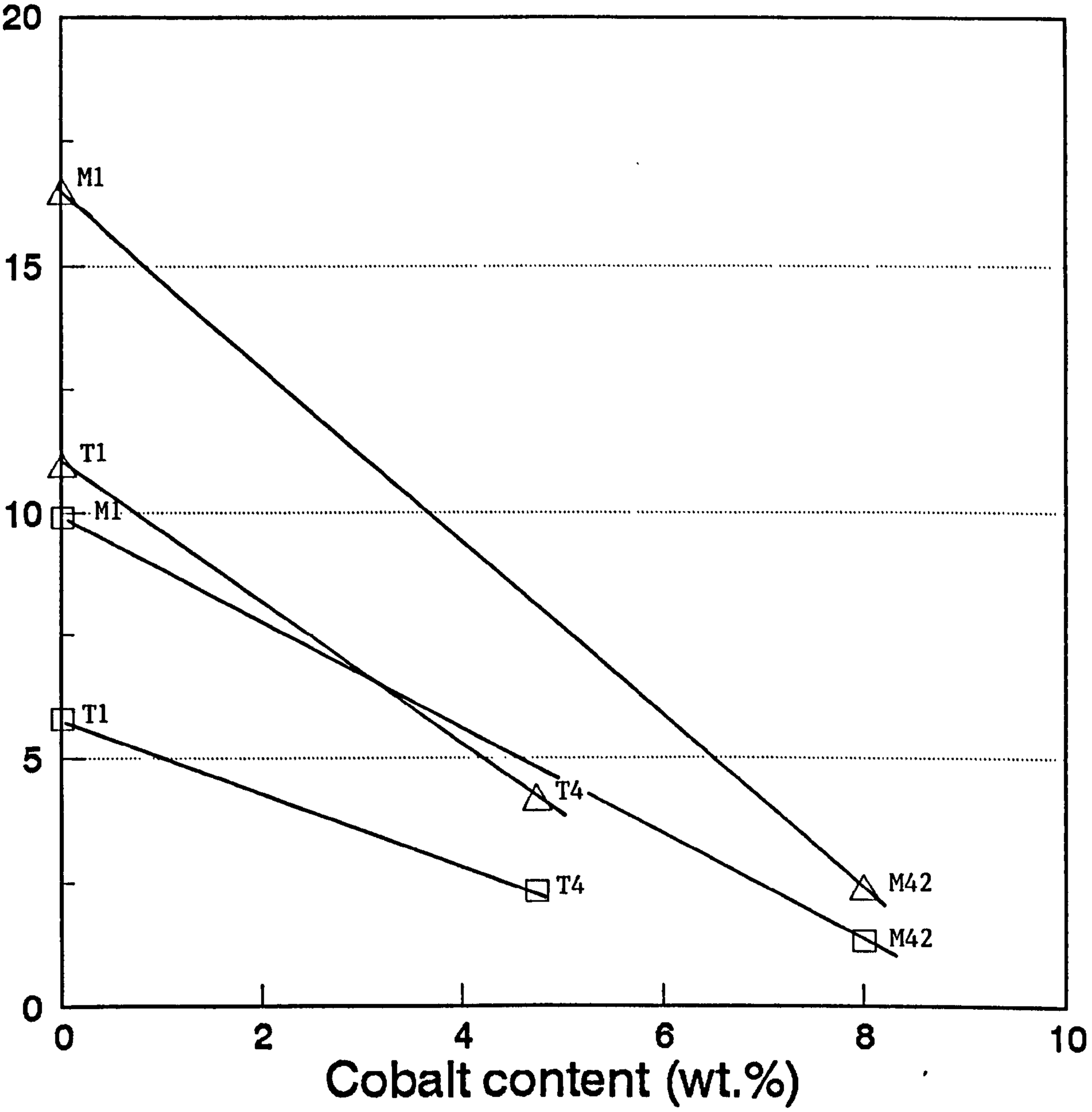

Figure 7.27 - Effect of cobalt content on the wheel-wear parameter (G-ratio) when grinding workpiece materials M1, M42, T1 and T4. The results are also dependent on the bond used in the abrasive structure. The bonds compared in this case are type R (□) and type X (△).

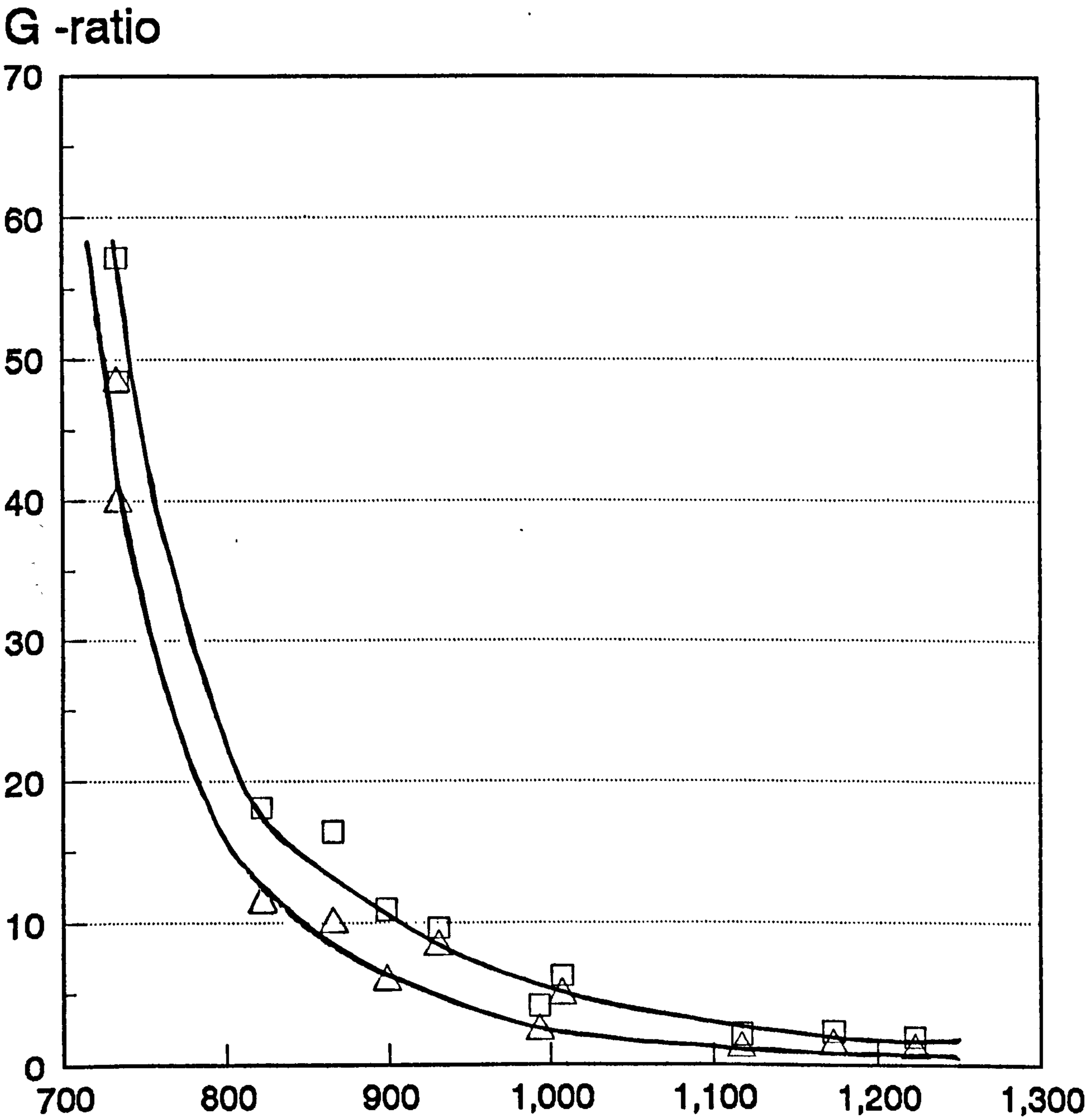

Figure 7.28 - Effect of abrasive number on the wheel-wear parameter (G-ratio) using bond compositions R (△) and X (□) in the abrasive structure.

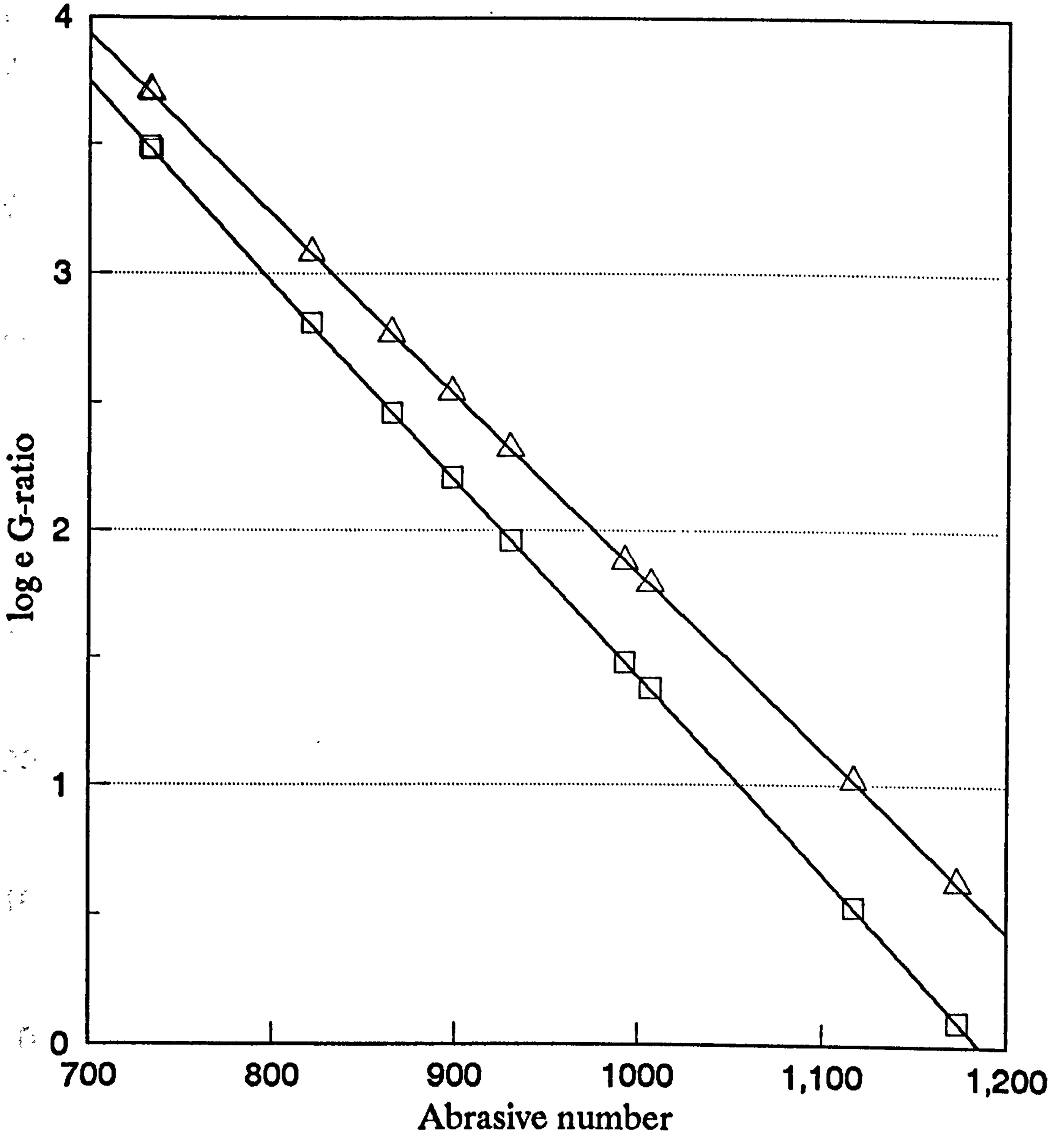

Figure 7.29 - Effect of abrasive number on log G-ratio for various workpiece materials using bond compositions R (□) and X (△) in the abrasive structure.

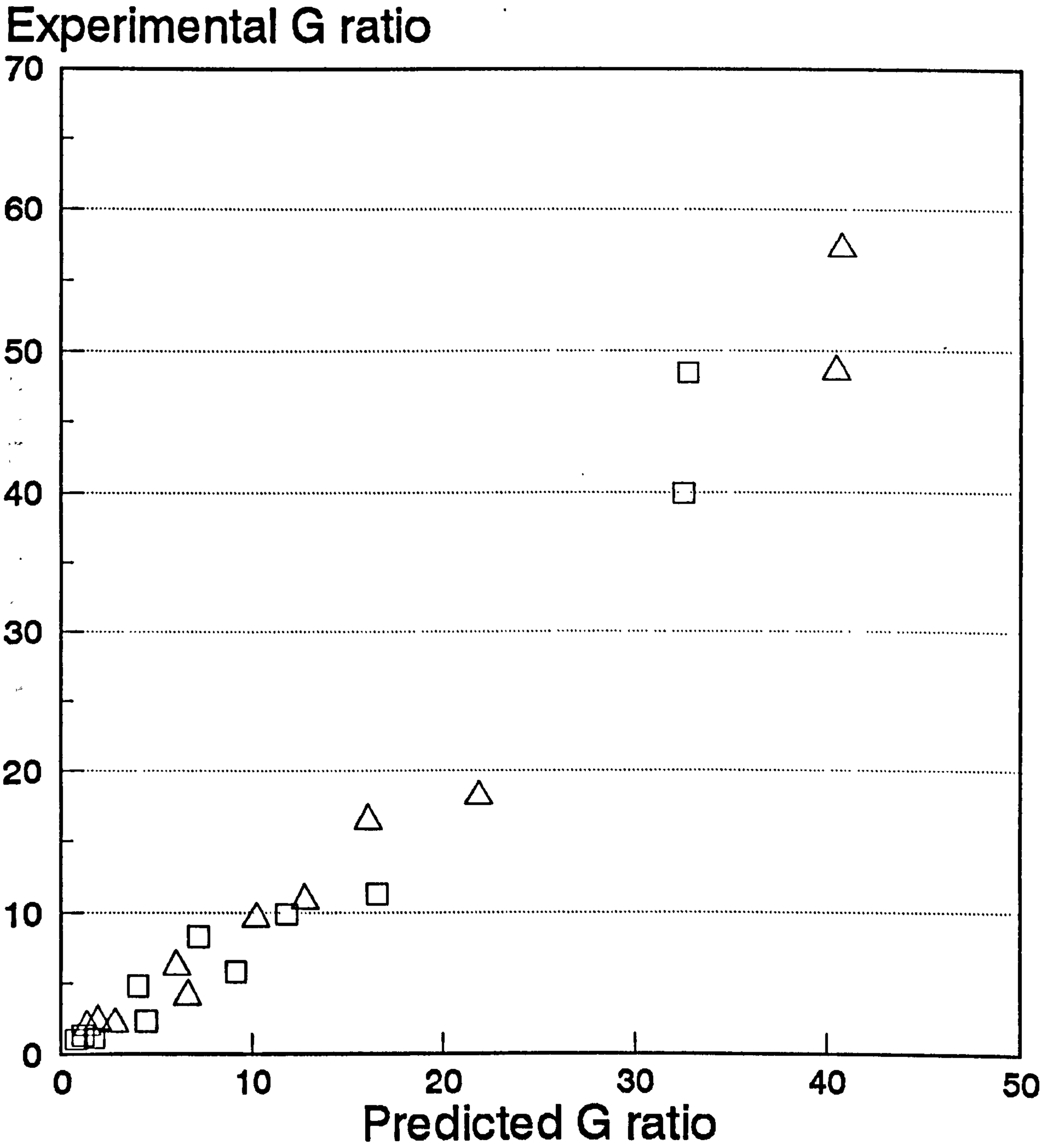

Figure 7.30 - Correlation between experimental and predicted G-ratios using the empirical relationships for bond compositions R (□) and X (△) grinding a variety of workpiece materials. The empirical relationship used is given by equation 7.19.

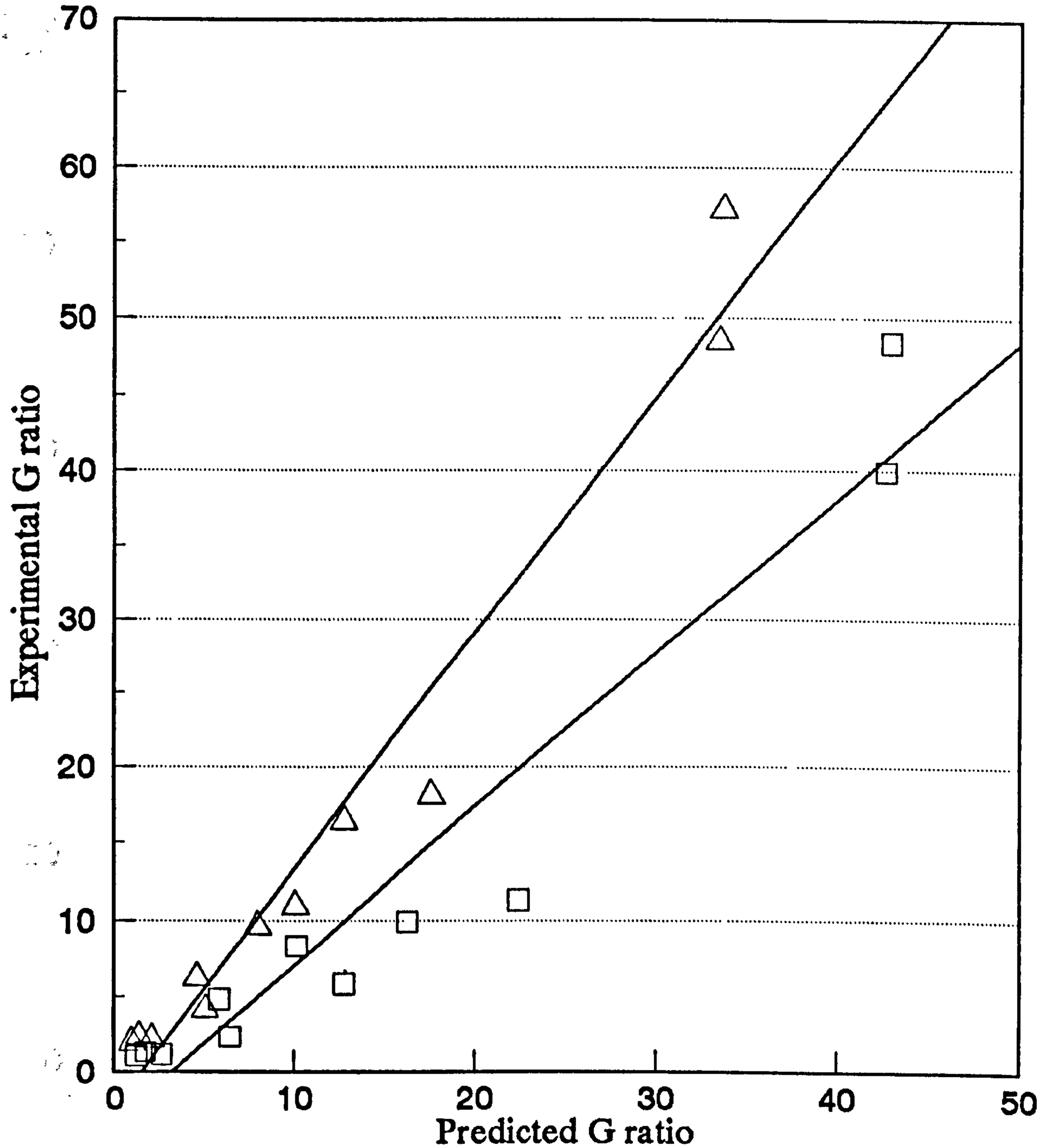

Figure 7.31 - Correlation between experimental and predicted G-ratios using the empirical relationships for bond composition R (□) and X (△). The empircial relationship used is given by equation 7.21a.

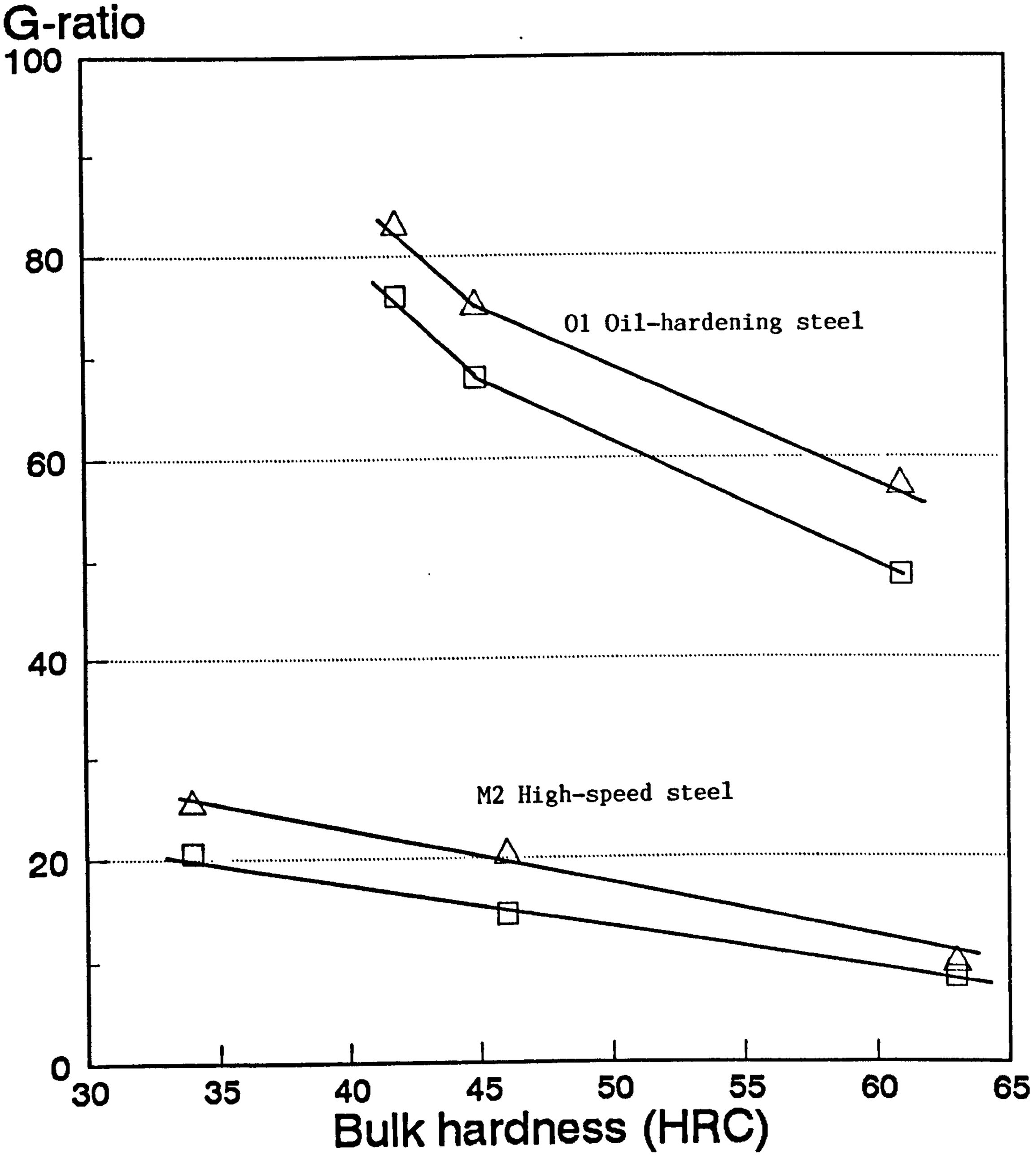

Figure 7.32 - Effect of bulk hardness on the wheel-wear parameter (G-ratio) for M2 and 01 workpiece materials using bond composition R (□) and X (△).

% Clay	% Flux	% Quartz	% Liq.	% Mullite	% Silica	Mix
40	10	50	19.88	21.32	58.8	
50	10	40	22.05	26.83	51.12	A
60	10	30	24.27	32.49	43.23	B
70	10	20	25.56	38.32	35.12	C
80	10	10	28.92	44.32	26.76	D
90	10	0	31.35	50.50	18.15	
40	15	45	26.04	21.64	52.32	
50	15	35	28.29	27.13	44.58	
60	15	25	30.60	32.80	36.60	E
70	15	15	32.97	38.62	28.41	F
80	15	5	35.41	44.72	19.87	
40	20	40	31.86	21.76	46.38	
50	20	30	34.49	27.46	38.05	G
60	20	20	36.88	33.11	30.01	H
70	20	10	39.34	38.92	21.74	J
80	20	0	41.87	44.89	13.24	
40	25	35	38.26	22.28	39.46	
50	25	25	40.67	27.76	31.57	
60	25	15	43.14	33.41	23.45	K
70	25	5	45.68	39.21	15.11	
75	25	0	46.98	42.17	10.85	
40	30	30	44.33	22.60	33.07	
50	30	20	46.82	28.08	25.10	L
60	30	10	49.37	33.71	16.92	M
70	30	0	51.99	39.50	8.51	
40	35	25	50.38	22.92	26.70	
50	35	15	52.93	28.28	18.69	
60	35	5	55.57	34.00	10.43	
65	35	0	56.92	36.88	6.20	
40	40	20	56.39	23.23	20.38	
50	40	10	59.03	28.69	12.28	N
60	40	0	61.74	34.31	3.95	
40	50	10	68.35	23.85	7.8	P
30	50	20	65.63	18.56	15.81	Q
20	50	30	63.00	13.39	23.61	R
30	60	10	77.33	19.19	3.48	S
20	60	20	74.59	14.05	11.36	T
10	60	30	75.79	9.52	14.69	U
25	70	5	87.46	12.54	-	V
20	70	10	86.82	13.18	-	W
15	80	5	98.91	1.09	-	X
10	80	10	98.66	1.34	-	Y

Table 4.1 Equilibrium Constitution Data of Bond Mixtures at 985°C.

Mixture	Apparent Porosity (%)	Liquid Content (%) at 985°C
A	10.52	22.05
B	7.51	24.27
C	6.14	26.56
D	3.56	28.92
E	5.71	30.60
F	4.71	32.97
G	5.43	34.49
H	1.79	36.88
J	1.03	39.34
K	0.71	43.14
L	1.52	46.82
M	10.52	49.37
N	0.48	59.03
P	0.06	68.35
Q	N/A	65.63
R	0.42	63.00
S	N/A	77.33
T	0.035	74.59
U	N/A	75.79
V	0.021	87.46
W	0.053	86.82
X	0.012	98.91
Y	N/A	98.66

Table 4.2 Statistical correlation of apparent porosity values of bond mixtures fired at 1150°C with calculated equilibrium liquid contents at 985°C.

Mixture	Apparent Porosity (Measured) %	% Silica at 985°C Thermal Equilibrium
A	10.52	51.12
B	7.51	43.24
C	6.41	35.12
D	3.56	26.76
E	5.71	36.60
F	4.71	28.41
G	5.43	38.05
H	1.79	30.01
J	1.03	21.74
K	0.71	23.45
L	1.52	25.10
M	10.52	16.92
N	0.48	12.28
P	0.075	7.80
Q	N/A	15.81
R	3.34	23.61
S	N/A	3.48
T	1.172	11.36
U	N/A	14.69
V	0.061	-
W	0.043	-
X	0.026	-
Y	N/A	-

Table 4.3 Statistical correlation of apparent porosity and equilibrium silica constitution of bond mixtures at 1150°C.

Mixture	Water Absorption (Measured %)	% Liquid at 985°C (Thermal Equilibrium)	% Silica at 985°C (Thermal Equilibrium)
A	10.42	22.05	51.12
B	7.56	24.277	43.24
C	6.14	26.56	35.12
D	3.05	28.92	26.76
E	6.25	30.60	36.60
F	3.52	32.97	28.41
G	7.52	34.49	38.05
H	4.74	36.88	30.01
J	2.14	39.34	21.74
K	2.06	43.14	23.45
L	3.74	46.82	25.10
M	1.60	49.37	16.92
N	1.75	59.03	12.28
P	0.61	68.35	7.80
Q	N/A	65.63	15.81
R	5.43	63.00	23.61
S	N/A	77.33	3.48
T	2.69	74.59	11.36
U	N/A	75.79	14.69
V	0.46	87.46	0.00
W	0.26	86.82	0.00
X	1.87	98.91	0.00
Y	N/A	98.66	0.00

Table 4.4 Statistical correlation of water absorption values of bond mixtures fired at 1150°C with calculated equilibrium constitution liquid and silica contents at 985°C.

Mixture	W.A. (Theo.)	W.A. (Exp.)	A.P. (Theo.)	A.P. (Exp.)
A	10.68	10.42	9.87	10.52
B	7.96	7.56	7.03	7.51
C	5.25	6.14	4.10	6.14
D	2.45	3.05	1.08	3.52
E	6.344	6.25	5.88	5.71
F	3.614	3:52	2.94	4.71
G	7.404	7.52	7.61	5.43
H	4.734	4.74	4.74	1.79
J	1.984	2.14	1.79	1.03
K	3.134	2.06	3.61	0.71
L	4.244	3.74	5.36	1.52
M	1.544	1.60	2.48	10.52
N	1.114	1.75	3.14	0.48
P	0.702	0.61	3.78	0.07
Q	3.32	N/A	6.54	N/A
R	5.87	5.43	9.23	3.34
S	0.301	N/A	1.53	N/A
T	2.87	2.69	7.09	1.17
U	4.27	N/A	8.89	N/A
V	0.367	0.46	5.69	0.06
W	0.281	0.26	5.51	0.04
X	1.91	1.87	8.9	0.02
Y	1.87	N/A	8.83	N/A

Table 4.5 Comparison between experimental and theoretical vitrification measures. W.A. = % water absorption; A.P. = % apparent porosity.

1150°C	A	B	C	D	E	F	G	H	J	K	L	M	N	P	R	T	V	W	X	Y
1hr	24.50	21.72	21.41	18.45	19.26	17.84	19.20	15.17	12.65	12.10	12.42	7.20	5.32	2.08	5.02	4.29	4.02	3.05	2.15	N/A
3hr	23.89	20.35	18.08	15.78	18.52	16.42	18.11	13.67	9.31	9.24	11.62	5.74	3.69	1.31	4.14	2.97	2.15	1.56	1.34	N/A
6hr	22.14	21.06	17.21	14.24	15.17	12.01	15.41	11.42	7.98	6.94	7.95	3.54	1.47	0.64	3.47	2.63	1.07	0.75	0.85	N/A
10hr	20.60	16.42	15.18	11.58	13.40	11.11	13.31	10.70	6.42	4.87	7.12	2.06	0.75	0.23	4.43	1.47	0.65	0.64	0.44	N/A
20hr	16.14	12.13	12.43	8.76	10.74	9.654	10.61	7.61	4.54	1.23	5.08	16.14	0.42	0.12	3.49	1.35	0.32	0.31	0.23	N/A
30hr	12.42	10.76	9.89	6.04	7.59	5.82	7.58	4.52	2.05	0.63	3.47	12.42	0.45	0.09	3.37	1.24	0.21	0.17	0.15	N/A
40hr	10.52	7.51	6.14	3.56	5.71	4.71	5.43	1.79	1.03	0.71	1.52	10.52	0.48	0.075	3.34	1.172	0.061	0.043	0.026	N/A
1200°C																				
1hr	23.44	19.30	17.23	14.25	16.51	14.13	16.75	12.37	8.53	8.38	9.24	4.66	3.01	1.20	8.56	2.42	1.98	1.12	0.25	N/A
3hr	22.25	17.95	15.47	11.83	16.02	12.02	15.43	10.76	6.61	6.47	7.89	3.48	2.06	0.65	1.75	1.26	1.03	0.67	0.13	N/A
6hr	20.12	17.41	13.93	9.96	12.46	8.89	13.04	8.34	5.11	4.58	5.23	2.15	0.87	0.21	1.56	0.69	0.57	0.32	0.075	N/A
10hr	18.10	14.25	12.41	8.39	10.74	7.93	10.86	7.93	3.74	3.13	4.72	1.22	0.51	0.15	1.42	0.64	0.26	0.19	0.033	N/A
20hr	14.40	10.92	9.98	5.85	8.02	6.09	8.18	5.01	2.75	0.91	3.13	1.36	0.308	0.08	1.37	0.61	0.11	0.11	0.02	N/A
30hr	12.26	9.46	7.53	3.85	5.78	4.15	5.72	3.22	1.11	0.53	2.15	0.44	0.287	0.06	1.30	0.58	0.05	0.07	0.02	N/A
40hr	10.55	7.34	5.28	2.54	4.63	3.37	4.38	1.75	0.36	0.45	0.95	0.39	0.262	0.055	1.25	0.55	0.031	0.014	0.01	N/A
1250°C																				
1hr	21.62	16.89	12.95	9.75	13.75	10.41	14.20	9.58	4.42	4.67	6.07	2.13	0.72	0.43	1.25	0.85	0.31	0.26	0.07	N/A
3hr	20.62	15.56	12.86	7.81	13.53	7.63	12.80	8.01	3.91	3.71	4.26	1.61	0.33	0.25	0.64	0.41	0.15	0.14	0.034	N/A
6hr	18.19	13.75	10.75	5.69	9.76	5.78	10.67	5.26	2.25	2.22	2.61	0.76	0.27	0.09	0.51	0.29	0.07	0.05	0.021	N/A
10hr	15.61	12.08	9.63	5.21	8.08	4.76	8.40	5.17	1.13	1.39	2.32	0.34	0.25	0.04	0.43	0.26	0.04	0.05	0.016	N/A
20hr	13.48	10.23	6.73	3.17	6.25	2.71	6.26	2.65	0.69	0.95	1.27	0.16	0.19	0.041	0.39	0.26	0.04	0.04	0.15	N/A
30hr	12.11	8.24	5.18	1.67	3.97	2.48	3.93	1.93	0.17	0.37	0.84	0.13	0.12	0.02	0.34	0.17	0.03	0.025	0.101	N/A
40hr	10.59	7.17	4.43	1.53	3.71	2.03	3.33	1.72	0.14	0.19	0.38	0.135	0.06	0.02	0.32	0.17	0.02	0.01	0.010	N/A

Table 4.6 Apparent porosity results at various heat treatment schedules for all bond mixtures.

1100°C	H	J	K	L	N	P	R	T	V	W	X
10hrs	13.53	8.40	6.59	9.16	4.89	4.23	6.47	6.01	5.73	4.87	3.97
20hrs	11.40	6.81	5.81	7.52	2.13	2.04	5.14	3.46	3.16	2.61	1.62
30hrs	10.60	5.43	4.06	7.13	1.87	1.51	4.21	2.71	2.07	1.44	0.89
40hrs	9.53	4.21	3.25	6.71	1.73	0.65	3.94	2.34	1.14	0.75	0.23
50hrs	5.75	2.11	2.56	5.93	1.42	0.60	2.81	2.05	1.17	0.81	1.54
60hrs	4.43	1.78	1.96	4.41	1.15	0.47	1.47	2.13	1.21	0.88	1.62
70hrs	2.46	1.53	1.11	3.67	1.18	-	-	-	-	-	-
80hrs	1.03	1.22	1.25	1.53	1.24	-	-	-	-	-	-

Table 4.7a Optimum vitrification data (apparent porosity) for bond mixtures at 1100°C.

1150°C	H	J	K	L	N	P	R	T	V	W	X
10hrs	10.70	6.42	4.87	7.12	0.75	2.08	5.02	4.29	4.02	3.05	2.15
20hrs	7.61	4.54	1.23	5.08	0.42	0.12	3.49	1.35	0.32	0.31	0.23
30hrs	4.52	2.05	0.63	3.47	0.45	0.09	3.37	1.24	0.21	0.17	0.25
40hrs	1.79	1.03	0.71	1.52	0.48	0.075	3.34	1.172	0.061	0.243	0.326
50hrs	1.23	0.85	0.75	0.48	0.47	0.061	3.13	1.23	0.07	0.26	0.35
60hrs	1.21	0.83	0.12	0.24	0.56	0.069	3.21	1.35	0.073	0.28	0.41
70hrs	1.03	0.75	0.37	0.16	0.55	-	-	-	-	-	-
80hrs	1.14	1.04	0.52	0.22	0.59	-	-	-	-	-	-

Table 4.7b Optimum vitrification data (apparent porosity) for bond mixtures at 1150°C.

1200°C	H	J	K	L	N	P	R	T	V	W	X
10hrs	7.93	3.74	3.13	4.72	0.51	0.15	1.42	0.64	0.26	0.19	0.033
20hrs	5.01	2.75	0.91	3.13	0.308	0.08	1.37	0.61	0.11	0.11	0.08
30hrs	3.22	1.11	0.53	2.15	0.287	0.06	1.30	0.58	0.05	0.17	0.12
40hrs	1.75	0.36	0.45	0.95	0.262	0.055	1.35	0.55	0.081	0.314	0.15
50hrs	1.69	0.08	0.32	0.24	0.06	0.063	1.38	0.71	0.09	0.23	0.17
60hrs	1.03	0.07	0.35	0.16	0.07	-	-	-	-	-	-
70hrs	1.21	0.05	0.36	0.22	0.09	-	-	-	-	-	-
80hrs	1.40	0.21	0.39	0.24	0.12	-	-	-	-	-	-

Table 4.7c Optimum vitrification data (apparent porosity) for bond mixtures at 1200°C.

1250°C	H	J	K	L	N	P	R	T	V	W	X
10hrs	5.17	1.13	1.39	2.32	0.25	0.04	0.43	0.26	0.04	0.05	0.016
20hrs	2.42	0.97	0.64	1.19	0.196	0.025	0.35	0.23	0.045	0.08	0.03
30hrs	1.93	0.17	0.37	0.84	0.22	0.02	0.34	0.27	0.08	0.13	0.04
40hrs	1.72	0.14	0.19	0.38	0.26	0.025	0.38	0.31	0.12	0.16	0.04
50hrs	1.14	0.05	0.26	0.15	0.27	0.04	0.43	0.37	0.17	0.21	0.05
60hrs	1.33	0.02	0.27	0.15	0.29	-	-	-	-	-	-
70hrs	1.37	0.08	0.32	0.17	0.34	-	-	-	-	-	-
80hrs	1.42	0.09	0.39	0.21	0.41	-	-	-	-	-	-

Table 4.7d Optimum vitrification data (apparent porosity) for bond mixtures at 1250°C.

1150°C	H	J	K	L	N	P	R	T	V	W	X
1hr	2.204	2.261	2.25	2.23	2.34	2.379	2.443	2.42	2.396	2.385	2.361
3hr	2.236	2.314	2.23	2.241	2.382	2.391	2.453	2.441	2.41	2.397	2.39
6hr	2.256	2.41	2.347	2.297	2.419	2.407	2.47	2.463	2.44	2.41	2.428
10hrs	2.269	2.42	2.378	2.331	2.424	2.436	2.49	2.49	2.48	2.43	2.439
20hrs	2.271	2.45	2.404	2.381	2.446	2.457	2.51	2.491	2.49	2.46	2.43
30hrs	2.282	2.45	2.42	2.441	2.464	2.463	2.69	2.534	2.49	2.47	2.44
40hrs	2.289	2.47	2.446	2.448	2.479	2.471	2.74	2.61	2.53	2.51	2.48

Table 4.8a Effect of soaking time on bulk density (bond samples) at 1150°C. Bulk density units are g/cm³.

1200°C	H	J	K	L	N	P	R	T	V	W	X
1hr	2.718	2.425	2.375	2.346	2.438	2.476	2.56	2.63	2.64	2.59	2.542
3hr	2.309	2.446	2.397	2.406	2.446	2.491	2.59	2.65	2.69	2.632	2.567
6hr	2.424	2.472	2.462	2.418	2.445	2.53	2.634	2.67	2.79	2.639	2.591
10hrs	2.428	2.483	2.457	2.432	2.447	2.56	2.697	2.68	2.81	2.71	2.645
20hrs	2.432	2.473	2.465	2.441	2.447	2.56	2.71	2.69	2.834	2.73	2.691
30hrs	2.436	2.485	2.475	2.449	2.447	2.593	2.73	2.69	2.891	2.81	2.74
40hrs	2.439	2.496	2.476	2.448	2.448	2.614	2.731	2.718	2.94	2.83	2.79

Table 4.8b Effect of soaking time on bulk density (bond samples) at 1200°C. Bulk density units are g/cm³.

STRUCTURE NO	BOND VOL %	SOAKING TIME						
		1hr	3hr	6hr	10hrs	20hrs	30hrs	40hrs
5	6.0	2.17	2.162	2.159	2.156	2.163	2.164	2.165
7	10	2.225	2.227	2.248	2.235	2.237	2.236	2.236
10	16	2.303	2.309	2.317	2.342	2.345	2.228	2.229
12	20	2.385	2.394	2.397	2.396	2.388	2.391	2.390

Table 4.9 The effect of soaking time on the bulk density of alumina wheel samples fired at 1200°C for a J-grade grinding wheel manufactured with 60 grit white alumina, bond mixture P, and cold pressed to structure numbers 5, 7, 10, 12. The corresponding volume porosities are 44%, 42%, 40%, and 38%, respectively. Bulk density units are g/cm³.

BOND MIXTURE	SOAKING TEMPERATURE			
	1100°C	1150°C	1200°C	1250°C
H	80	70	60	50
J	80	70	70	60
K	70	60	50	40
L	80	70	60	50
N	60	40	40	20
P	60	50	40	30
R	60	50	30	30
T	50	40	30	20
V	40	40	30	20
W	40	30	20	10
X	30	20	10	10

Table 4.10 Data on optimum heat treatment for bond mixtures. The optimum soaking period, in hours, are for the temperatures shown. The rate of heating was 2.91°C/min.

BOND MIXTURE	EXPERIMENTAL FACTOR (Q/R)	RATE EQUATION	
		THEORETICAL	EMPIRICAL
H	1854.6	$K_t \frac{e^{1.47}}{e^{(1854.6/t+273)}}$	$K_t = e^{0.001(t-985)}$
J	2883.8	$K_t \frac{e^{2.29}}{e^{(2883.8/t+273)}}$	$K_t = e^{0.002(t-985)}$
K	4673.2	$K_t \frac{e^{3.71}}{e^{(4673.2/t(273)}}$	$K_t = e^{0.0025(t-985)}$
L	6527.8	$K_t \frac{e^{5.19}}{e^{(6527.8/t+273)}}$	$K_t = e^{0.0035(t-985)}$
N	5631.4	$K_t \frac{e^{4.47}}{e^{(5631.4/t+273)}}$	$K_t = e^{0.0032(t-985)}$
P	11400	$K_t \frac{e^{9.062}}{e^{(11400/t+273)}}$	$K_t = e^{0.006(t-985)}$
R	16980	$K_t \frac{e^{13.49}}{e^{(16980/t+273)}}$	$K_t = e^{0.01(t-985)}$
T	13780	$K_t \frac{e^{10.95}}{e^{(13780/t+273)}}$	$K_t = e^{0.007(t-985)}$
V	5580	$K_t \frac{e^{4.43}}{e^{(5580/t+273)}}$	$K_t = e^{0.003(t-984)}$
W	13800	$K_t \frac{e^{10.97}}{e^{(131800/t+273)}}$	$K_t = e^{0.008(t-985)}$
X	21980	$K_t \frac{e^{17.47}}{e^{(21980/t+273)}}$	$K_t = e^{0.012(t-985)}$

Table 4.11 Experimental factors and theoretical/empirical rate equations.

BOND MIXTURE	TEMPERATURE													
	1100°C (1371K)		1150°C (1423K)		1200°C (1473K)		1250°C (1523K)		1300°C (1573K)		1350°C (1623K)		1400°C (1673K)	
	K_t theo.	K_t emp.	K_t theo.	K_t emp.	K_t theo.	K_t emp.	K_t theo.	K_t emp.	K_t theo.	K_t emp.	K_t theo.	K_t emp.	K_t theo.	K_t emp
H	1.131	1.122	1.186	1.18	1.24	1.24	1.29	1.30	1.34	1.37	1.39	1.44	1.44	1.51
J	1.21	1.25	1.301	1.39	1.394	1.53	1.49	1.69	1.58	1.87	1.67	2.07	1.76	2.29
K	1.36	1.33	1.531	1.51	1.71	1.71	1.89	1.94	2.09	2.19	1.29	2.49	1.5	1.82
L	1.546	1.495	1.827	1.78	2.14	2.12	2.47	2.53	3.35	3.01	3.21	3.58	3.63	4.27
N	1.44	1.45	1.67	1.69	1.91	1.99	2.16	2.33	2.43	2.74	2.72	3.21	3.02	3.77
P	2.136	1.99	2.85	2.69	3.75	3.63	4.84	4.90	6.13	6.62	7.67	8.93	9.46	12.0
R	3.07	3.16	4.74	5.21	7.11	8.58	10.39	14.15	14.81	23.3	20.65	38.47	28.23	63.43
T	2.49	2.24	3.54	3.17	4.93	4.50	6.7	6.39	8.93	9.07	11.7	12.87	15.07	18.26
V	1.441	1.41	1.61	1.64	1.89	1.90	2.15	2.21	2.42	2.57	2.69	2.98	2.98	3.47
W	2.51	2.51	3.57	3.74	4.96	5.58	6.75	8.33	8.99	12.43	11.79	18.54	1.52	27.66
X	4.31	3.97	7.56	7.24	12.78	13.19	20.86	24.05	33.0	43.81	50.76	79.83	76.09	145.47

Table 4.12 Data calculated from theoretical and empirical rate equations which show rate of vitrification (arb. units) for a range of temperatures.

Temperature (°C) Bond Mixture	1100 [1373K]	1150 [1423K]	1200 [1473K]	1250 [1523K]
H	103.38 (12.4%) 80	96.51 (13.96%) 70	88.57 (16.01%) 60	79.15 (18.28%) 50
J	103.89 (6.92%) 80	86.04 (9.23%) 60	99.4 (8.83%) 65	98.93 (9.82%) 60
K	101.19 (6.02%) 70	117.52 (5.87%) 70	93.41 (8.39%) 50	84.85 (10.46%) 40
L	128.55 (3.79%) 80	133.7 (4.35%) 70	113.67 (6.1%) 50	131 73 (6.28%) 50
N	91.89 (5.61%) 60	89.54 (6.76%) 50	83.5 (8.53%) 40	94.96 (8.81%) 40
P	131.95 (2.86%) 60	148.11 (3.45%) 50	157.08 (4.4%) 40	154.58 (6.08%) 30
R	188.03 (1.91%) 60	243.28 (2.44%) 50	223.33 (4.41%) 30	328.07 (4.98%) 30
T	128.31 (2.84%) 50	148.24 4.28%) 40	155.2 (4.74%) 30	144.49 (7.26%) 20
V	63.05 (8.53%) 40	72.76 (8.57%) 40	51.43 (41.1%) 30	46.45 (18.21%) 20
W	103.85 (3.44%) 40	112.39 (4.75%) 30	107.14 (7.41%) 20	79.46 (15.1%) 10
X	133.12 (2.84%) 30	158.11 (4.35%) 20	140.42 (8.97%) 10	231.8 (9.9%) 10

Table 4.13 Degree of vitrification data (empirical) for bond mixtures heat treated to various temperatures. Note: 1st entry is the total degree of vitrification (arbitary units); 2nd entry is % contribution to heating and cooling; 3rd entry is the optimum soaking time in hours.

Bond Mixture	Optimum vitrification temperature and soaking period (°C and hours)	
H	1100	80
J	1100	80
K	1150	70
L	1150	70
N	1250	40
P	1200	40
R	1250	30
T	1200	30
V	1150	40
W	1150	30
X	1250	10

Table 4.14 Optimum heat treatment schedules for grinding wheel bond mixtures.

Temperature (°C)	Rate of vitrification at soaking temperature		Difference
	K_t theoretical	K_t empirical	
1100	1.358	1.33	0.028 (1.04%)
1150	1.53	1.51	0.02 (0.067%)
1200	1.71	1.71	0.00 (0.00%)
1250	1.89	1.94	-0.05 (-1.3%)

Table 4.15 Error in calculating the rate of vitrification using empirical and theoretical rate equations for bond mixture K.

MIXTURE			% QUARTZ	% MULLITE		% CRISTOBALITE		% LIQUID	
% CLAY	% FELDSPAR	% QUARTZ	EXPERIMENTAL	EXPERIMENTAL	THEORETICAL	EXPERIMENTAL	THEORETICAL	EXPERIMENTAL	THEORETICAL
70	0	30	27.7	36.7	42.4	28.0	32.2	0.0	0.0
58	12	30	25.7	29.9	35.4	6.0	9.0	37.4	31.2
46	24	30	22.9	20.1	28.0	0.0	0.0	56.2	62.3
34	36	30	19.7	15.0	20.8	0.0	0.0	64.1	82.4
22	48	30	19.7	8.0	13.6	0.0	0.0	72.6	88.9
10	60	30	17.9	0.0	6.3	0.0	0.0	81.8	95.7

Table 5.1 Brindley and Ougland's experimental and theoretical constitutions of mixtures fired at 1200°C for 2 hours.

MIXTURE	% CLAY	% FLUX	% QUARTZ	% SILICA		% MULLITE		% LIQUID (GLASS)	
				EXPERIMENTAL	THEORETICAL	EXPERIMENTAL	THEORETICAL	EXPERIMENTAL	THEORETICAL
A	50	10	40	38.88	47.98	20.89	27.09	40.23	24.93
B	60	10	30	31.69	42.19	25.04	31.44	43.27	26.37
C	70	10	20	20.22	34.12	32.53	37.03	47.25	28.85
D	80	20	10	9.94	25.84	39.98	42.78	50.08	31.38
E	60	15	25	24.48	32.18	27.46	33.16	48.06	34.66
F	70	15	15	14.64	23.64	34.41	39.01	50.95	37.35
G	50	20	30	29.08	33.08	22.45	27.86	48.47	39.07
H	60	20	20	24.76	29.97	24.36	28.25	50.88	41.78
J	70	20	10	10.45	16.05	36.18	39.38	53.37	44.57
K	60	25	15	15.52	17.22	30.31	33.91	54.17	48.87
L	50	30	20	20.23	18.33	23.53	28.63	56.24	53.04
M	60	30	10	10.78	9.78	32.09	34.29	57.13	55.93
N	50	40	10	11.63	3.73	24.09	29.40	63.47	66.87
P	40	50	10	9.87	3.00	20.28	25.00	69.85	72.00
R	20	50	30	29.45	23.61	5.67	13.39	64.88	63.00
T	20	60	20	21.12	6.46	8.81	14.83	70.07	78.71
V	25	70	5	4.88	0.00	16.99	6.79	78.13	93.21
W	20	70	10	9.97	0.00	13.69	8.38	76.34	91.62
X	15	80	5	4.24	0.00	12.20	1.09	83.56	98.91
Y	10	80	10	11.04	0.00	6.79	0.00	82.17	100.00

Table 5.2 Experimental and theoretical constitutions of bonds samples fired at 1200°C for 40 hours. Note: % silica refers to free silica present as quartz and cristobalite (theoretical) and quartz (experimental); % liquid refers to glass in the solid state and to liquid in theoretical equilbrium at the soaking temperature.

MIXTURE	% CLAY	% FELDSPAR	% QUARTZ	% SILICA	% LIQUID		% MULLITE	
				THEORETICAL	EXPERIMENTAL	THEORETICAL	EXPERIMENTAL	THEORETICAL
A	50	10	40	7.8	44.23	40.23	47.97	20.89
B	60	10	30	9.55	41.26	43.27	49.15	25.04
C	70	10	20	10.88	39.02	47.25	50.15	32.53
D	80	10	10	11.92	37.27	50.08	50.81	39.98
E	60	15	25	5.34	48.37	48.06	46.29	27.46
F	70	15	15	7.07	45.45	50.95	47.48	34.41
G	50	20	30	- 0.9	58.89	48.47	42.01	22.45
H	60	20	20	1.69	54.53	50.88	43.78	24.36
J	70	20	10	3.71	51.12	53.37	45.17	36.18
K	60	25	15	- 1.51	59.92	54.17	41.59	30.31
L	50	30	20	- 7.29	69.67	56.24	37.62	23.53
N	50	30	20	-12.19	77.93	57.13	34.62	32.09

Table 5.3 Theoretical and experimental constitutions of bond samples fired at 1200°C for 40 hours assuming quartz does not react.

MIXTURE	C	F	Q	% A.P.	% T.P.
A	50	10	40	10.55	12.30
B	60	10	30	7.34	9.75
C	70	10	20	5.28	8.01
D	80	10	10	2.54	5.78
E	60	15	25	4.63	8.45
F	70	15	15	3.37	7.05
G	50	20	30	4.38	9.81
H	60	20	20	1.75	6.23
J	70	20	10	0.36	4.55
K	60	25	15	0.45	6.30
L	50	30	20	0.95	5.95
M	60	30	10	0.39	4.60
N	50	40	10	0.262	5.50
P	40	50	10	0.055	7.41
R	20	50	30	1.25	9.30
T	20	60	20	0.55	8.80
V	25	70	5	0.031	6.12
W	20	70	10	0.014	6.01
X	15	80	5	0.01	6.52
Y	10	80	10	-	-

Table 5.4 Apparent and true porosity data for specimens fired at 1200°C for 40 hours.

SPECIMEN	FLEXURAL STRENGTH σ_o (MN/m^2)	WEIBULL MODULUS, M	NO OF TEST PIECES FRACTURED	TENSILE STRENGTH σ_t (MN/m^2)	Log_e σ_t
A	32.4	18.1	20	26.49	3.27
B	39.6	15.8	19	31.70	3.46
C	40.8	10.1	21	30.02	3.40
D	42.3	5.3	20	26.22	3.26
E	37.1	8.3	20	26.09	3.26
F	43.9	5.8	20	27.99	3.33
G	40.1	6.2	21	26.08	3.26
H	44.7	5.45	20	27.56	3.33
I	51.4	9.6	20	37.40	3.62
K	50.3	10.5	22	37.30	3.61
L	45.1	11.3	21	33.90	3.52
M	50.8	11.7	20	38.53	3.65
N	53.6	12.4	20	41.11	3.72
P	60.35	13.1	19	46.77	3.84
R	59.9	12.8	20	46.22	3.83
T	64.8	13.2	20	50.29	3.91
V	73.2	13.3	20	56.88	4.04
W	67.75	12.75	21	52.24	3.95
X	76.1	13.1	21	58.50	4.07
Y	74.4	13.2	20	57.74	4.06

Table 5.5. Strength data for bond mixtures fired at 1200°C for 40 hours.

TEMPERATURE (°C)	TIME (hrs)	LUNDIN'S EXPERIMENTAL RESULT (% wt)	JACKSON'S EXPERIMENTAL RESULT (% wt)	JACKSON'S MODEL (% wt)
1200 (1473K)	1	24.1	24.2	24.1
1200	1	24.7	24.3	24.1
1200	1	26.1	24.8	24.1
1200	2	23.7	23.8	23.3
1200	2	23.6	23.9	23.3
1200 *	2	23.4	23.4	23.3
1200	4	21.3	22.2	22.2
1200	8	20.3	20.9	20.77
1200	18	19.0	18.5	18.51
1200	18	18.9	18.6	18.51
1200	48	15.2	15.1	14.88
1250 (1523K)	1	22.7	22.0	22.04
1250 *	2	20.6	20.6	20.53
1250	4	18.0	18.5	18.57
1250	8	15.5	16.0	16.11
1250	18	12.6	12.5	12.6
1250	48	8.3	7.8	8.0
1300	0.5	22.6	20.4	20.51
1300	0.5	21.0	20.9	20.51
1300	1	20.0	18.3	18.55
1300	2	16.1	15.9	16.1
1300	4	13.4	12.8	13.2
1300	8	10.0	9.7	9.9
1300	18	5.9	5.8	6.1
1300	50	1.6	1.8	2.3
1300	120	0.3	0.2	0.6

Table 6.1 Residual quartz content for different heat treatments of Lundin's experimental data compared with Jackson's experimental data and the theoretical model.

N.B. Asterisk indicates values used for deriving empirical model.

TEMPERATURE (°C)	MASS OF QUARTZ (% wt)	
	CALCULATED	EXPERIMENTAL
1100	24.88	24.1
1120	24.37	25.2
1150	23.28	22.9
1170	22.27	22.5
1200	20.22	20.3
1220	18.46	18.5
1250	15.22	16.1
1270	12.75	13.2
1300	8.83	8.7

Table 6.2 Calculated and experimental data for the bond composition considered for a fixed soaking time of 10 hours.

Time (hours)	Lundin's Experimental Data	Jander [191]	Krause & Keetman [189]	Mattyasovsky - Zsolnay [88]	Theoretical Model
0	41.9	41.90	-	-	41.90
0.5	35.9	41.72	22.55	20.26	34.61
1	32.8	41.54	20.76	18.75	31.97
2	29.2	41 19	18.97	17.33	28.58
4	23.2	40.49	17.18	15.98	24.39
8	19.5	39.11	15.39	14.70	19.49
18	13.3	35.72	13.30	13.30	13.30
24	10.7	33.74	12.56	12.81	11.13
48	6.9	26.18	10.77	11.71	6.43
120	3.6	7.85	28.92	10.36	2.17
190	2.7	-	7.22	9.72	1.00
258	2.0	-	6.43	9.31	0.54

Table 6.3 Residual quartz content (% wt.) for different soaking times at 1300°C for a bond mixture 40% wt. kaolin, 40% wt. quartz and 20% wt. flux (Lundin's body M21) compared with other models.

M_6C	$M_{23}C_6$	MC	Cubic M_2C	Reference
1.108				193
1.104				193
1.104	1.064	0.413-0.41		194
1.126				195
1.1095-1.114				196
1.104 -1.108	1.0638-1.051	0.43		198
	1.0618			199
1.104	1.051 -1.0638	0.43		200
1.1064-1.12				201
1.10823	1.0621	0.416		202
1.105	1.059	0.4175		203
1.108	1.059	0.4175		203
1.108	1.064			204
1.104	1.0659		0.414	205

Table 7.1 - Reported values of lattice parameters of high-speed steel carbides in the pure form and as precipitated. Units are nanometer,nm.

Steel Type	Symbol	Type Analysis (wt.%)							Hardening Temperature (°C)	Tempering Temperature (°C)	Vickers' Hardness (VPN)
		C	Cr	W	Mo	V	Co	Mn			
High Speed Steel	M1	0.85	4.0	1.8	8.75	1.1	-	-	1192/1210	550/560	804
	M2	0.9	4.15	6.35	4.95	1.85	-	-	1230/1240	550/560	865
	M15	1.55	4.7	6.5	3.0	5.0	5.0	-	1200/1220	540	951
	M42	1.08	4.0	1.5	5.5	1.15	8.0	-	1170/1210	550/580	964
	T1	0.75	4.0	18.0	-	1.1	-	-	1280/1300	560	824
	T4	0.80	4.25	18.0	0.65	1.55	4.75	-	1290/1310	560/580	892
	T15	1.35	4.15	2.0	0.85	3.75	5.0	-	1300	560	1025
Die Steel	D2	1.55	12.0	-	0.8	1.0	-	-	1010	510	689
	D3	2.20	12.50	-	-	0.25	-	-	960	490	748
Oil-Hardened Steel	01	0.9	0.5	0.5	-	0.2	-	1.25	780/810	190/220	733
Powder Metallurgy Material	ASP23	1.27	4.2	6.4	5.0	3.1	-	-	1160/1180	540/560	869

Table 7.2 - Chemical composition and thermal treatments of workpiece materials used in this study.

Symbol	Average Hardness (VPN)	Carbide Volume %			Abrasive Number (Kg/mm^2)	Carbide Diameter		
		MC	M_6C	$M_{23}C_6$		MC	M_6C	$M_{23}C_6$
M1	804	0.66	5.79	-	866	1.38	1.75	-
M2	865	1.31	5.16	-	931	1.01	1.31	-
M15	951	7.52	3.41	-	1117	3.12	1.89	-
M42	964	6.35	13.10	-	1173	2.47	2.03	-
T1	824	0.14	8.77	-	899	2.15	1.46	-
T4	892	0.25	12.68	-	993	2.54	1.73	-
T15	1025	7.36	10.35	-	1223	2.84	3.87	-
D2	689	-	-	7.34	734	3.01	2.91	-
D3	748	-	-	13.45	822	-	-	4.7
01	733	-	-	-	733	-	-	-
ASP23	869	4.94	5.24	-	1007	1.01	0.87	-

Table 7.3 - Quantitative metallographic data related to tool steels used in this work.

Structure, Ns	0	1	2	3	4	5	6	7	8	9	10	11	12	13	14
Percentage Volume of Grit, Vg (%)	62	60	58	56	54	52	48	46	44	44	42	40	38	36	34
Wheel Structure	Close					Medium					Wide				

Table 7.4 - Structure of grinding wheels based on % volume contribution of abrasive grit.

Hardness scale (ISO)		E	F	G	H	I	J	K	L	M	N	O	P	Q	R	S	T	U
		Pore volume (%)																
Structure number	Grain volume (%)	49.5	48.0	46.5	45.0	43.5	42.0	40.5	39.0	37.5	36.0	34.5	33.0	31.5	30.0	28.5	27.0	25.5
		Binder volume (%)																
0	62	—	—	—	—	—	—	—	—	0.5	2.0	3.5	5.0	6.5	8.0	9.5	11.0	12.5
1	60	—	—	—	—	—	—	—	1.0	2.5	4.0	5.5	7.0	8.5	10.0	11.5	13.0	14.5
2	58	—	—	—		—	—	1.5	3.0	4.5	6.0	7.5	9.0	10.5	12.0	13.5	15.0	16.5
3	56	—	—	—	—	0.5	2.0	3.5	5.0	6.5	8.0	9.5	11.0	12.5	14.0	15.5	17.0	18.5
4	54	—	—	—	1.0	2.5	4.0	5.5	7.0	8.5	10.0	11.5	13.0	14.5	16.0	17.5	19.0	20.5
5	52	—	—	1.5	3.0	4.5	6.0	7.5	9.0	10.5	12.0	13.5	15.0	16.5	18.0	19.5	21.0	22.5
6	50	0.5	2.0	3.5	5.0	6.5	8.0	9.5	11.0	12.5	14.0	15.5	17.0	18.5	20.0	21.5	23.0	24.5
7	48	2.5	4.0	5.5	7.0	8.5	10.0	11.5	13.0	14.5	16.0	17.5	19.0	20.5	22.0	23.5	25.0	26.5
8	46	4.5	6.0	7.5	9.0	10.5	12.0	13.5	15.0	16.5	18.0	19.5	21.0	22.5	24.0	25.5	27.0	28.5
9	44	6.5	8.0	9.5	11.0	12.5	14.0	15.5	17.0	18.5	20.0	21.5	23.0	24.5	26.0	27.5	29.0	30.5
10	42	8.5	10.0	11.5	13.0	14.5	16.0	17.5	19.0	20.5	22.0	23.5	25.0	26.5	28.0	29.5	31.0	32.5
11	40	10.5	12.0	13.5	15.0	16.5	18.0	19.5	21.0	22.5	24.0	25.5	27.0	28.5	30.0	31.5	33.0	34.5
12	38	12.5	14.0	15.5	17.0	18.5	20.0	21.5	23.0	24.5	26.0	27.5	29.0	30.5	32.0	33.5	35.0	36.5

Table 7.5 - The relationship between hardness, structure number and volume proportions of grit, bond and porosity in vitrified grinding wheels.

Oxide	Winkelmann and Schott [208]	English and Turner [209]	Gilard and Dubrul [210]	Hall [211]
SiO_2	2.67	0.5	0.4	1.4
B_2O_3	0.33	- 6.53	- 4+0.1p	2
Na_2O	33.33	41.6	51-0.33p	38
K_2O	28.33	39	42-0.33p	30
MgO	0.33	4.5	0	2
CaO	16.67	16.3	7.5+0.35p	15
Zno	6.0	7	7.75-0.25p	10
BaO	10.0	14.0	9.7+0.14p	12
PbO	10.0	10.6	11.5-0.05p	7.5
Al_2O_3	16.67	1.4	2	5

Table 7.6 - Constants for oxides according to various researchers [208-211].

Glass Frit	Oxide Wt. %						Coefficient of Thermal Expansion ($10^{-6}/°C$)				
	SiO_2	B_2O_3	Al_2O_3	Na_2O	CaO	MgO	Experimental	Winkelmann and Schott [208]	English and Turner [209]	Gilard and Dubrul [201]	Hall [211]
F1	59.2	26.2	9.2	5.4	-	-	5	5	0.96	2.13	3.86
F2	38	25	30	5	2	-	8.8	8.1	1.38	-0.52	4.73
F3	44	29	14.4	-	2.2	10.4	4.7	4.07	-0.64	-0.34	2.45
F4	69.8	2.6	3.7	17.6	6.3	-	10.1	9.4	8.58	9.68	8.79
F5	71.5	5.05	13.70	4.35	0.60	0.66	6.1	5.76	2.15	65.04	3.66
F6	63.59	15.48	4.27	5.84	5.54	3.37	6.05	5.34	2.85	55.15	4.35
F7	60.6	13.49	17.09	1.66	2.81	0.14	5.05	5.53	1.63	55.08	3.03
F8	68.7	6.84	18.71	0.25	1.36	0.13	4.75	4.42	1.55	59.1	2.33
F9	70.96	3.68	18.20	2.81	0.11	0.13	5.85	5.89	1.56	55.14	3.06
F10	54.50	12.80	16.40	1.84	0.06	0.13	5.87	4.85	0.45	55.05	2.56

Table 7.7 - Experimental and empirical expansion coefficients for various borosilicate glasses. Empirical results based on published data [208-211].

Bond Composition	Oxide (Wt.%)						Coefficient of Thermal Expansion (10^{-6}/°C)	
	Al_2O_3	SiO_2	K_2O	Na_2O	CaO	MgO	Experimental	Hall[211]
P	22.67	63.14	6.19	1.66	0.1	0.11	4.9	4.52
R	16.00	72.82	5.85	1.63	0.07	0.08	4.4	4.20
T	17.74	69.64	6.95	1.95	0.08	0.05	4.6	4.70
V	21.14	64.04	8.14	2.27	0.10	0.10	5.4	5.27
W	19.47	66.46	8.05	2.27	0.09	0.09	5.0	5.21
X	19.54	65.70	9.06	2.58	0.09	0.10	5.6	5.62

Table 7.8 - Experimental and empirical expansion coefficients for alumino-silicate glasses used in this study. Empirical results are based on data published by Hall [211].

Test Number	Bond Grade And Composition					
	KP	KR	KT	LV	LW	LX
1	M1	ASP23	01	D3	D2	T14
2	M2	M1	ASP23	01	D3	D2
3	M15	M2	M1	ASP23	01	D3
4	M42	M15	M2	M1	ASP23	01
5	T1	M42	M15	M2	1	ASP23
6	T4	T1	M42	M15	M2	M1
7	T15	T4	T1	M42	M15	M2
8	D2	T15	T4	T1	M42	M15
9	D3	D2	T15	T4	T1	M42
10	01	D3	D2	T15	T4	T1
11	ASP23	01	D3	D2	T15	T4

Table 7.9 - Pseudo-random order of workpiece materials and grinding wheel bond compositions used in the experimental trials.

Abrasive Number	Workpiece Material	G-Ratio (mm^3/mm^3)					
		Bond Composition					
		P	R	T	V	W	X
866	M1	11.1	9.9	12.6	14.9	13.8	16.4
931	M2	8.8	8.3	7.9	9.1	8.4	9.6
1117	M15	1.3	1.1	1.4	1.9	1.7	2.1
1172	M42	1.5	1.3	1.6	2.1	1.8	2.3
899	T1	6.8	5.8	7.6	9.7	8.7	10.9
993	T4	2.6	2.3	3.1	3.8	3.5	4.1
1223	T15	1.2	1.0	1.1	1.5	1.4	1.9
734	D2	41.2	39.9	42.6	46.8	44.5	48.5
822	D3	12.8	11.3	13.9	16.6	15.2	18.1
733	O1	49.7	48.4	51.1	55.4	53.7	57.2
1007	ASP23	5.0	4.8	5.4	6.0	5.7	6.2

Table 7.10 - The effect of bond composition on the G-ratio for workpiece materials used in this work.

APPENDIX A

EXPERIMENTAL DETERMINATION OF THE MEASURES OF VITRIFICATION

In order to measure water absorption, apparent porosity, and bulk density of each specimen, test pieces were first weighed in air to an accuracy of 0.001g. This produced the weight of the sample in air, W_A. In order to cause water to fill the pores of the test piece, the test piece was immersed in a container of distilled water and boiled for two hours until all the pores were infiltrated with water to room temperature. The test piece was placed in a dish suspended from the arm of the balance into the water and weighed. This resulted in a value for the weight of the test piece in water, W_s. The test pieces were weighed in air with water filling the pores of the test piece. This gave a value corresponding to the weight of test piece with water filling the pores, W_w.

The following equations for vitrification measures were made assuming that the density of water is $1 g/cm^3$:

$$\% \text{ Water absorption (W.A.)} = \frac{W_w - W_A}{W_A} \times 100 \quad \ldots(A.1.)$$

$$\% \text{ Apparent porosity (A.P.)} = \frac{W_w - W_A}{W_w - W_s} \times 100 \quad \ldots(A.2.)$$

$$\text{Bulk density (B.D.)} = \frac{W_A}{W_w - W_s} \cdot \rho_{\text{water}} \ (g/cm^3) \quad \ldots(A.3)$$

APPENDIX B

COMPOSITION OF RAW MATERIALS

The raw materials used in the experimental work were ball clay (Hymod Prima) supplied by E.C.C., china clay (Standard Porcelain) also supplied by E.C.C., potash feldspar supplied by Cookson Ceramic Materials, and synthetic quartz (silica flour) supplied by Hepworth Minerals.

The chemical analyses of all raw materials appears below. A rational analysis was performed to reveal the mineralogical composition of the raw materials. These results were compared with characteristic x-ray spectra generated for these raw materials.

COMPOUND (Wt %)	CHINA CLAY	BALL CLAY	POTASH FELDSPAR	QUARTZ
Al_2O_3	37.0	31.0	18.01	0.65
SiO_2	48.0	52.0	66.60	98.40
K_2O	1.65	1.8	11.01	0.35
Na_2O	0.1	0.2	3.2	0.04
CaO	0.07	0.2	0.09	-
MgO	0.03	0.3	0.09	-
TiO_2	0.02	0.9	-	0.07
Fe_2O_3	0.68	1.1	0.11	0.029
Loss	12.50	16.5	0.89	0.20

Chemical analyses of raw materials used in the experimental work.

COMPOUND (Wt %)	CHINA CLAY	BALL CLAY	POTASH FELDSPAR	QUARTZ
Quartz	4.05	12.77	4.93	98.40
Orthoclase	-	15.23	64.96	-
Kaolinite	79.70	62.71	2.17	-
Mica	13.94	-	-	-
Soda Feldspar	0.8	1.69	27.07	-
Miscellaneous Oxides & Losses	1.51	7.60	0.87	1.60

Mineralogical analyses of raw materials used in the experimental work.

APPENDIX C

EXPERIMENTAL DETERMINATION OF POWDER DENSITY AND TRUE POROSITY

Powders ground from test pieces used for x-ray analysis were used for powder density measurements. A liquid displacement technique was used to measure powder density using a specific gravity bottle. Distilled water was used throughout the procedure - density 1.00g/cm^3.

Firstly, the specific gravity bottle was washed and dried, and the weight of the bottle and stopper, W_{bottle}, was measured. Secondly, the bottle was filled to one third of its volume with powder and the weight, W_{powder}, measured. In all cases the weight of the stopper was included in all measurements. The weight of the powder was then given by subtracting W_{bottle} from W_{powder}. All measurements were accurate to 0.001g.

To determine the volume of the powder, the bottle was filled with distilled water until all air bubbles were expelled from the vessel. The stopper was inserted and excess liquid removed using filter paper. The total weight, W_{total}, was then measured. In order to standardise each test, the same procedure was used with the bottle filled with water then measuring the weight, W_{liquid}, in the same way as stated. Assuming the density of water to be ρ_{water}, the powder density was calculated using the formula,

P. D. =

$$\frac{(W_{powder} - W_{bottle}).\rho_{water}}{(W_{liquid}-W_{bottle})-(W_{total}-W_{powder})} \quad \ldots(C1)$$

From this equation the magnitude of the true porosity of the specimen can be found using the equation,

$$\% \text{ T.P.} = 100 \quad 1 - \frac{\text{Bulk density}}{\text{Powder density}} \quad \ldots(C2)$$

APPENDIX D

QUANTITATIVE X-RAY ANALYSIS OF BOND COMPOSITION

X-ray diffraction of the raw materials was performed on a Phillips 1710 x-ray generator with a 40kV tube voltage and a 30mA current. Monochromatic Cu k_{α} radiation, λ = 0.154060nm, was employed. A scanning speed of 2°/minute for diffraction angles of 2θ was used between 2θ angles of 10° and 80°, and the x-ray intensity was recorded using a computer. The spectrum was then analysed and compared with known spectra which was stored on CD-ROM medium.

Test pieces were prepared by crushing in a mortar in preparation for quantitative x-ray diffraction. To eliminate the requirement of knowing mass absorption coefficients of ceramic samples for quantitative x-ray diffraction, Alexander and Klug [219] introduced the use of an internal standard. Firstly, the ceramic sample is crushed to form a powder - the sizes of particles should be small enough to make extinction and micro-absorption effects negligible. Secondly, the internal standard to be added should have a mass absorption coefficient at a radiation wavelength such that intensity peaks from the phase(s) being measured are not diminished or amplified. It should be noted that the powder diffraction mixture should be homogeneous on a scale of size smaller than the amount of material exposed to the x-ray beam and free from preferred orientation. The powder bed which is 'x-rayed' should be deep enough to give maximum diffracted intensity.

The expected equilibrium phases from the fired mixtures are quartz (unreacted and partially dissolved), mullite, cristobalite and glass. However, from the samples tested, the compounds quartz, mullite and glass were successfully detected. A calibration curve was constructed using a suitable internal standard (calcium fluoride), a diluent (glass made by melting potash feldspar), and a synthetic form of the phase(s) to be measured. The synthetic mullite was supplied by Keith Ceramic Materials (> 99.8% purity), and powdered quartz supplied by Hepworth Minerals (98.4% SiO_2). The method used for the quantitative analysis was based on that used by Khandewal and Cook [220].

The internal standard, CaF_2, gave a fairly intense (111) reflection (d = 0.1354nm) lying between the (100) reflection for quartz (d = 0.4257nm) and the (200) reflection for mullite (d = 0.3773nm). Using copper k_α radiation (λ = 0.15405nm), the corresponding values of diffraction angle 2θ are: (100) quartz = 20.82°; (111) CaF_2 = 28.3°; and (200) mullite = 32.26°. Figure 1 shows the calibration curve generated by varying proportions of CaF_2 and synthetic quartz and mullite. From this curve, the weight fractions of the crystalline phases in the phases can be read from the calibration lines by measuring the intensity ratio of the phase(s) to the standard. Figure 2 shows the three diffraction peaks of interest for quantitative analysis lying between 15° and 40° of the diffraction angle 2θ. The figure shows the reflections of the (111) plane of calcium fluoride, (200) plane of mullite, and the (100) plane of quartz. Figure 3 shows the complete range of planes for the bond used. In order to calculate the weight fractions of quartz and mullite in the mixture the height of the chosen diffraction peak and its width at half-height, were measured from the diffraction spectrum.

The product of these measures was then compared with that of the internal standard and the resultant intensity ratio used to find the exact weight fraction of the phase(s) measured in the material that has been x-rayed.

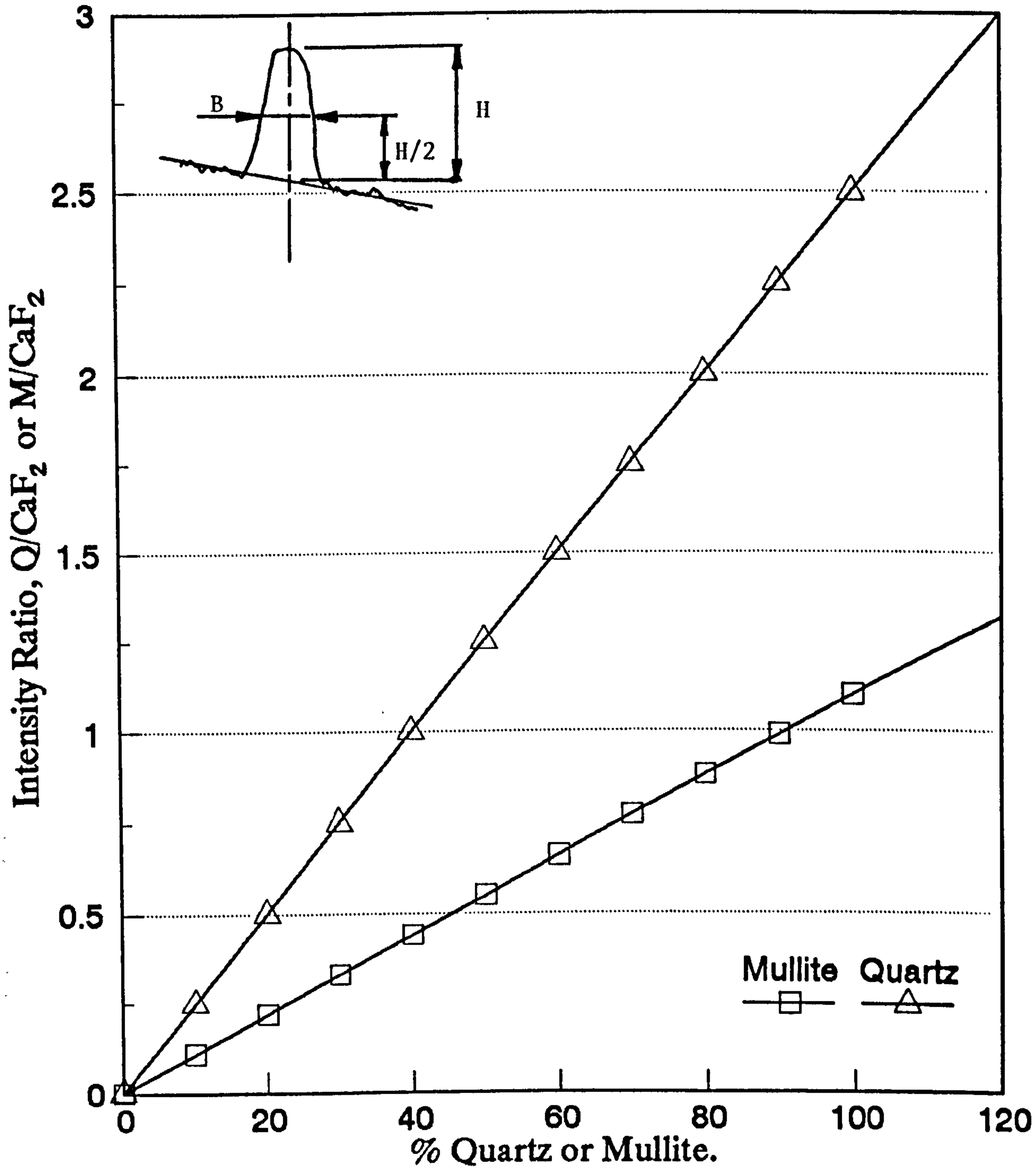

Figure 1. Calibration curve for quantitative analysis of x-ray determined quartz and mullite using the CaF_2 (111) plane generated by the internal standard.

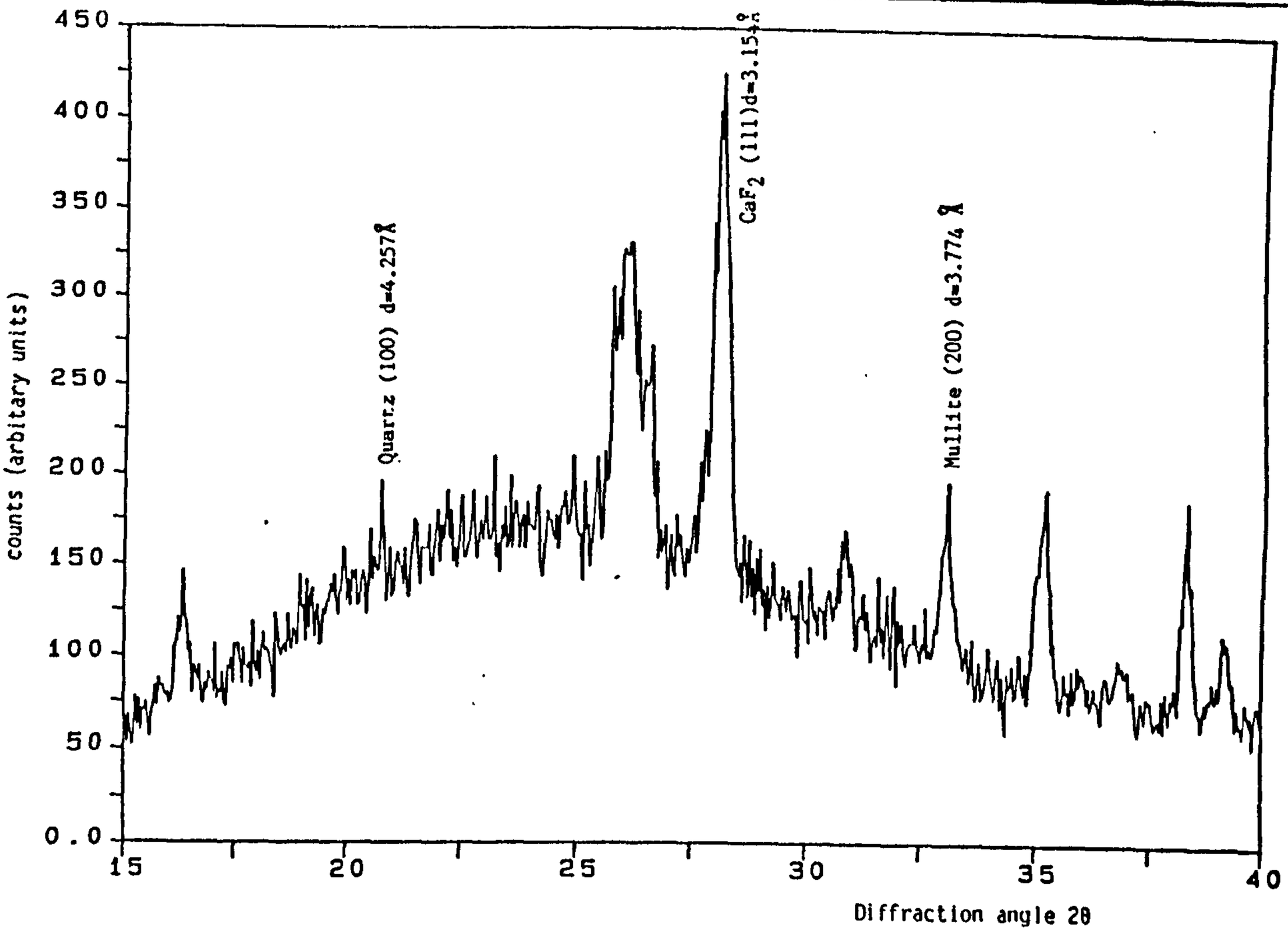

Figure 2. X-ray diffraction spectrum of fired bond plus 0.2g of CaF_2 (internal standard) scanned between the 2θ angles of 15°-40°. The scan rate was 2°/minute. The spectrum shows the characteristic peaks used for quantitative analysis.

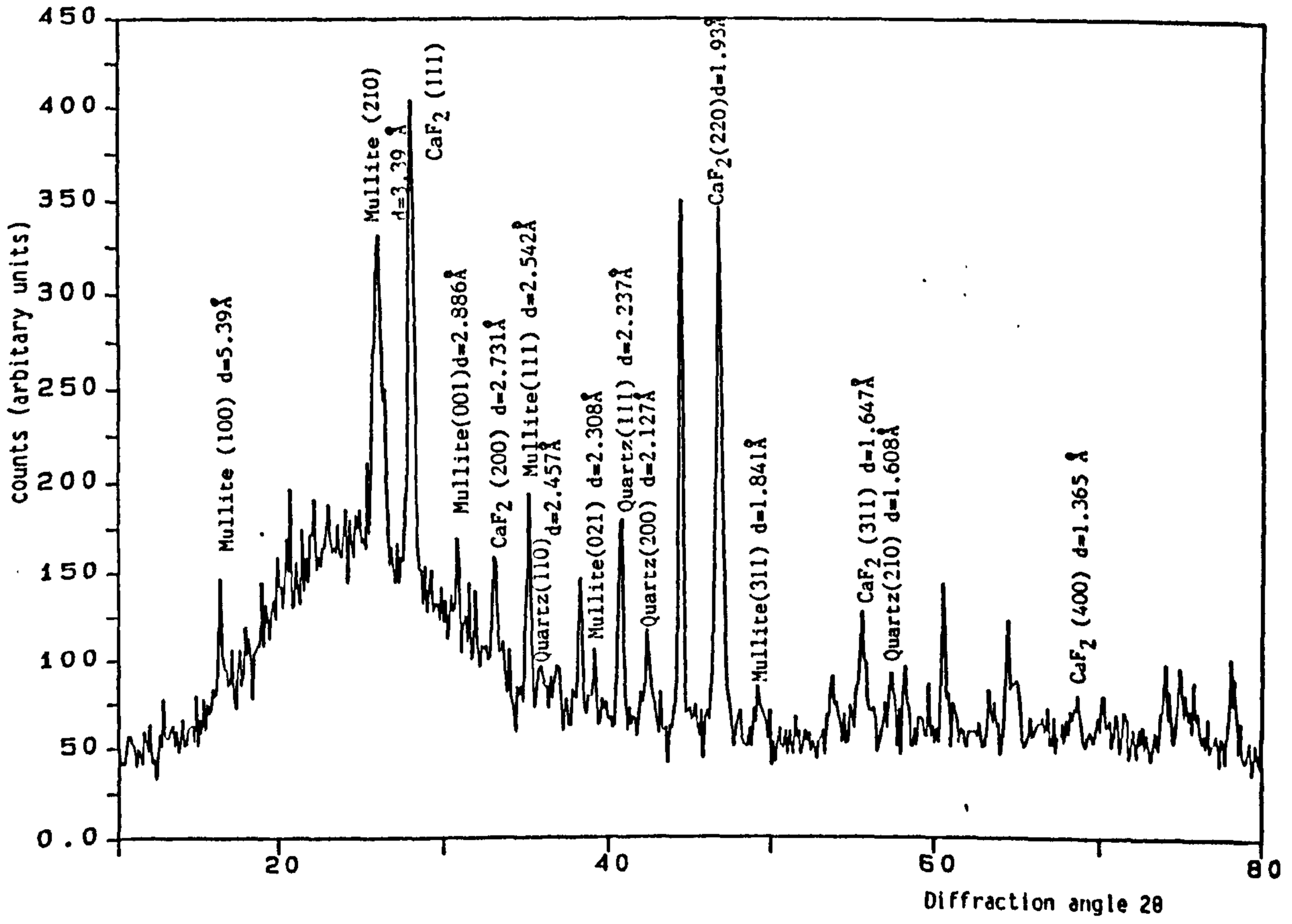

Figure 3. X.R.D. spectrum of fired bond showing interplanar distances of crystallographic planes of mullite, quartz and CaF_2. Scan rate was 2°/minute.

APPENDIX E

EXPERIMENTAL DETERMINATION OF THE TENSILE STRENGTH OF VITRIFIED BONDS

The measurement of tensile strength of ceramic materials requires the use of Weibull statistics. Owing to the large variation in strength between test samples due to the size and distribution of pores within the material, Weibull estimated that in order to reduce the % error in the Weibull modulus parameter, m, at least twenty specimens are required to be fractured. Since it is impractical to test each bar in pure tension due to the occurrence of 'crumbling' of the test pieces, it is necessary to fracture the specimens in flexure. Ideally, the whole volume of the test piece should be subjected to the bending load. However, it may not be possible to do this. In this case, the differences in stress field within the test specimens can be related to their volumes using the Weibull modulus, m.

Initially, each test sample is fractured in flexure. The bending strength is given by the equation,

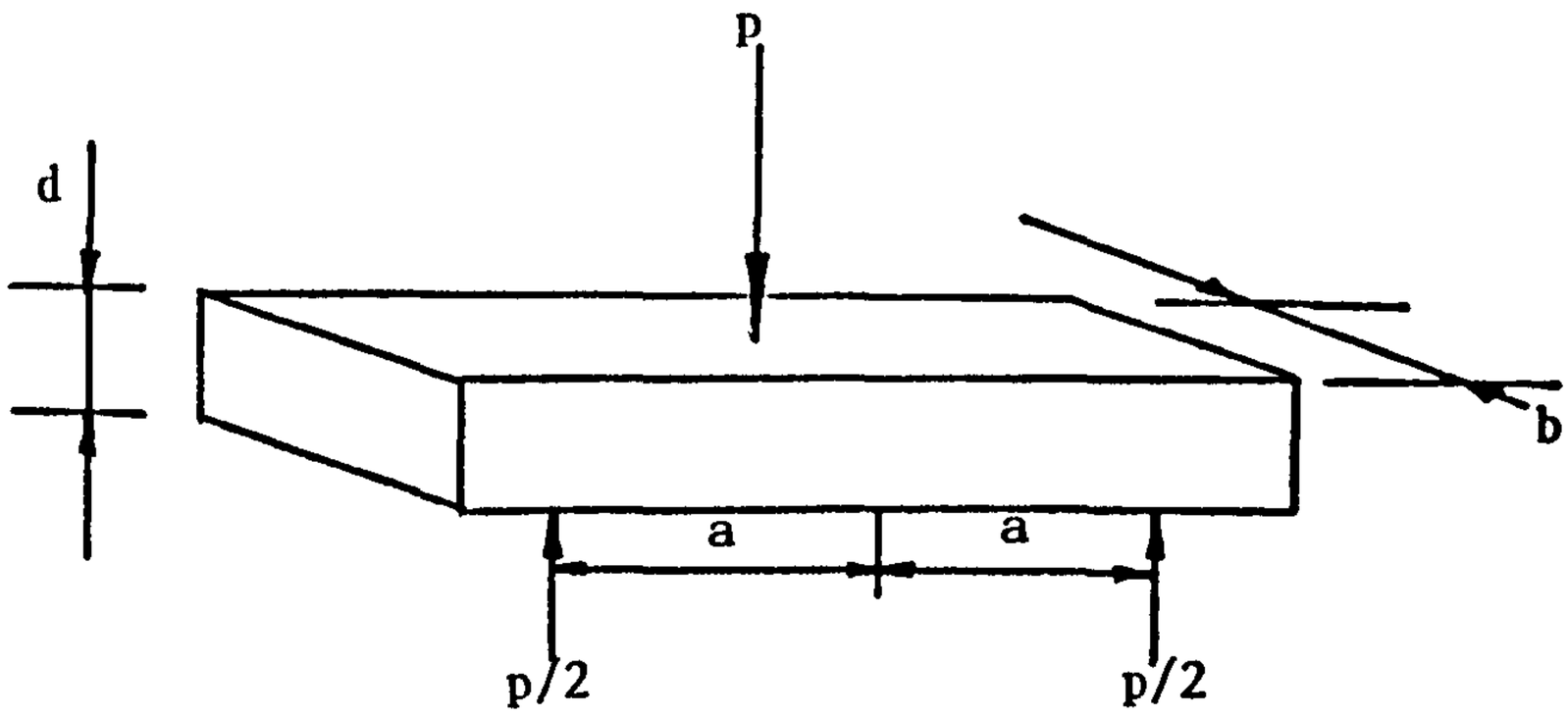

THREE-POINT BENDING ARRANGEMENT

$$\sigma_{flexure} = \frac{3.p.a}{b.d^2} \qquad \ldots(E1)$$

Once fractured, the specimens are ranked in order of bending strength magnitude. The average bending strength is found using a method developed by Gumbel [221] based on the statistical treatment of extremes. The average strength is found by locating the average extreme, or in statistical terms, the j_o sample.

The j_o sample is found using the equation,

$$j_o = (0.63 \times \text{number of specimens}) + 0.55 \qquad \ldots(E2)$$

From this, the j_o sample will have a particular bending strength which is denoted, σ_o.

Weibull predicted the failure probability to be,

$$F_j = \frac{j - 0.3}{\text{Number of specimens} + 0.4} \qquad \ldots(E3.)$$

where j is the representative sample. The survival probability of each sample is simply,

$$S_j = 1 - F_j = 1 - \left\{\frac{j - 0.3}{\text{Number of specimens} + 0.4}\right\} \qquad \ldots(E4.)$$

from which the Weibull modulus can be found by plotting $1n.1n\ (1/S_j)$ as ordinate and $1n\ (\sigma_j/\sigma_o)$ as absissa.

As a consequence of different stress fields in geometrically similar specimens, if the specimen is subject to bending then the tensile stress will vary from point to point. In this case the tensile stress, σ_t, has become a geometric variable, $\sigma\ (x,y,z)$, so that the element of volume, dv, becomes (dx, dy, dz). Weibull's equation for survival probability for a set of test pieces with constant volume is,

$$S = \exp\left\{ - \int_{v} \left[\frac{\sigma}{\sigma_o}\right]^m \frac{dv}{v} \right\} \qquad \ldots(E5)$$

Considering stress as a geometric variable, equation E5 becomes,

$$S = \exp\left\{ - \int\int\int \left[\frac{\sigma\,(x,y,z,)}{\sigma_o}\right]^m \frac{dxdydz}{v} \right\} \qquad \ldots(E6)$$

The integration over volume requires the stress distribution over that volume. The bar specimens are subjected to bending stresses. These values are required to be converted into tensile stresses. The specimens are thus subjected to both cases, i.e.

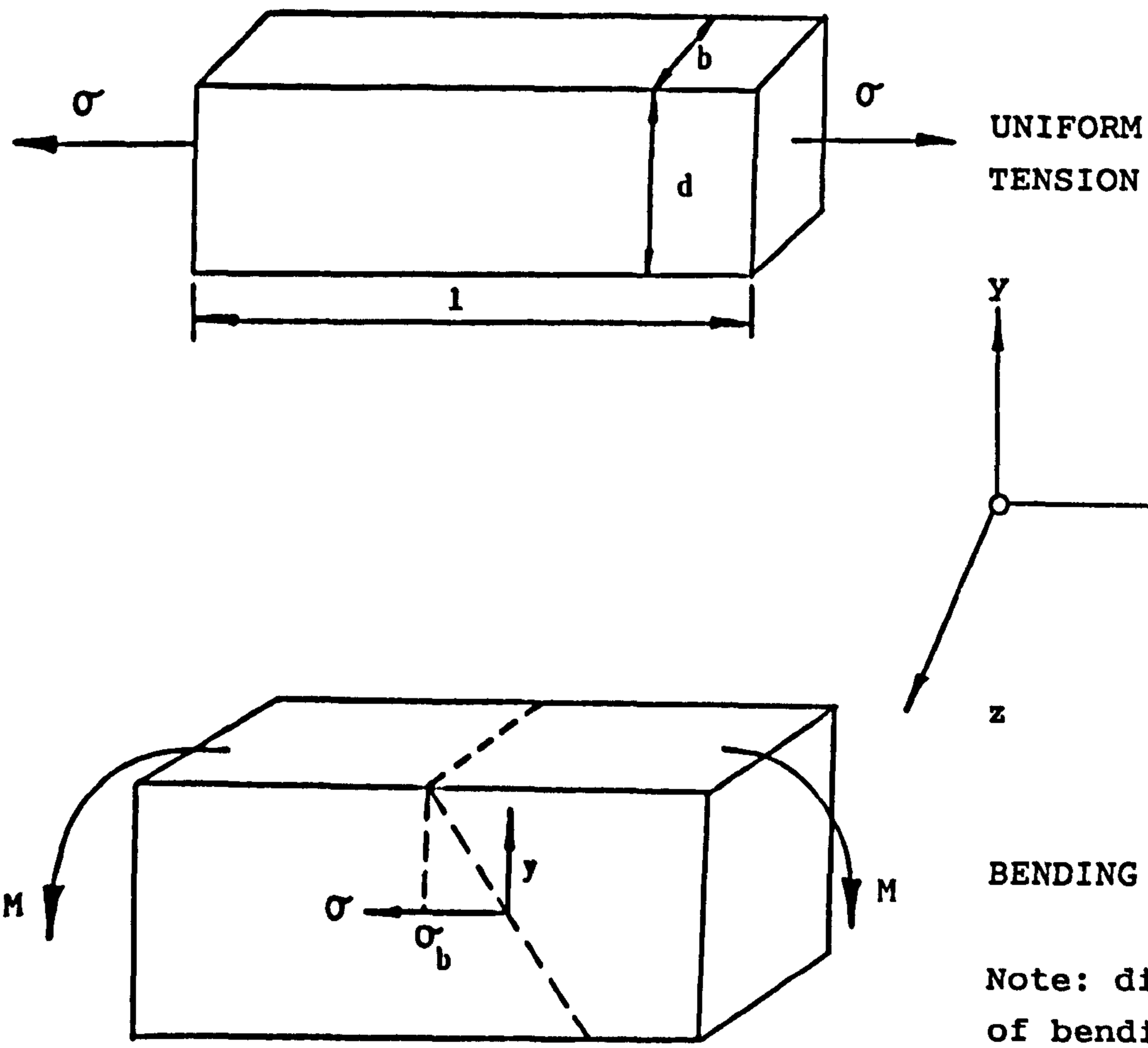

Note: distribution of bending stress is plotted onto the surface of the specimen.

TENSION

Here, the tensile stress is constant throughout the specimen and σ is not a function of x, y and z. The exponent in equation E6 is simply,

$$\int_0^l \int_0^d \int_0^b \left[\frac{\sigma(x,y,z)}{\sigma_o}\right]^m \frac{dxdydz}{v} = \frac{ldb}{v}\left[\frac{\sigma_t}{\sigma_o}\right]^m \qquad \ldots(E7)$$

PURE BENDING

The tensile stress in bending varies linearly with distance in the y - direction; in the x and z directions, σ is constant for a given value of y. If the bending stress is σ_b at the top surface (y=d/2) then at any value of y, the stress $\sigma(y) = 2\sigma_b y/t$. This stress is tensile only at the points above the neutral axis ($o \leq y \geq d/2$). The exponent in equation E6 is simply,

$$\int_0^l \int_0^a \int_0^b \left[\frac{\sigma(y)}{\sigma_o}\right]^m \frac{dxdydz}{v} = \frac{lb}{v}\int_0^{d/2}\left[\frac{2\sigma_b y}{\sigma_o t}\right]^m dy$$

$$\int_0^l \int_0^a \int_0^b \left[\frac{\sigma(y)}{\sigma_o}\right]^m \frac{dxdydz}{v} = \frac{lb}{v}\left[\frac{2\sigma_b}{\sigma_o t}\right]\int_0^{d/2} y^m dy$$

$$\int_0^l \int_0^a \int_0^b \left[\frac{\sigma(y)}{\sigma_o}\right]^m \frac{dxdydz}{v} = \frac{lb}{v}\left[\frac{2\sigma_b}{\sigma_o t}\right]\left[\frac{y^{m+1}}{m+1}\right]_0^{d/2}$$

$$\int_0^l \int_0^a \int_0^b \left[\frac{\sigma(y)}{\sigma_o}\right]^m \frac{dxdydz}{v} = \frac{ldb}{2(m+1)}\left[\frac{\sigma_b}{\sigma_o}\right]^m \frac{1}{v}$$

$$\ldots(E8)$$

Assuming the probability of survival to be the same in the two specimens then equations E8 and E7 must be equal:

$$\frac{1db}{v}\left\{\frac{\sigma_t}{\sigma_o}\right\}^m = \frac{1db}{2(m+1)}\left\{\frac{\sigma_b}{\sigma_o}\right\}^m \frac{1}{v}$$

Re-arranging yields

$$\sigma_t = \frac{\sigma_b}{\{2\ (m+1)\}^{1/m}} \qquad \ldots(E9)$$

This is the ratio of strengths of the two test piece samples for a given probability of failure. It is used to relate the strength of ceramic geometrically similar test pieces with different stress fields. It can be seen that the bending strength is higher due to the effect of a smaller stressed volume when subjected to tensile stresses.

APPENDIX F

UNIVERSAL

E·A·C

Doxey Road, Stafford, England, ST16 1EA. Tel: (0785) 223281. Telex: 36139. Fax: (0785) 213487

GRINDING SEGMENTS FOR LIVERPOOL JOHN MOORES UNIVERSITY

The following segments have been speed tested, without failure, to 45 m/s.

KP	Nos. 1 - 6
KR	Nos. 1 - 6
KT	Nos. 1 - 6
LV	Nos. 1 - 6
LW	Nos. 1 - 6
LX	Nos. 1 - 6
LY	Nos. 1 - 6

P. J. Derbyshire

Peter Derbyshire
Process & Product Development Manager

APPENDIX G

EXPERIMENTAL DETERMINATION OF THE LINEAR COEFFICIENT OF THERMAL EXPANSION

The linear coefficient of thermal *expansion* was measured using a Linseis dilatometer. The measurements were taken between 20°C and 1000°C (below the glass transition point of the bond mixture). The expansion of the glass was determined on a rod specimen (length 30mm), the expansion of which was measured relative to the reference specimen, i.e. fused silica. The relative expansion was measured using a linear differential transformer. The specimen was heated up at a rate of 5°C per minute. The schematic diagram appears below.

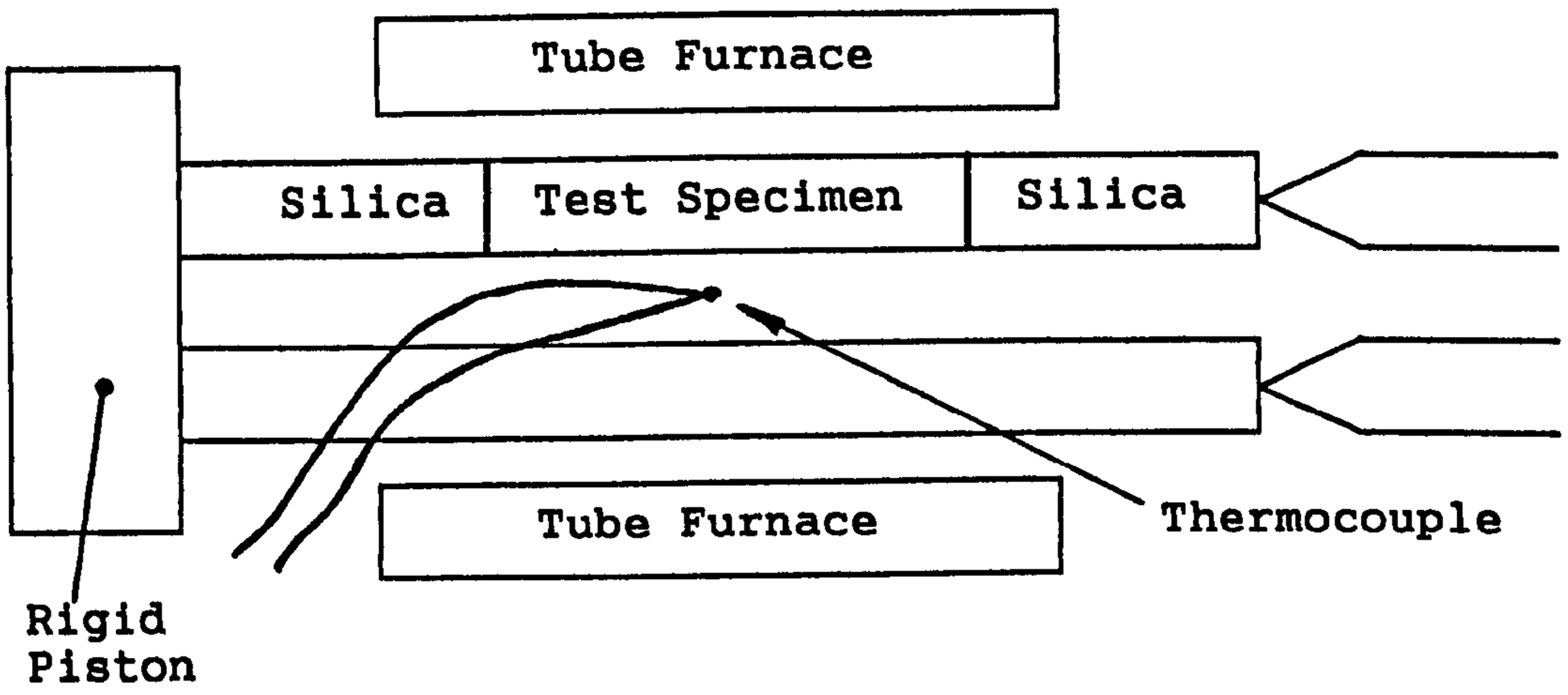

The thermocouple is placed in the centre of the measuring system, whilst the difference in length is measured at the right-hand side of the schematic diagram. The mean coefficient of linear expansion is given by applying the following equation:

$$\alpha_{exp} = \frac{1}{\ell_1} \cdot \frac{\Delta \ell}{\Delta T} \qquad \ldots(G.1)$$

where $\Delta \ell = \ell_2 - \ell_1$, which is the increase in the length of the specimen (ℓ_1 is the original length) when heated over the temperature range ΔT ($= T_2 - T_1$).